Doctoral Thesis

Thesis Title

Structural and Magnetic Properties for Bilayers of Cubic and Tetragonal Heusler Alloys

Department of Applied Physics

Graduate School of Engineering,

TOHOKU UNIVERSITY

Reza Ranjbar Dizaj

(ID No. B2TD3010)

January 2015

Abstract

The requirements for high density spin transfer torque magnetoresistance random access memory (STT-MRAM) application in generally are the tunnel magnetoresistance (TMR) ratio more than 100% at room temperature, the critical current density less than 0.5 MA/cm^2, and thermal stability factor larger than 60 for 10 years longevity. Perpendicular magnetic tunnel junctions (p-MTJs) based on MnGa with perpendicular magnetic anisotropy (PMA) is one of the good candidate for satisfying the above mentioned properties. One of the issues related to MnGa alloy based MgO-MTJs is small TMR ratio, which is probably due to the large lattice mismatch between MnGa and MgO and also the oxidation of interface. The relatively high TMR ratio has been reported in the p-MTJs based on MnGa electrode with an ultra-thin ferromagnetic metal/alloy interlayer between MnGa and MgO barrier. Interestingly, the magnetic interfacial exchange coupling (J_{ex}) was found to be ferromagnetic (antiferromagnetic) for the Fe (Co)-rich interlayer, when the FeCo alloys interlayer were introduced. So, further investigation of this coupling in magnetic bilayer with MnGa is meaningful because the antiferromagnetic coupling is very rare in the magnetic films with PMA and is technologically important to achieve synthetic ferrimagnetic structure for memory applications. To reduce critical current density with maintaining thermal stability factor, thickness of this synthetic ferrimagnet should be less than 5 nm which is important to use as free layer in p-MTJs based on MnGa alloy. In This dissertation we study on the structural and magnetic properties of the bilayer consisting of in plane magnetic anisotropy materials (IMA) and $D0_{22}$-MnGa film. The Co-B binary and Co-based cubic Heusler alloys including Co_2FeAl (CFA), Co_2FeSi (CFS), Co_2MnAl (CMA), and Co_2MnSi (CMS) were used as IMA materials. Objectives of this research to satisfy requirements for STT-MRAM are:

1) Investigation of structure and magnetic properties of cubic Heusler/tetragonal $D0_{22}$-MnGa bilayer film.

2) Investigation of J_{ex} of cubic Heusler/tetragonal $D0_{22}$-MnGa bilayer to get strong antiferromagnetic J_{ex}.

3) Make clear the origin of the J_{ex} for cubic Heusler/tetragonal $D0_{22}$-MnGa bilayer.

4) Reduction of thickness of cubic Heusler/tetragonal $D0_{22}$-MnGa bilayer to achieve synthetic ferrimagnet with PMA.

To investigate structural and magnetic properties of IMA/$D0_{22}$-MnGa bilayers we have fabricated different bilayers with the stacking structure of (100) single crystalline MgO substrate / Cr (10) / $D0_{22}$-MnGa (30) / IMA (20) / Cr (5) (thickness is in nanometers). The epitaxial bilayers were fabricated using an ultrahigh vacuum magnetron sputtering system with a base pressure of less than 1×10^{-7} Pa. All the layers were deposited at room temperature. The in-situ annealing was employed at 400ºC after the MnGa deposition. Annealing temperature dependence has been investigated by rapid thermal annealing (RTA) system. In order to fabricate synthetic ferrimagnet with good PMA, the thickness of IMA materials were decreased. Two series IMA (1-20)/$D0_{22}$-MnGa (30) bilayer films without and with post annealing at optimized annealing temperature were fabricated. Finally the thickness of CMS Heusler alloy and $D0_{22}$-MnGa were decreased to achieve ultra-thin synthetic ferrimagnet. For characterization of structural and magnetic properties, the X-ray diffractometer (XRD) with the Cu K_α radiation, polar magneto optical Kerr effect (P-MOKE) system at laser wavelength of 400 nm, and a vibrating sample magnetometer (VSM) were used.

All the bilayer films have been successfully grown even for un-annealed samples. Large critical annealing temperature (450°C) were observed for the CFA/MnGa and CMA/MnGa bilayer, which shows the good structural stability. The antiferromagnetic J_{ex} were observed for CFS/MnGa (J_{ex} = -0.4 ~ -1 erg/cm^2), CMA/MnGa (J_{ex} = -0.75 ~ -1.15 erg/cm^2), and CMS/MnGa (J_{ex} = -2.5 ~ -3.2 erg/cm^2) bilayers, whereas both kinds of J_{ex} were observed in the CFA/MnGa (J_{ex} = 0.8 ~ -1.5 erg/cm^2) bilayer depending on annealing temperature. The ferromagnetic and antiferromagnetic J_{ex} in Co-based cubic Heusler alloys and tetragonal $D0_{22}$-MnGa film originate from their electronic band structure at Fermi level. The relative strong J_{ex} about -3.2 erg/cm^2 was observed for CMS/MnGa bilayer which is comparable with Fe-Co/MnGa work. The large critical thickness between 5 and 10 nm was observed for CMS/MnGa bilayer which originates from strong antiferromagnetic J_{ex} and moderate saturation magnetization compared to other Co-based cubic Heusler alloys. The bilayer with 1-nm-thick CMS and 7.5-nm-thick $D0_{22}$-MnGa shows good PMA which makes this bilayer as good choice for making free electrode of p-MTJ based on MnGa alloy.

Acknowledgements

I would like to express my sincere thanks to my supervisors, Prof. Yasuo Ando and Prof. Shigemi Mizukami, WPI-AIMR Tohoku University; for their great support, valuable guidance and encouragement during this period. Their beneficial advices, creative comments during this work. I am very glad and honored to be one of their students in Ando and Mizukami spintronics laboratory.

I would like to especially thank emeritus Prof. Terunobu Miyazaki in Tohoku University, for his support and helps in this research and my life in Japan.

I would like to thank Prof. Sakuma and Prof. Kitakami for their referee.

I would also like to thank Associate Prof. Mikihiko Oogane and Assistant Prof. Hiroshi. Naganuma in Ando spintronics laboratory for their guidance and support.

I would like to thank Assistant Prof. Takahide Kubota in AIMR (currently belong to IMR) who is belong to Takanashi laboratory in Tohoku University for his wonderful and great helps during my research. I would like to thank Prof. Xianmin Zhang in AIMR who is now belong to Northeastern University of China for his useful comments and advise.

The most valuable experiments for this research were performed with the help of other staff members of Mizukami laboratory, Dr. Qinli Ma, Atsushi Sugihara and Kazuya Suzuki. They kindly performed a lot of falling experiments and generously proposed performing real fall accidents which was very valuable and useful in fulfilment of this project. Performing these experiments were not possible without the support and help of Mr. Yukio Kondo who is technical staff of Mizukami laboratory. I would like to thank Mr. Kazuhiro Sugiyama who is researcher in WPI-AIMR.

I would like also to thank Ms. Rie Nakayama, Ms. Chika Hosokawa, and Ms. Mayumi Yamaguchi for their kindly helps and support during my stay in Japan.

I would also like to thank all the students in our laboratory specially Mr. Satoshi Iihama who helped me a lot and made this period more enjoyable and comfortable for me.

I would like finally to thank WPI program, JGC-S (Nikki), and JASSO scholarships to make my life easier in Japan.

List of publications/presentations

Paper in Journal:

1. "Magnetic properties of $L1_0$-$Mn_{57}Ga_{43}$/Co bilayer films with different Co thicknesses", R. Ranjbar, S. Mizukami, Y. Ando, T. Kubota, Q. L. Ma, X. M. Zhang, T. Miyazaki., J. Magn. Magn. Mater. 346, 53-57 (2013).
2. "Magnetization dynamics for $L1_0$ MnGa/Fe exchange coupled bilayers", S. Mizukami, T. Kubota, S. Iihama, R. Ranjbar, Q. Ma, X. Zhang, Y. Ando, and T. Miyazaki., J. Appl. Phys. 115, 17C119 (2014).
3. "The interfacial exchange coupling in cubic Heusler Co_2FeZ (Z=Al and Si)/tetragonal Mn_3Ga bilayers", R. Ranjbar, K. Suzuki, A. Sugihara, Q. L. Ma, X. M. Zhang, T. Miyzaki, Y. Ando, and S. Mizukami., J. Appl. Phys. (Accepted)

Conferences:

1. "The Interfacial Exchange coupling in cubic Heusler/tetragonal Heusler Mn_3Ga Bilayers", R. Ranjbar, S. Mizukami, Q. L. Ma, A. Sugihara, K. Suzuki, X. M. Zhang, Y. Ando, and T. Miyzaki., The 59th Annual Magnetism and Magnetic Materials (MMM) Conference, Honolulu, Nov. 7, 2014.
2. "Interfacial Exchange Coupling of Mn_3Ga/Co_2FeZ (Z=Al, Si) Heusler Bilayers", R. Ranjbar, S. Mizukami, Q. L. Ma, A. Sugihara, X. M. Zhang, K. Suzuki, Y. Ando, and T. Miyzaki., The 75th JSAP Autumn Meeting, Sapporo, Sept. 17, 2014.
3. "Spin wave propagation in Co/$L1_0$-MnGa bilayer", S. Mizukami, T. Kubota, R. Ranjbar, S. Iihama, Y. Ando, Q. L. Ma, K. Suzuki, A. Sugihara, X. M. Zhang, and T. Miyzaki., The 75th JSAP Autumn Meeting, Sapporo, Sept. 20, 2014.
4. Anti-ferromagnetic Exchange Interaction of $D0_{22}$-$Mn_{70}Ga_{30}$/CoB Bilayer, Ranjbardizaj Reza, Shigemi Mizukami, Yasuo Ando, Xianmin Zhang, Qinli Ma, Atsushi Sugihara, and Terunobu Miyazaki., 第61回応用物学会春季学術講演会 2014年3月7日.

5. “Anti-ferromagnetic Exchange Interaction of $L1_0$-$Mn_{57}Ga_{43}$/Co Bilayer”, R. Ranjbar, S. Mizukami, Y. Ando, Q. L. Ma, T. Kubota, X. M Zhang and T. Miyazaki., AIMR International Symposium 2014, Feb. 17, 2014.

6. “Anti-ferromagnetic Exchange Coupling in $L1_0$-MnGa/Co Bilayer Films”, R. Ranjbar, A. Sugihara, S. Mizukami, Q. L. Ma, S. Iihama, Y. Ando, and T. Miyazaki, 2013 International Conference on Solid State Devices and Materials, Fukuoka, Sep. 25, 2013.

7. “$L1_0$-MnGa/Co Bilayer Films with Anti-ferromagnetic Exchange Coupling”, R. Ranjbar, A. Sugihara, S. Mizukami, Q. L. Ma, S. Iihama, Y. Ando, and T. Miyazaki, The 74th JSAP Autumn Meeting, Kyoto, Sep. 16, 2013.

8. “Spin resonance on AF coupled Co/MnGa bilayer films”, R. Ranjbar, T. Kubota, S. Mizukami, Q. L. Ma, X. M. Zhang, A. Sugihara, S. Iihama, Y. Ando, and T. Miyazaki, The annual meeting on Advanced Spintronic Materials and Transport phenomena, Dresden, 2013.

9. “Magnetic properties of $L1_0$-$Mn_{57}Ga_{43}$/Co bilayer films with different Co thicknesses”, R. Ranjbar, S. Mizukami, Y. Ando, T. Kubota, Q. L. Ma, X. M. Zhang, and T. Miyazaki, The annual meeting in conjunction with Japan -Russia Workshop, Akio, 2012.

10. “Effect of annealing temperature on magnetic properties of MnGa/Co bilayer”, R. Ranjbardizaj, S. Iihama, Q. L. Ma, T. Kubota, S. Mizukami, H. Naganuma, M. Oogane, Y. Ando, and T. Miyazaki, Japan Society of Applied Physics, Tohoku division, Sendai, Dec. 7, 2012.

Contents

Chapter 1 Introduction 1

1.1 Spintronics 1

1.2 Magnetoresistance Effect 2

1.2.1 Giant Magnetoresistance (GMR) 3

1.2.2 Tunnelling Magnetoresistance (TMR) 4

1.3 Half-Metal Material 7

1.4 Magnetic Anisotropy 7

1.5 Magnetic Memories 9

1.5.1 Magnetic Random Access Memories (MRAM) 10

1.5.2 Spin Transfer Torque Random Access Memories (STT-RAM) 11

1.6 Landau-Lifshitz-Gilbert Description of STT 15

1.7 MnGa Alloys with Perpendicular Magnetic Anisotropy (PMA) 16

1.7.1 Issues 21

1.8 Objectives of the Research 25

Chapter 2 Experimental Method 28

2.1 Substrate Preparation 28

2.1.1 Magnetron Sputtering 28

2.1.2 Film Deposition 29

2.2 Structural Properties 34

2.2.1 X-Ray Diffraction 34

2.2.2 Transmission electron microscopy 35

2.3 Magnetic Properties 35

2.3.1 Vibrating sample magnetometer (VSM) 35

2.3.2 Magneto Optical Kerr Effect (MOKE) 36

Chapter 3 Structural and Magnetic Properties for Bilayer of the Co-B Binary and Tetragonal Heuseler Mn-Ga Compounds 38
3.1 Annealing Temperature Dependence of Co (20 nm)/$D0_{22}$-MnGa (30 nm) Bilayer 38
3.1.1 Structural Properties 38
3.1.2 Magnetic Properties 40
3.1.1 Discussion and Summary 43
3.2 Thickness Dependence of Co (t_{Co})/$D0_{22}$-MnGa (30 nm) Bilayer 45
3.2.1 Structural Properties 45
3.2.1 Magnetic properties 47
3.2.2 Discussion and Summary 50
3.3 Annealing Temperature Dependence of CoB (20 nm)/$D0_{22}$-MnGa (30 nm) Bilayer 52
3.3.1 Structural Properties 52
3.3.1 Magnetic Properties 53
3.3.2 Calculation Method for Estimation of Interfacial Exchange Coupling Constant 55
3.3.3 Discussion and Summary 60
3.4 Thickness Dependence of CoB (t_{CoB})/$D0_{22}$-MnGa (30 nm) Bilayer 63
3.4.1 Structural Properties 64
3.4.2 Magnetic Properties 66
3.4.3 Discussion and Summary 67
Chapter 4 Structural and Magnetic Properties for Bilayer of the Cubic and Tetragonal Heusler Alloys 70
4.1 Annealing Temperature Dependence of Co_2FeAl (20 nm)/$D0_{22}$-MnGa (30 nm) Bilayer 70
4.1.1 Structural Properties 71
4.1.2 Magnetic Properties 74
4.1.3 Discussion and Summary 74
4.2 Thickness Dependence of Co_2FeAl (t_{CFA})/$D0_{22}$-MnGa (30 nm) Bilayer 77
4.2.1 Structural Properties 77

4.2.2 Magnetic Properties 79
4.2.3 Discussion and Summary 82
4.3 Annealing Temperature Dependence of Co_2FeSi (20 nm)/$D0_{22}$-MnGa (30 nm) Bilayer 84
4.3.1 Structural Properties 84
4.3.2 Magnetic Properties 86
4.3.3 Discussion and Summary 88
4.4 Thickness Dependence of Co_2FeSi (t_{CFS})/$D0_{22}$-MnGa (30 nm) Bilayer 91
4.4.1 Structural Properties 92
4.4.2 Magnetic Properties 94
4.4.3 Discussion and Summary 94
4.5 Annealing Temperature Dependence of Co_2MnAl (20 nm)/$D0_{22}$-MnGa (30 nm) Bilayer 97
4.5.1 Structural Properties 97
4.5.2 Magnetic Properties 100
4.5.3 Discussion and Summary 101
4.6 Thickness Dependence of $CoMn_2Al$ (t_{CMA})/$D0_{22}$-MnGa (30 nm) Bilayer 104
4.6.1 Structural Properties 105
4.6.2 Magnetic Properties 107
4.6.3 Discussion and Summary 107
4.7 Annealing Temperature Dependence of Co_2MnSi (20 nm)/$D0_{22}$-MnGa (30 nm) Bilayer 110
4.7.1 Structural Properties 110
4.7.2 Magnetic Properties 113
4.7.1 Discussion and summary 115
4.8 Thickness Dependence of Co_2MnSi (t_{CMS})/$D0_{22}$-MnGa (30 nm) Bilayer 119
4.8.1 Structural Properties 120
4.8.2 Magnetic Properties 122
4.8.3 Discussion and Summary 123
Chapter 5 Reduction of the Thickness of CoMnSi (t_{CMS})/$D0_{22}$-MnGa (t_{MnGa}) Bilayer 126

5.1 Thickness Dependence of the $D0_{22}$-MnGa (t_{MnGa}) Films 126
5.1.1 Structural Properties 126
5.1.2 Magnetic Properties 127
5.1.3 Discussion and Summary 129
5.2 Thickness Dependence of the Co_2MnSi (t_{CMS})/$D0_{22}$-MnGa (t_{MnGa}) Bilayer 131
5.2.1 Structural Properties 132
5.2.2 Magnetic Properties 135
5.2.3 Discussion and Summary 136
Chapter 6 Discussion 137
7 Chapter 7: Conclusion and Future perspective 144
7.1 Conclusion 144
7.2 Future perspective 145
References 146

List of Tables

Table 6-1 Summary of structural and magnetic parameters for different IMA materials in this study. 138

List of Figures

Figure 1-1 The giant magnetoresistance curves at 4.2 K of (Fe/Cr) multilayer. 3

Figure 1-2 Schematic of spin scattering from FM/NM/FM tree layers with different magnetization configuration. 4

Figure 1-3 The schematic of the Tunnelling magnetoresistance in both parallel configuration (up) and antiparallel configuration (down) 6

Figure 1-4 Schematic of classification of material based on the spin polarization. 7

Figure 1-5 (a) Schematic of MRAM design and (b) resistivity curve versus magnetic field for different magnetization configuration. 10

Figure 1-6 Schematic illustration of spin transfer torque 12

Figure 1-7 (a) Spin transfer switching and (b) Writing current as a function of memory cell size. 13

Figure 1-8 (a) Critical current density (J_{C0}) due to spin injection magnetization reversal and (b) thermal stability ($\Delta = K_u V/k_B T$) as a function of saturation magnetization of junction electrode. Solid curves in figure indicate perpendicular magnetization film, while broken curves indicate magnetization in plane film. Parameter s in Eq. 1-11 are α = 0.01, g = 0.5, d = nm and junction area φ = 100 nm 14

Figure 1-9 Schematic of damping, precession and spin transfer torque of magnetization vector in the presence of effective magnetic field. 15

Figure 1-10 Illustration of crystal structure of (a) $L2_1$ structured cubic Heusler alloys, (b) tetragonal $L1_0$ and (c) $D0_{22}$ structured MnGa alloys 17

Figure 1-11 Mn–Ga binary phase diagrams reported by (a) Lu *et al*. and (b) Minakuchi *et al.* 18

Figure 1-12 Spin dependent density of states for tetragonal (a) $L1_0$ and (b) $D0_{22}$ structured Heusler-like alloys 19

Figure 1-13 Out-of-plane and in-plane magnetization curves for 30-nm thick Mn_xGa_{1-x} alloy films grown on MgO substrates with Cr buffer layers (a) x = 0.54 and (b) x = 0.62. 20

Figure 1-14 Gilbert damping (or effective damping) constant and the effective PMA constant for various kinds of PMA films reported. 21

Figure 1-15 TMR data at room temperature for Mn–Ga based p-MTJ with the interlayer of (a) Co, (b) Fe, (c) CoFeB and (d) Fe/Co.The data are plotted with different thickness of the interlayer and different Mn–Ga compositions. 22

Figure 1-16 *M-H* loops of MnGa 30 nm/ $Fe_{1-x}Co_x$ (1.5 nm) with x equal to 20% (a) and 60% (b). The gray line is the *M-H* loop of 30-nm MnGa single films included for comparison. (c) and (d) are the corresponding MR (*H*) loops of p-MTJs tested in a perpendicular direction at room temperature. The solid lines in (c) and (d) are the fits based on the FM and AFM J_{ex} in MnGa/$Fe_{80}Co_{20}$ and MnGa/$Fe_{40}Co_{60}$ interfaces, respectively. 23

Figure 1-17 (a) The reported MR ratio of p-MTJs based on MnGa alloy with inserting ultra-thin ferromagnetic metal/alloy. (b) Stacking structure of p-MTJs. 24

Figure 1-18 Stacking structure for target of this study 27

Figure 2-1 Schematic of magnetron sputtering system. 29

Figure 2-2 (a) The staking structure of Co/MnGa bilayer, Co and MnGa references films for investigation of annealing temperature dependence. (b) The staking structure of Co/MnGa bilayer films for investigation of thickness dependence. 30

Figure 2-3 (a) The staking structure of CoB/MnGa bilayer, CoB and MnGa references films for investigation of annealing temperature dependence. (b) The staking structure of CoB/MnGa bilayer films for investigation of thickness dependence. 31

Figure 2-4 (a) The staking structure of CFA/MnGa bilayer, CFA and MnGa references films for investigation of annealing temperature dependence. (b) The staking structure of CFA/MnGa bilayer films for investigation of thickness dependence. 31

Figure 2-5 (a) The staking structure of CFS/MnGa bilayer, CFS and MnGa references films for investigation of annealing temperature dependence. (b) The staking structure of CFS/MnGa bilayer films for investigation of thickness dependence. 32

Figure 2-6 (a) The staking structure of CMA/MnGa bilayer, CMA and MnGa references films for investigation of annealing temperature dependence. (b) The staking structure of CMA/MnGa bilayer films for investigation of thickness dependence. 32

Figure 2-7 (a) The staking structure of CMS/MnGa bilayer, CMS and MnGa references films for investigation of annealing temperature dependence. (b) The staking structure of CMS/MnGa bilayer films for investigation of thickness dependence. 33

Figure 2-8 (a) The staking structure of MnGa film and (b) CMS/MnGa bilayer film for investigation of thickness dependence. 33

Figure 2-9 Schematic of X-ray diffraction 34

Figure 2-10 Schematic of VSM system. 36

Figure 2-11 The three different types of Kerr effect: (a) polar, (b) longitudinal and (c) transverse. 37

Figure 3-1 (a) The XRD pattern of Co/MnGa bilayers for un-annealed sample and annealed samples at 200, 250, 300, 350, 400, and 450ºC. (b) The annealing temperature dependence of *c* lattice constant and (c) FWHM of (004) peak of MnGa film. 39

Figure 3-2 (a) The typical out-of plane (blue colour) and in-plane (red colour) VSM *M-H* loops of MnGa and (b) Co reference films. 40

Figure 3-3 The typical out-of plane (blue colour) and in-plane (red colour) VSM *M-H* loops of Co (20 nm)/MnGa (30 nm) bilayers for un-annealed sample and annealed samples at 200, 250, 300, 350, 400, and 450ºC. 41

Figure 3-4 (a) The typical polar Kerr rotation angle versus the applied field of MnGa and (b) Co reference films. 42

Figure 3-5 The typical polar Kerr rotation angle versus the applied field of Co (20 nm)/MnGa (30 nm) bilayers for un-annealed sample and annealed samples at 200, 250, 300, 350, 400, and 450ºC. 43

Figure 3-6 (a) The annealing temperature dependence of saturation magnetization for Co film. (b) The annealing temperature dependence of remnant magnetization and (c) switching field for Co (20 nm)/MnGa (30 nm) bilayer film. 44

Figure 3-7 (a) The XRD pattern of Co (0-20 nm)/MnGa (30 nm) bilayers for the un-annealed sample. (b) The Co thickness dependence of *c* lattice constant and (c) FWHM of (004) peak of MnGa film. . 46

Figure 3-8 (a) The XRD pattern of Co (t_{Co}=0-20 nm)/MnGa (30 nm) bilayers for the samples annealed at 350ºC. (b) The Co thickness dependence of *c* lattice constant and (c) FWHM of (004) peak of MnGa film. 47

Figure 3-9 The typical out-of plane (blue colour) and in-plane (red colour) VSM *M-H* loops of Co (1-20 nm)/MnGa (30 nm) bilayers for un-annealed samples and annealed samples at 350ºC. 48

Figure 3-10 The typical polar Kerr rotation angle versus the applied field of Co (1-20 nm)/MnGa (30 nm) bilayers for un-annealed samples and annealed samples at 350ºC. 49

Figure 3-11 (a) The Co thickness dependence of saturation magnetization for Co film. (b) The Co thickness dependence of remnant magnetization and (c) switching field for Co (1-20 nm)/MnGa (30 nm) bilayer films. 51

Figure 3-12 (a) The XRD pattern of CoB/MnGa bilayers for un-annealed sample and annealed samples at 200, 250, 300, 350, and 400ºC. (b) The annealing temperature dependence of *c* lattice constant and (c) FWHM of (004) peak of MnGa film. 53

Figure 3-13 The typical out-of plane (blue colour) and in-plane (red colour) VSM *M-H* loops of CoB (20 nm)/MnGa (30 nm) bilayers for un-annealed sample and annealed samples at 200, 250, 300, 350, and 400ºC. 54

Figure 3-14 The typical polar Kerr rotation angle versus the applied field of CoB (20 nm)/MnGa (30 nm) bilayers for un-annealed sample and annealed samples at 200, 250, 300, 350, and 400ºC. 55

Figure 3-15 Illustration for a magnetic bilayer with antiferromagnetic exchange interaction present at an interface. Each layer has an in-plane (IMA) and perpendicular magnetic anisotropy (PMA). (b) Schematic expression of coordinate system used for the calculation of magnetic properties. 56

Figure 3-16 (a) The calculation of typical out-of-plane *M-H* of CoB(20)/MnGa(30) bilayer film for J_{ex}= -1.5 erg/cm^3 and (b) J_{ex}= 0 erg/cm^3. (c) Schematic expression of spin configuration. 59

Figure 3-17 (a) The calculation of typical polar Kerr rotation angle versus applied magnetic field of CoB (20)/MnGa (30) bilayer film for J_{ex}= -1.5 erg/cm^3 and (b) J_{ex}= 0 erg/cm^3. (c) Schematic expression of spin configuration. 60

Figure 3-18 (a) The annealing temperature dependence of saturation magnetization for CoB film. (b) The annealing temperature dependence of remnant magnetization, (c) switching and (d) saturation fields for CoB (20 nm)/MnGa (30 nm) bilayer film. 61

Figure 3-19 The annealing temperature dependence of interfacial exchange coupling constant CoB (20 nm)/MnGa (30 nm) bilayer film. 62

Figure 3-20 (a) The XRD pattern of CoB (0-20 nm)/MnGa (30 nm) bilayers for the un-annealed samples. (b) The Co thickness dependence of *c* lattice constant and (c) FWHM of (004) peak of MnGa film. 63

Figure 3-21 (a) The XRD pattern of CoB (0-20 nm)/MnGa (30 nm) bilayers for the samples annealed at 350ºC. (b) The Co thickness dependence of *c* lattice constant and (c) FWHM of (004) peak of Mn Ga film. 64

Figure 3-22 The typical out-of plane (blue colour) and in-plane (red colour) VSM *M-H* loops of CoB (1-20 nm)/MnGa (30 nm) bilayers for un-annealed samples and annealed samples at 350ºC. 65

Figure 3-23 The typical polar Kerr rotation angle versus the applied field of CoB (1-20 nm)/MnGa (30 nm) bilayers for un-annealed samples and annealed samples at 350ºC. 66

Figure 3-24 (a) The CoB thickness dependence of saturation magnetization for CoB film. (b) The CoB thickness dependence of remnant magnetization, (c) switching and (d) saturation fields for CoB (1-20 nm)/MnGa (30 nm) bilayer films. 68

Figure 4-1 (a) The XRD pattern of CFA/MnGa bilayers for un-annealed sample and annealed samples at 200, 250, 300, 350, 400, and 450ºC. (b) The annealing temperature dependence of *c* lattice constant and (c) FWHM for CFA and MnGa films. 71

Figure 4-2 The typical out-of plane (blue colour) and in-plane (red colour) VSM *M-H* loops of CFA (20 nm)/MnGa (30 nm) bilayers for un-annealed sample and annealed samples at 200, 250, 300, 350, 400, and 450ºC. 72

Figure 4-3 The typical polar Kerr rotation angle versus the applied field of CFA (20 nm)/MnGa (30 nm) bilayers for un-annealed sample and annealed samples at 200, 250, 300, 350, 400, and 450ºC. .. 73

Figure 4-4 (a) The annealing temperature dependence of saturation magnetization for CFA film. (b) The annealing temperature dependence of remnant magnetization, (c) switching and (d) saturation fields for CFA (20 nm)/MnGa (30 nm) bilayer film. 75

Figure 4-5 The annealing temperature dependence of interfacial exchange coupling constant for the CFA (20 nm)/MnGa (30 nm) bilayer film. 76

Figure 4-6 (a) The XRD pattern of CFA (0-20 nm)/MnGa (30 nm) bilayers for the un-annealed samples. (b) The Co thickness dependence of *c* lattice constant and (c) FWHM for CFA and MnGa film. 78

Figure 4-7 (a) The XRD pattern of CFA (0-20 nm)/MnGa (30 nm) bilayers for the samples annealed at 450ºC. (b) The Co thickness dependence of *c* lattice constant and (c) FWHM for CFA and MnGa film. 79

Figure 4-8 The typical out-of plane (blue colour) and in-plane (red colour) VSM *M-H* loops of CFA (1-20 nm)/MnGa (30 nm) bilayers for un-annealed samples and annealed samples at 450ºC. 80

Figure 4-9 The typical polar Kerr rotation angle versus the applied field of CFA (1-20 nm)/MnGa (30 nm) bilayers for un-annealed samples and annealed samples at 350ºC. 81

Figure 4-10 (a) The CFA thickness dependence of saturation magnetization for CFA film. (b) The CFA thickness dependence of remnant magnetization, (c) switching and (d) saturation fields for CFA (1-20 nm)/MnGa (30 nm) bilayer films. 83

Figure 4-11 The XRD pattern of CFS/MnGa bilayers for un-annealed sample and annealed samples at 200, 250, 300, 350, 400, and 450ºC. (b) The annealing temperature dependence of *c* lattice constant and (c) FWHM for CFS and MnGa films. 85

Figure 4-12 The typical out-of plane (blue colour) and in-plane (red colour) VSM *M-H* loops of CFS (20 nm)/MnGa (30 nm) bilayers for un-annealed sample and annealed samples at 200, 250, 300, 350, 400 and 450ºC. 86

Figure 4-13 The typical polar Kerr rotation angle versus the applied field of CFS (20 nm)/MnGa (30 nm) bilayers for un-annealed sample and annealed samples at 200, 250, 300, 350, 400, and 450ºC. .. 87

Figure 4-14 (a) The annealing temperature dependence of saturation magnetization for CFS film. (b) The annealing temperature dependence of remnant magnetization, (c) switching (d) saturation fields for CFS (20 nm)/MnGa (30 nm) bilayer film. 89

Figure 4-15 The annealing temperature dependence of interfacial exchange coupling constant CFS (20 nm)/MnGa (30 nm) bilayer film. 90

Figure 4-16 (a) The XRD pattern of CFS (0-20 nm)/MnGa (30 nm) bilayers for the un-annealed samples. (b) The CFS thickness dependence of *c* lattice constant and (c) FWHM for CFS and MnGa films. 91

Figure 4-17 (a) The XRD pattern of CFS (t_{CFS}=0-20 nm)/MnGa (30 nm) bilayers for the samples annealed at 300ºC. (b) The CFS thickness dependence of *c* lattice constant and (c) FWHM for CFS and MnGa films. 92

Figure 4-18 The typical out-of plane (blue colour) and in-plane (red colour) VSM *M-H* loops of CFS (1-20 nm)/MnGa (30 nm) bilayers for un-annealed samples and annealed samples at 300ºC. 93

Figure 4-19 The typical polar Kerr rotation angle versus the applied field of CFS (1-20 nm)/MnGa (30 nm) bilayers for un-annealed samples and annealed samples at 300ºC. 95

Figure 4-20 (a) The CFS thickness dependence of saturation magnetization for CFS film. (b) The CFS thickness dependence of remnant magnetization, (c) switching and (d) saturation fields for CFS (1-20 nm)/MnGa (30 nm) bilayer films. 96

Figure 4-21 (a) The XRD pattern of CMA/MnGa bilayers for un-annealed sample and annealed samples at 200, 250, 300, 350, 400, 450, 500 and 550ºC. (b) The annealing temperature dependence of *c* lattice constant and (c) FWHM for CMA and MnGa films. 98

Figure 4-22 The typical out-of plane (blue colour) and in-plane (red colour) VSM *M-H* loops of CMA (20 nm)/MnGa (30 nm) bilayers for un-annealed sample and annealed samples at 200, 250, 300, 350, 400, 450, 500 and 550ºC. 99

Figure 4-23 The typical polar Kerr rotation angle versus the applied field of CMA (20 nm)/MnGa (30 nm) bilayers for un-annealed sample and annealed samples at 200, 250, 300, 350, 400, 450, 500 and 550ºC 100

Figure 4-24 (a) The annealing temperature dependence of saturation magnetization for CMA film. (b) The annealing temperature dependence of remnant magnetization, (c) switching and (d) saturation fields for CMA (20 nm)/MnGa (30 nm) bilayer film. 102

Figure 4-25 The annealing temperature dependence of interfacial exchange coupling constant CMA (20 nm)/MnGa (30 nm) bilayer film. 103

Figure 4-26 (a) The XRD pattern of CMA (0-20 nm)/MnGa (30 nm) bilayers for the un-annealed samples. (b) The CMA thickness dependence of *c* lattice constant and (c) FWHM for CMA and MnGa films. 104

Figure 4-27 (a) The XRD pattern of CMA (0-20 nm)/MnGa (30 nm) bilayers for the samples annealed at 450ºC. (b) The CMA thickness dependence of *c* lattice constant and (c) FWHM for CMA and MnGa films. 105

Figure 4-28 The typical out-of plane (blue colour) and in-plane (red colour) VSM *M-H* loops of CMA (1-20 nm)/MnGa (30 nm) bilayers for un-annealed samples and annealed samples at 450ºC. 106

Figure 4-29 The typical polar Kerr rotation angle versus the applied field of CMA (1-20 nm)/MnGa (30 nm) bilayers for un-annealed samples and annealed samples at 450ºC. 108

Figure 4-30 (a) The CMA thickness dependence of saturation magnetization for CMA film. (b) The CMA thickness dependence of remnant magnetization, (c) switching and (d) saturation fields for CMA (1-20 nm)/MnGa (30 nm) bilayer films. 109

Figure 4-31 (a) The XRD pattern of CMS/MnGa bilayers for un-annealed sample and annealed samples at 200, 250, 300, 350, 400, and 450ºC. (b) The annealing temperature dependence of *c* lattice constant and (c) FWHM for CMS and MnGa films. 111

Figure 4-32 (a) A cross-sectional HRTEM image and (b) nanobeam electron diffraction (spot size 1 nm) of sample annealed at 400°C. 112

Figure 4-33 The typical out-of plane (blue colour) and in-plane (red colour) VSM *M-H* loops of CMS (20 nm)/MnGa (30 nm) bilayers for un-annealed sample and annealed samples at 200, 250, 300, 350, 400 and 450ºC. 114

Figure 4-34 The typical polar Kerr rotation angle versus the applied field of CMS (20 nm)/MnGa (30 nm) bilayers for un-annealed sample and annealed samples at 200, 250, 300, 350, 400, and 450ºC. 115

Figure 4-35 (a) The annealing temperature dependence of saturation magnetization for CMS film. (b) The annealing temperature dependence of remnant magnetization, (c) switching (d) saturation fields for CMS (20 nm)/MnGa (30 nm) bilayer film. 116

Figure 4-36 The annealing temperature dependence of interfacial exchange coupling constant CMS (20 nm)/MnGa (30 nm) bilayer film. 117

Figure 4-37 (a) The XRD pattern of CMS (0-20 nm)/MnGa (30 nm) bilayers for the un-annealed samples. (b) The CMS thickness dependence of *c* lattice constant and (c) FWHM for CMS and MnGa films. 119

Figure 4-38 (a) The XRD pattern of CMS (0-20 nm)/MnGa (30 nm) bilayers for the samples annealed at 400ºC. (b) The CMS thickness dependence of *c* lattice constant and (c) FWHM for CMS and MnGa films 120

Figure 4-39 The typical out-of plane (blue colour) and in-plane (red colour) VSM *M-H* loops of CMS (1-20 nm)/MnGa (30 nm) bilayers for un-annealed samples and annealed samples at 400ºC. 121

Figure 4-40 The typical polar Kerr rotation angle versus the applied field of CMS (1-20 nm)/MnGa (30 nm) bilayers for un-annealed samples and annealed samples at 4000ºC. 122

Figure 4-41 (a) The CMS thickness dependence of saturation magnetization for CMS film. (b) The CMS thickness dependence of remnant magnetization, (c) switching and (d) saturation fields for CMS (1-20 nm)/MnGa (30 nm) bilayer films. 124

Figure 5-1 The XRD pattern for different thicknesses of MnGa (5-30 nm) film. (b) The MnGa thickness dependence of *c* lattice constant and (c) FWHM for (004) peak of MnGa film. 127

Figure 5-2 The typical out-of plane (blue colour) and in-plane (red colour) VSM *M-H* loops for different thicknesses of MnGa (5-30 nm) films. 128

Figure 5-3 The typical polar Kerr rotation angle versus the applied field for different thicknesses of MnGa (5-30 nm) films. 129

Figure 5-4 (a) The MnGa thickness dependence of saturation magnetization and (b) switching for MnGa (5-30 nm) films. 130

Figure 5-5 The XRD pattern of CMS (1-7 nm)/MnGa (7.5 nm) bilayers for the un-annealed samples. (b) The CMS thickness dependence of *c* lattice constant and (c) FWHM for CMS and MnGa films 131

Figure 5-6 The XRD pattern of CMS (1-7 nm)/MnGa (7.5 nm) bilayers for the samples annealed at 400ºC. (b) The CMS thickness dependence of *c* lattice constant and (c) FWHM for CMS and MnGa films. 132

Figure 5-7 The typical out-of plane (blue colour) and in-plane (red colour) VSM *M-H* loops of CMS (1-7 nm)/MnGa (7.5 nm) bilayers for un-annealed samples and annealed samples at 400ºC. 133

Figure 5-8 The typical polar Kerr rotation angle versus the applied field of CMS (1-7 nm)/MnGa (7.5 nm) bilayers for un-annealed samples and annealed samples at 400ºC. 134

Figure 5-9 (a) The CMS thickness dependence of remnant magnetization and (b) switching for CMS (1-7 nm)/MnGa (7.5 nm) bilayer films. 136

Figure 6-1 The annealing temperature dependence of interfacial exchange coupling constant for different Heusler alloys. 138

Figure 6-2 (a) J_{ex} in the $Fe_{1-x}Co_x$/MnGa interface as a function of $Fe_{1-x}Co_x$ composition. (b) Spin-up (black up triangle) and spin-down (gray down triangle) density of states at the Fermi level of $Fe_{1-x}Co_x$ alloy with bcc structure. (c) Illustration of the band structure of bcc$Fe_{1-x}Co_x$ and $L1_0$ MnGa alloys. 139

Figure 6-3 The electronic band structure of (a) Co_2FeAl, (b) Co_2FeSi, (c) Co_2MnAl, and (d) Co_2FeAl. 140

Figure 6-4 (left column) Total DOS for Co_2MnAl in four different structures; (right column) same for Co_2MnSi. 141

Figure 6-5 (left) Cubic lattice structure of the Heusler compounds with four inequivalent sites. (right) Chemical elements per site for all considered structures.[67] 142

Figure 7-1 Stacking structure of p-MTJ based on CMS/MnGa bilayer as free electrode. 145

Chapter 1 Introduction

1.1 Spintronics

Discovery of spin-dependent electron transport effect in devices including magnetic metal layers in the 1980 has been opened new research area. Johnson and Silsbee (1985)[1] have reported electrons that have spin polarization can inject from a ferromagnetic metal to a normal metal. In 1988, Fert *et al.*[2] and Grünberg *et al.*[3] independently have discovered giant magnetoresistance (GMR) effect. These observations made new research area which is called Spintronics The spintronics originates from previous investigation related to ferromagnet/superconductor tunneling experiments performed by Meservey and Tedrow, and first experiments of tunnel magnetoresistance effect (TMR) in magnetic tunnel junctions (MTJs) by Julliere in the 1970.[4] The idea of using semiconductors for spintronics is comes from theoretical proposal of a spin field-effect-transistor by Datta and Das in 1990.[5] By discovery of GMR and TMR[4,6] developing of Spintronics has starred from 25 years ago. During this period of time many devices using magnetoresistance effect were proposed and some of them were practical used. Magnetic random access memory (MRAM) is one of them and its memory capacity is continuously increasing. However, the memory capacity of MRAM used practically is 4-16 Mbit at most and the market is restricted. The new challenge is making a large capacity MRAM, which will be realized by using the new magnetization switching technology called spin transfer torque (called STT-MRAM). The 64 Mbits STT-MRAM has been produced in 2012, and the large capacity STT-MRAM more than 10 Gbits is now being developed for main non-volatile memories of various information technology devices used at

present. So in this chapter many expression related to spintronics will be explained to get more information concerning to spintronics subject.

1.2 Magnetoresistance Effect

The external magnetic field can change electrical resistance of conducting materials. This change is called Magnetoresistance (MR) which divided into variable case. The resistivity changes even if the magnetic field is applied not to the ferromagnetic conducting materials but to non-magnetic ones. This is called ordinary MR effect. The simplest origin of MR is the effect of magnetic fields on the trajectory of the electrons, known as the Lorentz force. It deflects charge carriers from the current direction. Once a charge carrier begins to orbit around the magnetic field, it does not contribute to the current density until it is scattered.

On the other hand, interaction of the magnetic field with conducting materials that have spontaneous magnetizations such as ferromagnetic materials makes the change of resistivity in this materials depending on magnetized state. This phenomena is called anomalous MR effect. The change of resistivity in ferromagnetic films, such as Permalloy, depends on the direction of the magnetization with respect to the direction of applied current. These are called anisotropic magnetoresistance effect (AMR).[7] The physical origin of AMR is quite different from the ordinary MR effect observed in non-magnetic conductors. In addition above mentioned MR effects, different types of MR effects are known depending on the characteristics of the conducting materials. Until now, a number of new devices structures and materials were discovered, which exhibit new kinds of MR effects, such as GMR and TMR. The MR ratio is defined as the ratio of the change in resistance when the field is applied to the resistance at zero field

$$MR = \frac{R_H - R_0}{R_0} = \frac{\Delta R}{R_0} \qquad 1\text{-}1$$

Where ΔR is the change in resistance in an applied field and R_0 is the resistance in the absence of an applied field. A material that has a larger resistance in the presence of a field than in the absence of a field is defined to have a positive MR, whereas if the field reduces the resistance, the MR is negative. Magnetoresistive materials are incorporated in a number of commercially available technologies such as magnetic sensors, magnetic recording heads and

magnetic memories. In this section an overview of the different types of magnetoresistance effect will be discussed.

1.2.1 Giant Magnetoresistance (GMR)

Changing of electrical resistance due to an applied magnetic field is giant magnetoresistance which has discovered from Fe/Cr multilayer[2] application. In this multilayer the magnetic field makes large decrement of the resistivity as shown in Fig. 1-1. This effect was larger than both ordinary and anisotropic magnetoresistance and was, therefore, called "giant magnetoresistance" or GMR. In Fe/Cr/Fe trilayers[3] a similar effect also was discovered.

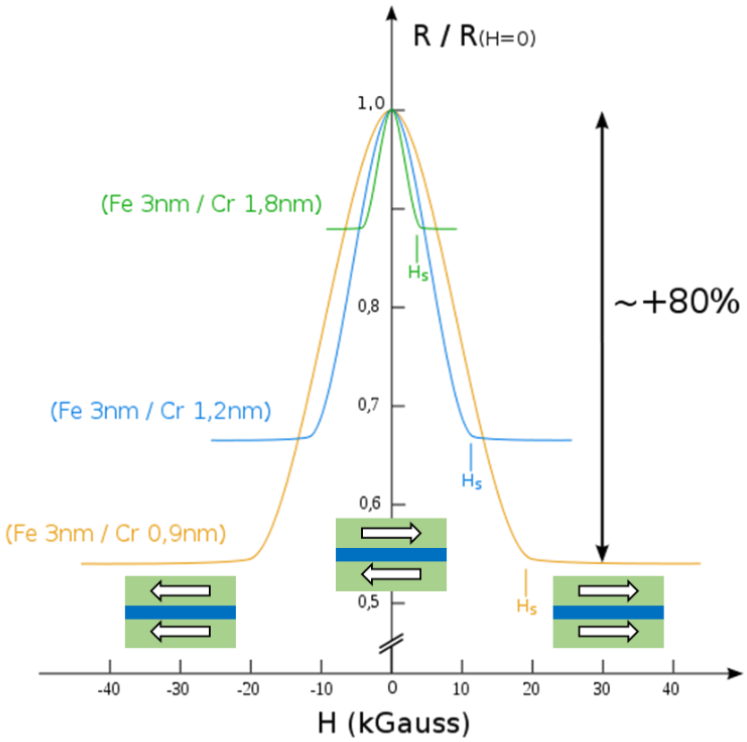

Figure 1-1 The giant magnetoresistance curves at 4.2 K of (Fe/Cr) multilayer.[2]

The basic mechanism of GMR is based on understanding the spin dependent transport in ferromagnets as explained by Mott in 1936. He showed that at low temperature the conductivity in a ferromagnet can be considered as a sum of the two currents which are coming from the spin up and spin down electrons. This is known as the two current model. The two spin channels of current (spin up and spin down electrons) have different scattering probabilities depending on the

magnetization of the layer. When a thin layer of nonmagnetic material is sandwiched between two ferromagnetic electrodes as shown in Fig. 1-2, the resistance of the parallel configuration is low, whereas the resistance of the antiparallel configuration is high. For devices with good quality expectation of change of resistance was found to be 100% which was known as the giant magneto resistance (GMR) effect.

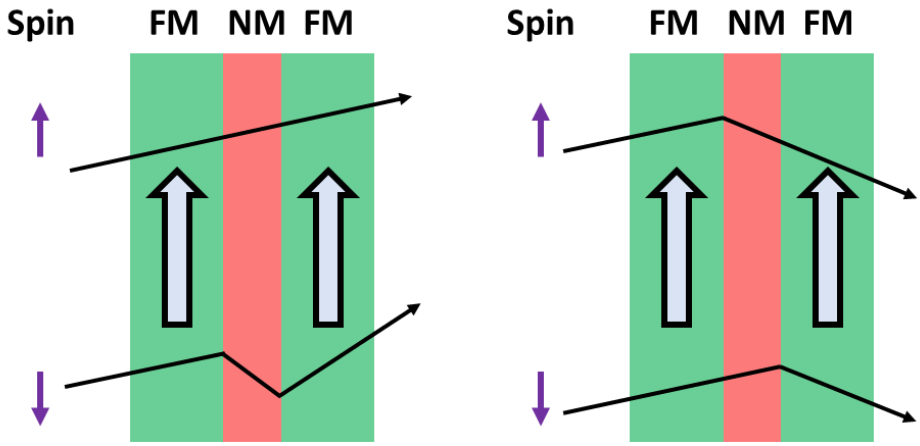

Figure 1-2 Schematic of spin scattering from FM/NM/FM tree layers with different magnetization configuration.

Two popular types of GMR structures are: Current in plane (CIP) GMR and current perpendicular to the plane (CPP) GMR. The first type of GMR, CIP GMR, were observed by the teams led by Fert and Grünberg. The physics of these two types of GMR are completely different. In CIP GMR current is parallel to the planes of the magnetic films, whereas in CPP GMR the current is perpendicular to the magnetic films. Measuring of the resistance in CIP geometry is easier than CPP geometry, because in CPP geometry the resistance of the metallic film is usually very small across its thickness. The thickness of the metallic films in CPP geometry must remain small compared with the distance over which the electrons remember their spin. This distance is usually of the order of one to twenty nanometers in the magnetic materials. So in order to get a CPP GMR device, the lateral dimensions of the device should be of the order of the thickness of the magnetic layers. Although CPP GMR is very attractive from an application point of view, there are experimental difficulties in fabricating relatively small structures of the order of 10 nm.

1.2.2 Tunnelling Magnetoresistance (TMR)

Tunnelling magnetoresistance is a quantum mechanical effect which occurs when two ferromagnets layer are separated by a thin layer of insulator. Depending on the parallel or

antiparallel alignment of ferromagnets layer, the conductance of such a tunnelling junction can change remarkable. The first discovery of TMR was found in Fe/Ge-O/Co junctions at 4.2 K in 1975 by M. Jullière. He has observed change of resistance around 14% which did not attract much attention.[4] Terunobu Miyazaki also has reported an effect of 2.7% at room temperature in 1991. Later, Miyazaki and Jagadeesh Mooderaalso found change of resistance about18% and 11.8% in junctions of iron separated by an amorphous aluminum oxide insulator[6] and CoFe/Co junction[8], respectively in 1994. The largest value of TMR ratio at room temperature about 70% was observed with aluminum oxide insulators. Using crystalline magnesium oxide (MgO) as tunnel barriers has been started from year 2000. Butler and Mathon independently have reported theoretically several thousand percent of TMR ratio for iron as the ferromagnet and MgO as the insulator in 2001.[9,10] A large TMR ratio in Fe/MgO/FeCo (001) film based on MgO magnetic tunnel junction was reported experimentally by Bowen *et al*. in the same year.[11] Parkin and Yuasa also have reported 200% TMR at room temperature for Fe/MgO/Fe junctions in 2004.[12,13] In 2009, TMR ratio about 600 and 1100% at room temperature and 4.2 K were observed in junctions of CoFeB/MgO/CoFeB, respectively.[14]

TMR like GMR effect having same applications. However, their physics made difference between them. The physics of GMR is related to spin-dependent electronic transport, whereas the physics of TMR is based on spin-polarized tunnelling. TMR effect can only be seen in CPP geometry. The tunnel current is related to the overlap of exponentially decaying wave functions within the barrier thus, the current will decrease with the increasing thickness of barrier. The TMR ratio can be defined similar as the GMR ratio which is given by following formula:

$$TMR(\%) = \frac{\Delta R}{Rp} = \frac{R_{ap} - R_p}{R_p} \qquad 1\text{-}2$$

Here R_{p} and R_{ap} denote resistivity in parallel and antiparallel magnetization state, respectively. TMR is because of spin-dependent tunneling which can be understood in terms of Julliere's model. The spin polarization P can be calculated from the spin dependent density of states (DOS) at the Fermi energy:

$$P = \frac{D_{\uparrow}(E_f) - D_{\downarrow}(E_f)}{D_{\uparrow}(E_f) + D_{\downarrow}(E_f)} \qquad 1\text{-}3$$

When external magnetic field is parallel to spin of electrons we have spin-up electrons, whereas the spin-down electrons have anti-parallel alignment with the external field. The changing of resistivity can be defined by the spin polarizations of the two ferromagnets, P_1 and P_2:

$$TMR = \frac{2P_1P_2}{1-P_1P_2} \times 100 \qquad 1\text{-}4$$

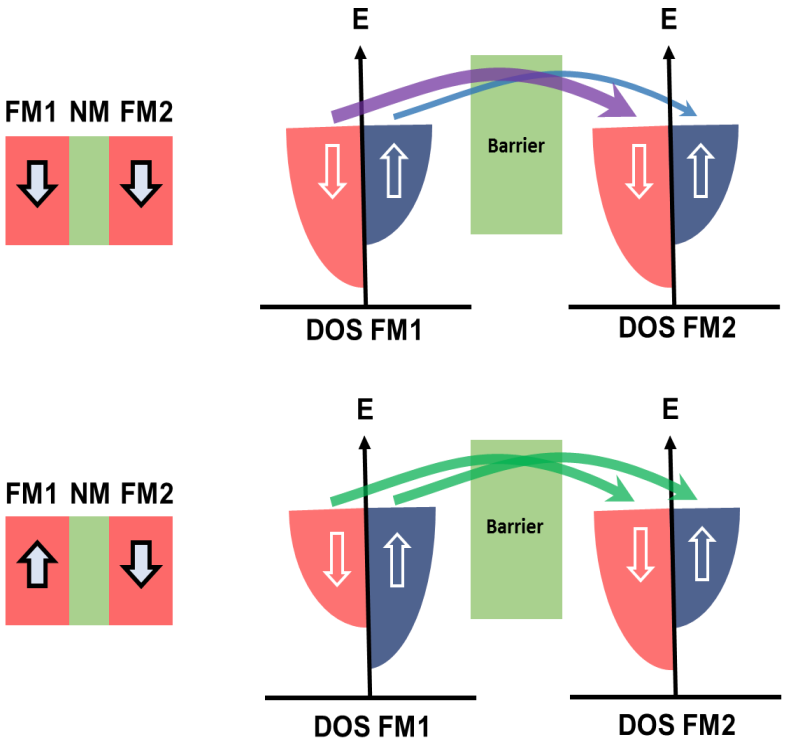

Figure 1-3 The schematic of the Tunnelling magnetoresistance in both parallel configuration (up) and antiparallel configuration (down).

In the presence of a bias voltage, electrons can tunnel to just the positive electrode, whereas in the absent of bias voltage, electrons are able to tunnel in both directions in which they have equal rates. The Julliere's model explains, during the tunneling, spin is conserved, therefore current can be described in a two-current models. Two partial currents contribute in the total current. First partial current is coming from the spin-up electrons and second current is originates from the spin-down electrons. These vary depending on the magnetic state of the junctions as shown in Fig.1-3.

1.3 Half-Metal Material

It is well known to be able to classify the material in to conductor (metal), the semiconductor and the insulator depending on magnitude of electric resistivity. Similar to this, another classification of material is based on the spin polarization of material which defined as the ratio of the density of states of up-spin and down-spin electrons at a Fermi level, as shown in Eq. 1-3. The schematic of classification of material based on spin polarization is shown in Fig. 1-4. When electrons with up and down spins have equal density of states, P is zero for nonmagnetic materials, whereas for ferromagnetic materials density of states are different and P is between 0 and 1. On the other hand, when the minority spin band of DOS shows a band gap similar to semiconductors at a Fermi level and the majority spin of DOS, shows metallic behavior we have special material which is called half-metal. In this case P is 1 because only electrons with up spin exist at Fermi level. This materials are desired materials to get relative large TMR and GMR ratio.

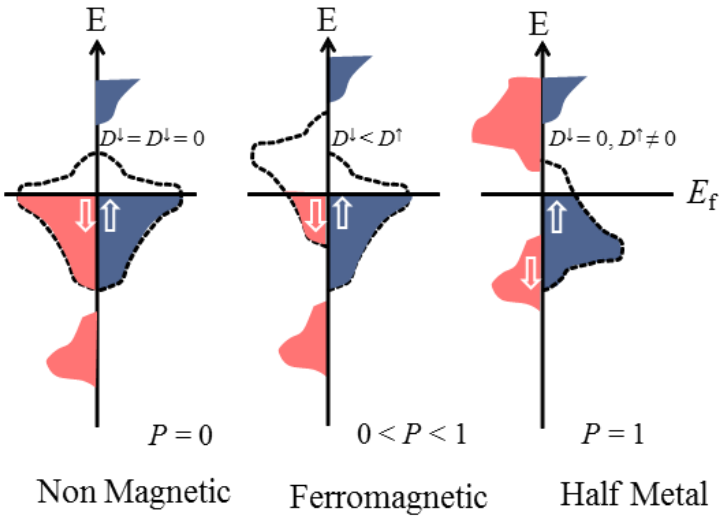

Figure 1-4 Schematic of classification of material based on the spin polarization.

1.4 Magnetic Anisotropy

The magnetization of material prefer to orient regard to one or several axes in magnetic solids. The energy term that describes the dependence of the internal energy on the direction of the magnetization is the magnetic anisotropy energy which may be originated by the

crystalline electric field of the solid, the shape or surface of the magnetic body, and mechanical stress etc. There are different kinds of magnetic anisotropy such as magnetocrystalline, shape, magnetoelastic, and exchange anisotropy. The reason of magnetocrystalline anisoteropy is a crystal structure which introduces preferential directions for the magnetization. When the particle is not spherical the demagnetization field in material changes. Basically, the demagnetization field depends on the shape of particle which causes to different demagnetizing field for different direction of material. This is called the shape anisotropy. On the other hand, change of magnetic behavior due to tension is called the magnetoelastic anisotropy. The latest case is exchange anisotropy which originates from antiferromagnetic and ferromagnetic interactions.

The reason of magnetocrystalline anisotropy is spin-orbit interaction in which the spin of electron is coupled to the orbit of electron. To overcome the spin-orbit interaction for rotation of the electron spins the magnetic field or energy is needed. Normally, the magnetic anisotropy energy has the symmetry of the crystal structure of the material. In addition, it is invariant to the inversion of the magnetization. Therefore, the magnetic anisotropy energy must be an expansion of even functions of the angles enclosed by the magnetization and the magnetic axes. Here, four types of magnetic anisotropy energy are classified as following cases:

Cubic symmetry: In this case we denote α_i (i=1, 2, and 3) as the cosines of the angles between the magnetization and the axes X; Y; Z which are parallel to the fourfold axes. So, magnetic anisotropy energy is given by following equation:

$$E_a = K_0 + K_1(\alpha_1^2\alpha_2^2 + \alpha_2^2\alpha_3^2 + \alpha_3^2\alpha_1^2) + K_2(\alpha_1^2\alpha_2^2\alpha_3^2) + ... \quad 1\text{-}5$$

Where K_0, K_1, K_2 are the anisotropy constants, which are material dependent.

Tetragonal symmetry: If the angles θ and φ describe polar coordinates, and also Z describes the axis parallel to the sixfold axis [001], then magnetic anisotropy is given by:

$$E_a = K_1 \sin^2(\theta) + K_2 \sin^4(\theta) + K_3 \sin^6(\theta) + K_4 \sin^4(\theta)\cos(6\varphi) + ... \quad 1\text{-}6$$

Quadratic symmetry: In this case there is a fourfold axis [001] in which Z is the axis parallel to that axis. Then magnetic anisotropy can be defined as:

$$E_a = K_1 \sin^2(\theta) + K_2 \sin^4(\theta) + K_3 \sin^4(\theta)\cos(4\varphi) + ... \quad 1\text{-}7$$

Uniaxial symmetry: In this case, tetragonal, rhombohedral and quadratic symmetries are same when we consider first terms of the expansion of magnetic anisotropy. Basically in this expansion the magnitude of second term is one order smaller. Therefore, if we consider only the first term, in this expansion we are able to conclude the magnetic anisotropy only depends on the angle between the magnetic moment and the axis of the largest symmetry θ, as is given by:

$$E_a = K_u \sin^2(\theta) \quad 1\text{-}8$$

Here, K_u is uniaxial anisotropy constant. The anisotropy energy is minimum and maximum when the magnetization lies along an easy axis (θ=0°, 180°) and perpendicular to the easy axis (θ=90°, 270°), respectively. By measuring anisotropy field H_K we are able to measure the magnitude of the anisotropy constant K_u as shown in the following formula:

$$H_K = \frac{2K_u}{\mu_0 M_S} \quad 1\text{-}9$$

where M_s is the saturation magnetization.

1.5 Magnetic Memories

To store information for long time periods (10 years), in the form of hard disk drive and magnetic tape storage systems magnetism plays very important role. Basically, access time is limited in these two examples because of their mechanical systems. Only solid state memories like Dynamic Random Access Memory (DRAM) and the Static Random Access Memory (SRAM) are able to read and write with ns access times. However, these memories are volatile and data is stored only as long as power is supplied to refresh the capacitor charge in DRAM and to keep the transistors on in SRAM. As demand for using Flash memory is increasing, making a non-volatile memory is essential in digital research area. However, slow write access time in the μ_s range and poor bit cyclability limited to 10^6 write events are problems of Flash technology. Magnetic random access memories (MRAM) and spin transfer torque magnetic

random access memories (STT-MRAM) are new technology proposing to solve these difficulties between existing volatile and non-volatile memory technologies.[15]

1.5.1 Magnetic Random Access Memories (MRAM)

When an insulator layer sandwiched by two ferromagnetic electrodes we have magnetic tunnel junction structure. This can make cell element of the magnetic random access memory. One of the ferromagnetic layer is called reference layer which is fixed using an exchange biasing antiferromagnetic layer. Another ferromagnetic electrode is free layer in which the magnetic field is able to change magnetization direction of this layer. The tunneling current depends on the orientation of the magnetization in both electrodes. The resistance changes between the low and high resistance values due to parallel and antiparallel alignments, respectively. Typically, if two layers have the same magnetization this is considered to mean "1", while if the two layers have antiparallel magnetization the resistance will be higher and this means "0" as shown in Fig 1-5 (a) and (b). As can be seen from Fig 1-5 (a) there are two bit and word lines which are used for writing of particular cell. All the cells are arranged similar to array in matrix. By passing the current through the special bit and word lines, magnetization of free layer of particular cell can be changed and then we are able to store information as 1 or 0 depending on magnetization configuration. On the other hand, for reading the information, the current flowing thought the bit line and then resistivity can be measured.

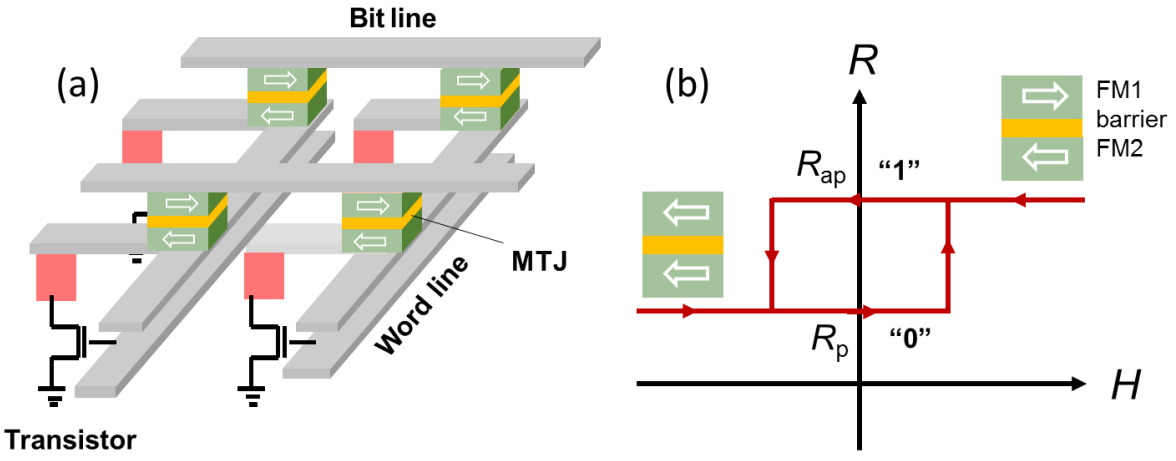

Figure 1-5 (a) Schematic of MRAM design and (b) resistivity curve versus magnetic field for different magnetization configuration.

Potential of MRAM as universal memory has been attracted several large IC companies such as Freescale, IBM, NEC, Toshiba, and Samsung to enter in this research area. They have started to develop MRAM memory with the above-mentioned write scheme, known as 'Stoner-Wohlfarth approach' or Field Induced Magnetic Switching approach (FIMS). Investigators have found this approach would fail because there were some difficulties to increase memory density. Indeed, very narrow distribution of switching field is needed to avoid write errors. This imposes difficult conditions on the process of fabrication of the memory elements and prevents the realization of large memory arrays. In order to produce relatively large magnetic fields for writing of cell, a currents of several mA is needed. To increase the memory density, the cell size should decreases more and more. Therefore, the amount of current density will increase. To satisfy the scalability issues of FIMS-MRAM, several solutions have been suggested. These include different way for writing the information in the memory cell i.e, switching the magnetization of the storage layer. One of the solution is writing by using the spin-transfer torque (STT) to switch the magnetization of the storage layer rather than field induced switching.[16,17]

1.5.2 Spin Transfer Torque Random Access Memories (STT-RAM)

It was well known for long time the spin-polarized tunnelling current carries spin angular momentum which originates from the intrinsic spin of each electron. However, depending on the magnetic-device size, the torque was considered negligible when it interacts with the magnetic moment of a ferromagnetic layer. Basically, spin torque is able to precess magnetic bit when the size of device is less than 100 nm.[18,19] Schematic of spin transfer torque is shown in Fig. 1-6.

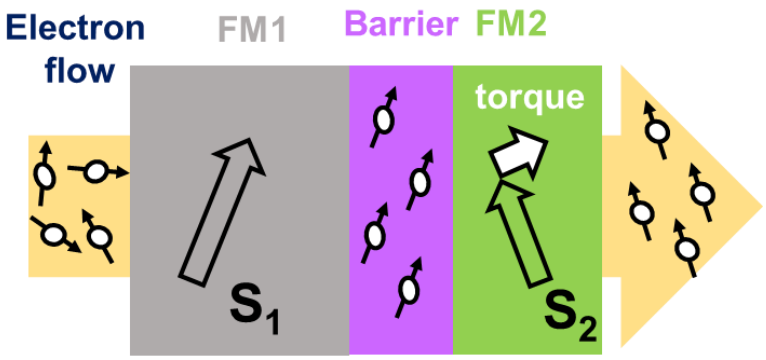

Figure 1-6 Schematic illustration of spin transfer torque.

As shown in Fig. 1-6 conducting electrons have random spin polarization. When these electrons flowing through a fixed magnetic layer (FM1) in a magneto resistive device due to interaction with magnetization of FM1, their spin polarization would change from random to same direction with the magnetization of FM1. With passing these spin-polarized electrons through another magnetic layer (FM2), the polarization direction will change depending on relative orientation of FM1 and FM2. Indeed, in this effect, the FM2 layer feels a torque related to the transfer of spin angular momentum from conducting electrons. If current be enough large, the spin torque is able to switch the magnetization of FM2 and overcome to magnetic damping. The magnetization of nano scaled free layer can be controlled by the flowing current direction. On the basis of calculation by Slonczewski, the reversal spin condition is given by

$$\alpha M_S V H_{eff} < g(\theta)\frac{h}{2}\frac{|I|}{e} \qquad 1\text{-}10$$

Where α, M_s, V, and H_{eff} are damping constant, the saturation magnetization, the volume and the effective magnetic field in FM2 layer, respectively. The symbol g (θ) is spin transfer efficiency that is function of spin polarization. Each of h/2, I and e is the angular momentum, the current and electron charge. To get memory with high density (>Gbits), the cell size of memory should be less than 100 nm. Therefore, a large current is needed for a conventional magnetic field reversing method. However, we are able to decrease current by the flux reversal technology using this spin transfer torque.

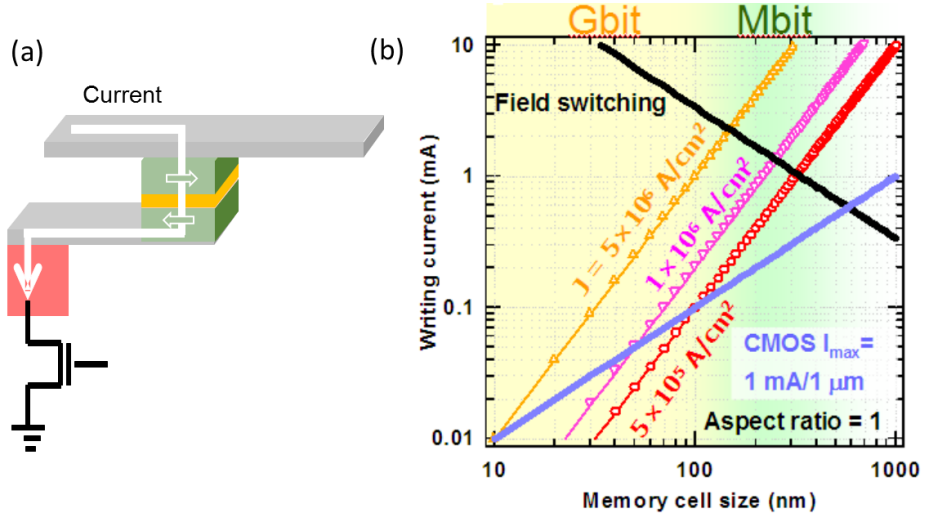

Figure 1-7 (a) Spin transfer switching and (b) Writing current as a function of memory cell size [7].

The development of MRAM has been increased every year. However, large power consumption about 4 mA per cell is one of the difficulty in this technology. Actually, such large power consumption is needed for switching of the magnetization by the magnetic field in conventional writing current method. Therefore, it seems to be difficult to achieve large memory capacity. However, this problem can be solved by using spin-transfer-torque effect for reversing of the magnetization, as mentioned above. Fig. 1-7 shows the writing current at different current density by spin-transfer switching as a function of memory size. When the memory size is 100 nm, the current density less than 3×10^5A/cm^2 is required.

The challenge in STT-MRAM is optimizing two physical quantity. The first one is the critical current density (J_{c0}) which is given by Slonczewski

$$J_{c0} = \frac{2e\alpha}{hg(\theta)} dM_s H_{eff} \qquad 1\text{-}11$$

Where d is the film thickness of magnetic free layer. The value of 0.5 MA/cm^2 is expected as J_{c0} practically. The second parameter is thermal stability factor. When the size decreases to nm scale, magnetization in cell tends to rotate easily by thermal energy k_BT due to super parmagnetism effect. To overcome to super parmagnetism effect magnetic materials with large uniaxial anisotropy are needed.

The thermal stability factor is defined as the following equation:

$$\Delta = \frac{K_u V}{k_B T} \qquad 1\text{-}12$$

The thermal stability factor larger than 60 is required for MRAM application to keep information for 10 years. The uniaxial anisotropy in Eq. 1-12 is proportional to the effective magnetic field in Eq. 1-11. So, enhancement of thermal stability factor leads to increasing of critical current density which is not desired for MRAM application. Basically, two different types of magnetic material can be used for magnetic electrodes of MTJs in STT-MRAM application. Magnetic material with in-plane and perpendicular magnetic anisotropy. These materials show different effective magnetic field. The effective magnetic field of in-plane and perpendicular magnetic material are $H_{k\parallel} + 2\pi M_s$ and $H_{k\perp} - 4\pi M_s$, respectively. The critical current density and thermal stability factor has been calculated by T. Miyazaki and H. Jin [7] for in-plane and perpendicular magnetic material as shown in Fig. 1-8(a) and (b), respectively. To satisfy necessary requirements ($J_{c0} < 0.5$ MA/cm^2 and $\Delta > 60$) the perpendicular magnetic material with saturation magnetization between 100 and 400 emu/cm^2 is needed.

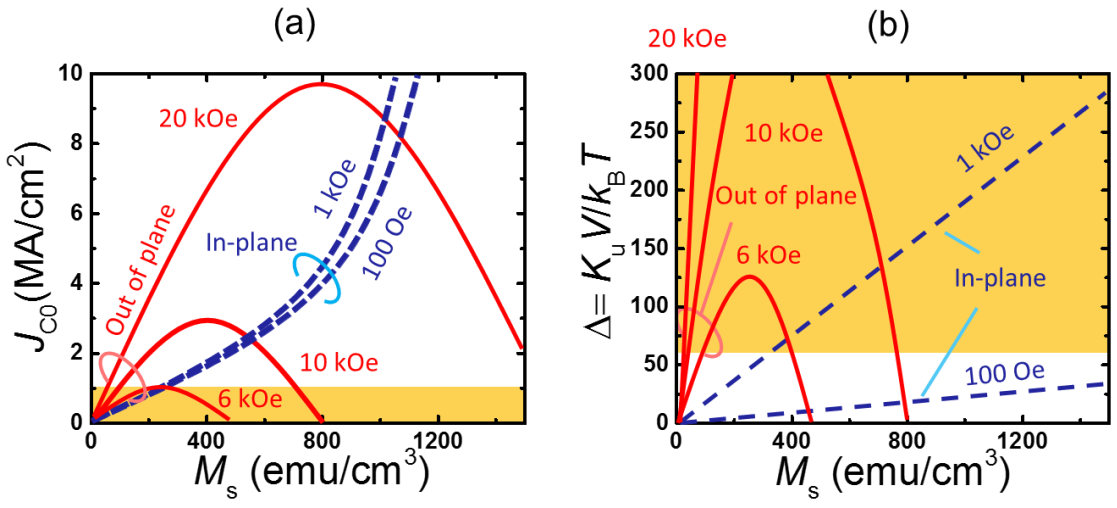

Figure 1-8 (a) Critical current density (J_{C0}) due to spin injection magnetization reversal and (b) thermal stability ($\Delta = K_u V/k_B T$) as a function of saturation magnetization of junction electrode. Solid curves in figure indicate perpendicular magnetization film, while broken curves indicate magnetization in plane film. Parameter s in Eq. 1-11 are $\alpha = 0.01$, $g = 0.5$, d = nm and junction area $\varphi = 100$ nm [7]

1.6 Landau-Lifshitz-Gilbert Description of STT

The Landau-Lifshitz-Gilbert (LLG) equation[20] describes the magnetization reversal under a spin-polarized current which is given by

$$\frac{d\vec{m}_1}{dt} = -\gamma\vec{m}_1 \times H_{eff} + \alpha\vec{m}_1 \times \frac{d\vec{m}_1}{dt} - \eta(\theta)\frac{\mu_B I}{eV}\vec{m}_1 \times (\vec{m}_1 \times \vec{m}_2) \qquad \text{1-13}$$

Here, $\vec{m}_1$ and $\vec{m}_2$ are the unit vector of magnetization for free and fixed layers, respectively. Each symbol of γ, α, η, μ_B, and e is gyromagnetic factor, damping constant, spin transfer efficiency, Bohr magneton and electron charge, respectively. In addition H_{eff}, I and V denote effective magnetic field, applied current and free layer volume, respectively.

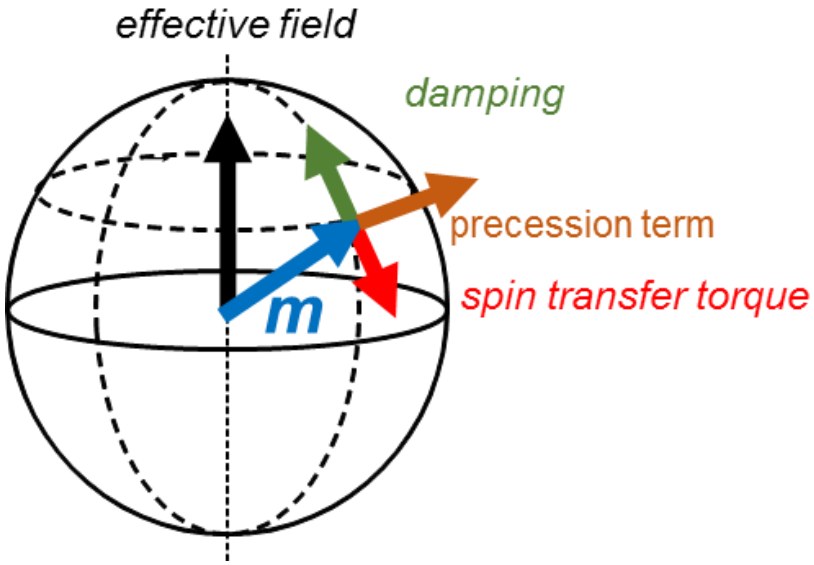

Figure 1-9 Schematic of damping, precession and spin transfer torque of magnetization vector in the presence of effective magnetic field.

In Eq. 1-13 the first term is coming from precession that describes the rotation of the magnetic moment around the applied field, whereas the second term is corresponding to damping component which acts to bring the magnetic moment back to its lowest energy state in the direction of the applied field. The last term shows the spin transfer torque (STT) which either acts with or against the damping torque depending on the direction of the applied current.

Schematic of damping, precession and spin transfer torque of magnetization vector in the presence of effective magnetic field is shown in Fig. 1-9. Three condition is considered. First, the magnetic moment will align itself with the effective field if both damping and STT terms have same direction. Second, a steady state with stable precession is expected if the STT is equal but opposite to the damping term. Third, current induced magnetization switching will occur when an opposite and sufficiently larger STT is present.

1.7 MnGa Alloys with Perpendicular Magnetic Anisotropy (PMA)

As we have explained in the section1.5.2, magnetic materials with perpendicular magnetic anisotropy are desired for memory application such as STT-MRAM. To optimize thermal stability factor and critical current density the material with large magnetic anisotropy, low damping constant, the small saturation magnetization and high spin polarization is needed. Until now several kind of material which show perpendicular magnetic anisotropy have been investigated to satisfy above mentioned requirement. Basically, perpendicular magnetic anisotropy materials can classify to four group. (1) Films of ordered alloys with an axial symmetric crystal structure, which exhibit uniaxial magnetic anisotropy even in bulk such as (Fe, Co)Pt ordered alloys[21,22], (2) ultra-thin films having interfacial PMA owing to symmetry breaking such as ultra-thin CoFeB film[23], (3) multilayer and superlattice films having an interfacial as well as bulk PMA such as Co/(Pt, Pd, Ni) multilayers[24–26], (4) films of amorphous rare-earth alloys having PMA such as TbFeCo and GdCoFe alloys[27,28].

Another candidate for satisfying the above mentioned properties are Mn-based alloys such as tetragonal MnGa and MnAl alloys which can classify to first group. However, MnAl alloy is not stable compared with MnGa alloy.

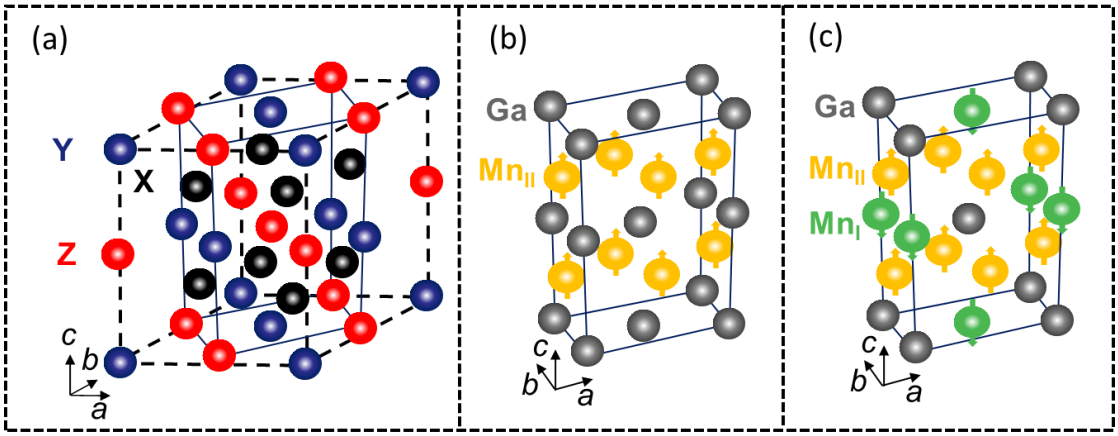

Figure 1-10 Illustration of crystal structure of (a) $L2_1$ structured cubic Heusler alloys, (b) tetragonal $L1_0$ and (c) $D0_{22}$ structured MnGa alloys

Basically, tetragonal MnGa alloys are derivative structure of cubic Heusler alloys. The Heusler alloys have the chemical formula of X_2YZ and structure of cubic $L2_1$ as shown in Fig. 1-10 (a) which is perfect ordered. These materials also assume B2 and A2 structures depending on the site disordered state, in which (Y, Z) and (X, Y, Z) are randomly substituted. There are many elemental combinations of X, Y and Z which exhibit various physical properties. Some Heusler alloys and compounds are known to be half-metals Such as Co-based Hesuler alloys, which has been demonstrated in the MTJs with the Co_2MnSi Heusler alloy electrodes in 2006.[29] These materials were used for spintronic application, however, they show the in plane magnetic properties.

The tetragonal MnGa alloys have two crystal structures: $L1_0$ and $D0_{22}$ ordered depending on Mn composition as shown in Fig1-10 (b) and (c). The magnetic properties of MnGa alloy originate from Mn element. The $L1_0$ ordered has Mn atom with perpendicular magnetic moment (Mn_{II}), whereas the $D0_{22}$ has two type of Mn atoms which show perpendicular magnetic moment with up (Mn_{II}) and down (Mn_I) directions.

The MnGa binary phase diagrams reported by Lu *et al.*[30] and Minakachi *et al.*[31] are shown in Fig. 1-11 (a) and (b), respectively. The γ_3 and γ_2 in Fig. 1-11 (a) are correspond to $L1_0$ and $D0_{22}$ ordered of MnGa alloy which mean these two structures are stable. However, MnGa

binary phase diagram is different in Fig. 1-11 (b). The $L1_0$ phase designated as γ_1 and γ_2 appears in two individual composition ranges of 65-68 at % Mn and 58-61 at % Mn, respectively. There is no phase related to $D0_{22}$ ordered in this phase diagram which suggested metastable phase for $D0_{22}$ ordered of MnGa alloy. However, the fabrication of metastable phase is very difficult, there are many report related to epitaxy of $D0_{22}$ ordered of MnGa alloy. Therefore, we think $D0_{22}$ ordered is stable phase.

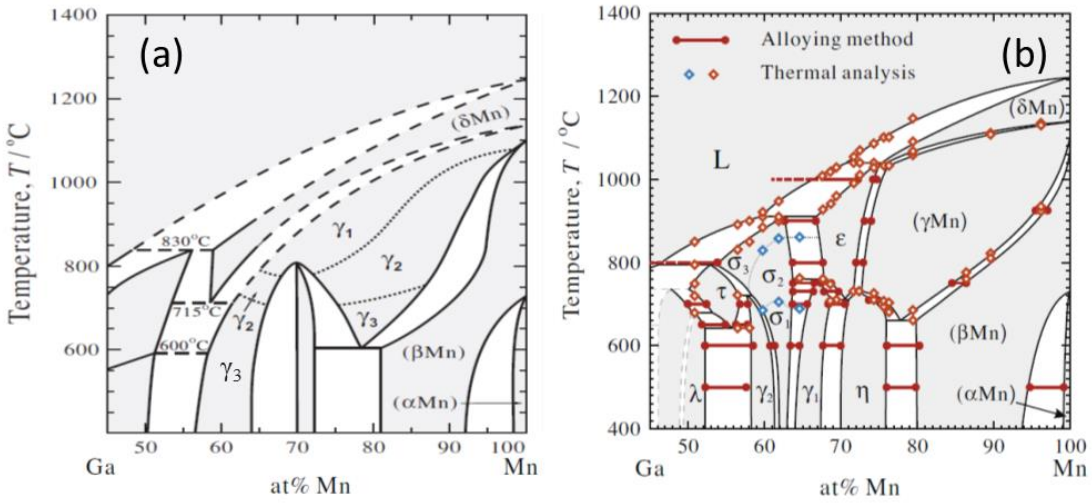

Figure 1-11 Mn–Ga binary phase diagrams reported by (a) Lu *et al*.[30] and (b) Minakuchi *et al*.[31]

The electronic band structure of tetragonal $L1_0$ and $D0_{22}$ structured MnGa alloys have been investigate by Mizukami *et al*.[32] are shown in Fig 1-12. In these figures spin ↑ (↓) is corresponds to majority (minority) spin band. The spin dependent density of states for tetragonal $L1_0$ and $D0_{22}$ structured MnGa alloys show non-half-metal properties at Fermi level which means density of states of neither majority nor minority spin at Fermi energy level is zero. The $L1_0$ structured MnGa alloy has largest peak of the density of states in the minority (majority) spin band is located at an energy level greater (lesser) than the Fermi energy level which is attributed to the *d* orbitals of the Mn atoms at the Mn_{II} sites. These peaks also appear for $D0_{22}$ structured MnGa alloy. This suggested the magnetic moment of the Mn atoms at Mn_{II} sites in $D0_{22}$ structured MnGa alloy is not largely different from that for $L1_0$ structured MnGa alloy. Mizukami *et al*. have reported the magnetic moment of Mn at the Mn_{II} site for tetragonal $L1_0$ and $D0_{22}$ structured MnGa alloys are 2.6 and 2.5 μ_B, respectively. The estimation value for the

magnetic moment of Mn at the Mn_I site is -3.1 μ_B. The $D0_{22}$ structured MnGa shows larger spin polarization at Fermi level compared with $L1_0$ structured MnGa as can be seen from Fig. 1-12.

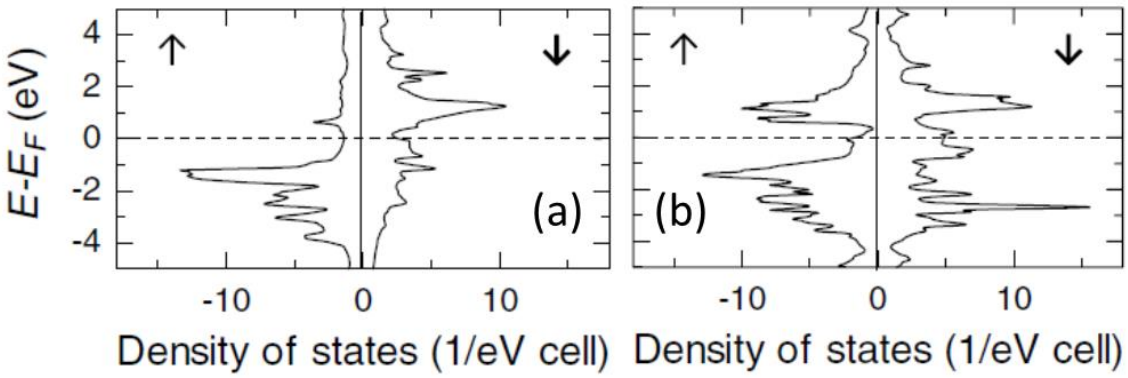

Figure 1-12 Spin dependent density of states for tetragonal (a) $L1_0$ and (b) $D0_{22}$ structured Heusler-like alloys. [38]

The $L1_0$ ordered exhibit good stability when content of Mn is 50 to about 65%.[33] For the Mn content of about 65–75%, the $D0_{22}$ structure appears and exhibits strong ferrimagnetism as confirmed by neutron scattering.[34] Magnetization decreases with increasing Mn contents, whereas the alloys have a large uniaxial magnetic anisotropy with magnetically easy axis parallel to the c-axis in the above compositions. The out-of-plane and in-plane magnetization curves for 30-nm thick Mn_xGa_{1-x} alloy films grown on MgO substrates with Cr buffer layers with different composition are shown in Fig. 1-13. As Mn content increases magnetization decreases, whereas coercive field (H_c) increases. The tunable magnetization values are about 200-600 emu/cm^2 depending on Mn content.[32] The K_u value about 15 Merg/cm^3 was reported by Mizukami *et al*. for $L1_0$ ordered, whereas for the $D0_{22}$ ordered K_u value decreases to 10 Merg/cm^3.

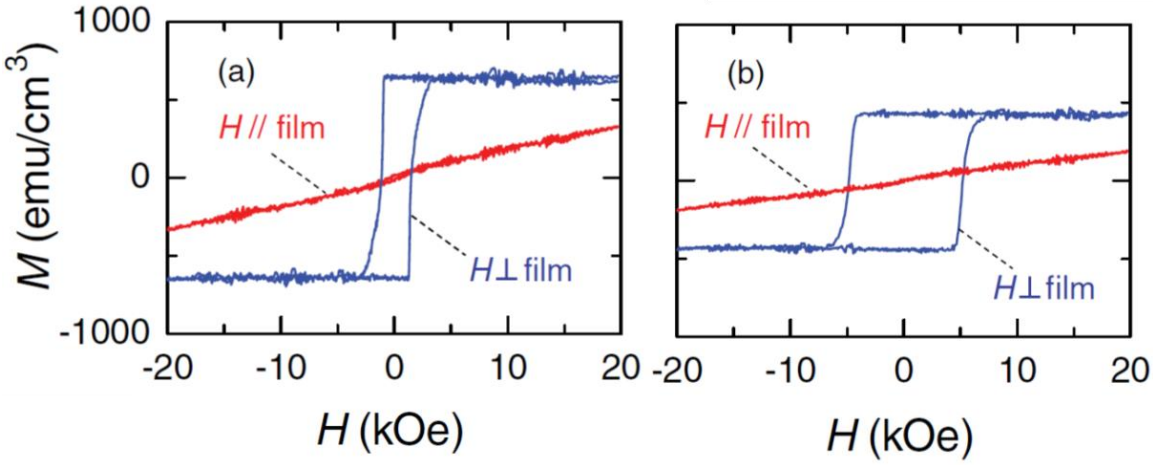

Figure 1-13 Out-of-plane and in-plane magnetization curves for 30-nm thick Mn_xGa_{1-x} alloy films grown on MgO substrates with Cr buffer layers (a) x = 0.54 and (b) x = 0.62. [32]

The spin polarization of the $D0_{22}$ Mn_3Ga and Mn_2Ga epitaxial films have been investigated by Kurt *et al*. They have reported the spin polarization of 0.58 and 0.4 for $D0_{22}$ Mn_3Ga and Mn_2Ga epitaxial films, respectively by using the point contact Andreev refection (PCAR) method.[35] Bulk *et al*. have reported the Curie temperature above 730 K for $D0_{22}$ Mn_3Ga compensated ferrimagnet.[36]

Another point of MnGa alloy is small Gilbert damping constant. The comparison of Gilbert damping (or effective damping) constant and the effective PMA constant for various kinds of PMA films reported is shown in Fig. 1-14. The small Gilbert damping constant and effective PMA compared with another PMA films made MnGa more and more applicable for STT-MRAM application. The $L1_0$ structure shows smaller Gilbert damping constant (0.008) compared with $D0_{22}$ structure (0.015). However, the $L1_0$ structure shows larger K_u value and smaller Gilbert damping constant compared with $D0_{22}$ structure, the advantages of $D0_{22}$ structure are relative small saturation magnetization and larger spin polarization. Therefore in this study $D0_{22}$ structure were used as PMA material.

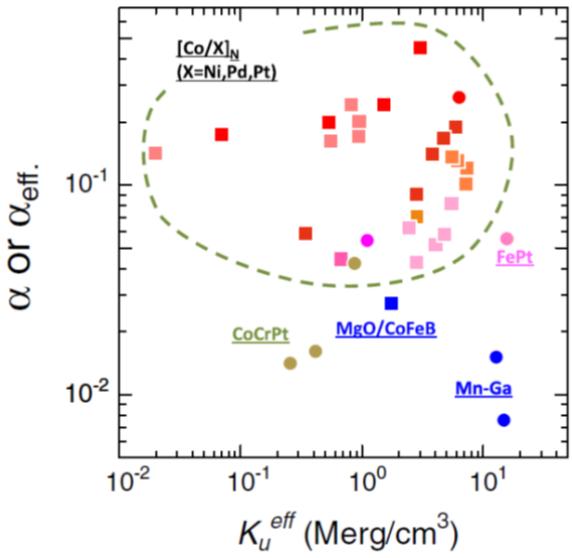

Figure 1-14 Gilbert damping (or effective damping) constant and the effective PMA constant for various kinds of PMA films reported.[38]

1.7.1 Issues

Until now many studies focused on structural, magnetic, transport properties, spin polarization, and magnetization dynamics of MnGa alloys.[32,33,35–47] Based on these studies, MnGa alloys have small and tunable saturation magnetization abut 200-600 emu/cm^3, large K_u value about 10-15 Merg/cm^3, high spin polarization about 0.4-0.58, high Curie temperature above 730 K and low Gilbert damping constant less than 0.01 which make this material as good candidate for spintroncs application such as STT-MRAM based on MgO-MTJs. One of the issues related to MnGa alloy based MgO-MTJs is small TMR ratio less than 10%, which is probably due to the large lattice mismatch between MnGa and MgO and also the oxidation of interface. The relatively high TMR ratio has been reported in the perpendicular magnetic tunnel junctions (p-MTJs) based on MnGa electrode with an ultra-thin ferromagnetic metal/alloy interlayer between MnGa and MgO barrier.[37,43,44,48] The TMR data at room temperature for different MnGa compositions based p-MTJ with different thickness interlayer of Co, Fe, CoFeB, and Fe/Co are shown in Fig. 1-15 (a), (b), (c), and (d), respectively. The TMR data shows maximum value when interlayer thickness is 1.5 nm for $Mn_{62}Ga_{38}$ alloy. The maximum TMR value for $Mn_{62}Ga_{38}$ alloy could be related to thermal stability of MnGa alloys, namely atomic diffusion at interface is not significant in the intermediate compositions.[38]

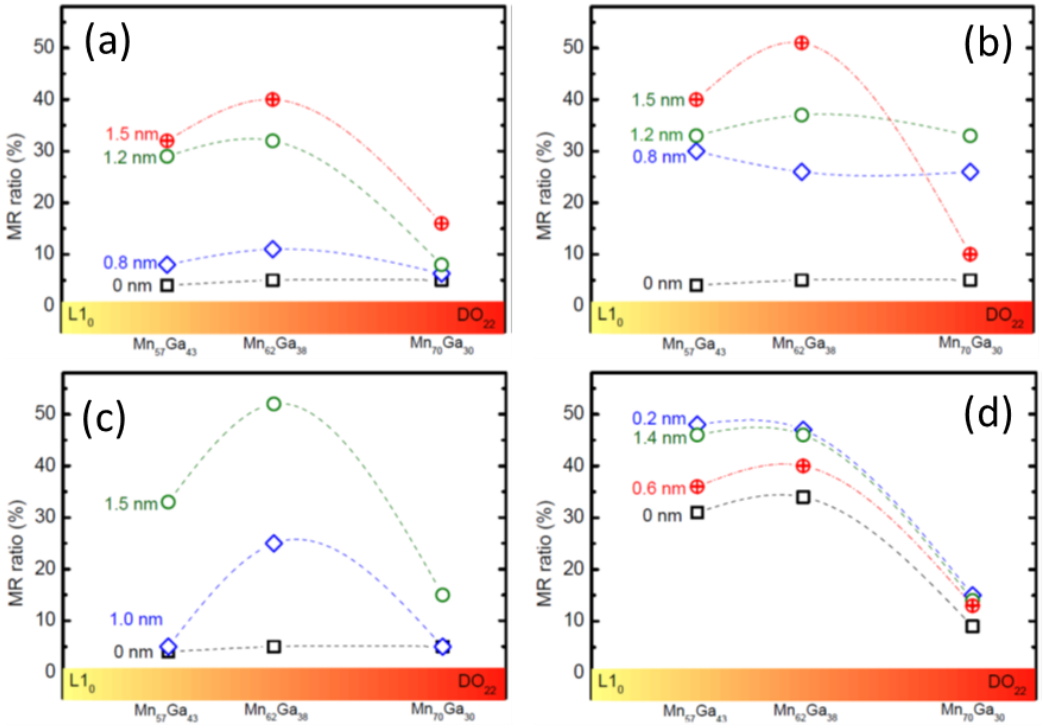

Figure 1-15 TMR data at room temperature for Mn–Ga based p-MTJ with the interlayer of (a) Co, (b) Fe, (c) CoFeB and (d) Fe/Co.The data are plotted with different thickness of the interlayer and different Mn–Ga compositions.[38]

Ma *et al*. have reported the magnetic interfacial exchange coupling was found to be ferromagnetic (antiferromagnetic) for the Fe (Co)-rich interlayer, when the FeCo alloys interlayer were introduced.[37] The *M*-*H* loops of MnGa (30 nm)/ $Fe_{1-x}Co_x$ (1.5 nm) with x equal to 20% and 60% are shown in Fig. 1-16 (a) and (b), respectively. The *M*-*H* loop of 30-nm MnGa single films also shown for comparison. The magnetization curves show larger and smaller remnant magnetization compared to 30-nm MnGa single film for x equal to 20% and 60%, respectively. The MR (*H*) loops of p-MTJs tested in a perpendicular direction at room temperature for x equal to 20% and 60% are shown in Fig. 1-16 (b) and (c), respectively. They observed the normal and inverted MR (*H*) loops for x equal to 20% and 60%, which are due to ferromagnetic and antiferromagnetic exchange coupling, respectively.

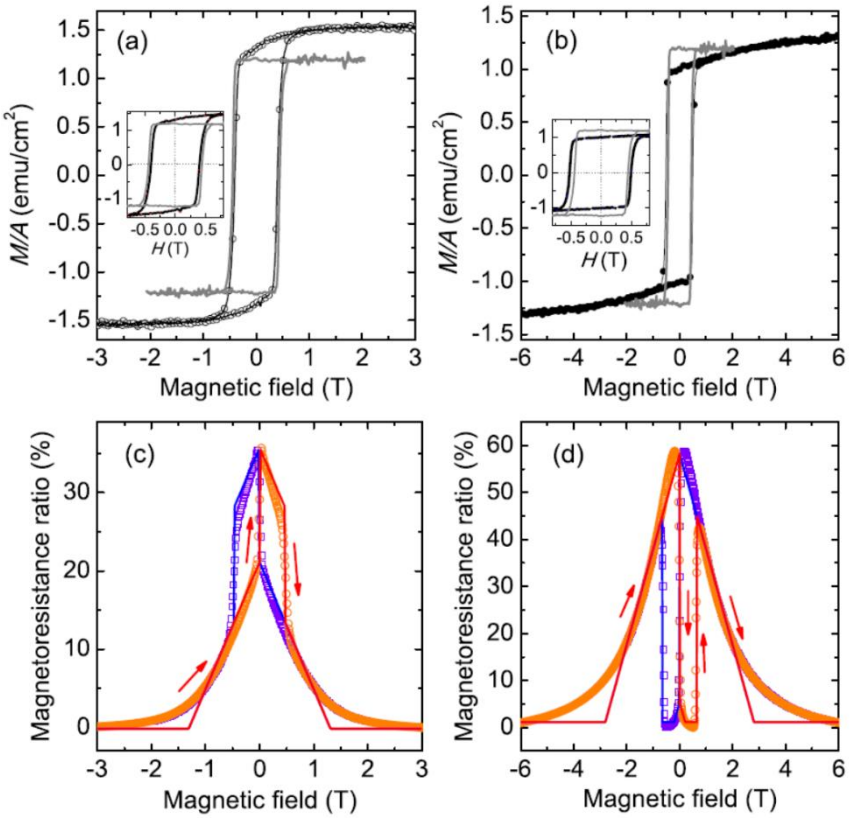

Figure 1-16 *M-H* loops of MnGa 30 nm/ $Fe_{1-x}Co_x$ (1.5 nm) with x equal to 20% (a) and 60% (b). The gray line is the *M-H* loop of 30-nm MnGa single films included for comparison. (c) And (d) are the corresponding MR (*H*) loops of p-MTJs tested in a perpendicular direction at room temperature. The solid lines in (c) and (d) are the fits based on the FM and AFM J_{ex} in MnGa/$Fe_{80}Co_{20}$ and MnGa/$Fe_{40}Co_{60}$ interfaces, respectively.[37]

The reported MR ratio of p-MTJs based on MnGa alloy with inserting ultra-thin ferromagnetic metal/alloy is summarized in Fig 1-17 (a). The stacking structure of p-MTJs is also shown in Fig. 1-17 (b). So exchange coupling constant (J_{ex}) plays important role to get high TMR ratio in p-MTJs based on MnGa alloy. The strong ferromagnetic and antiferromagnetic exchange coupling between MnGa alloy and interlayer can increase TMR ratio. However, the antiferromagnetic exchange coupling reduces stray field and also this coupling is very rare in the magnetic films with PMA and is technologically important to achieve synthetic ferrimagnetic structure for memory applications. Therefore, further investigation of this coupling in magnetic bilayer with MnGa is meaningful.

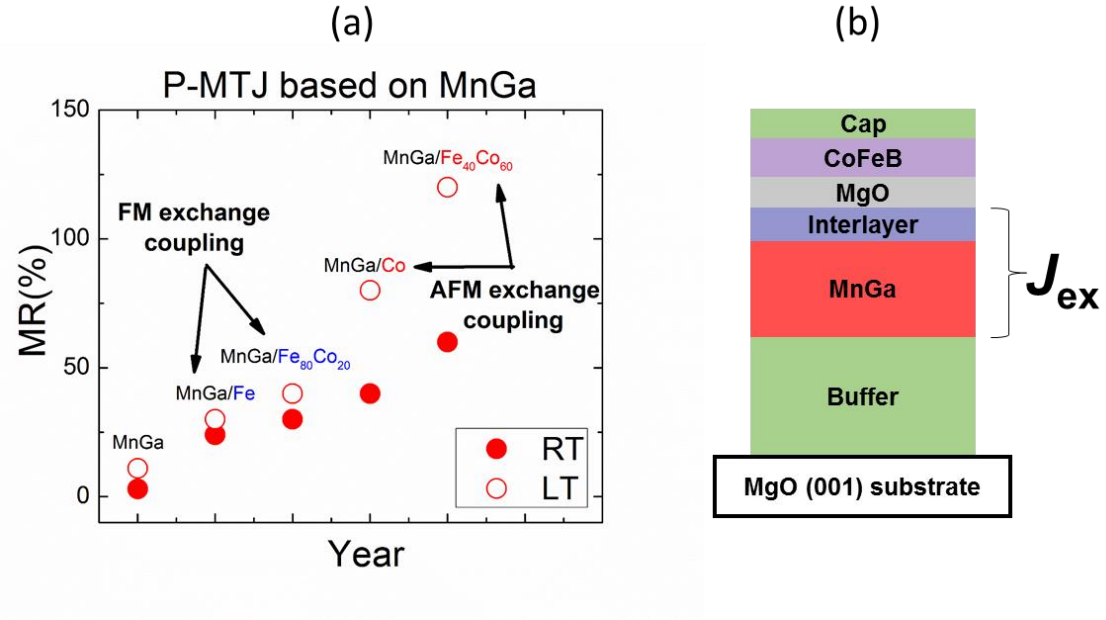

Figure 1-17 (a) The reported MR ratio of p-MTJs based on MnGa alloy with inserting ultra-thin ferromagnetic metal/alloy.[37,43,44] (b) Stacking structure of p-MTJs.

Finding and designing new material to overcome difficulty to use in spintronics application such as STT-MRAM is very important. Although many type of materials have been investigated until now, but still the window is open for researchers to fabricate new materials for developing of STT-MRAM application. Therefore, focusing on structural and magnetic properties of new materials is essential in this area. The MnGa alloys show very unique properties and this makes MnGa alloys as good candidate for STT-MRAM application. However, this material showed very small TMR ratio which is not comparable with predicted TMR value (600 %) reported by Kubota *et al.*[49] for $D0_{22}$ Mn_3Ga/MgO/$D0_{22}$ Mn_3Ga p-MTJs. So with an interlayer insertion we are able to increase TMR ratio and also control structural and magnetic properties depending on desired application. The cubic Co-based Hesuler alloys have potential to use as an interlayers in this study. As we discussed in section 1.7 MnGa alloys are derivative structure of cubic Heusler alloys. So, fabrication of bilayer of MnGa and cubic Co-based Hesuler alloys is meaningful.

The special properties of Co-based Hesuler alloys such as half-metal properties, large in plane TMR ratio, and low Gilbert damping constant, as well as high Curie temperature are other motivations for our study. In contrast with 3d ferromagnetic layer, there are advantages

of using Co-based Hesuler alloys as interlayer. The magnetization and spin polarization of Co-based Hesuler alloys are smaller and larger than 3d ferromagnetic films such as Fe and Co, respectively. To get high TMR ratio, the spin polarization has very important role which means by using materials that have large spin polarization between MnGa and MgO barrier layer possibility to achieve high TMR ratio will increase. In addition, Co-based Hesuler alloys are in the same category family materials with MnGa alloys. Therefore, we expect better matching between Co-based Hesuler alloys and MnGa film causes to making bilayer films with good quality.

1.8 Objectives of the Research

Magnetic tunnel junctions (MTJs) with magnetic electrodes of perpendicular magnetic anisotropy (PMA) have been studied significantly for the high density spin-transfer-torque magnetoresistance random access memory (STT-MRAM). In this application, it is crucial that magnetic films with PMA for electrode possess a low saturation magnetization (M_s), low damping constant (α), and high spin polarization (P) for optimizing the thermal stability factor and the switching current density in STT-MRAM. The requirements needed for STT-MRAM application in generally are the tunnel magnetoresistance (TMR) ratio more than 100% at room temperature, the critical current density less than 0.5 MA/cm^2, and thermal stability factor larger than 60 for 10 years longevity.

The MnGa is one of the good candidate for satisfying the properties mentioned above. One of the issues related to MnGa alloy based MgO-MTJs is small TMR ratio, which is probably due to the large lattice mismatch between MnGa and MgO and also the oxidation of interface. The relatively high TMR ratio has been reported in the perpendicular magnetic tunnel junctions (p-MTJs) based on MnGa electrode with an ultra-thin ferromagnetic metal/alloy interlayer between MnGa and MgO barrier. Interestingly, the magnetic interfacial exchange coupling (J_{ex}) was found to be ferromagnetic (antiferromagnetic) for the Fe (Co)-rich interlayer, when the FeCo alloys interlayer was introduced. So, further investigation of this coupling in magnetic bilayer with MnGa is meaningful because the antiferromagnetic coupling is very rare in the magnetic films with PMA and is technologically important to achieve synthetic ferrimagnetic structure for memory applications. To reduce critical current density with remaining thermal stability factor, thickness of this synthetic ferrimagnet should be less than 5 nm which is very important to use as free layer in p-MTJs based on MnGa alloy.

In this dissertation we study on the structural and magnetic properties of the bilayer consisting of in plane magnetic anisotropy materials (IMA) and $D0_{22}$-MnGa film. First, Co-B binary was tested as IMA materials in this study. The Co film and CoB alloy have crystalized and amorphous structures, respectively which help us to better understanding what kinds of material is necessary to get strong exchange coupling in bilayer films. Then the Co-based cubic Heusler alloys including Co_2FeAl (CFA), Co_2FeSi (CFS), Co_2MnAl (CMA), and Co_2MnSi (CMS) were used as IMA materials. The half-metal properties and large in plane TMR ratio make these materials interesting in this area. In addition, tetragonal $D0_{22}$-MnGa alloy is derivative structure of cubic Heusler alloys which suggested better compatibility of Heusler alloys with tetragonal $D0_{22}$-MnGa alloy.

Objectives of this research to satisfy needed requirements for STT-MRAM are summarized as followings:

- Investigation of structure and magnetic properties of cubic Heusler/tetragonal $D0_{22}$-MnGa bilayer film to get epitaxy with good quality.
- Investigation of interfacial exchange coupling constant of cubic Heusler/tetragonal $D0_{22}$-MnGa bilayer film to get strong antiferromagnetic J_{ex}.
- Make clear the origin of the interfacial exchange coupling for cubic Heusler/tetragonal $D0_{22}$-MnGa bilayer film.
- Reduction of thickness of cubic Heusler/tetragonal $D0_{22}$-MnGa bilayer film to achieve synthetic ferrimagnet with PMA.

In Fig. 1-18 the stacking structure of target of this research is shown.

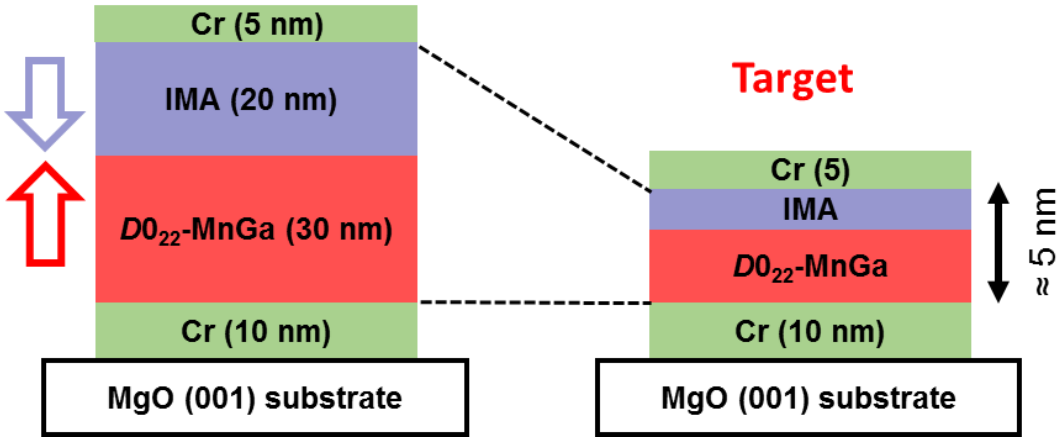

Figure 1-18 Stacking structure for target of this study

This dissertation is organized as following:

- In Chapter 1, the introduction of spintronics, magnetic tunnel junctions, application of magnetic tunnel junctions in magnetic memories and their requirements, MnGa alloys with perpendicular magnetic anisotropy and objectives of my research have been explained.
- In the next chapter, the experimental techniques will be presented.
- In Chapter 3, the influence of annealing temperature and thickness effect of Co-B binary as IMA materials on structural and magnetic properties of IMA/$D0_{22}$-MnGa bilayer will be discussed.
- In Chapter 4, the influence of annealing temperature and thickness effect of Co-Based cubic Heusler alloys as IMA materials on structural and magnetic properties of IMA/$D0_{22}$-MnGa bilayer will be described.
- In Chapter 5, dependence of structure and magnetic properties on the thickness of $D0_{22}$-MnGa and Co_2Mnsi films for Co_2Mnsi/ $D0_{22}$-MnGa bilayer film will be explained.
- In Chapter 6 discussion and conclusion of my research will be presented.
- Finally, in chapter 7 future perspective of my research will be suggested.

Chapter 2 Experimental Method

In this chapter experimental techniques and equipment which were used for investigation of structural and magnetic properties of MnGa film with different IMA layer will be explained. The epitaxial bilayers were fabricated using an ultrahigh vacuum magnetron (UHV) sputtering system with a base pressure of less than 1×10^{-7} Pa. Annealing temperature process has been investigated using post annealing by rapid thermal annealing (RTA) system. Film compositions estimated by the inductively coupled plasma spectroscopy. For structural characterization the X-ray diffractometer (XRD) with the Cu K_α radiation was used. Magnetic properties have been investigated by vibrating sample magnetometer (VSM), polar magneto optical Kerr effect (P-MOKE) system at laser wavelength of 400 nm.

2.1 Substrate Preparation

Bilayer films were deposited onto MgO (001) (10×10 mm^2). We cleaned the substrates by using a bath of acetone, ethanol, and pure water with ultrasonic system for 15, 15, and 2 minutes, respectively. They were then dried using nitrogen gas.

2.1.1 Magnetron Sputtering

There are many different ways for deposition of materials such as metals, ceramics, and plastics onto a substrate as thin film. Sputtering is one of the popular ways to fabricate thin films which use physical vapor deposition (PVD) process for depositing materials onto a substrate. In this method atoms was ejected from materials and then deposited onto a substrate in a high vacuum environment. Argon atoms whose are electrically neutral introduced into a vacuum chamber with pressure of 1 to 10 mTorr in which a DC voltage is placed between the target and substrate. This DC voltage ionizes Argon atoms and then a plasma creates in the chamber. This plasma is also known as a glow discharge due to the light emitted. Anode target absorb Argon ions which have charge and acceleration. Then atoms ejects from target and move to the substrate due to collision with Argon ions. In chamber also there are electrons and these electrons have important role in ionization of Argon atoms. Basically, there are different

ways to enhance efficiency of sputtering. One of the popular way is magnetron sputtering system is shown in Fig. 2-1.

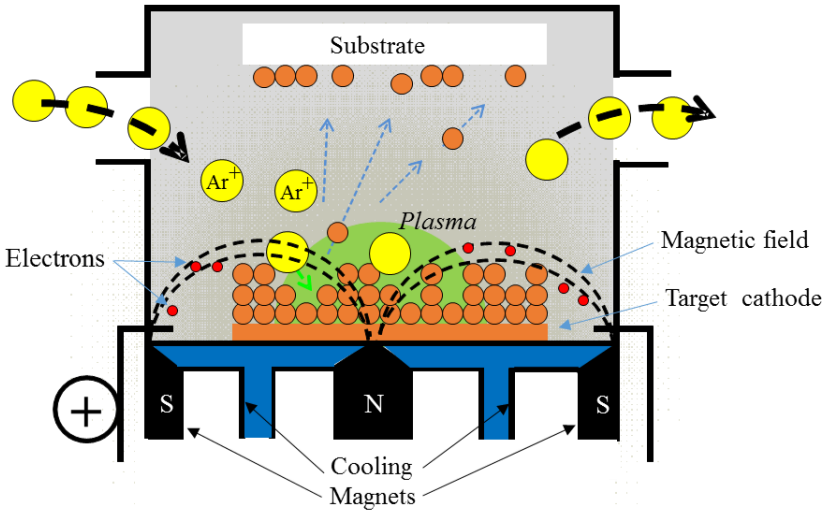

Figure 2-1 Schematic of magnetron sputtering system.

The magnetron sputtering has strong magnetic field near the target area compared with basic DC sputtering system described above. This field makes electrons to travel spiral along magnetic flux lines near the target instead of being attracted toward the substrate. By this method we are able to limit the plasma near the target, and then prevent damaging of the thin film. Moreover, electrons can travel longer distance which increases the probability of further ionizing Argon atoms. This tends to generate a stable plasma with high density of ions. Therefore, efficiency of the sputtering process will increase due to existence of more ions and ejected atoms.

2.1.2 Film Deposition

We investigated the influence of annealing temperature on the structural and magnetic properties of IMA (20 nm)/$D0_{22}$-MnGa (30 nm) bilayer films. The binary of Co-B and different Heusler alloys including Co_2FeAl (CFA), Co_2FeSi (CFS), Co_2MnAl (CMA), and Co_2MnSi (CMS) were used as IMA materials in IMA (20 nm)/$D0_{22}$-MnGa (30 nm) bilayer films. The stacking structure of all bilayers were: the (100) single crystalline MgO substrate /Cr (10) $D0_{22}$-MnGa (30) / IMA (20) / Cr (5) (thickness is in nanometers) which prepared by using ultra high vacuum magnetron sputtering with a base pressure of less than 1×10^{-7} Pa.

All the layers were deposited at room temperature. The in-situ annealing was employed at 400ºC after the MnGa deposition. Annealing temperature dependence has been investigated using post annealing by rapid thermal annealing (RTA) system. We also prepared epitaxial 30-nm-thick MnGa film without IMA layer with the same stacking structure and also a single IMA layer as reference samples.

In order to fabricate synthetic ferrimagnet with good perpendicular magnetic anisotropy (PMA), the thickness of IMA materials were decreased. Two series IMA (1-20 nm)/$D0_{22}$-MnGa (30 nm) bilayer films without and with post annealing at optimized annealing temperature were fabricated. The staking structure of all the bilayers were: the (100) single crystalline MgO substrate /Cr (10) $D0_{22}$-MnGa (30) / IMA (1-20) / Cr (5).

The thickness of $D0_{22}$-MnGa film were decreased to determine minimum critical thickness to see good structural and magnetic properties. Six sample with different thicknesses of 5, 7.5, 10, 15, 20, and 30 nm thickness were fabricated. Finally, two series CMS (1-7 nm)/$D0_{22}$-MnGa (7.5 nm) bilayer films without and with post annealing at 400ºC were prepared.

The stacking structure of all the samples for each material are shown in Fig. 2-2, 2-3, 2-4, 2-5, 2-6, 2-7, and 2-8.

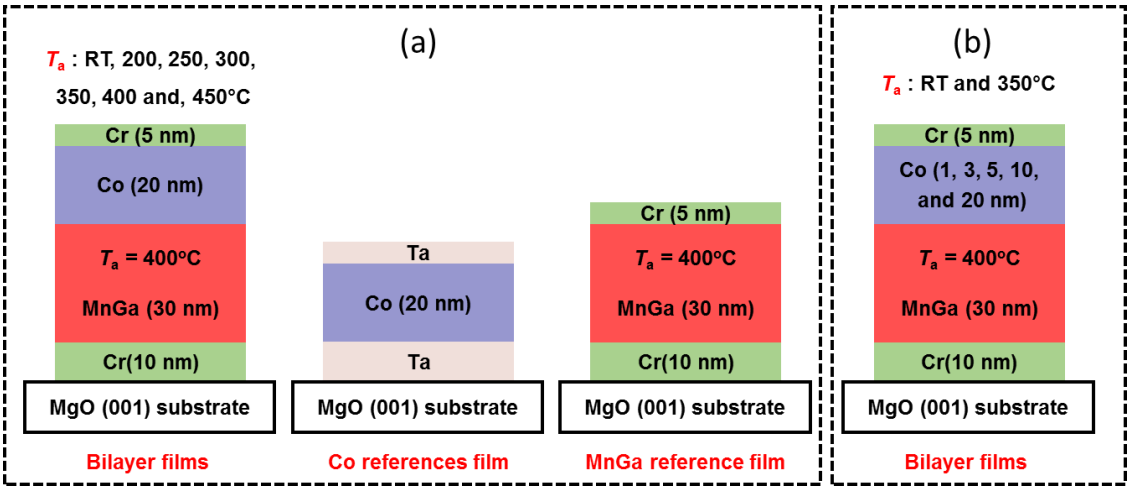

Figure 2-2 (a) The staking structure of Co/MnGa bilayer, Co and MnGa references films for investigation of annealing temperature dependence. (b) The staking structure of Co/MnGa bilayer films for investigation of thickness dependence.

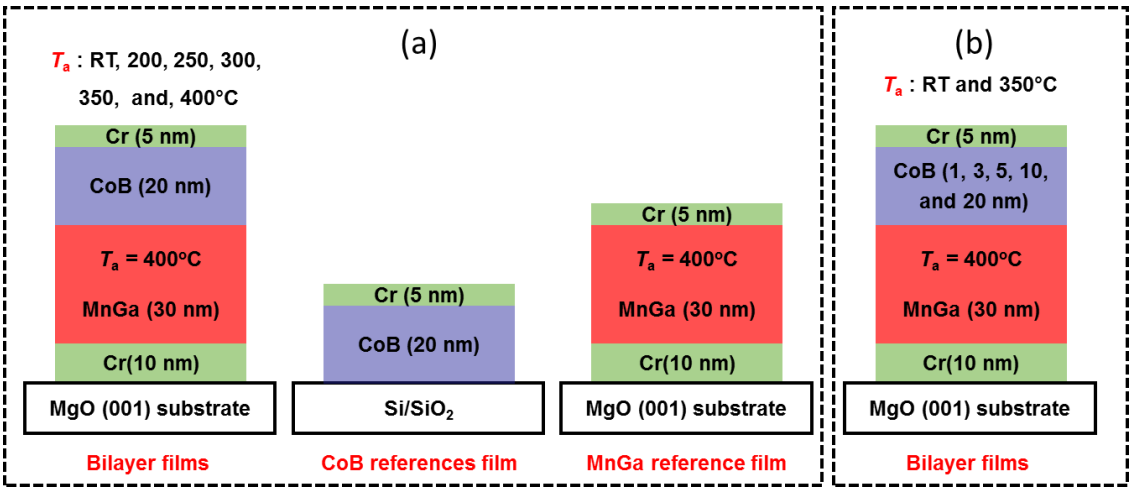

Figure 2-3 (a) The staking structure of CoB/MnGa bilayer, CoB and MnGa references films for investigation of annealing temperature dependence. (b) The staking structure of CoB/MnGa bilayer films for investigation of thickness dependence.

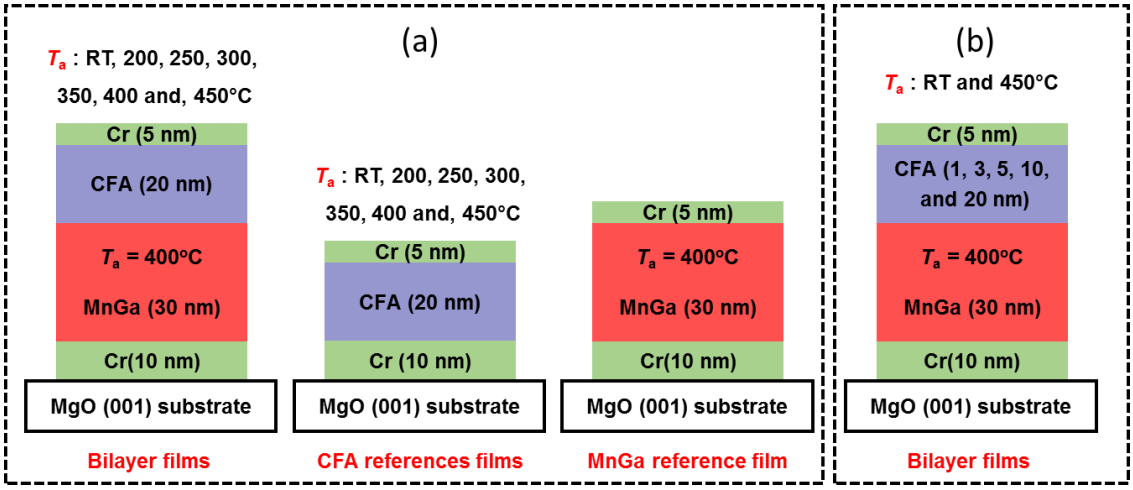

Figure 2-4 (a) The staking structure of CFA/MnGa bilayer, CFA and MnGa references films for investigation of annealing temperature dependence. (b) The staking structure of CFA/MnGa bilayer films for investigation of thickness dependence.

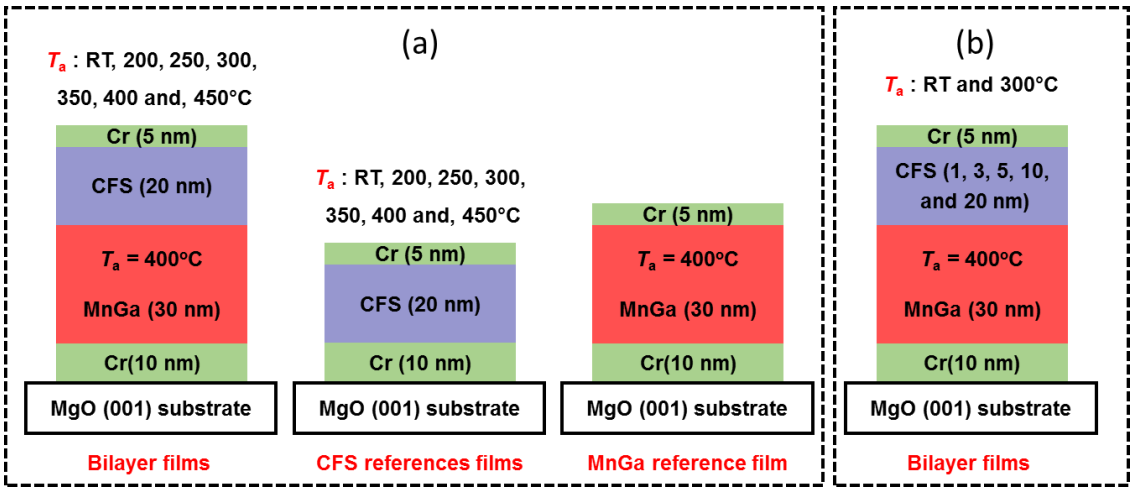

Figure 2-5 (a) The staking structure of CFS/MnGa bilayer, CFS and MnGa references films for investigation of annealing temperature dependence. (b) The staking structure of CFS/MnGa bilayer films for investigation of thickness dependence.

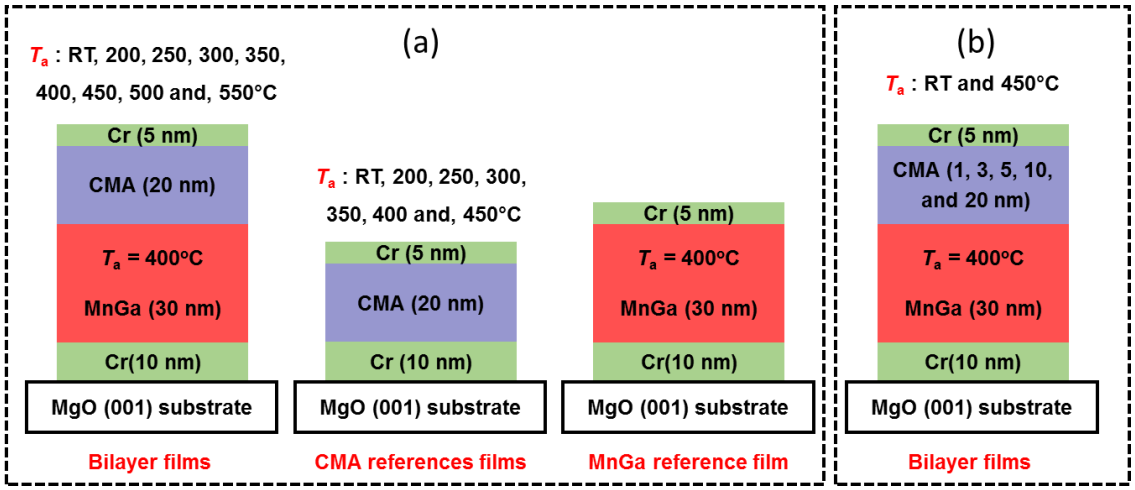

Figure 2-6 (a) The staking structure of CMA/MnGa bilayer, CMA and MnGa references films for investigation of annealing temperature dependence. (b) The staking structure of CMA/MnGa bilayer films for investigation of thickness dependence.

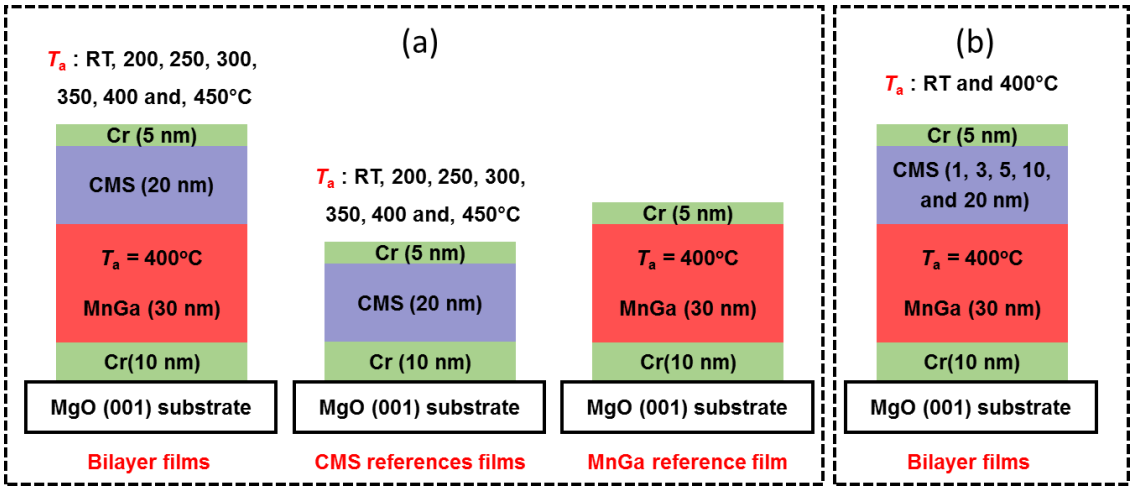

Figure 2-7 (a) The staking structure of CMS/MnGa bilayer, CMS and MnGa references films for investigation of annealing temperature dependence. (b) The staking structure of CMS/MnGa bilayer films for investigation of thickness dependence.

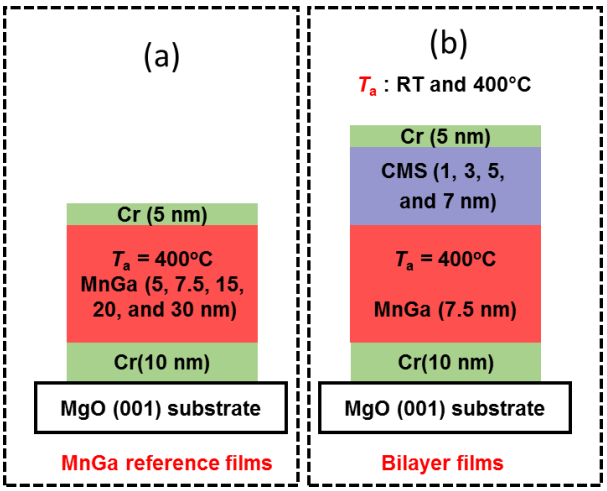

Figure 2-8 (a) The staking structure of MnGa film and (b) CMS/MnGa bilayer film for investigation of thickness dependence.

2.2 Structural Properties

2.2.1 X-Ray Diffraction

The discovery of X-rays in 1895 enabled scientists to probe crystalline structure at the atomic level.[50] X-ray diffraction has been used in two main areas. The firs is fingerprint characterization of crystalline materials and the second is determination of their structure. The X-ray powder pattern can be used as a fingerprint for crystalline identification as each crystalline solid has its unique characteristic. As the material has been identified, we are able to determine structure of material by X-ray diffraction measurement. Therefore, it is possible to say how the atoms order in the crystalline state and also what the interatomic distance and angle they have. Basically, for structure characterization in solid state chemistry and materials science the X-ray diffraction is one of the most popular tools. Moreover, by this measurement we can also determine the size and the shape of the unit cell. The peaks in an X-ray diffraction pattern are directly related to the atomic distance which is based on the elastic scattering of x-rays and only those planes which fulfill Bragg's law ($n\lambda = 2d\sin\theta$) are detected X-rays are produced by bombarding a metal target (Cu, Mo usually) with a beam of electrons emitted from a hot filament (often tungsten). To investigate the crystallographic properties of the films the X-ray diffraction is used in this study. The out of plane θ-2θ scan measurement were used to estimate c lattice constant of films. The incident beam makes an angle of θ with the film surface and 2θ with the diffracted beam as shown in Fig. 2-9.

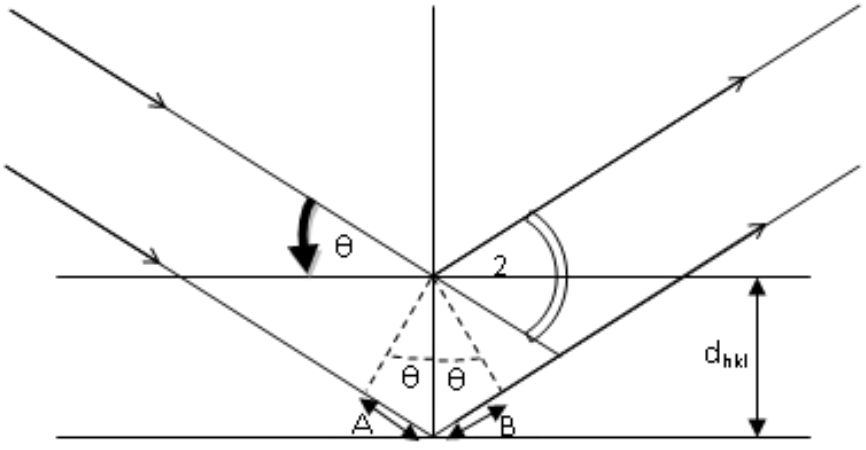

Figure 2-9 Schematic of X-ray diffraction

2.2.2 Transmission electron microscopy

In this study we have examined the structure and microstructure of the samples by using transmission electron microscopy (TEM) observations. A beam of electrons is transmitted through an ultra-thin specimen and then due to interaction with the specimen, we are able to create an image that is magnified by transmission electron microscopy measurement. The resolution of TEM image is relatively large when it compared with resolution of light microscopes image. Therefore, this enables us to examine fine detail-even as small as a single column of atoms, which is thousands of times smaller than the smallest resolvable object in a light microscope.

2.3 Magnetic Properties

2.3.1 Vibrating sample magnetometer (VSM)

Vibrating Sample Magnetometer is a versatile and sensitive method of measuring magnetic properties developed by Foner[51] and is based on the flux change in a coil when the sample is vibrated near it. By this measurement we are able to measure the magnetic properties of materials as a function of temperature and field. Schematic of VSM system is shown in Fig. 2-10. The magnetic sample should fix in special region to locate in uniform magnetic film. The magnetic sample is connected at the end of a rigid rod (sample holder) attached to a mechanical resonator, which oscillates the sample at a fixed frequency. Basically, the sample can vibrated up and down in a region which surrounded by several pickup coils in a magnetometer. As the magnetic sample vibrated up and down magnetic flux changes during time. This can create an induction voltage in the coils that is proportional to the magnetization of the sample based on Faraday's law of magnetic induction. Therefore, by measuring this voltage we are able to measure magnetic properties of magnetic sample. In this work, the VSM is used for obtaining the magnetization curves of magnetic samples. The maximum applied field for the VSM measurement was 20 kOe. We used two types of measurement including in-plane and out-of-plane measurements. In the in-plane measurement the normal vector of plane of magnetic film is perpendicular to direction of magnetic field. However, in the out-of-plane measurement the normal vector of magnetic film is parallel to the direction of the applied field.

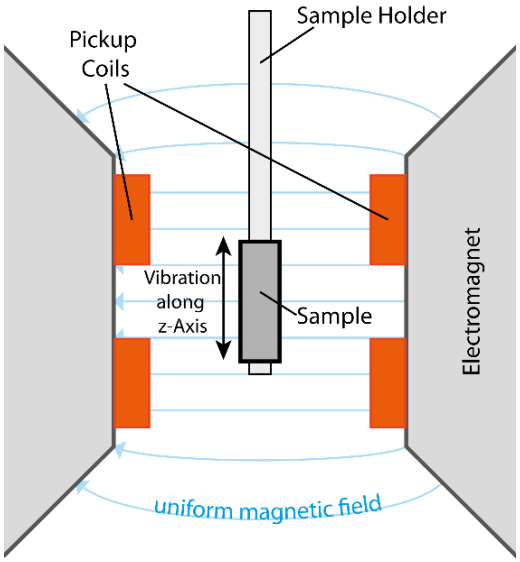

Figure 2-10 Schematic of VSM system.

2.3.2 Magneto Optical Kerr Effect (MOKE)

In physics the magneto-optic Kerr effect (MOKE) describes the changes to light reflected from a magnetized surface which is used in materials science to investigate the magnetization structure of materials. The polarization and intensity of light can change when it reflect from a magnetized surface. Normally, the effect is similar to the Faraday's effect. The Faraday's effect describes changes to light transmitted through a magnetic material, while the Kerr effect describes changes to light reflected from a magnetic surface. Because of the different magnetization directions relative to the plane of the incident light there are three different configurations for MOKE as shown in Fig. 2-11. In the polar Kerr effect configuration (a) the magnetization *M* lies perpendicularly to the sample surfaces. In the case of longitudinal Kerr effect (b) *M* lies parallel to the sample surfaces and to the plane of incidence. In the equatorial or transverse configuration (c) *M* lies parallel to the sample surfaces and perpendicular to the plane of incidence. The polar magneto-optic Kerr effect measurement was used in this study.

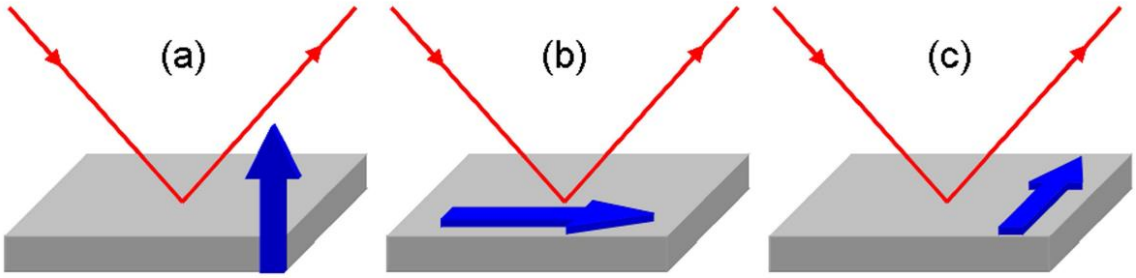

Figure 2-11 The three different types of Kerr effect: (a) polar, (b) longitudinal and (c) transverse.

Chapter 3 Structural and Magnetic Properties for Bilayer of the Co-B Binary and Tetragonal Heuseler Mn-Ga Compounds

3.1 Annealing Temperature Dependence of Co (20 nm)/$D0_{22}$-MnGa (30 nm) Bilayer

To investigate structural and magnetic properties of Co (20 nm)/$D0_{22}$-MnGa bilayer we have fabricated seven samples at different post annealing temperature with the stacking structure of (100) single crystalline MgO substrate / Cr(10) / $D0_{22}$-MnGa (30) / Co (20) / Cr(5) (thickness is in nanometers). The epitaxial bilayers were fabricated using an ultrahigh vacuum magnetron sputtering system with a base pressure of less than 1×10^{-7} Pa. All the layers were deposited at room temperature. The in-situ annealing was employed at 400ºC after the MnGa deposition. Annealing temperature dependence has been investigated using post annealing by rapid thermal annealing (RTA) system. We also prepared epitaxial 30-nm-thick MnGa film without Co layer with the same stacking structure and also a single Co layer buffered and capped by Ta layer on MgO substrate as reference samples. Film compositions of MnGa alloy was $Mn_{70}Ga_{30}$, estimated by the inductively coupled plasma spectroscopy. For characterization of structural and magnetic properties, the X-ray diffractometer (XRD) with the Cu K_α radiation, polar magneto optical Kerr effect (P-MOKE) system at laser wavelength of 400 nm, and a vibrating sample magnetometer (VSM) were used.

3.1.1 Structural Properties

3.1.1.1 XRD

The out-of-plane XRD patterns of Co/MnGa bilayers for different annealing temperatures (T_a) are shown in Fig. 3-1(a). The peaks of MnGa (002), and (004) corresponding to tetragonal structure of $D0_{22}$-MnGa are clearly observed. In addition these peaks, the (002) peak of Cr film was observed. Another peaks in the XRD pattern are coming from MgO substrate. The annealing temperature dependence of the *c* lattice constant of MnGa of bilayer film is shown in Fig. 3-1(b). The *c* lattice constant of MnGa is constant and very close to value of the reference MnGa film (7.00 Å) for the un-annealed sample and samples annealed at 200ºC up

to 350ºC. Then the *c* lattice constant of MnGa reduces slowly and finally drastically reduces for the sample annealed at 450ºC. These changes are attributed to inter diffusion effect at high annealing temperature regime. As can be seen clearly in XRD patterns, the Co/MnGa bilayer film annealed at 400ºC have broad (002) and (004) peaks of MnGa and their positions also change. By further annealing temperature (002) and (004) peaks of tetragonal structure of MnGa completely disappear and another (002) and (004) peaks appear at larger angle might be attributed to cubic MnGa-Co alloy because of inter diffusion effect. No peak was observed for Co film.

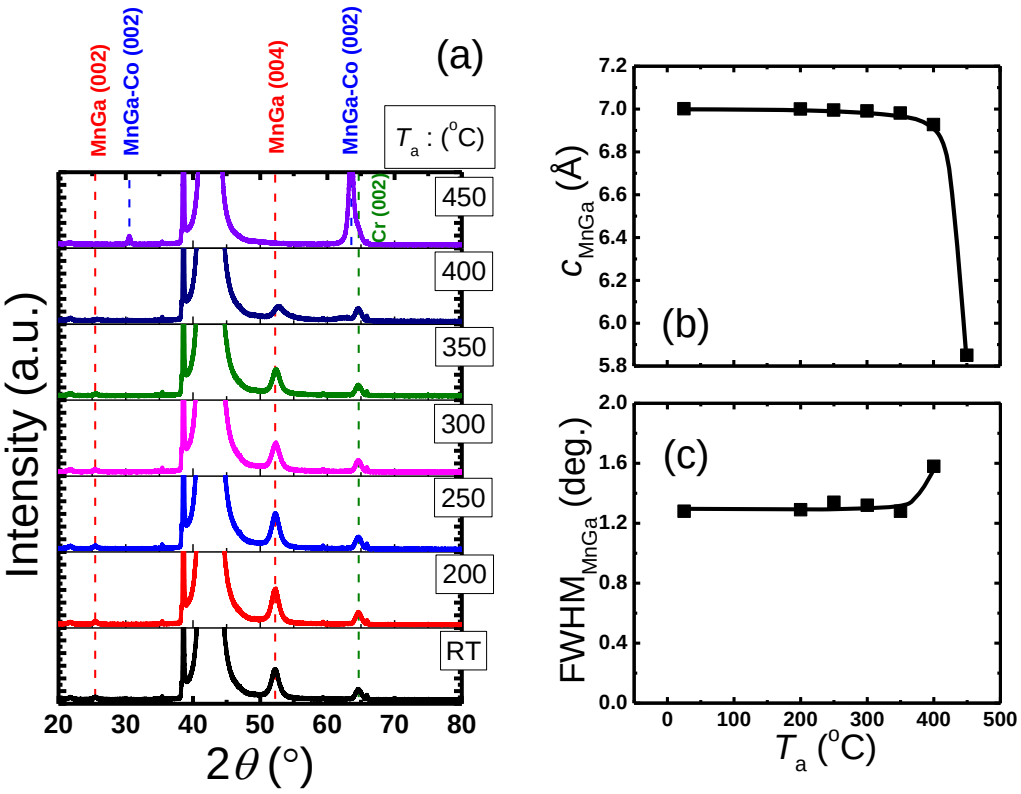

Figure 3-1 (a) The XRD pattern of Co/MnGa bilayers for un-annealed sample and annealed samples at 200, 250, 300, 350, 400, and 450ºC. (b) The annealing temperature dependence of *c* lattice constant and (c) FWHM of (004) peak of MnGa film.

The annealing temperature dependence of the full width at half maximum (FWHM) for the MnGa film is shown in Fig. 3-1(c). The FWHM of (004) peak of MnGa film is constant for the un-annealed sample and samples annealed at 200 up to 400ºC. A drastic increase of FWHM

was observe for the sample annealed at 450ºC which is due to mixing of Co film to MnGa layer.

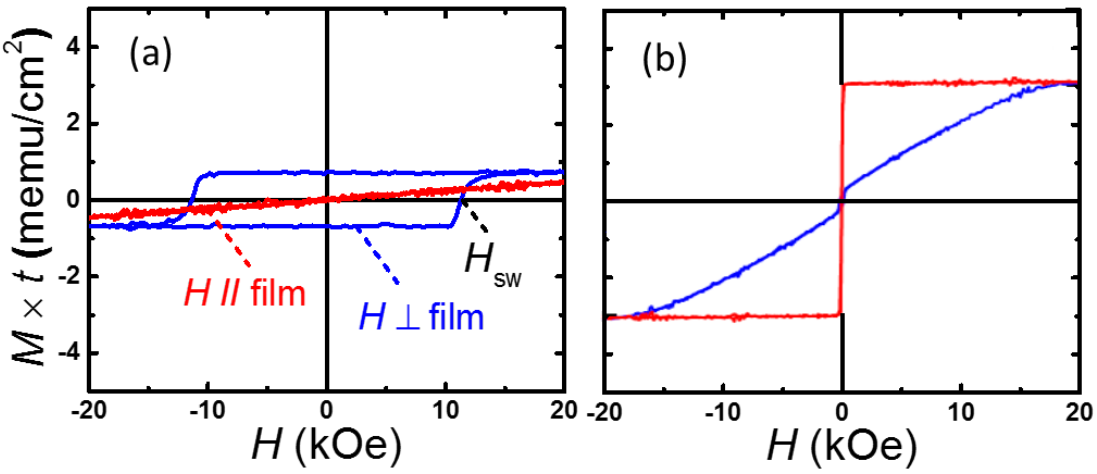

Figure 3-2 (a) The typical out-of plane (blue colour) and in-plane (red colour) VSM *M-H* loops of MnGa and (b) Co reference films.

3.1.2 Magnetic Properties

3.1.2.1 VSM

The typical out-of-plane and in-plane *M-H* loops measured by VSM system for the MnGa and Co reference films are shown in Fig. 3-2(a) and (b), respectively. The MnGa film show PMA property. The saturation magnetization and switching field (H_{sw}) are about 250 emu/cm^3, 11.3 kOe, respectively. These values are comparable with previous studies.[32] As can be seen in Fig. 3-2(b) Co film has IMA property and saturation magnetization about 1400 emu/cm^3. The out-of plane *M-H* loop show the saturation field about 17 kOe. The typical out-of-plane and in-plane *M-H* loops measured by VSM system for the Co (20 nm)/MnGa (30 nm) bilayer film for un-annealed sample and annealed samples at 200, 250, 300, 350, 400, and 450ºC are shown in Fig.3-3. As can be seen from this figure it seems the magnetization of Co/MnGa bilayer film is combination of magnetization of MnGa and Co films with tacking account of exchange coupling at the interface of MnGa and Co films. The out of plane VSM *M-H* loop did not saturate even at 20 kOe magnetic field. This indicates larger field is needed for saturation of magnetization of Co/MnGa bilayer film. Annealed bilayer up to 350ºC show similar curves, but different switching filed and remnant magnetization were observed. After

annealing sample at 400ºC VSM *M-H* loop changes too much and finally IMA property was observed for sample annealed at 450ºC. These results are consistent with XRD analysis might be attributed to mixing of MnGa film to Co layer at high annealing temperature regime.

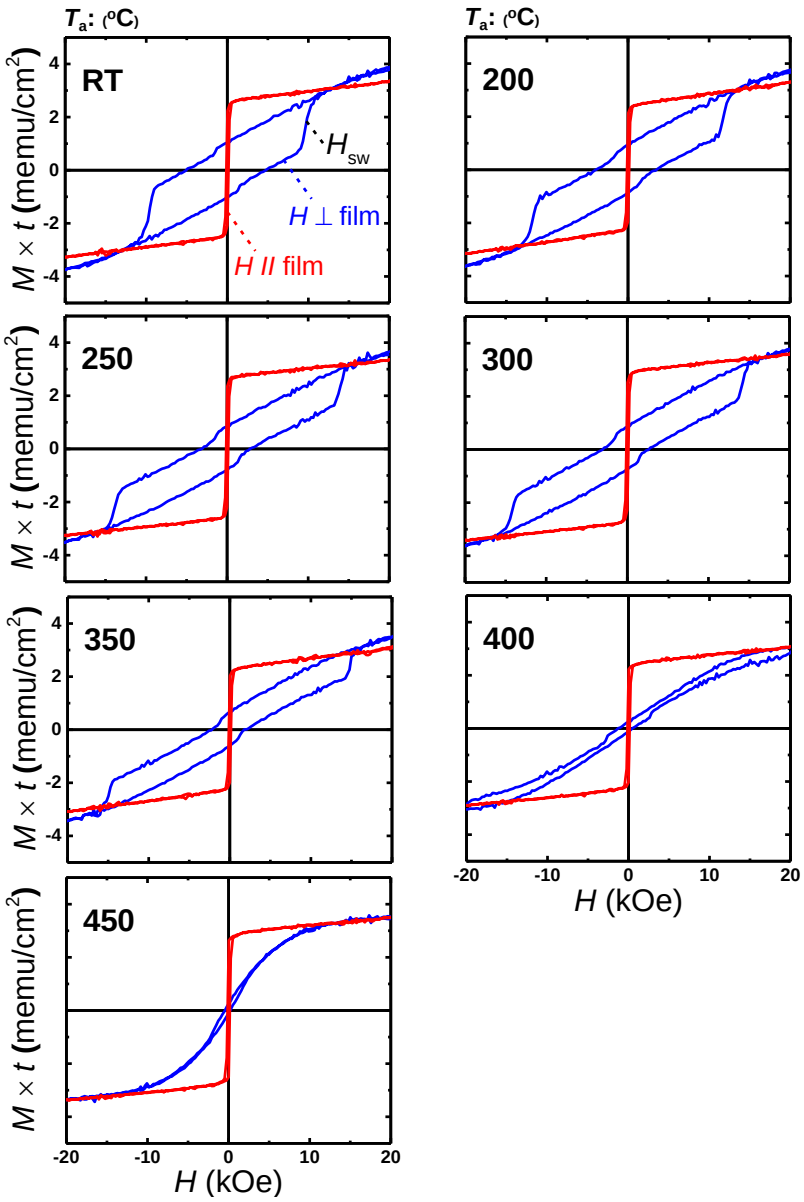

Figure 3-3 The typical out-of plane (blue colour) and in-plane (red colour) VSM *M-H* loops of Co (20 nm)/MnGa (30 nm) bilayers for un-annealed sample and annealed samples at 200, 250, 300, 350, 400, and 450ºC.

3.1.2.2 MOKE

Polar magneto optical Kerr effect measurement shows more informative information about hysteresis loop. First, PMOKE hysteresis loops of MnGa and Co reference films are shown in Fig. 3-4(a) and (b), respectively. The MOKE measurement for MnGa and Co reference films are consistent with VSM measurement. The same switching and saturation fields were observed for MnGa and Co reference films, respectively.

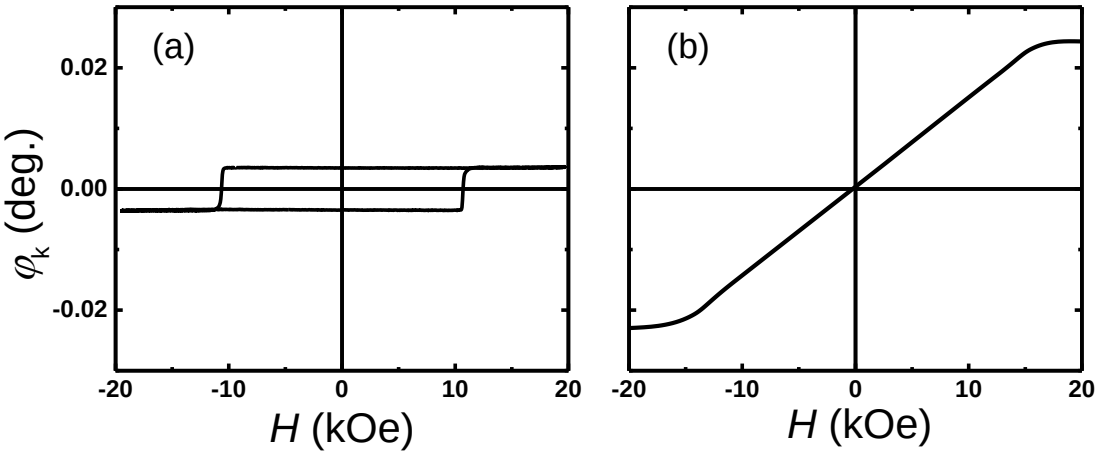

Figure 3-4 (a) The typical polar Kerr rotation angle versus the applied field of MnGa and (b) Co reference films.

The typical polar Kerr rotation angle versus the applied field of Co (20 nm)/MnGa (30 nm) bilayers for un-annealed sample and annealed samples at 200, 250, 300, 350, 400, and 450ºC are shown in Fig. 3-5. Hysteresis loops are different from magnetization curves in Fig. 3-3 because those dominantly stem from magnetization process of Co layer, thanks the Co layer thickness is comparable to the penetration depth for the laser light with wavelength of 400 nm used in this study. The un-annealed Co/MnGa bilayer film shows summation of those for MnGa and Co and did not saturate even at 20 kOe magnetic field. After annealing switching filed changes and in the high temperature regime in plane magnetic anisotropy property was observed which is consistent with VSM *M-H* loops.

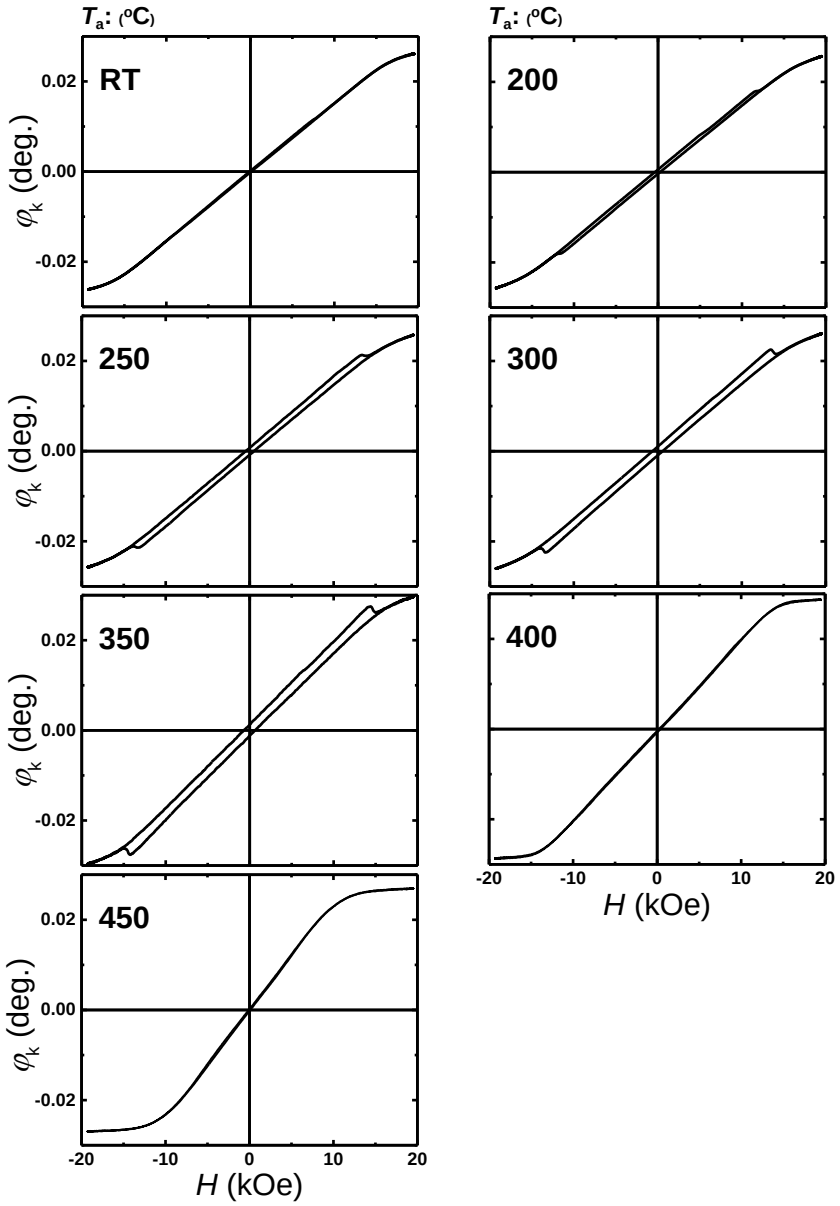

Figure 3-5 The typical polar Kerr rotation angle versus the applied field of Co (20 nm)/MnGa (30 nm) bilayers for un-annealed sample and annealed samples at 200, 250, 300, 350, 400, and 450°C.

3.1.1 Discussion and Summary

Fig. 3-6(a) show the T_a dependence of saturation magnetization of Co layer which is estimated from in-plan *M-H* loop of Co/MnGa bilayer film. The average of saturation magnetization value of Co is about 1250 emu/cm^3. This value is smaller than value of Co reference film. The T_a dependence and H_{sw} of Co (20 nm)/MnGa (30 nm) are shown in Fig. 3-6(b) and (c),

respectively. The remnant magnetization ($M\times t_{(0\ kOe)}$) and H_{sw} of 30-nm-thick MnGa plotted with dashed line for comparison. As can be seen from Fig. 3-6(b), $M\times t_{(0\ kOe)}$ of un-annealed bilayer film is larger than values of 30-nm-thick-MnGa film and then decreases with increasing T_a up to 350ºC. By further T_a, the $M\times t_{(0\ kOe)}$ reduces too much which is attributed to structure changes at high temperature regime because of inter diffusion as shown in XRD pattern. Moreover, PMA property changes to IMA when the bilayer film annealed at 400 and 450ºC.

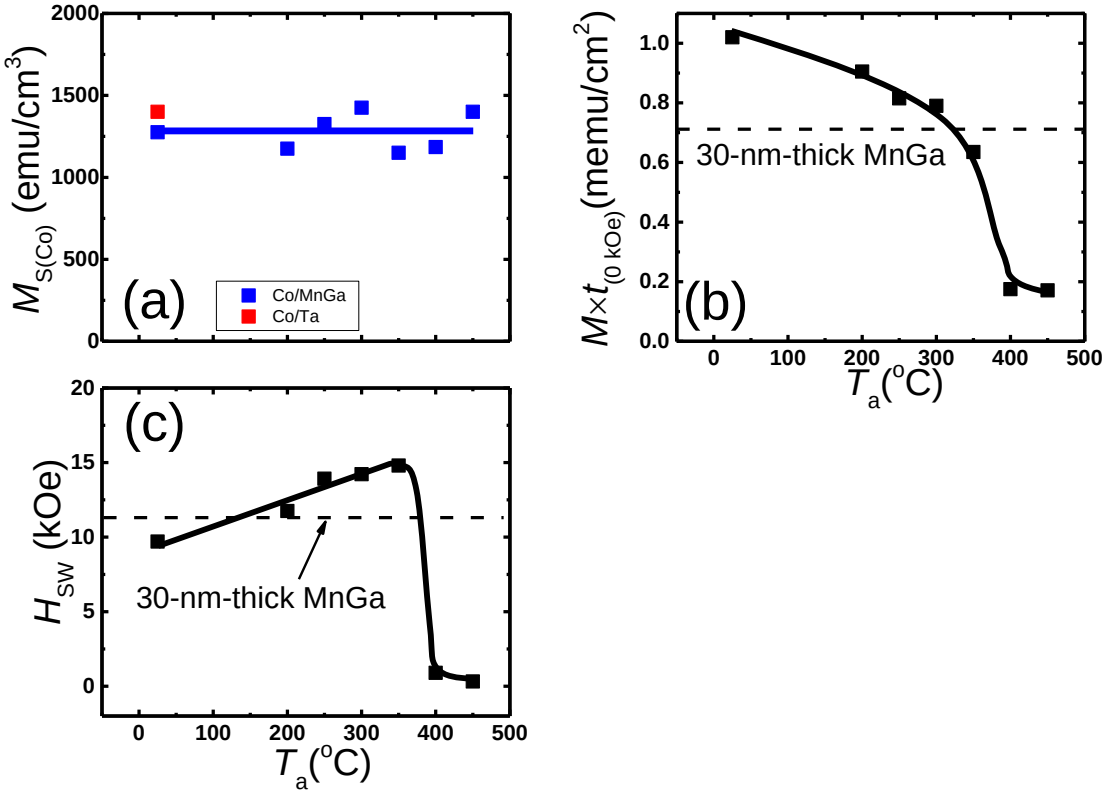

Figure 3-6 (a) The annealing temperature dependence of saturation magnetization for Co film. (b) The annealing temperature dependence of remnant magnetization and (c) switching field for Co (20 nm)/MnGa (30 nm) bilayer film.

The T_a dependence of H_{sw} show the different behavior. The H_{sw} increases to maximum value for T_a=350ºC and then drastically reduces because of IMA property. The smaller $M\times t_{(0\ kOe)}$ and larger H_{sw} for the Co/MnGa bilayer annealed at 350ºC suggested the stronger antiferromagnetic exchange coupling at interfaces of Co and MnGa compared to un-annealed bilayer film. When a hard magnetic film (MnGa) combined with the soft magnetic film (Co) in the case of no coupling H_{sw} and $M\times t_{(0\ kOe)}$ of bilayer are same as those for hard magnetic film, whereas in the case antiferromagnetic coupling, larger H_{sw} and smaller $M\times t_{(0\ kOe)}$are expected as reported in

the FePt (hard)/Fe (soft) spring system work.[52] For the estimation of interfacial exchange coupling constant between Co and MnGa large field measurement is needed to get saturation field of Co/MnGa bilayer film. The estimation model will be explained later.

A short summary will be presented here. We investigated the influence of annealing temperature on the structural and magnetic properties of Co/$D0_{22}$MnGa bilayer films. The bilayer films have been successfully grown. The Co/$D0_{22}$MnGa bilayer films is very sensitive to annealing temperature. The optimized annealing temperature was 350ºC which did not show significant mixing of Co and MnGa films. It seems there is interfacial antiferromagnetic exchange coupling between Co and MnGa films and also coupling strength should be larger for bilayer film annealed at 350ºC. However, we are not able to evaluate exchange coupling constant. For the estimation of exchange coupling constant large field measurement is needed.

3.2 Thickness Dependence of Co (t_{Co})/$D0_{22}$-MnGa (30 nm) Bilayer

Two series samples without post annealing and with post annealing at 350ºC by RTA system with different Co thicknesses of 1, 3, 5, 10 and 20 nm were prepared by using an ultrahigh vacuum magnetron sputtering system with a base pressure of less than 1×10^{-7} Pa. The stacking structure of each series were: the (100) single crystalline MgO substrate / Cr (10) / $D0_{22}$-MnGa (30) / Co (t_{Co}) / Cr (5) (thickness is in nanometers) All the layers were deposited at room temperature. The in-situ annealing was employed at 400ºC after the MnGa deposition. For characterization of structural and magnetic properties, the X-ray diffractometer (XRD) with the Cu K_α radiation, polar magneto optical Kerr effect (P-MOKE) system at laser wavelength of 400 nm, and a vibrating sample magnetometer (VSM) were used.

3.2.1 Structural Properties

3.2.1.1 XRD

The XRD pattern of Co (0-20 nm)/MnGa (30 nm) bilayers for the un-annealed samples and annealed samples at 350ºC are shown in Fig 3-7 (a) and 3-8 (a). The peaks of MnGa (002), and (004) corresponding to tetragonal structure of $D0_{22}$-MnGa are clearly observed in both series samples. The Co thickness (t_{Co}) dependence of the *c* lattice constant of MnGa of bilayer film without and with post annealing are shown in Fig 3-7 (b) and 3-8 (b). The *c* lattice constant of MnGa is constant with increasing t_{Co} for both series samples and very close to value of the

reference MnGa film (7.00 Å). The t_{Co} dependence of the FWHM (004) peak of MnGa of bilayer film without and with post annealing are shown in Fig 3-7 (c) and 3-8 (c). The t_{Co} dependence of the FWHM shows an increasing for the bilayer with 3 nm Co and then FWHM is roughly constant for each thicknesses.

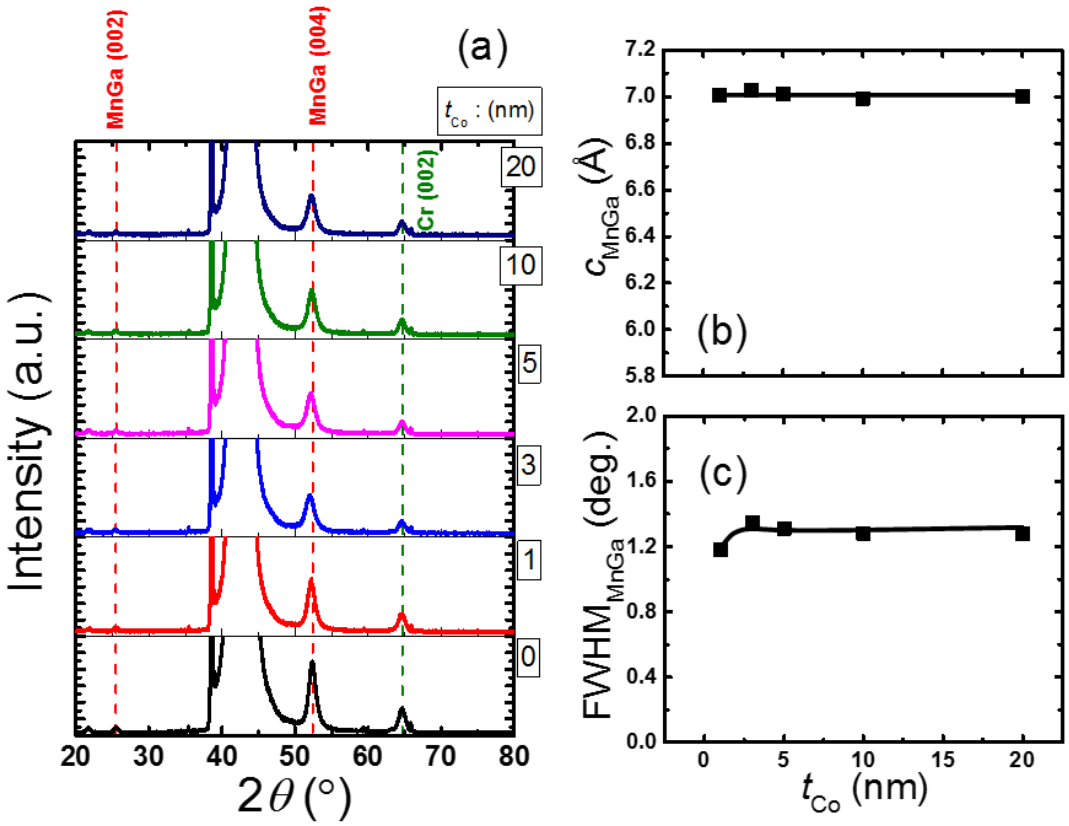

Figure 3-7 (a) The XRD pattern of Co (0-20 nm)/MnGa (30 nm) bilayers for the un-annealed sample. (b) The Co thickness dependence of *c* lattice constant and (c) FWHM of (004) peak of MnGa film.

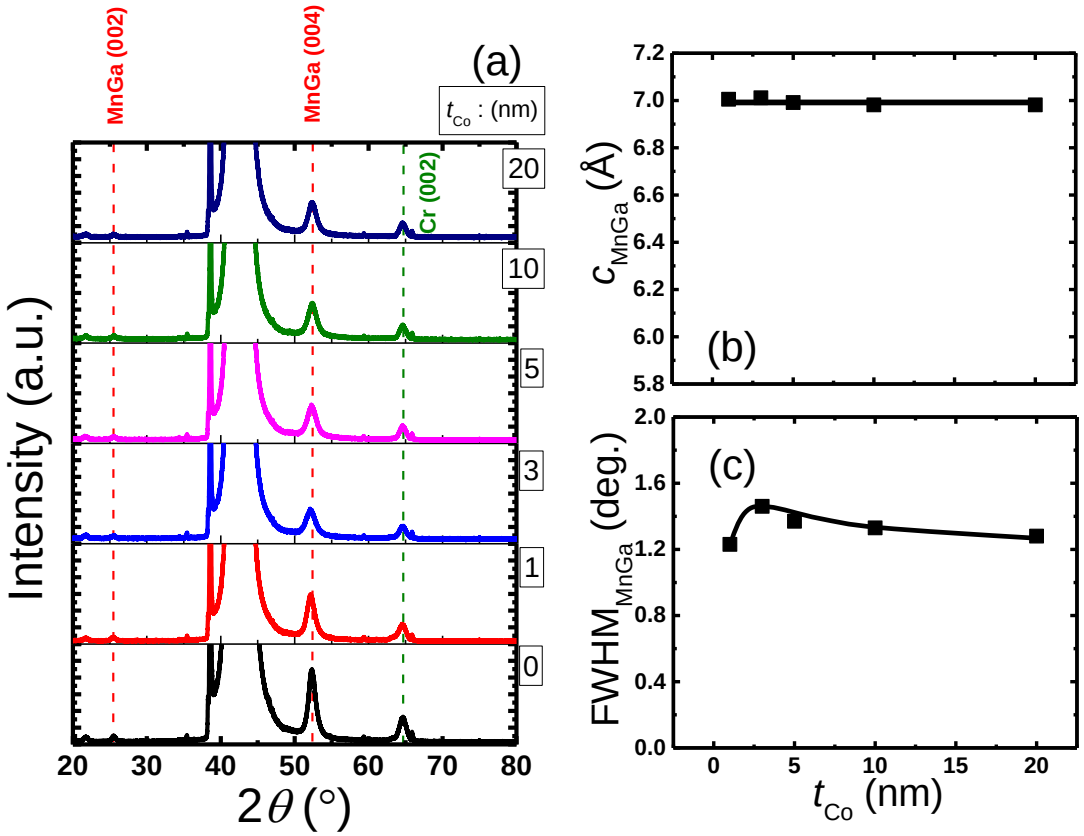

Figure 3-8 (a) The XRD pattern of Co (t_{Co}=0-20 nm)/MnGa (30 nm) bilayers for the samples annealed at 350ºC. (b) The Co thickness dependence of *c* lattice constant and (c) FWHM of (004) peak of MnGa film.

3.2.1 Magnetic properties

3.2.1.1 VSM

The typical out-of plane and in-plane VSM *M*-*H* loops of Co (1-20 nm)/MnGa (30 nm) bilayers for un-annealed samples and annealed samples at 350ºC are shown in Fig. 3-9. The un-annealed sample and sample annealed at 350ºC with 1 nm Co thickness show different *M*-*H* loop with 30-nm-thick MnGa. The larger $M \times t_{(0\ kOe)}$ and smaller H_{sw} were observed for the un-annealed sample whereas opposite behaviour was observed for the sample annealed 350ºC. However both samples did not saturate even at 20 kOe magnetic field. With increasing Co thickness, magnetization increases as clearly can be seen from in-plane hysteresis curves. The smaller out-of-plan and in-plane $M \times t_{(0\ kOe)}$ and larger H_{sw} for annealed sample compared to un-annealed sample suggested stronger antiferromagnetic exchange coupling after annealing

process. Even sample annealed at 350ºC with 1 nm Co insertion did not show fully PMA property like MnGa film.

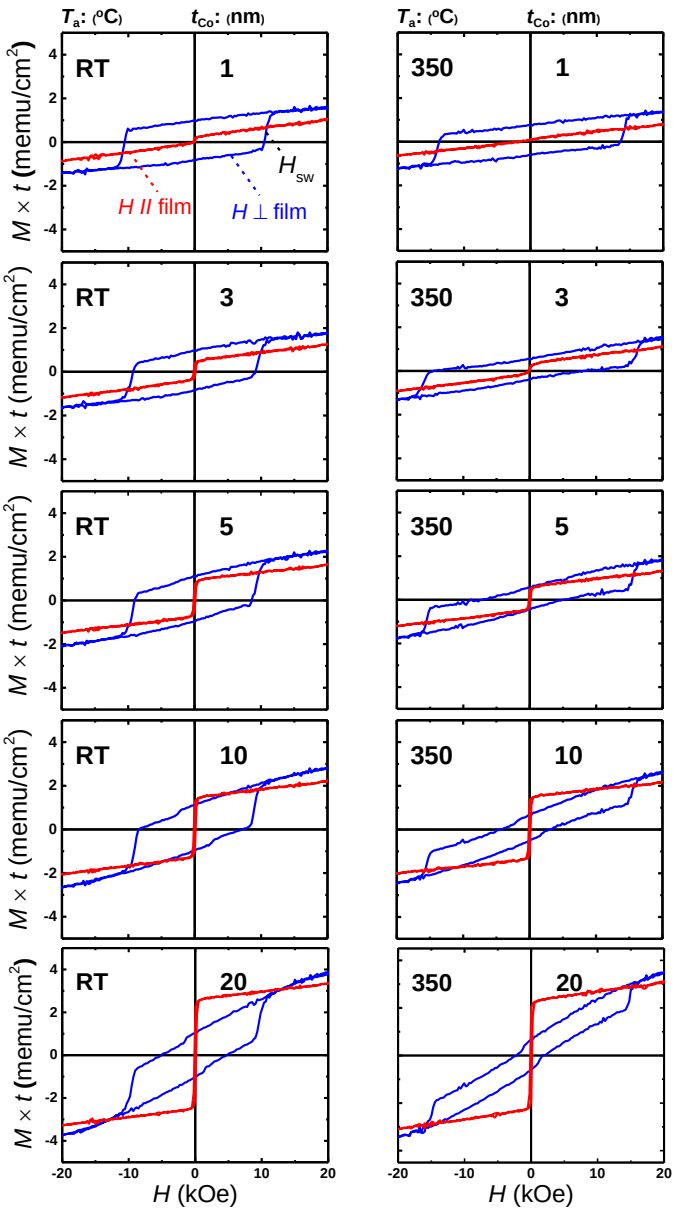

Figure 3-9 The typical out-of plane (blue colour) and in-plane (red colour) VSM *M-H* loops of Co (1-20 nm)/MnGa (30 nm) bilayers for un-annealed samples and annealed samples at 350ºC.

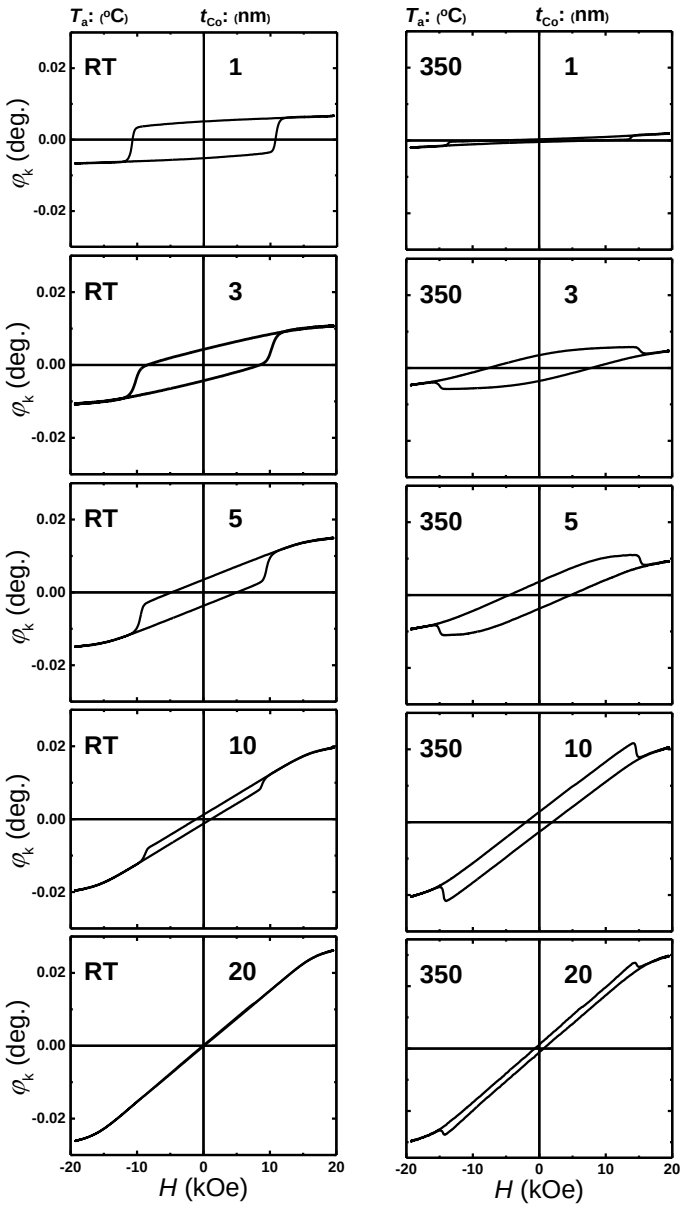

Figure 3-10 The typical polar Kerr rotation angle versus the applied field of Co (1-20 nm)/MnGa (30 nm) bilayers for un-annealed samples and annealed samples at 350ºC.

3.2.1.2 MOKE

In order to get informative information from interfaces of MnGa and Co films we have measured all the sample by using MOKE system. By using this measurement we are able to determine in which thickness, bilayer film can fully show perpendicular magnetic anisotropy which is very important for final goal of this study. The typical polar Kerr rotation angle versus

the applied magnetic field of Co (1-20 nm)/MnGa (30 nm) bilayers for un-annealed samples and annealed samples at 350ºC are shown in Fig. 3-10. The 30-nm-thick MnGa shows very flat hysteresis loop with good squareness. However, un-annealed bilayer film with 1 nm Co thickness shows smaller squareness and also it did not show very flat MOKE hysteresis loop which is due to tilting of magnetization of Co from perpendicular to in plane direction regard to MnGa films. This indicates Co and MnGa did not coupled fully perpendicularly. In the case of bilayer coupled fully perpendicular very flat hysteresis loop are expected in which applied magnetic field is 0 kOe. For this achievement strong antiferromagnetic or ferromagnetic exchange coupling is needed in the interfaces of MnGa and Co films. Even sample annealed at 350ºC did not show fully PMA property. As Co thickness increases to 3 nm we can see different MOKE hysteresis loop. The un-annealed sample show the normal MOKE hysteresis loop whereas the inverted loop was observed for the sample annealed at 350ºC. The reason of such inverted loop may interpret with antiferromagnetic exchange coupling between MnGa film and Co layer. By further increasing of Co thickness, different MOKE hysteresis loop with magnetization curve were observed specially for un-annealed and annealed sample with 20 nm Co thickness. This is due to Kerr rotation angle of Co is dominant in MOKE measurement.

3.2.2 Discussion and Summary

Fig. 3-11(a) shows the t_{Co} dependence of saturation magnetization of Co layer which is estimated from in-plan *M-H* loop of Co/MnGa bilayer film. Here, we have ignored estimation value of saturation magnetization of Co layer which are not reliable due large error especially when Co thickness is relatively small. The saturation magnetization value of Co for un-annealed and annealed samples is larger than 1100 emu/cm^3. This value is smaller than value of Co reference film. The t_{Co} dependence of $M \times t_{(0\ kOe)}$ and H_{sw} for un-annealed samples and samples annealed at 350ºC are shown in Fig. 3-11(b) and (c), respectively. The $M \times t_{(0\ kOe)}$ and H_{sw} of 30-nm-thick MnGa plotted with dashed line for comparison. As can be seen from Fig. 3-11(b), $M \times t_{(0\ kOe)}$ and H_{sw} of un-annealed bilayer film is larger and smaller than values of 30-nm-thick MnGa film, whereas smaller $M \times t_{(0\ kOe)}$ and larger H_{sw} were observed for the samples annealed at 350ºC. The t_{Co} dependence of $M \times t_{(0\ kOe)}$ and H_{sw} show the different behaviours for un-annealed samples and samples annealed at 350ºC. For the un-annealed samples as Co thickness is increasing $M \times t_{(0\ kOe)}$ and H_{sw}, increases and decreases, respectively and then these values saturated for bilayer films with thick Co film. However, for the annealed samples the

t_{Co} dependence of $M \times t_{(0\ kOe)}$ and H_{sw} show opposite trends. Such behaviours may related to quality of MnGa film when Co thickness increases. As can be seen from t_{Co} dependence of FHWM in Fig. 3-7(c) and 3-8(c) small enhancement of FWHM were observed for both un-annealed and annealed samples and the values of FWHM saturated similar to trends of $M \times t_{(0\ kOe)}$ and H_{sw}.

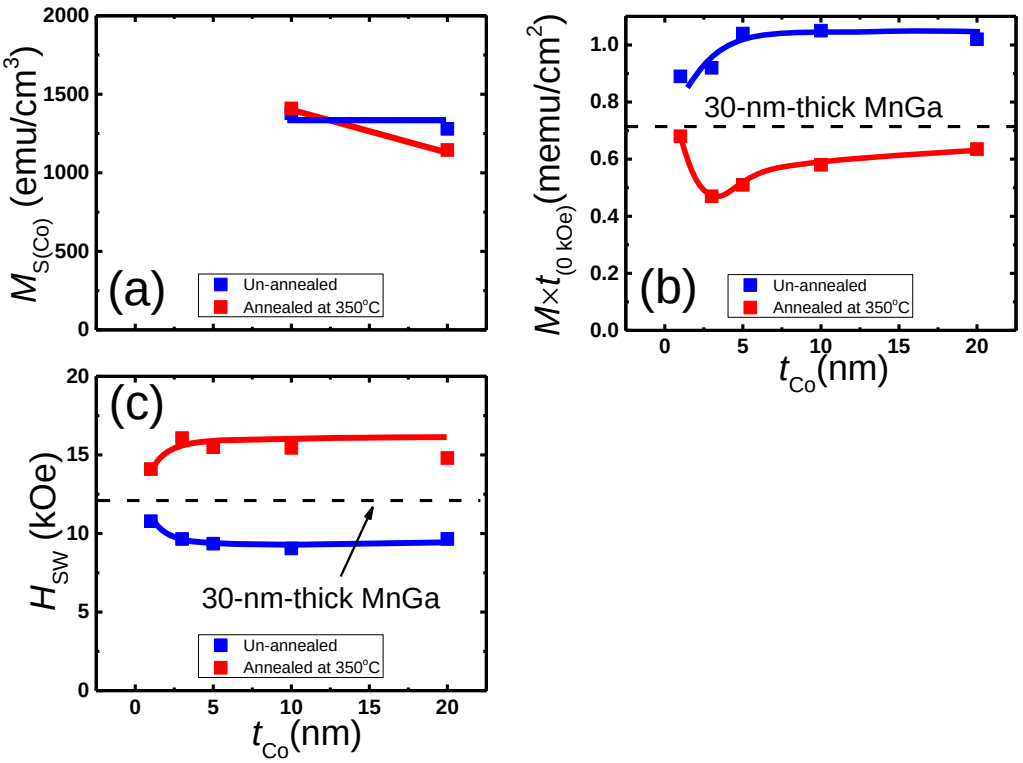

Figure 3-11 (a) The Co thickness dependence of saturation magnetization for Co film. (b) The Co thickness dependence of remnant magnetization and (c) switching field for Co (1-20 nm)/MnGa (30 nm) bilayer films.

A short summary will be presented here. We investigated the effect of Co thickness on the structural and magnetic properties of un-annealed samples and samples annealed at 350ºC for Co (1-20 nm)/$D0_{22}$MnGa (30 nm) bilayer films. The un-annealed and annealed samples did not show good PMA properties even for bilayer film with 1 nm thick Co film.

3.3 Annealing Temperature Dependence of CoB (20 nm)/$D0_{22}$-MnGa (30 nm) Bilayer

To investigate structural and magnetic properties of CoB / $D0_{22}$-MnGa six samples annealed at different post annealing temperature with the stacking structure of (100) single crystalline MgO substrate / Cr(10) / $D0_{22}$-MnGa (30) / CoB (20) / Cr(5) (thickness is in nanometers) have been fabricated. The epitaxial bilayers were fabricated using an ultrahigh vacuum magnetron sputtering system with a base pressure of less than 1×10^{-7} Pa. All the layers were deposited at room temperature. The in-situ annealing was employed at 400ºC after the MnGa deposition. Annealing temperature dependence has been investigated using post annealing by RTA system. In addition, the 30 (20)-nm-thick MnGa (CoB) films films were fabricated as reference films on MgO (Si/SiO_2) substrate. Film compositions of MnGa and CoB alloy were $Mn_{70}Ga_{30}$ and $Co_{69}B_{31}$ estimated by the inductively coupled plasma spectroscopy respectively. For characterization of structural and magnetic properties, the X-ray diffractometer (XRD) with the Cu Kα radiation, polar magneto optical Kerr effect (P-MOKE) system at laser wavelength of 400 nm, and a vibrating sample magnetometer (VSM) were used.

3.3.1 Structural Properties

3.3.1.1 XRD

The out-of-plane XRD patterns of CoB/MnGa bilayers for different annealing temperatures are shown in Fig. 3-12 (a). The peaks (002) and (004) of MnGa films corresponding to $D0_{22}$ structure of MnGa are clearly observed for un-annealed sample and sample annealed at 350ºC. For the sample annealed at 400ºC another peak was observed in addition (002) and (004) peaks of MnGa which shows with dashed blue line in the Fig. 3-12(a). This peak is coming from CoB-MnGa alloy. As annealing temperature increases the probability of inter diffusion increases. So by further annealing temperature, structure will be changed completely. There is no peak related to amorphous CoB film. Fig. 3-12(b) show the annealing temperature dependence of the *c* lattice constant of MnGa film. The *c* lattice constant of MnGa is constant and very close to value of the reference MnGa films (7.00 Å).

The annealing temperature dependence of the FWHM for the MnGa, CoB/MnGa and film is shown in Fig. 3-12 (b). The FWHM for MnGa peak did not change with increasing of T_a.

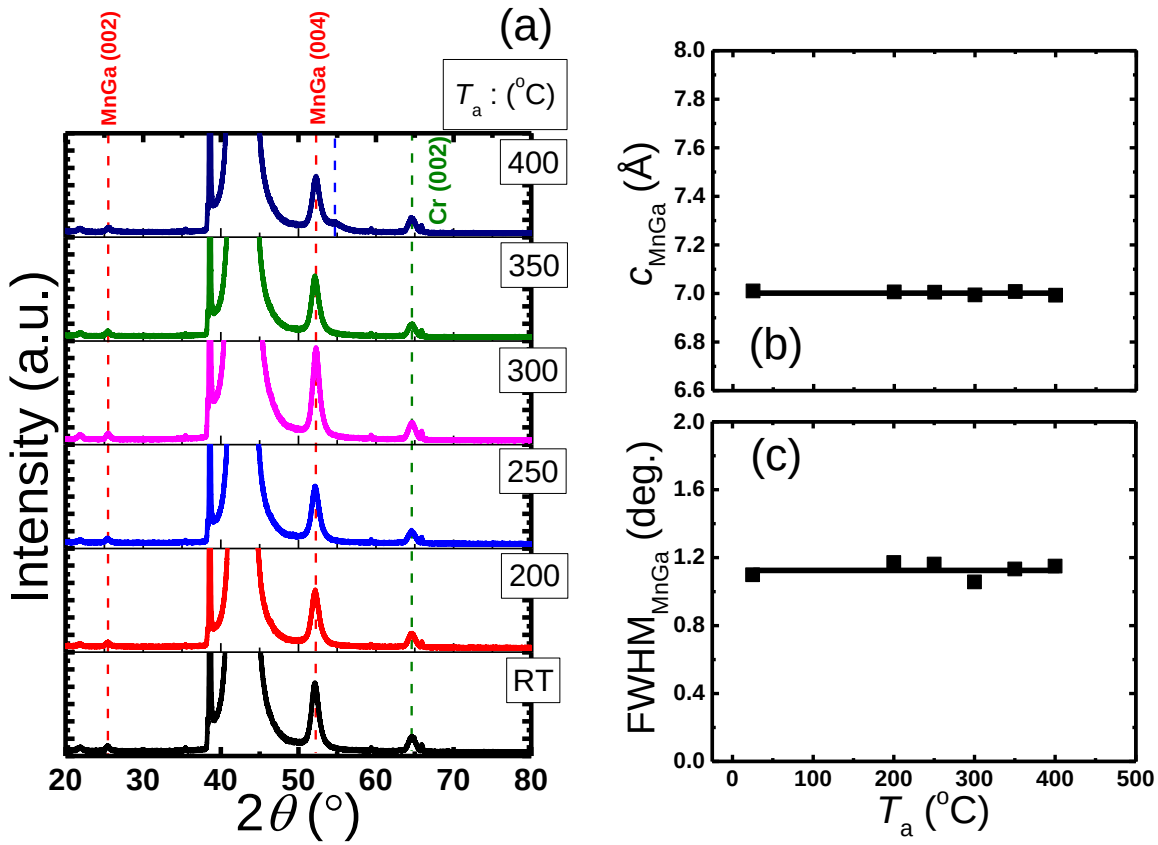

Figure 3-12 (a) The XRD pattern of CoB/MnGa bilayers for un-annealed sample and annealed samples at 200, 250, 300, 350, and 400ºC. (b) The annealing temperature dependence of *c* lattice constant and (c) FWHM of (004) peak of MnGa film.

3.3.1 Magnetic Properties

3.3.1.1 VSM

In Fig. 3-13 the typical out-of-plane and in-plane M-H loops measured by VSM system for the CoB (20 nm)/MnGa (30 nm) bilayer film for un-annealed sample and samples annealed at 200, 250, 300, 350, and 400ºC are shown. The 30-nm-thick MnGa and 20-nm-thick CoB films show the hard and soft magnetic properties, respectively. The *M-H* loop of all the bilayer films show summation of *M-H* loops for CoB and MnGa films with tacking account of interfacial exchange coupling between CoB film and MnGa layer. Later, the method for estimation of interfacial exchange coupling (J_{ex}) for the bilayer film will be explained.

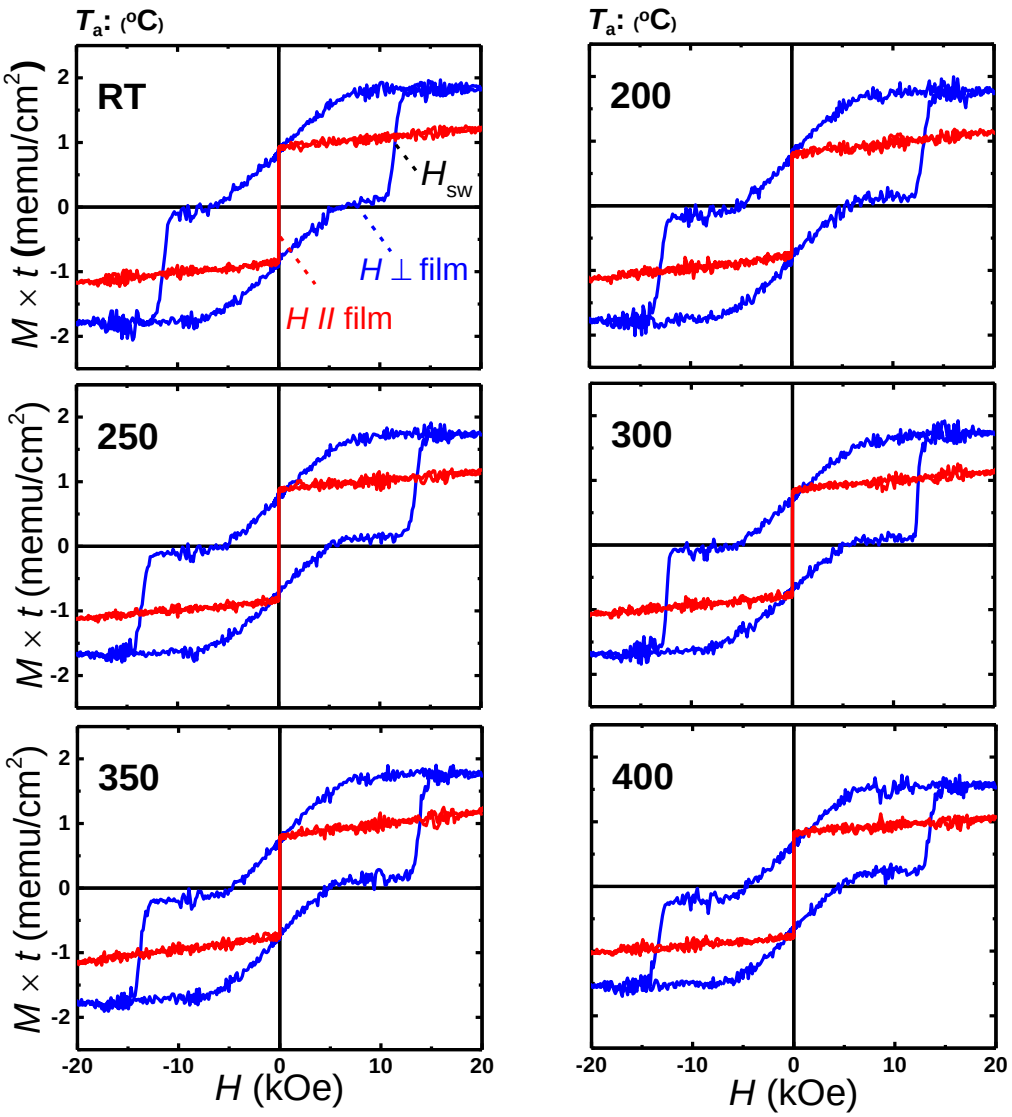

Figure 3-13 The typical out-of plane (blue colour) and in-plane (red colour) VSM *M-H* loops of CoB (20 nm)/MnGa (30 nm) bilayers for un-annealed sample and annealed samples at 200, 250, 300, 350, and 400ºC.

3.3.1.2 MOKE

In Fig. 3-14 the typical polar Kerr rotation angle versus the applied field of CoB (20 nm)/MnGa (30 nm) bilayers for un-annealed sample and annealed samples at 200, 250, 300, 350, and 400ºC are shown. The MOKE measurement is consistent with VSM result. The same switching field were observed in this measurement. The different shape was observed for

MOKE measurement compared to VSM measurement which originates from reflectance phase difference of the light at interface of bilayers in the MOKE measurement.

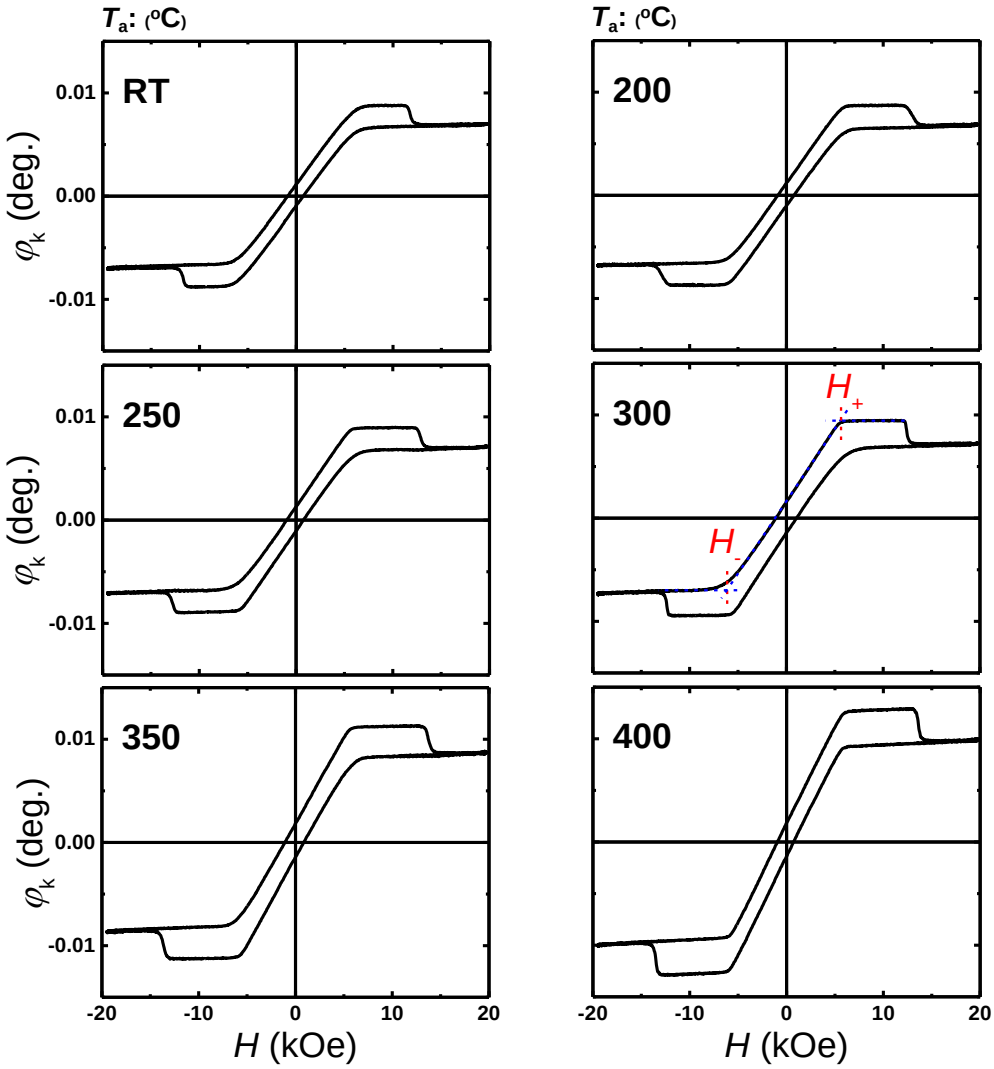

Figure 3-14 The typical polar Kerr rotation angle versus the applied field of CoB (20 nm)/MnGa (30 nm) bilayers for un-annealed sample and annealed samples at 200, 250, 300, 350, and 400°C.

3.3.2 Calculation Method for Estimation of Interfacial Exchange Coupling Constant

In Fig.3 15 the illustration for the IMA/PMA bilayer film with antiferromagnetic exchange interaction is shown. We set a model according to the previous studies. To calculate the

interfacial exchange coupling for the IMA/PMA bilayer films the one dimensional Landau-Lifshitz-Gilbert equation are modeled by:

$$\frac{\partial m_j(z,t)}{\partial t} = -\gamma_j m_j(z,t) \times H_j(z,t) + \frac{\gamma_j}{M_j} + \alpha_j m_j(z,t) \times \frac{\partial m_j(z,t)}{\partial t} \quad 3\text{-}1$$

$$H_j(z,t) = [H + H_j m_j(z,t) \cdot z] \quad 3\text{-}2$$

$$J_j(z,t) = -2A_j m_j(z,t) \times \frac{\partial m_j(z,t)}{\partial z} \quad 3\text{-}3$$

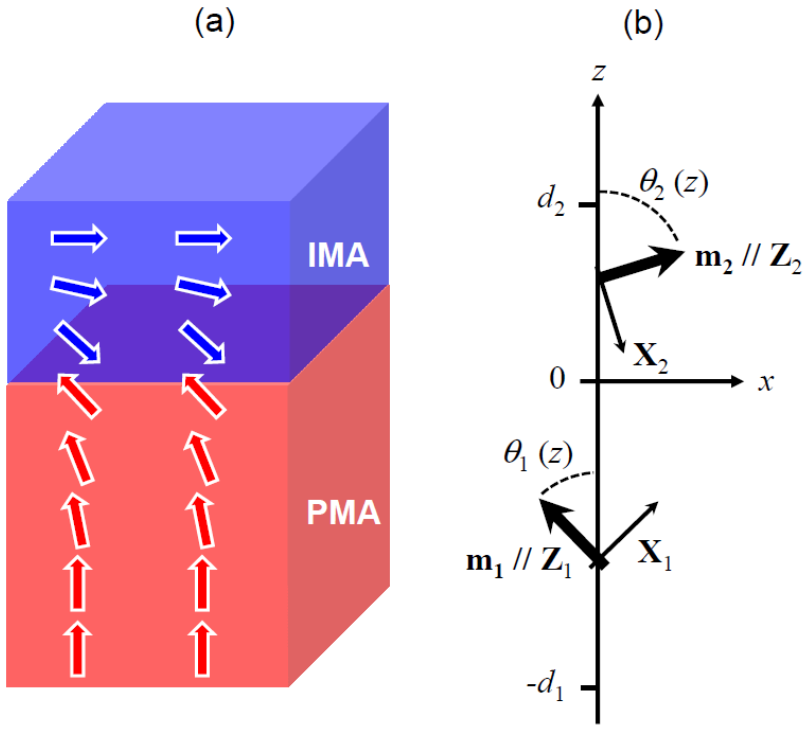

Figure 3-15 Illustration for a magnetic bilayer with antiferromagnetic exchange interaction present at an interface. Each layer has an in-plane (IMA) and perpendicular magnetic anisotropy (PMA). (b) Schematic expression of coordinate system used for the calculation of magnetic properties.

Here, the *j* denotes the variables for PMA (*j* = 1) and IMA (*j* = 2) layer. The *m* (*z; t*) is the unit vector of magnetization at position *z* and time *t*. *z* axis is perpendicular to the bilayers plane and an origin of *z* axis is taken at the interface of bilayer (Fig. 3-13). γ is the gyromagnetic

ratio, M the saturation magnetization, α the Gilbert damping constant, H the external magnetic field applied along z direction, A the exchange stiffness constant, and the H_j the perpendicular magnetic anisotropy field for j layer defined as $H_j = 2K_j/M_j - 4\pi M_j$. The K_j is the uniaxial anisotropy constant and an easy axis is perpendicular to a film plane if K_j is positive. Here, it is assumed that there are no surface anisotropies at the outer surfaces and only exchange interaction at the interface of IMA/PMA bilayer film. Then, the boundary conditions are given by

$$J_1(-d_1,t) = J_2(d_2,t) = 0 \tag{3-4}$$

$$J_1(-0,t) = J_2(+0,t) = 0 = J_{ex} m_1(-0,t) \times m_2(+0,t) \tag{3-5}$$

Where J_{ex} is the exchange interaction per unit area. It is considered that magnetizations spatially change in both the layers along z-direction, like a domain wall, thus it is convenient to transform the coordinate using equilibrium polar angle θ_j (z) of magnetization vector with assumption that all the magnetization are parallel to x-z plane under equilibrium. New coordinate can be expressed as the following equations:

$$Z_j(z) = -x\sin\theta_j(z) + z\cos\theta_j(z) \tag{3-6}$$

$$X_j(z) = y \times Z_j(z) \tag{3-7}$$

We find the solution of Eq. 3-1 satisfying Eq. 3-4 and Eq. 3-5, which is expressed as

$$m_j(z,t) = a_j(z,t)X_j(z) + b_j(z,t)y + Z_j(z) \tag{3-8}$$

Here, first two terms represent magnetization dynamics along the twisted magnetization, and third term stands the equilibrium twisted magnetization. Substituting Eq. 3-8 into Eq. 3-1, 3-4, and 3-5, the nonlinear second order partial derivative equation and boundary condition for θ_j (z) are obtained.

$$\frac{\partial^2\theta_j(z)}{\partial z^2} = \frac{Mj}{2Aj}[H\sin\theta_j(z) + H\sin 2\theta_j(z)] \quad 3\text{-}9$$

$$2A_1\frac{\partial\theta_1(-0)}{\partial z} = 2A_2\frac{\partial\theta_2(+0)}{\partial z} = J_{ex}\sin[\theta_2(+0) - \theta_1(-0)] \quad 3\text{-}10$$

$$\frac{\partial\theta_1(-d_1)}{\partial z} = \frac{\partial\theta_2(d_2)}{\partial z} = 0 \quad 3\text{-}11$$

Here, we have considered static magnetic properties. So, the out-of-plane *M-H* loop has been produced by using following equation:

$$M_{j,z} = \frac{M_j}{d_j}\int\cos\theta_j(z)dz \quad 3\text{-}12$$

The Kerr rotation angle also have been calculated by using following equation:

$$\varphi_k(H) \approx M_z^{IMA}(H)\left(1 - e^{\frac{-d_{IMA}}{L_{IMA}}}\right) + M_z^{PMA}\cos(\frac{d_{IMA}}{L_{IMA}})e^{\frac{-d_{IMA}}{L_{IMA}}} \quad 3\text{-}13$$

Where L_{IMA} is penetration depth of light in PMOKE measurement for the IMA layer. The typical out-of-plane *M-H* loops which are calculated using Eq. 3-12 for the CoB (20)/MnGa (30) bilayer film for J_{ex}= -1.5 and 0 erg/cm^3 are shown in Fig. 3-16 (a) and (b), respectively. The 30-nm-thick MnGa and 20-nm-thick CoB films show the PMA and IMA properties, respectively. For better understanding of magnetization process, certain points were marked with the numbers 1, 2, and 3 to show how magnetization is changing in presence of magnetic field. We also marked three magnetic fields with H_+, H_-, and H_{sw} corresponding to the saturation field in the parallel state ($H_{\uparrow\uparrow}$) and antiparallel state ($H_{\uparrow\downarrow}$), and the switching field, respectively. Here, we use following equation which have obtained from calculation method to define H_+, H_-, magnetic field.

$$H_{\pm} = \pm 4\pi M_{eff}^{IMA} - \frac{J_{ex}}{M_{IMA}d_{IMA}} \quad 3\text{-}14$$

In addition, the macro spin of magnetization process in CoB/MnGa bilayer film is shown in Fig. 3-16 (c). Magnetization of CoB and MnGa are parallel at $H > H_+$ in step 1 as shown in Fig.

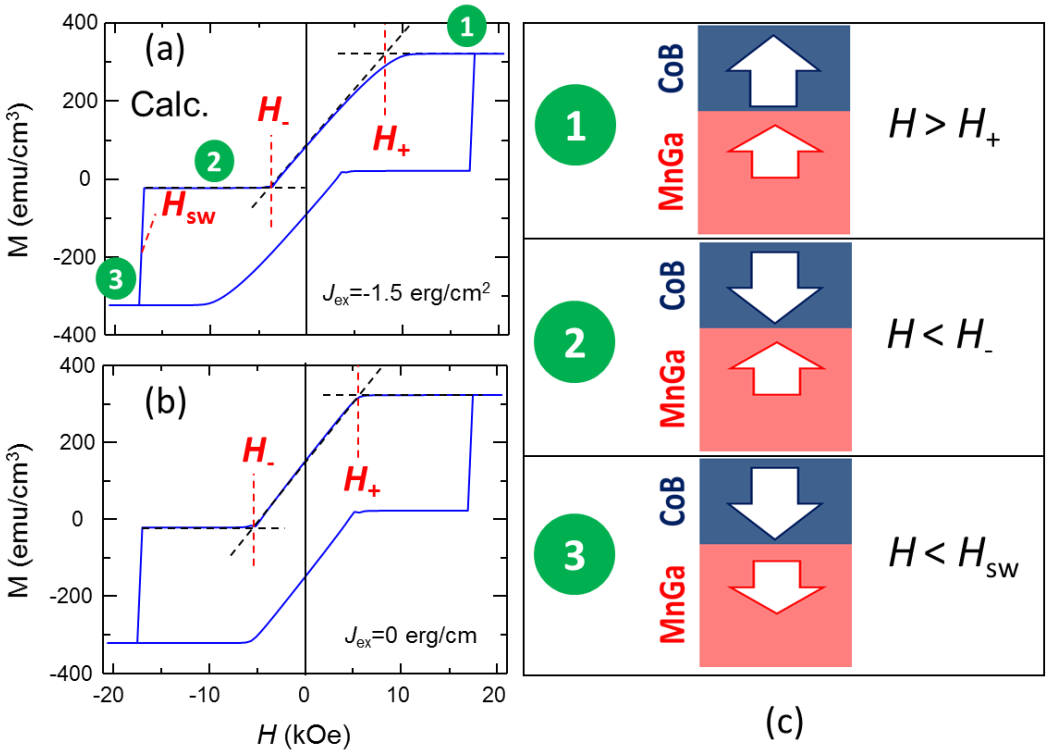

Figure 3-16 (a) The calculation of typical out-of-plane *M-H* of CoB(20)/MnGa(30) bilayer film for J_{ex}= -1.5 erg/cm^3 and (b) J_{ex}= 0 erg/cm^3. (c) Schematic expression of spin configuration.

3-16(c). With decreasing magnetic field, magnetization of CoB starts to rotate from a parallel to antiparallel state in step 2 and then the magnetization of MnGa switches from the up direction to down direction with further decrease of magnetic field in step 3. As the magnetic field is swept from -20 to 20 kOe, magnetization of CoB starts to rotate from the parallel state to antiparallel sate and finally with further increase of the magnetic field, magnetization of MnGa switches from downward to upward. If there is no exchange coupling at the interfaces of CoB and MnGa, H_+ and H_- fields have same absolute values and there is symmetry regard to H = 0 as is shown in Fig. 3-16 (b). On the other hand, with tacking account of antiferromagnetic exchange coupling at the interface, different values of H_+ and absolute H_- are expected. So, there is an asymmetry regard to H = 0 as is shown in Fig. 3-16(a). By increasing coupling strength, H_+ increases, whereas absolute value of H_- decreases. This indicates that larger and smaller magnetic fields are needed for alignment of total magnetization to the parallel state, and antiparallel state, respectively.

The calculation of typical polar Kerr rotation angle versus applied magnetic field of CoB (20)/MnGa (30) bilayer film for J_{ex}= -1.5 and 0 erg/cm^3 are shown in Fig. 3-17 (a) and (b), respectively. The macro spin of magnetization process in CoB/MnGa bilayer film also is shown

in Fig. 3-17 (c). The same method with out-of-plane magnetization is used for analysis of polar Kerr rotation angle hysteresis loop. As can be seen in Fig. 3-17(a) and (b) different shapes compared to out-of-plane *M-H* loops were observed which originates from reflectance phase difference of the light at interface of bilayers in the MOKE measurement. By using this method interfacial exchange coupling has been evaluated from experimental results for IMA/MnGa bilayer films. In this study we used CoB, and different Heusler alloys (Co_2Fe Al, Co_2Fe Si, Co_2MnAl, and Co_2MnSi) as IMA materials in IMA/MnGa bilayer films. For the estimation of H_+ and H_- fields PMOKE measurement is used. The magnetization has been estimated by VSM measurement.

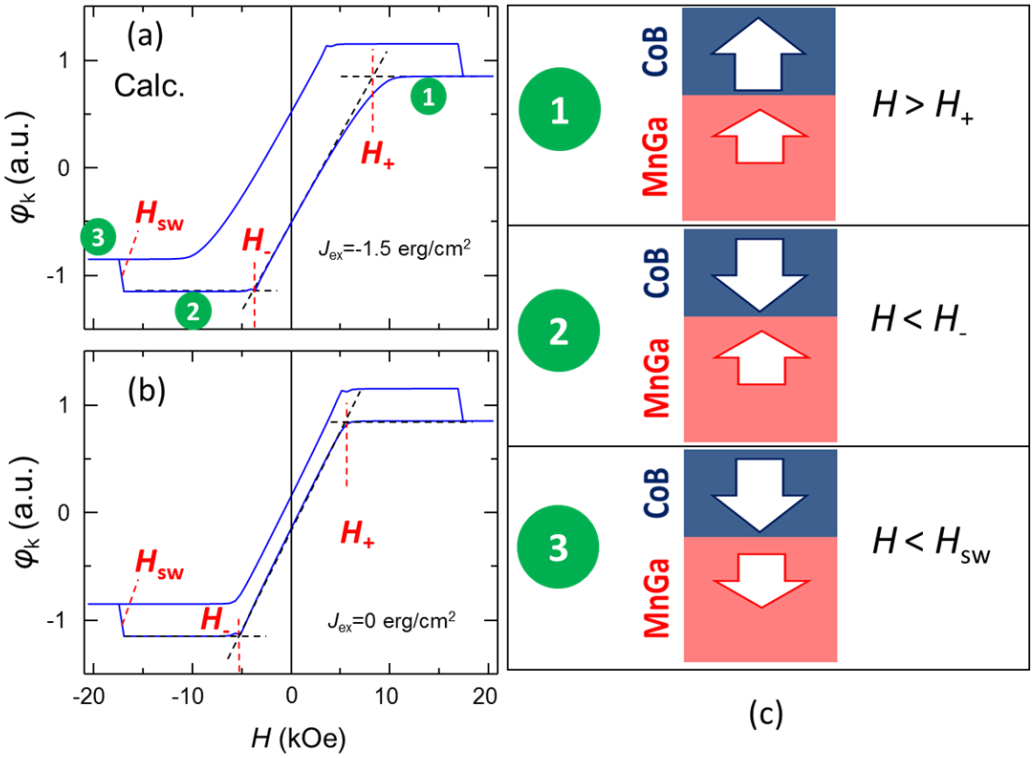

Figure 3-17 (a) The calculation of typical polar Kerr rotation angle versus applied magnetic field of CoB (20)/MnGa (30) bilayer film for J_{ex}= -1.5 erg/cm^3 and (b) J_{ex}= 0 erg/cm^3. (c) Schematic expression of spin configuration.

3.3.3 Discussion and Summary

Fig. 3-18 (a) show the T_a dependence of saturation magnetization which is estimated from out-of-plane *M-H* loop for the CoB/MnGa. The saturation magnetization of CoB/MnGa film is constant with increasing T_a up to 350ºC and then small reduction was observed for T_a=400ºC.

This is attributed to changing of structure as shown in XRD pattern because of inter diffusion effect. The T_a dependence of $M \times t_{(0\ kOe)}$ and H_{sw} are shown in Fig. 3-18 (b) and (c), respectively. The $M \times t_{(0\ kOe)}$ and H_{sw} of 30-nm-thick MnGa plotted with dashed line for comparison. As can be seen from Fig. 3-18 (b), $M \times t_{(0\ kOe)}$ of un-annealed bilayer film is larger than values of 30-nm-thick MnGa film and then decreases linearly with increasing T_a. The opposite behaviour was observed for T_a dependence of H_{sw}. The reduction of $M \times t_{(0\ kOe)}$ and enhancement of H_{sw} with increasing T_a suggested antiferromagnetic exchange coupling between CoB film and MnGa layer at high temperature regime.

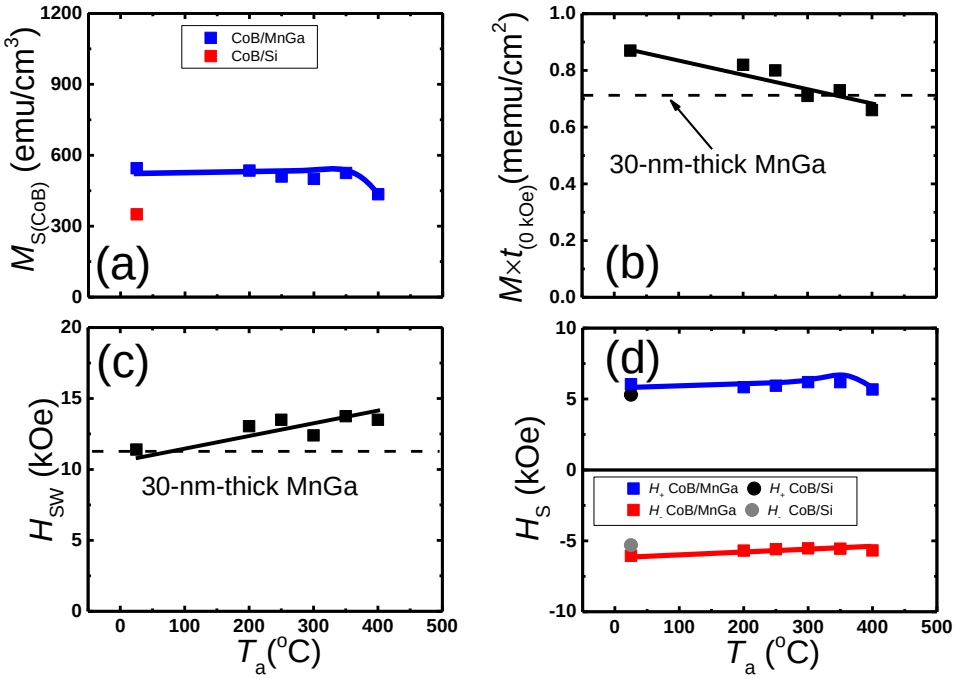

Figure 3-18 (a) The annealing temperature dependence of saturation magnetization for CoB film. (b) The annealing temperature dependence of remnant magnetization, (c) switching and (d) saturation fields for CoB (20 nm)/MnGa (30 nm) bilayer film.

Fig. 3-18 (d) shows the T_a dependence of H_+ and H_- for CoB films on MnGa. In addition, H_+ and H_- of CoB film fabricated on Si substrate is shown as a reference data. As can be seen from this figure, H_+ and H_- for CoB films on Si substrate shows a symmetry regard to H_s=0 axis as we expect for the no exchange coupling case, whereas for the CoB films on MnGa an asymmetry was observed specially for T_a= 350ºC which is due to exchange coupling between

MnGa and CoB film. The difference between H_+ and absolute H_- values reaches to maximum value at 350ºC and then decreases with increasing of T_a.

Fig. 3-19 shows T_a dependence of the interfacial exchange coupling constant. No exchange coupling was observed for bilayer film without post annealing. With increasing annealing temperature, the absolute value of J_{ex} increased up to about 0.3 erg/cm^2, and then decreases at the T_a more than 350ºC. The absolute values of negative J_{ex} is relatively smaller than those evaluated in the Co-Fe/Mn-Ga bilayers.[37] The weak antiferromagnetic interfacial exchange coupling in the CoB/MnGa bilayer could be interpreted by the interface structure. CoB film has amorphous structure in this study. So weak atomic ordering in the interface might be the reason of weak coupling strength between CoB and MnGa Films.

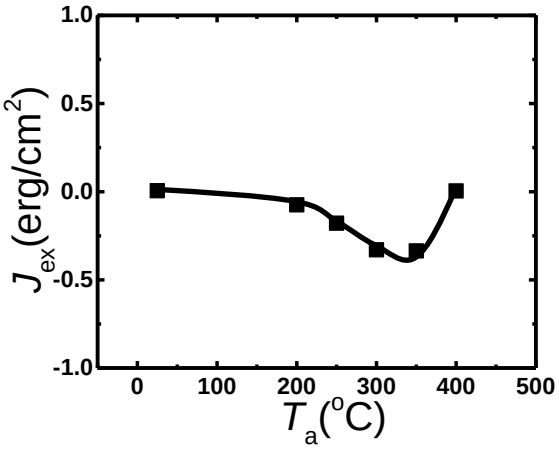

Figure 3-19 The annealing temperature dependence of interfacial exchange coupling constant CoB (20 nm)/MnGa (30 nm) bilayer film.

A short summary will be presented here. We investigated the influence of annealing temperature on the structural and magnetic properties of CoB (20 nm)/$D0_{22}$-MnGa (30 nm) bilayer films. The bilayer films have been successfully grown. The optimized annealing temperature was found to be 350ºC. The CoB (20 nm)/$D0_{22}$-MnGa (30 nm) bilayer films show better structure stability compared to Co (20 nm)/$D0_{22}$-MnGa (30 nm) bilayer film. We evaluated the interfacial exchange coupling constant for the bilayers with different annealing temperature. The weak antiferromagnetic interfacial exchange coupling (J_{ex} = 0 ~ -0.3 erg/cm^2) was observed.

3.4 Thickness Dependence of CoB (t_{CoB})/$D0_{22}$-MnGa (30 nm) Bilayer

Two series samples without post annealing and with post annealing at 350ºC by RTA system with different CoB thicknesses of 1, 3, 5, 10 and 20 nm were prepared by using an ultrahigh vacuum magnetron sputtering system with a base pressure of less than 1×10^{-7} Pa. The stacking structure of each series were: the (100) single crystalline MgO substrate / Cr (10) / $D0_{22}$-MnGa (30) / CoB (t_{CoB}) / Cr (5) (thickness is in nanometers) All the layers were deposited at room temperature. The in-situ annealing was employed at 400ºC after the MnGa deposition. For characterization of structural and magnetic properties, the X-ray diffractometer (XRD) with the Cu K_α radiation, polar magneto optical Kerr effect (P-MOKE) system at laser wavelength of 400 nm, and a vibrating sample magnetometer (VSM) were used.

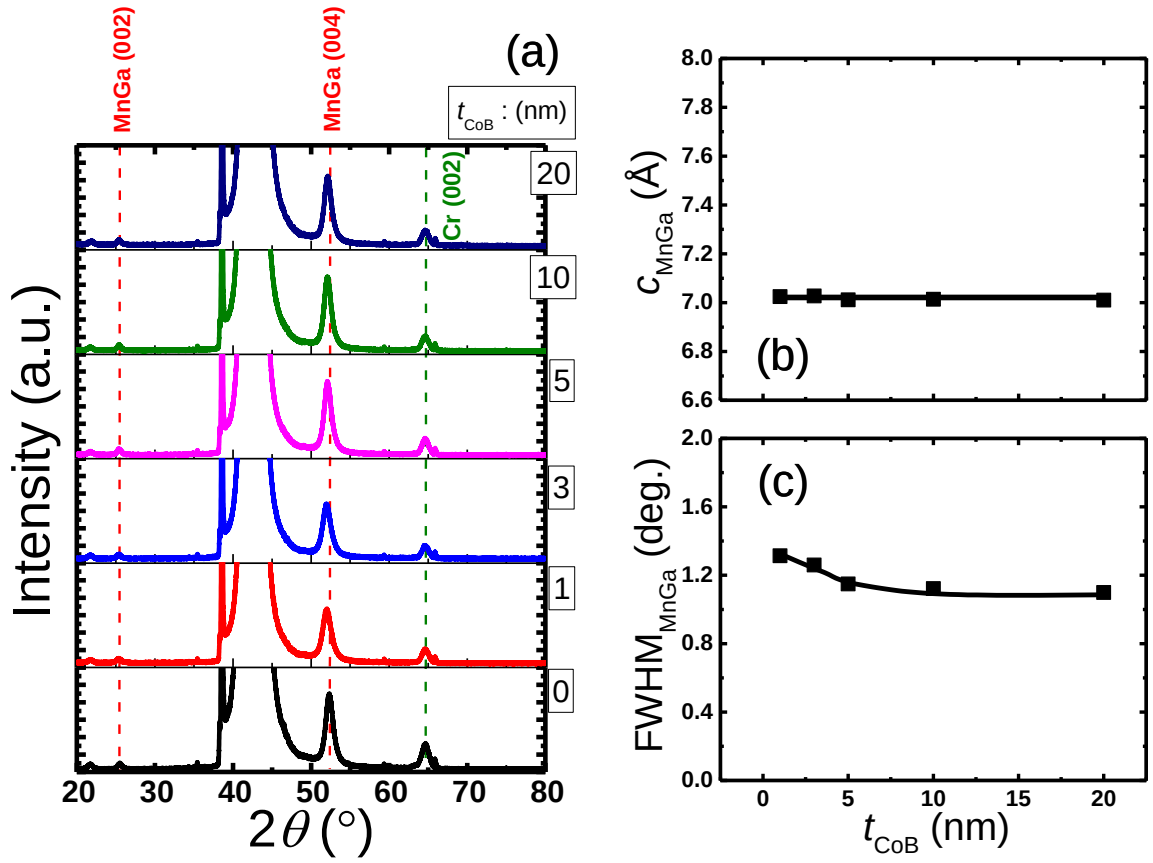

Figure 3-20 (a) The XRD pattern of CoB (0-20 nm)/MnGa (30 nm) bilayers for the un-annealed samples. (b) The Co thickness dependence of *c* lattice constant and (c) FWHM of (004) peak of MnGa film.

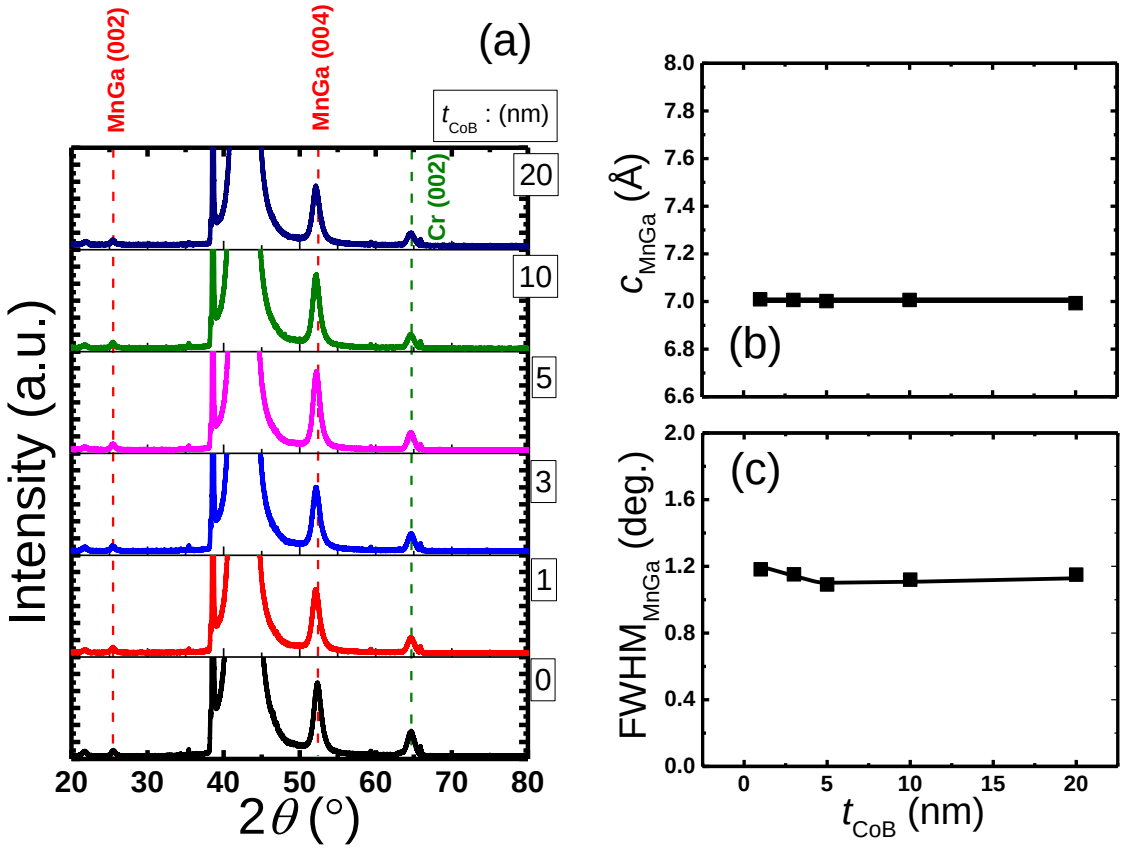

Figure 3-21 (a) The XRD pattern of CoB (0-20 nm)/MnGa (30 nm) bilayers for the samples annealed at 350ºC. (b) The Co thickness dependence of *c* lattice constant and (c) FWHM of (004) peak of Mn Ga film.

3.4.1 Structural Properties

3.4.1.1 XRD

The XRD pattern of CoB (0-20 nm)/MnGa (30 nm) bilayers for the un-annealed samples and annealed samples at 350ºC are shown in Fig 3-20 (a) and 3-21 (a), respectively. The peaks of MnGa (002), and (004) corresponding to tetragonal structure of $D0_{22}$-MnGa are clearly observed in both series samples. The t_{CoB} dependence of the *c* lattice constant of MnGa of bilayer film without and with post annealing are shown in Fig 3-20 (b) and 3-21 (b). The *c* lattice constant of MnGa is constant with increasing t_{CoB} for both series samples and very close to value of the reference MnGa film (7.00 Å). The t_{CoB} dependence of the FWHM (004) peak of MnGa of bilayer film without and with post annealing are shown in Fig 3-20 (c) and 3-21 (c). For both series samples the FWHM decreases as CoB thickness increases up to 5 nm and

the FWHM is constant for thicker CoB film. This indicates quality of MnGa film is improving with increasing of CoB thickness.

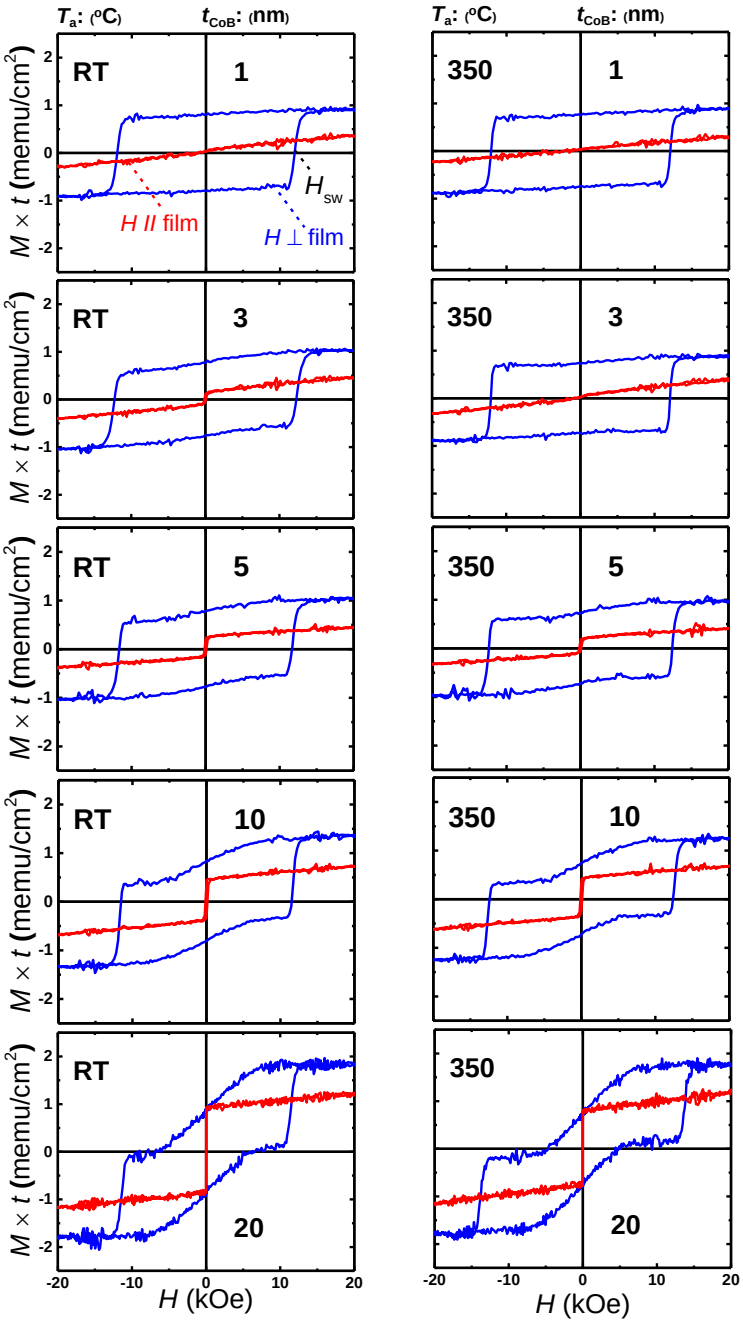

Figure 3-22 The typical out-of plane (blue colour) and in-plane (red colour) VSM *M*-*H* loops of CoB (1-20 nm)/MnGa (30 nm) bilayers for un-annealed samples and annealed samples at 350°C.

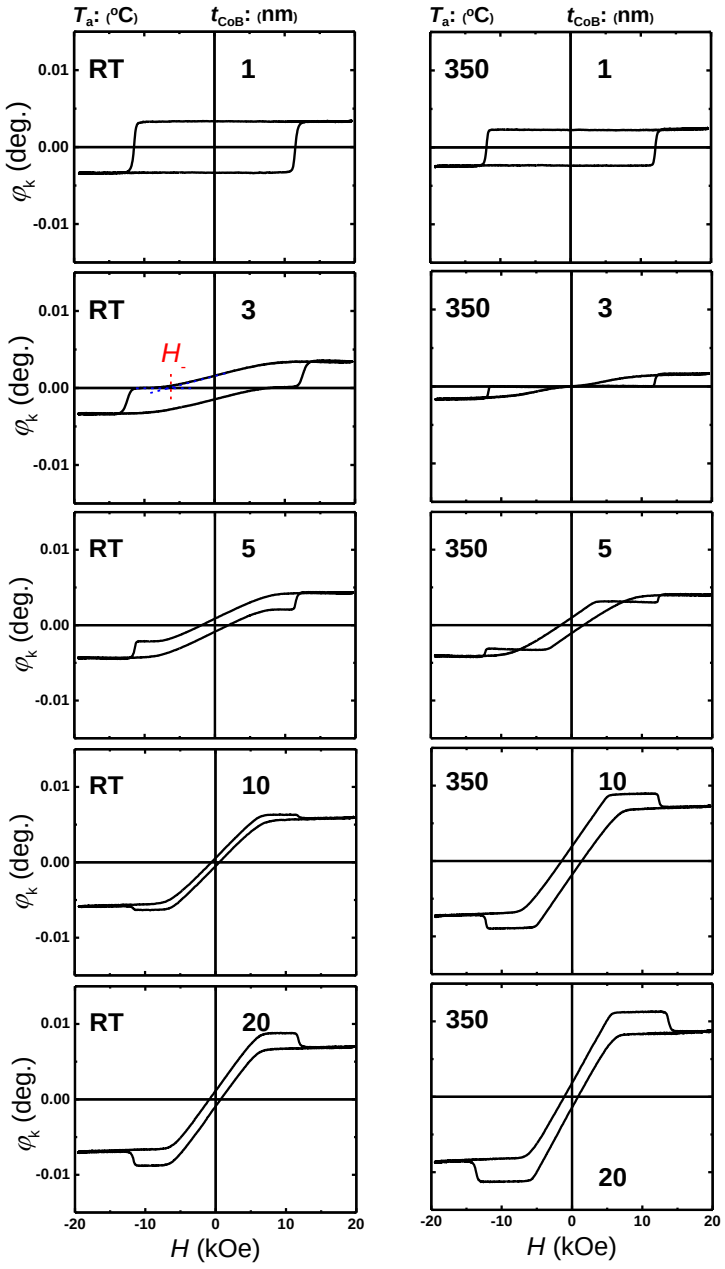

Figure 3-23 The typical polar Kerr rotation angle versus the applied field of CoB (1-20 nm)/MnGa (30 nm) bilayers for un-annealed samples and annealed samples at 350ºC.

3.4.2 Magnetic Properties

3.4.2.1 VSM

The typical out-of plane and in-plane VSM *M-H* loops of CoB (1-20 nm)/MnGa (30 nm) bilayers for un-annealed samples and samples annealed at 350ºC are shown in Fig. 3-22. The

un-annealed sample and sample annealed at 350ºC with 1 nm CoB thickness show similar *M-H* loop with 30-nm-thick MnGa. With increasing CoB thickness, shape of *M-H* loops have changed. Magnetization of in plane component increases because of IMA of CoB film. Un-annealed samples show larger in-plane component compared to samples annealed at 350ºC. Both series samples show the saturation field lees than 20 kOe. The CoB films has smaller saturation magnetization Compared to Co film, therefore smaller magnetic field is needed to overcome demagnetization of CoB film.

3.4.2.2 MOKE

To clarify magnetization process of CoB film and MnGa layer all the sample have been measured by MOKE system. The typical polar Kerr rotation angle versus the applied magnetic field of CoB (1-20 nm)/MnGa (30 nm) bilayers for un-annealed samples and annealed samples at 350ºC are shown in Fig. 3-23. The Un-annealed bilayer film with 1 nm CoB thickness shows flat MOKE hysteresis loop with good squareness hysteresis loop. It seems squareness and flatness of bilayer film with 1 nm CoB thickness enhance after annealing at 350ºC. This is may be due to stronger antiferromagnetic coupling for annealed sample compered to un-annealed sample. Both un-annealed and annealed samples show CoB film coupled fully perpendicular to MnGa film. As Co thickness increases magnetization of CoB tilted from perpendicular to in-plane direction because of large in-plane component. However, the sample annealed at 350ºC still show magnetization of CoB partially coupled perpendicular to MnGa film.

Same as Co study the inverted loop were observed for the some samples specially after annealing process. The reason of such inverted loop may interpret with antiferromagnetic exchange coupling between MnGa film and CoB layer.

3.4.3 Discussion and Summary

Fig. 3-24(a) shows the t_{CoB} dependence of saturation magnetization of CoB layer which is estimated from out-of-plane *M-H* loop of CoB/MnGa bilayer film. Here, we have ignored estimation value of saturation magnetization of CoB layer which are not reliable due to large error especially when Co thickness is relatively thin. The average of saturation magnetization value of CoB for un-annealed and annealed samples are about 615 and 530 emu/cm^3, respectively. These values are larger than value of CoB reference film. The t_{CoB} dependence of $M \times t_{(0\ kOe)}$ and H_{sw} for un-annealed samples and samples annealed at 350ºC are shown in Fig.

3-24 (b) and (c), respectively. The $M \times t_{(0\ kOe)}$ and H_{sw} of 30-nm-thick MnGa plotted with dashed line for comparison. As can be seen from Fig. 3-24(b), $M \times t_{(0\ kOe)}$ of un-annealed bilayer film is larger than value of 30-nm-thick MnGa film. Then $M \times t_{(0\ kOe)}$ increases monotonically with increasing of CoB thickness which is attributed to in-plane component of CoB film. However, the $M \times t_{(0\ kOe)}$ value of annealed samples are close to value of MnGa reference film and did not change with increasing CoB thickness. The t_{CoB} dependence of H_{sw} shows a constant value for un-annealed samples, whereas for the samples annealed at 350ºC, H_{sw} increases linearly.

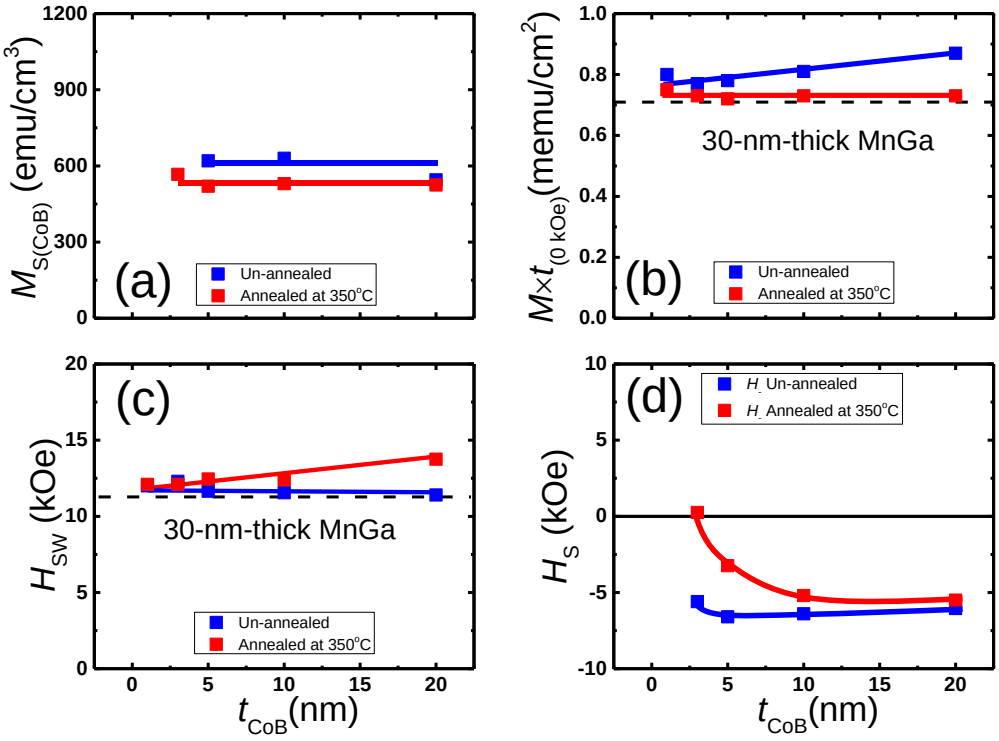

Figure 3-24 (a) The CoB thickness dependence of saturation magnetization for CoB film. (b) The CoB thickness dependence of remnant magnetization, (c) switching and (d) saturation fields for CoB (1-20 nm)/MnGa (30 nm) bilayer films.

Finally we have summarized H_- as a function of CoB thickness to determine critical thickness (t_c) of CoB film. We define this critical thickness as thickness for bilayer coupled fully perpendicular. As we have described for estimation of interfacial exchange coupling H_- is the saturation field in antiparallel state ($H_{\uparrow\downarrow}$). The t_{CoB} dependence of H_- for un-annealed samples and samples annealed at 350ºC are shown in Fig. 3-24(a). When H_- is positive we can conclude

magnetization of CoB coupled fully perpendicular to magnetization of MnGa. So, t_c is happening when the sign of H_- changes from negative to positive. For un-annealed samples t_c is less than 3 nm, whereas for the samples annealed at 350ºC, 3 nm CoB film show the positive value.

A short summary will be presented here. We investigated the effect of CoB thickness on the structural and magnetic properties of un-annealed samples and samples annealed at 350ºC for CoB (1-20 nm)/$D0_{22}$MnGa (30 nm) bilayer films. The annealed sample with 3 nm thick CoB film show good PMA properties.

Chapter 4 Structural and Magnetic Properties for Bilayer of the Cubic and Tetragonal Heusler Alloys

In this chapter the structural and magnetic properties for bilayer of the cubic and tetragonal Heusler alloys have been investigated. Different cubic Heusler alloys such as Co_2FeAl (CFA), Co_2FeSi (CFS), Co_2MnAl (CMA), and Co_2MnSi (CMS) were fabricated on $D0_{22}$-MnGa film same as Co-B binary film. Firstly, annealing temperature dependence will be discussed. After optimizing annealing temperature, to investigate thickness effect of Heusler alloys two series bilayer films with and without annealing were fabricated. Let's start from CFA/ $D0_{22}$-MnGa bilayer films.

4.1 Annealing Temperature Dependence of Co_2FeAl (20 nm)/$D0_{22}$-MnGa (30 nm) Bilayer

We have fabricated seven samples at different post annealing temperature with the stacking structure of (100) single crystalline MgO substrate / Cr (10) / $D0_{22}$-MnGa (30) / CFA (20) / Cr (5) (thickness is in nanometers). The epitaxial bilayers were fabricated using an ultrahigh vacuum magnetron sputtering system with a base pressure of less than 1×10^{-7} Pa. All the layers were deposited at room temperature. The in-situ annealing was employed at 400ºC after the MnGa deposition. Annealing temperature dependence has been investigated using post annealing by RTA system. In addition, the 30 (20)-nm-thick Mn-Ga (CFA) films with the same stacking structure without CFA (Mn-Ga) films were fabricated as reference films.

Film compositions of MnGa and CFA alloy were $Mn_{70}Ga_{30}$ and $Co_{46}Fe_{23}Al_{31}$ estimated by the inductively coupled plasma spectroscopy respectively. For characterization of structural and magnetic properties, the X-ray diffractometer (XRD) with the Cu K_α radiation, polar magneto optical Kerr effect (P-MOKE) system at laser wavelength of 400 nm, and a vibrating sample magnetometer (VSM) were used.

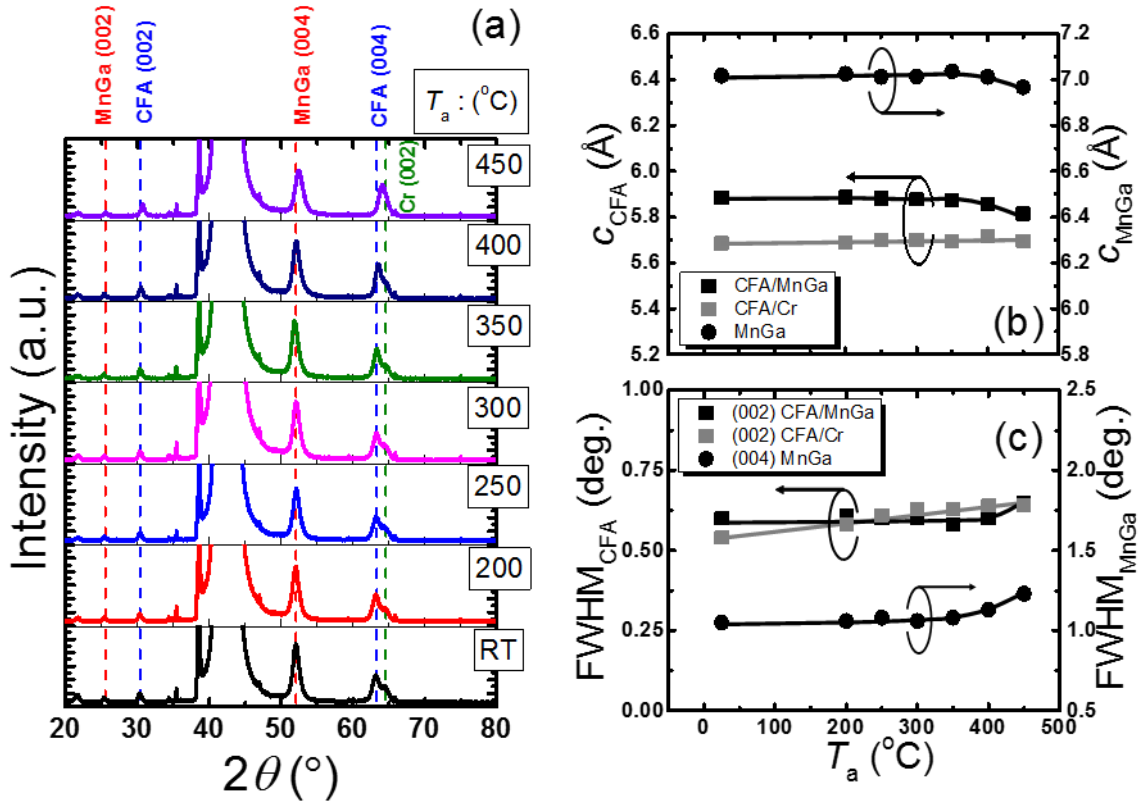

Figure 4-1 (a) The XRD pattern of CFA/MnGa bilayers for un-annealed sample and annealed samples at 200, 250, 300, 350, 400, and 450ºC. (b) The annealing temperature dependence of *c* lattice constant and (c) FWHM for CFA and MnGa films.

4.1.1 Structural Properties

4.1.1.1 XRD

The out-of-plane XRD patterns of CFA/MnGa bilayers for different annealing temperatures are shown in Fig. 4-1(a). The peaks (002) and (004) of MnGa and CFA corresponding to $D0_{22}$ and B2 structures of MnGa and CFA are clearly observed even for un-annealed sample. The annealing temperature dependence of the *c* lattice constant of MnGa and CFA of bilayer films (CFA/MnGa), and also CFA of reference films (CFA/Cr) are shown in Fig. 4-1(b). The *c* lattice constant of MnGa is constant and very close to value of the reference MnGa films (7.00 Å) for the un-annealed sample and samples annealed at 200 up to 400ºC. The *c* lattice constant of MnGa slightly reduce after annealing sample at 450ºC which shows with further annealing,

structure will be changed because of inter diffusion effect. For the *c* lattice constant of the CFA bilayer films the same behavior was observed, however *c* lattice constant of CFA film on MnGa reduces after annealing at 350ºC. The *c* lattice constant of CFA reference films is constant and close to bulk value which is 5.73 Å.[53] Difference between *c* lattice constant of CFA bilayer and reference films show an expansion of the *c* lattice constant in the out-of-plane direction for better matching of the CFA film to the MnGa layer.

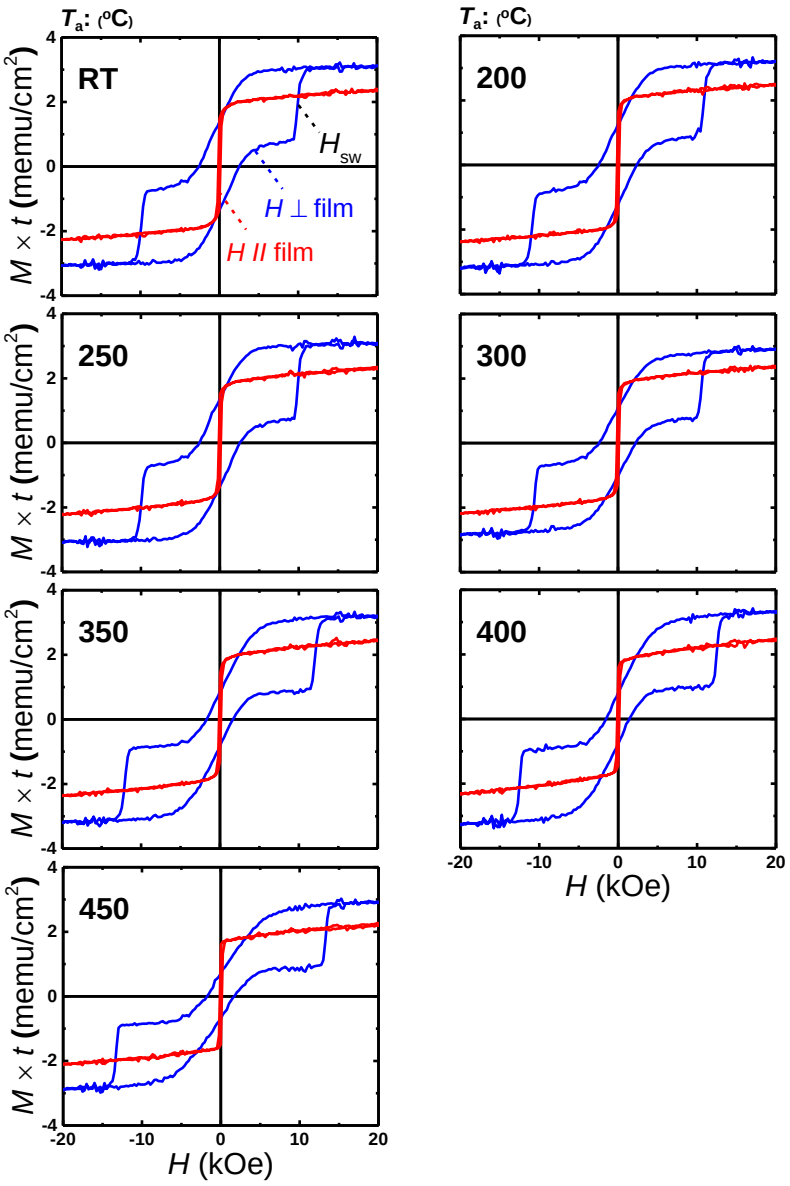

Figure 4-2 The typical out-of plane (blue colour) and in-plane (red colour) VSM *M-H* loops of CFA (20 nm)/MnGa (30 nm) bilayers for un-annealed sample and annealed samples at 200, 250, 300, 350, 400, and 450ºC.

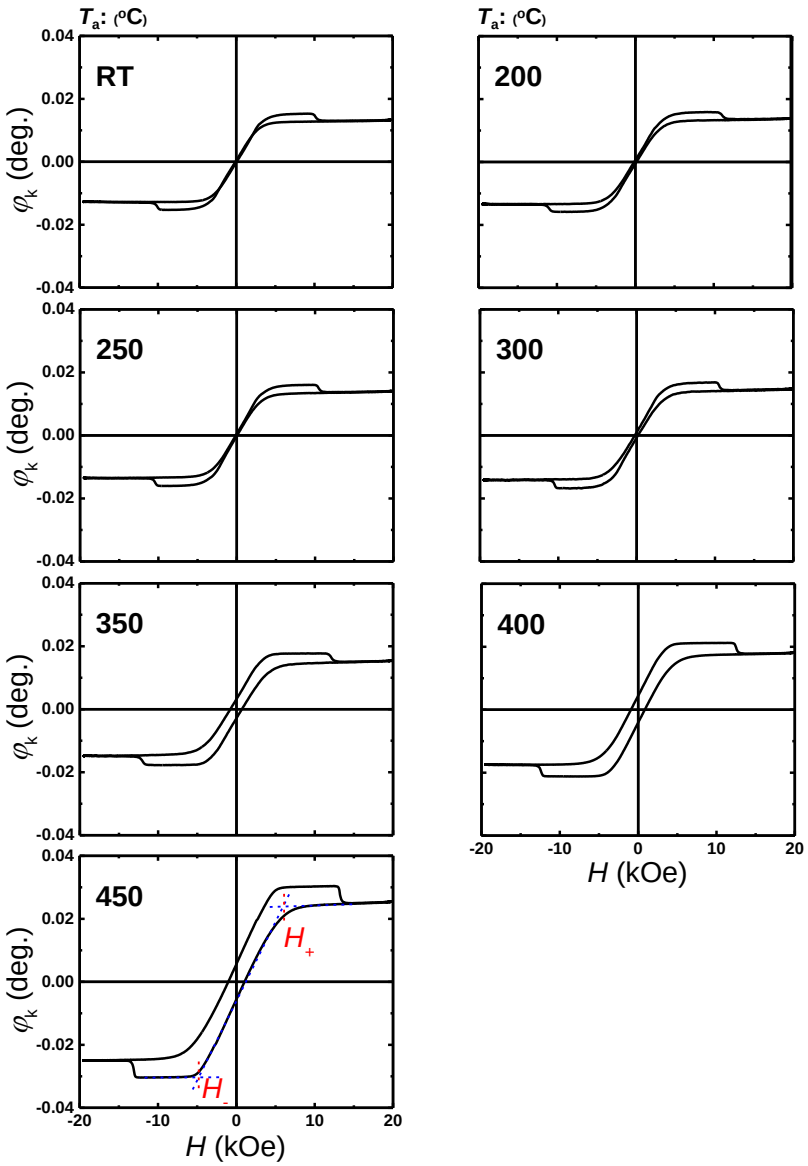

Figure 4-3 The typical polar Kerr rotation angle versus the applied field of CFA (20 nm)/MnGa (30 nm) bilayers for un-annealed sample and annealed samples at 200, 250, 300, 350, 400, and 450°C.

The annealing temperature dependence of the FWHM for the MnGa, CFA/MnGa and CFA/Cr films are shown in Fig. 4-1 (c). FWHM for CFA/Cr increases linearly whereas for the CFA/MnGa is constant and then increase for the sample annealed at 450°C. The same behavior with CFA/MnGa was observed for MnGa films. The smaller FWHM for CFA/MnGa compared to CFA/Cr at high temperature regime indicates the quality of the CFA film on MnGa layer is better than the CFA film on Cr layer.

4.1.2 Magnetic Properties

4.1.2.1 VSM

The typical out-of-plane and in-plane *M-H* loops measured by VSM system for the CFA (20 nm)/MnGa (30 nm) bilayer film for un-annealed sample and samples annealed at 200, 250, 300, 350, 400, and 450ºC are shown in Fig.4-2. Same as previous Co-B binary the 30-nm-thick MnGa and 20-nm-thick CFA films show the hard and soft magnetic properties, respectively. Therefore the same analysis method can be used in CFA/MnGa bilayer film. No in plane magnetic anisotropy was observed in CFA/MnGa film which indicates good structural stability. Even sample annealed at 450ºC shows similar *M-H* loop to un-annealed sample. However smaller $M \times t_{(0\ \mathrm{kOe})}$ and H_{sw} and also different H_{+} and H_{-} were observed for sample annealed at 450ºC. These changes is related to exchange coupling which will be explained in the summary section.

4.1.2.2 MOKE

The typical polar Kerr rotation angle versus the applied field of CFA (20 nm)/MnGa (30 nm) bilayers for un-annealed sample and annealed samples at 200, 250, 300, 350, 400, and 450ºC are shown in Fig. 4-3. MOKE measurement is consistent with VSM result. The same switching field, H_{+} and H_{-} were observed in this measurement. The different shapes of the Kerr hysteresis curve and *M-H* loop originates from reflectance phase difference of the light at interface of bilayers in the MOKE measurement. Some physical parameters such as saturation and remnant magnetizations, switching and saturation fields are summarized in next section to get more information from VSM and MOKE measurements.

4.1.3 Discussion and Summary

Fig. 4-4(a) show the T_{a} dependence of saturation magnetization which is estimated from out-of-plane *M-H* loop for the CFA/MnGa and CFA/Cr films. The saturation magnetization of CFA/MnGa and CFA/Cr films show constant trend versus T_{a}. The value of M_{s} for the CFA/Cr is about 1000 emu/cm^3 which is comparable with previous report,[53] whereas for the CFA/MnGa is about 1200 emu/cm^3. This enhancement might be attributed to better crystallization of CFA film on MnGa layer as shown in XRD result. The T_{a} dependence of remnant magnetization ($M \times t_{(0\ \mathrm{kOe})}$) and switching field are shown in Fig. 4-4(b) and 3(c), respectively. The $M \times t_{(0\ \mathrm{kOe})}$ and H_{sw} of 30-nm-thick MnGa plotted with dashed line for

comparison. When a hard magnetic film combined with the soft magnetic film in the case of no coupling H_{sw} and $M\times t_{(0\ kOe)}$ of bilayer are same as those for hard magnetic film, whereas in the case of ferromagnetic coupling smaller H_{sw} and larger $M\times t_{(0\ kOe)}$ are expected.[52] As can be seen from Fig. 4-4 (b), $M\times t_{(0\ kOe)}$ and H_{sw} of un-annealed bilayer film is larger and smaller than values of 30-nm-thick MnGa film, respectively which suggested ferromagnetic exchange coupling between CFA film and MnGa layer. With increasing T_a, $M\times t_{(0\ kOe)}$ and H_{sw} values decreases and increases linearly, respectively. Finally, the sample annealed at 450ºC show smaller and larger $M\times t_{(0\ kOe)}$ and H_{sw} values compared to 30-nm-thick MnGa, respectively which suggested antiferromagnetic exchange coupling between CFA film and MnGa layer.

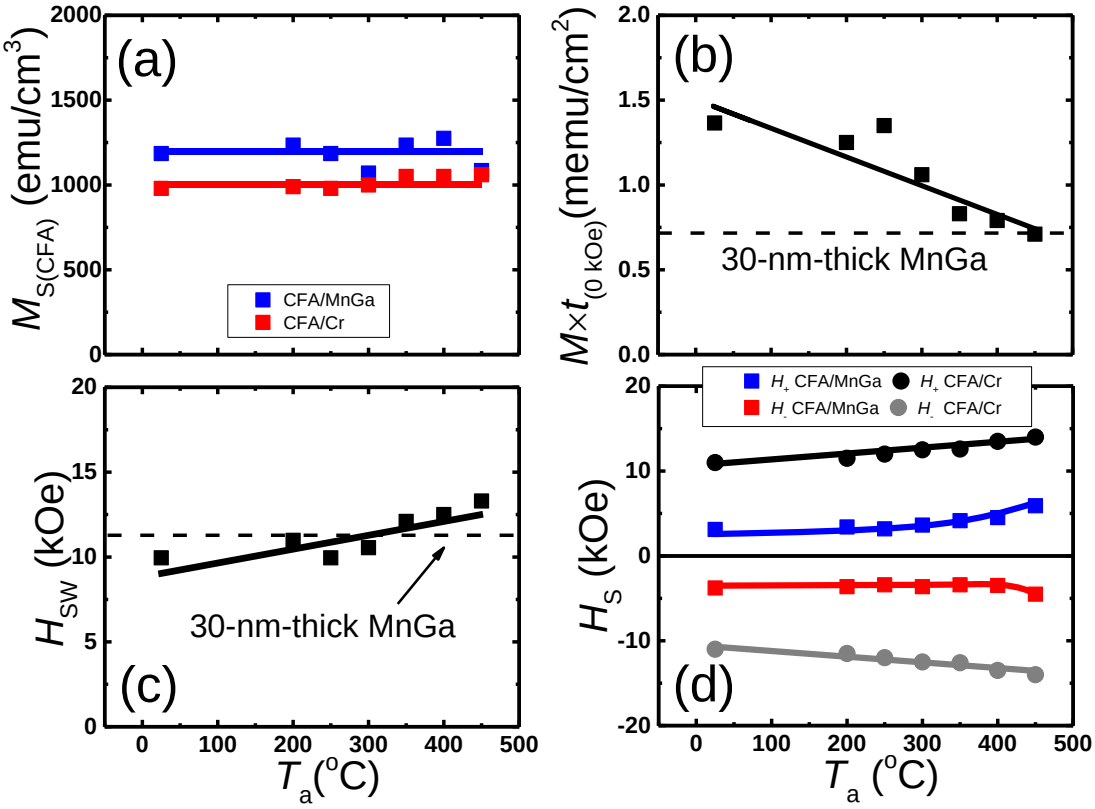

Figure 4-4 (a) The annealing temperature dependence of saturation magnetization for CFA film. (b) The annealing temperature dependence of remnant magnetization, (c) switching and (d) saturation fields for CFA (20 nm)/MnGa (30 nm) bilayer film.

The T_a dependence of H_+ and H_- for CFA films on MnGa and Cr layers are shown in Fig. 4-4 (d). As can be seen from this figure, H_+ and H_- for CFA films on Cr layers show a symmetry regard to x axis, as we expect for the no coupling case, whereas for the CFA films on MnGa an asymmetry was observed which is due to exchange coupling between MnGa and CFA films.

In the case of ferromagnetic coupling value of H_+ is smaller than absolute value of H_- which observed for the un-annealed at 200 , 250ºC. Then difference between H_+ and absolute value of H_- reaches to zero for the no exchange coupling which observed for the sample annealed at 300ºC. However, with increasing annealing temperature opposite behavior was observed due to antiferromagnetic exchange coupling between CFA film and MnGa layer.

Figure 4-5 shows T_a dependence of the interfacial exchange coupling constant for the CFA/ MnGa bilayer film. The J_{ex} value for the CFA/MnGa bilayer is about 0.8 erg/cm^2 without post annealing and decreases with increasing the annealing temperature. The sign of J_{ex} for the CFA/MnGa bilayer change from positive to negative at T_a= 300 ºC, and then the J_{ex} values continuously decreases down to about -1.5 erg/cm^2 at T_a= 450ºC. The absolute value of negative J_{ex} is relatively smaller than those evaluated in the Co-Fe/Mn-Ga bilayers.[37] The sign change in the interfacial exchange coupling in the CFA/MnGa bilayers could not be understood easily. One possibility is that the coupling is positive (ferromagnetic) in the CFA/MnGa interface with the ideal interface, which tends to change the sign in the interface with disordered or atomic mixing. Electronic structure of B2-ordered CFA without annealing has the Fermi level in the middle of minority spin band gap which is similar to Fe-rich in Fe-Co/MnGa bilayer with ferromagnetic exchange coupling.

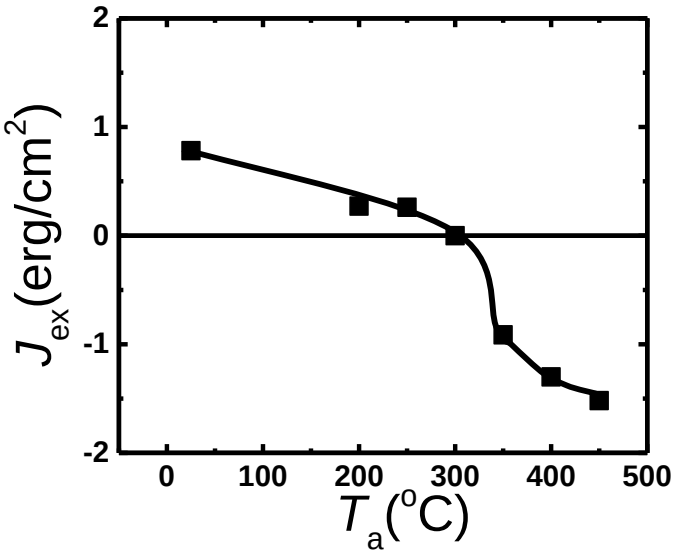

Figure 4-5 The annealing temperature dependence of interfacial exchange coupling constant for the CFA (20 nm)/MnGa (30 nm) bilayer film.

A short summary will be presented here. We investigated the influence of annealing temperature on the structural and magnetic properties of CFA (20 nm)/$D0_{22}$-MnGa (30 nm) bilayer films. The bilayer films have been successfully grown. The optimized annealing temperature was 450ºC. The CFA (20 nm)/$D0_{22}$-MnGa (30 nm) bilayer films show better structure stability compared to Co and CoB (20 nm)/$D0_{22}$-MnGa (30 nm) bilayer films. We evaluated the interfacial exchange coupling constant for the bilayers with different annealing temperature. Both ferromagnetic and antiferromagnetic interfacial exchange coupling (J_{ex} = 0.8 ~ -1.5 erg/cm^2) were observed depending on annealing temperature. The antiferromagnetic coupling strength was larger than CoB (20 nm)/$D0_{22}$-MnGa bilayer films.

4.2 Thickness Dependence of Co_2FeAl (t_{CFA})/$D0_{22}$-MnGa (30 nm) Bilayer

Two series samples without post annealing and with post annealing at 450ºC by RTA system with different CFA thicknesses of 1, 3, 5, 10 and 20 nm were prepared by using an ultrahigh vacuum magnetron sputtering system with a base pressure of less than 1×10^{-7} Pa. The stacking structure of each series were: (100) single crystalline MgO substrate / Cr (10) / $D0_{22}$-MnGa (30) / CFA (t_{CFA}) / Cr (5) (thickness is in nanometers) All the layers were deposited at room temperature. The in-situ annealing was employed at 400ºC after the MnGa deposition. For characterization of structural and magnetic properties, the X-ray diffractometer (XRD) with the Cu K_α radiation, polar magneto optical Kerr effect (P-MOKE) system at laser wavelength of 400 nm, and a vibrating sample magnetometer (VSM) were used.

4.2.1 Structural Properties

4.2.1.1 XRD

The XRD pattern of CFA (0-20 nm)/MnGa (30 nm) bilayers for the un-annealed samples and annealed samples at 450ºC are shown in Fig 4-6 (a) and 4-7 (a), respectively. The peaks of MnGa (002), and (004) corresponding to tetragonal structure of $D0_{22}$-MnGa are clearly observed in both series samples. The minimum thickness to see (002) peak of B2 structure of CFA film in XRD pattern is 5 nm for both series samples. The t_{CFA} dependence of the *c* lattice constant of MnGa and CFA films without and with post annealing are shown in Fig 4-6(b) and 4-7(b), respectively. The *c* lattice constant of MnGa film is constant with increasing t_{CFA} for

both series samples. However, *c* lattice constant of MnGa film for un-annealed samples is a little bit larger than annealed samples and it is close to value of the reference MnGa film (7.00 Å). The *c* lattice constant of CFA film is also constant with increasing t_{CFA} for both series samples. The t_{CFA} dependence of the FWHM (004) peak of MnGa and (002) peak of CFA films without and with post annealing are shown in Fig 4-6(c) and 4-7(c). The FWHM of MnGa peak is constant for both series samples with increasing CFA thickness, whereas the FWHM of CFA peak shows a nonlinear reduction as CFA thickness increases. This indicates quality of CFA film is improving with increasing of CFA thickness.

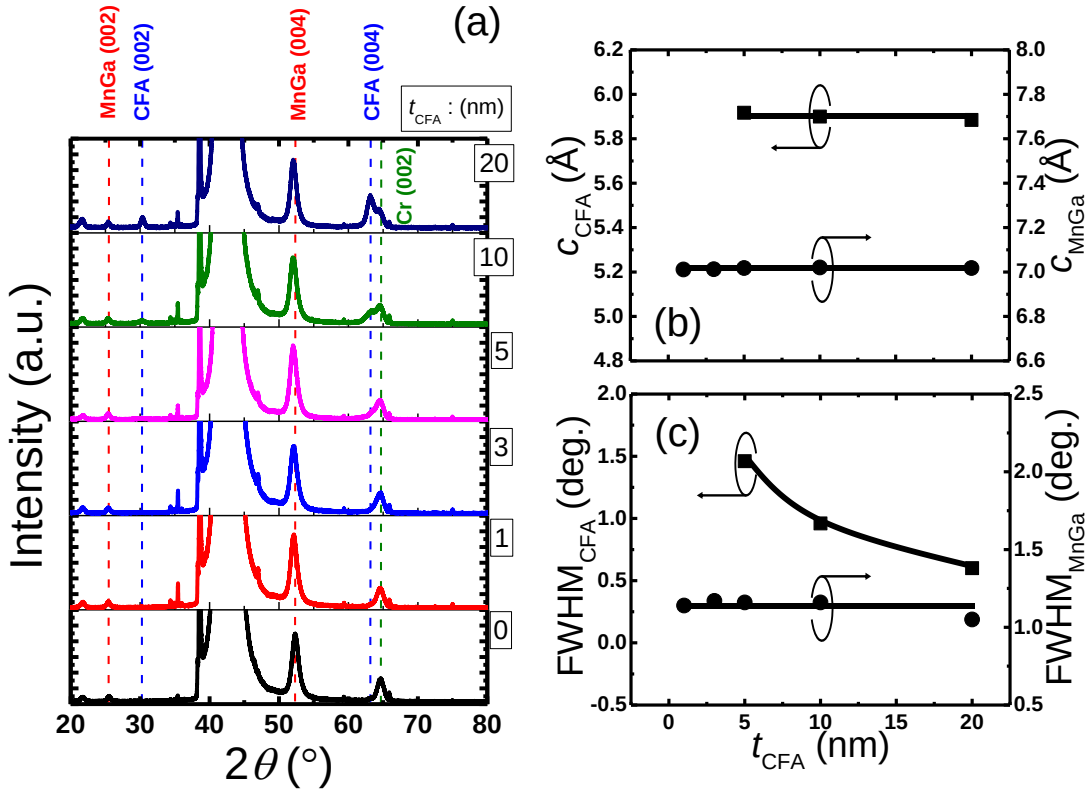

Figure 4-6 (a) The XRD pattern of CFA (0-20 nm)/MnGa (30 nm) bilayers for the un-annealed samples. (b) The Co thickness dependence of *c* lattice constant and (c) FWHM for CFA and MnGa film.

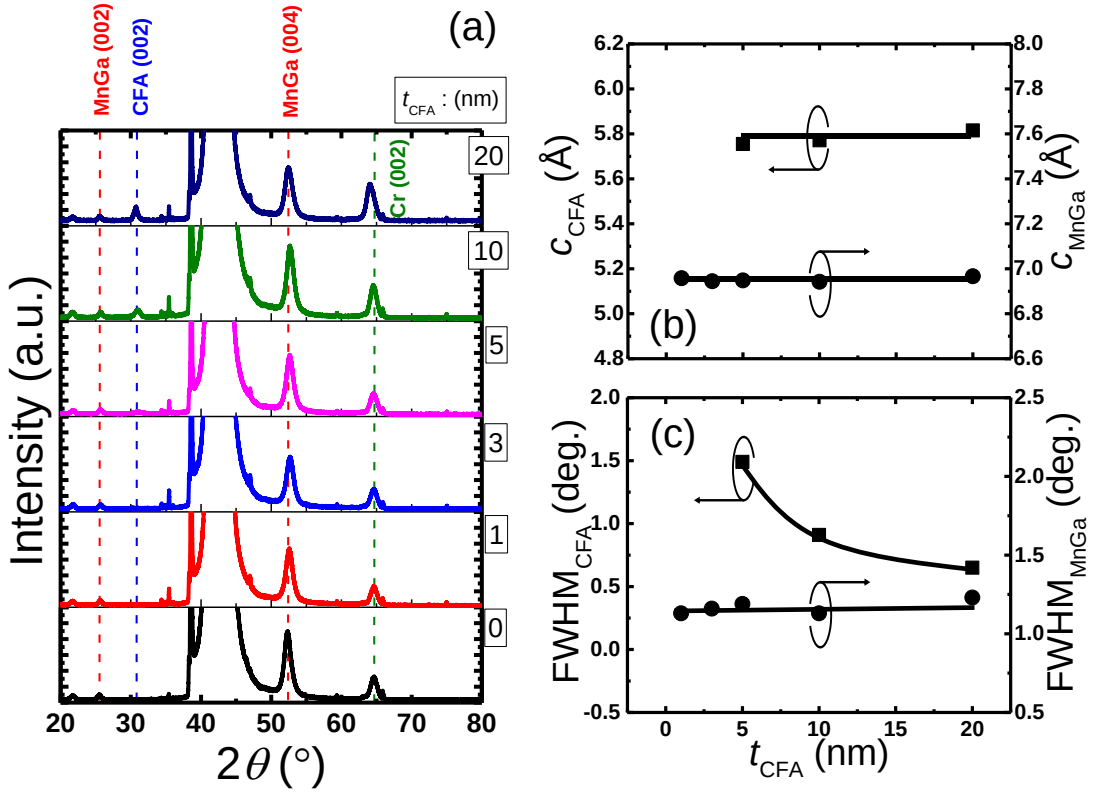

Figure 4-7 (a) The XRD pattern of CFA (0-20 nm)/MnGa (30 nm) bilayers for the samples annealed at 450ºC. (b) The Co thickness dependence of *c* lattice constant and (c) FWHM for CFA and MnGa film.

4.2.2 Magnetic Properties

4.2.2.1 VSM

The typical out-of plane and in-plane VSM *M-H* loops of CFA (1-20 nm)/MnGa (30 nm) bilayers for un-annealed samples and samples annealed at 450ºC are shown in Fig. 4-8. The un-annealed sample and sample annealed at 450ºC with 1 nm CFA thickness show similar *M-H* loop shape but different values of $M \times t_{(0\ kOe)}$ and H_{sw} compared to with 30-nm-thick MnGa. With increasing CFA thickness shape of *M-H* loops have changed and magnetization process step clearly appear. The in plane component of Magnetization increases as CFA thickness increase because of large in plane component of thicker CFA. Un-annealed samples show larger in-plane component compared to samples annealed at 350ºC. In addition different kind

of exchange coupling were observed for un-annealed samples and samples annealed at 450ºC as we have discussed in section of annealing temperature dependence.

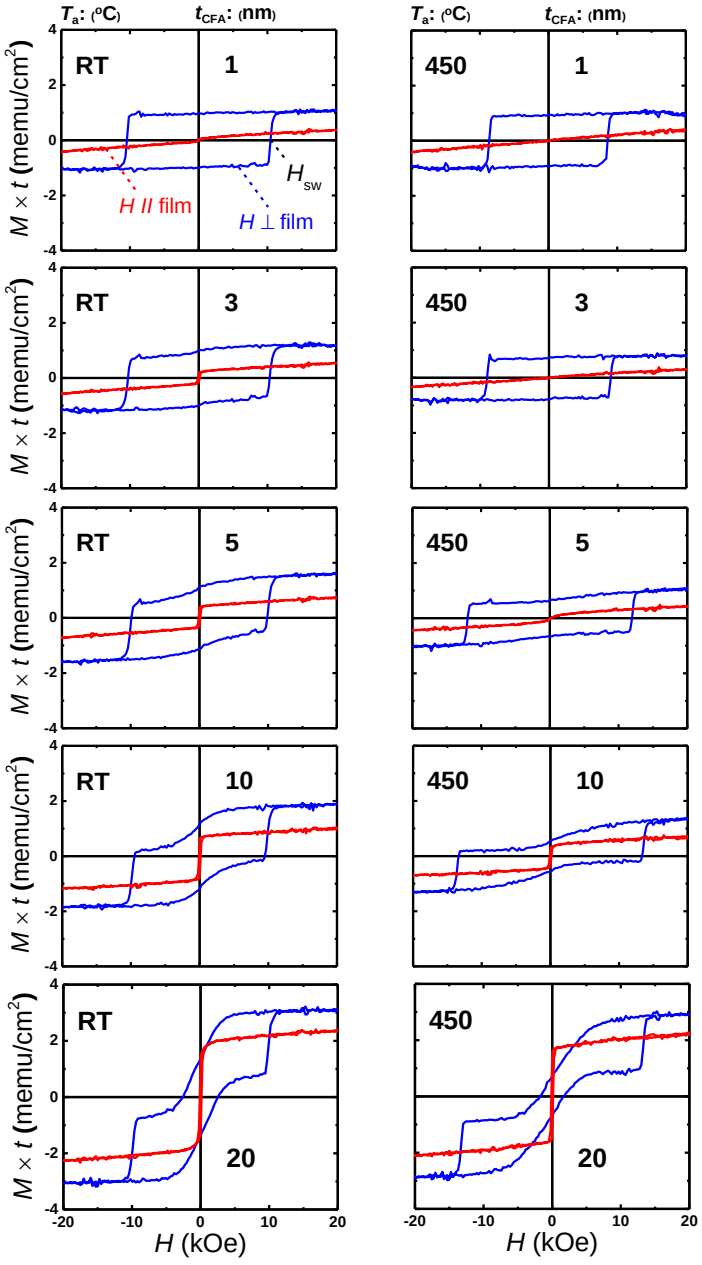

Figure 4-8 The typical out-of plane (blue colour) and in-plane (red colour) VSM *M*-*H* loops of CFA (1-20 nm)/MnGa (30 nm) bilayers for un-annealed samples and annealed samples at 450ºC.

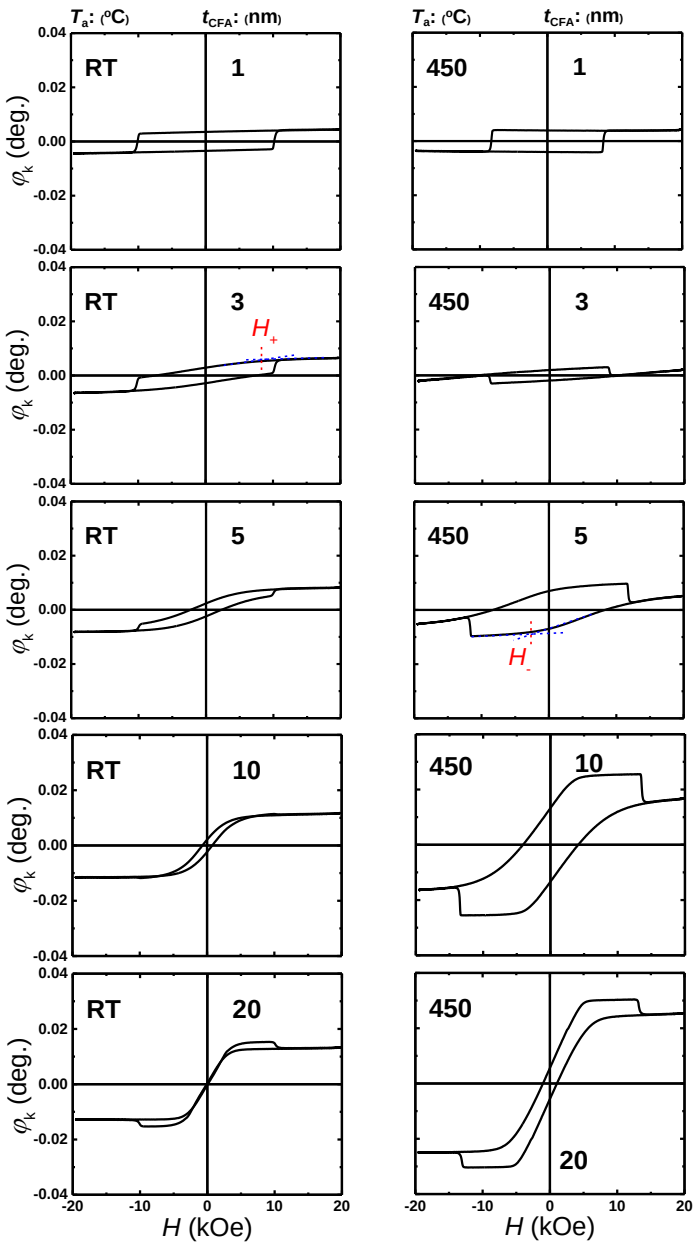

Figure 4-9 The typical polar Kerr rotation angle versus the applied field of CFA (1-20 nm)/MnGa (30 nm) bilayers for un-annealed samples and annealed samples at 350ºC.

4.2.2.2 MOKE

To clarify magnetization process of CFA film and MnGa layer all the sample have been measured by MOKE system. The typical polar Kerr rotation angle versus the applied magnetic field of CFA (1-20 nm)/MnGa (30 nm) bilayers for un-annealed samples and annealed samples

at 350ºC are shown in Fig. 4-9. The Un-annealed bilayer film with 1 nm CFA thickness shows flat MOKE hysteresis loop with good squareness. This samples show good PMA properties which means magnetization of CFA film coupled fully perpendicular to magnetization of MnGa film. As CFA thickness increases, magnetization of CFA start to tilt from perpendicular to in-plane direction because of large in-plane component for thicker CFA film. The un-annealed samples with 3, 5, and 10 nm thickness of CFA film show normal MOKE hysteresis loops, whereas after annealing the inverted MOKE hysteresis loops were observed. The different exchange coupling constant at interfaces of CFA film and MnGa layer is the reason of change in MOKE hysteresis loop.

4.2.3 Discussion and Summary

Fig. 4-10 (a) shows the t_{CFA} dependence of saturation magnetization of CFA layer which is estimated from out-of-plane *M-H* loop of CFA/MnGa bilayer film. Here, we have ignored estimation value of saturation magnetization of CFA layer which are not reliable due large error especially when Co thickness is relatively thin. The saturation magnetization value of CFA for un-annealed samples is about 1150 emu/cm^3 which is comparable with bulk material. However, t_{CFA} dependence of saturation magnetization shows different behaviour. The saturation magnetization is about 1100 emu/cm^3 for 20-nm-thick CFA film and then reduces to about 650 emu/cm^3 for 10 and 5-nm-thick CFA film. This reduction of saturation magnetization is related to reduction of quality of thinner CFA film as shown in Fig.4-7(c).

The t_{CFA} dependence of $M \times t_{(0\ kOe)}$ and H_{sw} for un-annealed samples and samples annealed at 450ºC are shown in Fig. 4-10 (b) and (c), respectively. The $M \times t_{(0\ kOe)}$ and H_{sw} of 30-nm-thick MnGa plotted with dashed line for comparison. As can be seen from Fig. 4-10(b), $M \times t_{(0\ kOe)}$ and H_{sw} of un-annealed bilayer film with 1 nm CFA is larger and smaller than value of 30-nm-thick-MnGa film. Then $M \times t_{(0\ kOe)}$ and H_{sw} show linear enhancement and constant behavior with increasing thickness of CFA film, respectively. For the annealed samples at 450ºC different behavior was observed. The $M \times t_{(0\ kOe)}$ and H_{sw} have been saturated after a reduction and enhancement, respectively with increasing thickness of CFA film. These results suggested ferromagnetic and antiferromagnetic exchange coupling for un-annealed and annealed samples, respectively.

We also have summarized H_+ for un-annealed samples and H_- for samples annealed at 450ºC as a function of CFA thickness to determine critical thickness of CFA film for remaining to

PMA. The t_{CFA} dependence of H_+ for un-annealed samples and H_- for samples annealed at 450ºC are shown in Fig. 4-10(d). Here, we did not include data of 1 nm CFA film. Un-annealed and annealed bilayer films with 1 nm CFA film show PMA as shown in VSM and XRD results. If the PMA exist for ferromagnetic exchange coupling (un-annealed samples) H_+ should be negative whereas antiferromagnetic exchange coupling (annealed samples) H_- should be positive. The t_{CFA} dependence of H_+ and H_- did not show negative and positive values. So, the critical thickness for remaining PMA is less than 3 nm for CFA/MnGa bilayer films.

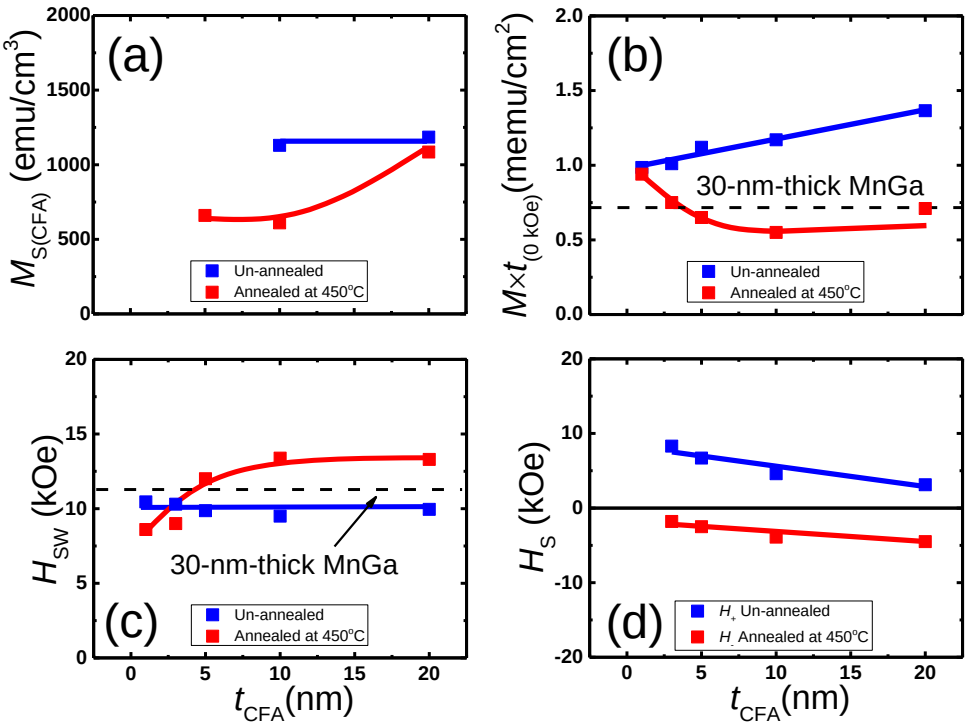

Figure 4-10 (a) The CFA thickness dependence of saturation magnetization for CFA film. (b) The CFA thickness dependence of remnant magnetization, (c) switching and (d) saturation fields for CFA (1-20 nm)/MnGa (30 nm) bilayer films.

A short summary will be presented here. We investigated the effect of CFA thickness on the structural and magnetic properties of un-annealed samples and samples annealed at 450ºC for CFA (1-20 nm)/$D0_{22}$MnGa (30 nm) bilayer films. The annealed samples and samples annealed at 450ºC with 3 nm thick CFA film did not show good PMA properties. The critical thickness to remaining PMA is less than 3 nm.

4.3 Annealing Temperature Dependence of Co_2FeSi (20 nm)/$D0_{22}$-MnGa (30 nm) Bilayer

To investigate structural and magnetic properties of Co_2FeSi (CFS)/ $D0_{22}$-MnGa seven samples at different post annealing temperature with the stacking structure of (100) single crystalline MgO substrate / Cr(10) / $D0_{22}$-MnGa (30) / CFS (20) / Cr(5) (thickness is in nanometers) have been fabricated. The epitaxial bilayers were fabricated using an ultrahigh vacuum magnetron sputtering system with a base pressure of less than 1×10^{-7} Pa. All the layers were deposited at room temperature. The in-situ annealing was employed at 400ºC after the MnGa deposition. Annealing temperature dependence has been investigated using post annealing by RTA system. In addition, the 30 (20)-nm-thick MnGa (CFS) films with the same stacking structure without CFS (MnGa) films were fabricated as reference films. Film compositions of MnGa and CFS alloy were $Mn_{70}Ga_{30}$ and $Co_{47}Fe_{24}Si_{29}$ estimated by the inductively coupled plasma spectroscopy respectively. For characterization of structural and magnetic properties, the X-ray diffractometer (XRD) with the Cu K_α radiation, polar magneto optical Kerr effect (P-MOKE) system at laser wavelength of 400 nm, and a vibrating sample magnetometer (VSM) were used.

4.3.1 Structural Properties

4.3.1.1 XRD

The out-of-plane XRD patterns of CFS/MnGa bilayers for different annealing temperatures are shown in Fig. 4-11(a). The peaks (002) and (004) of MnGa and (002) of CFS films corresponding to $D0_{22}$ and B2 structures of MnGa and CFA are clearly observed even for un-annealed sample. Fig. 4-11(b) show the annealing temperature dependence of the *c* lattice constant of MnGa and CFS of bilayer films (CFS/MnGa), and also CFS of reference films (CFS/Cr). The *c* lattice constant of MnGa is constant and very close to value of the reference MnGa films (7.00 Å) for the un-annealed sample and samples annealed at 200 up to 350ºC. The *c* lattice constant of MnGa drastically reduces after annealing sample at 400 and 450ºC. As can be seen clearly in Fig. 4-11(a), the CFS/MnGa bilayer film annealed at 400ºC has a broad (004) peak of MnGa and its position also changes. Finally this peak disappears and another peak appears very close to Cr peak for the sample annealed at 450ºC. This peak may be attributed to MnGa-CFS alloy because of inter diffusion effect.For the *c* lattice constant of

the CFS bilayer films the same behavior was observed, however *c* lattice constant of CFS film on MnGa slightly increases after annealing at 350ºC. The *c* lattice constant of CFS reference films is constant and close to bulk value which is 5.65 Å.[54] Difference between *c* lattice constant of CFS bilayer and reference films show an expansion of the *c* lattice constant in the out-of-plane direction for better matching of the CFS film to the MnGa layer.

The annealing temperature dependence of the FWHM for the MnGa, CFS/MnGa and CFS/Cr films are shown in Fig. 4-11 (c). FWHM for CFS/MnGa and CFS/Cr decrease linearly with increasing of T_a. The smaller FWHM for CFS/MnGa was observed compared to CFS/Cr which indicates the quality of the CFS film on MnGa layer is better than the CFS film on Cr layer. As can be seen from Fig. 4-11 (c), FWHM for the MnGa is constant when annealing temperature is less than 350ºC and the drastically increases because of inter diffusion effect.

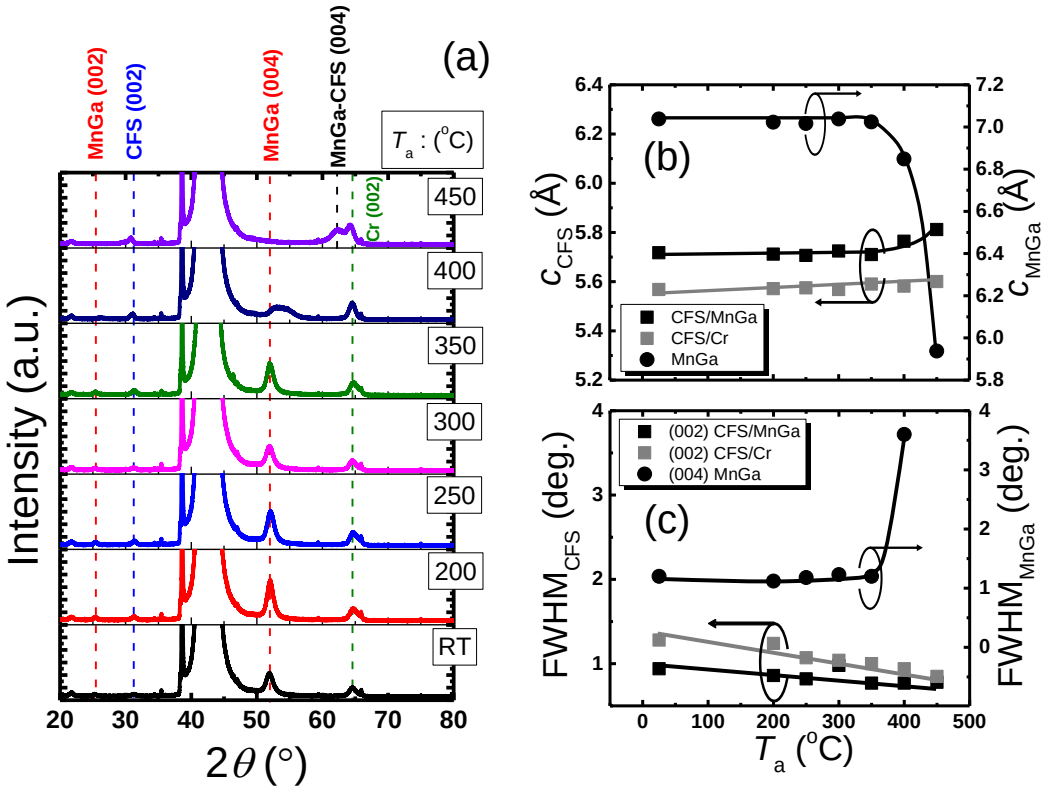

Figure 4-11 The XRD pattern of CFS/MnGa bilayers for un-annealed sample and annealed samples at 200, 250, 300, 350, 400, and 450ºC. (b) The annealing temperature dependence of *c* lattice constant and (c) FWHM for CFS and MnGa films.

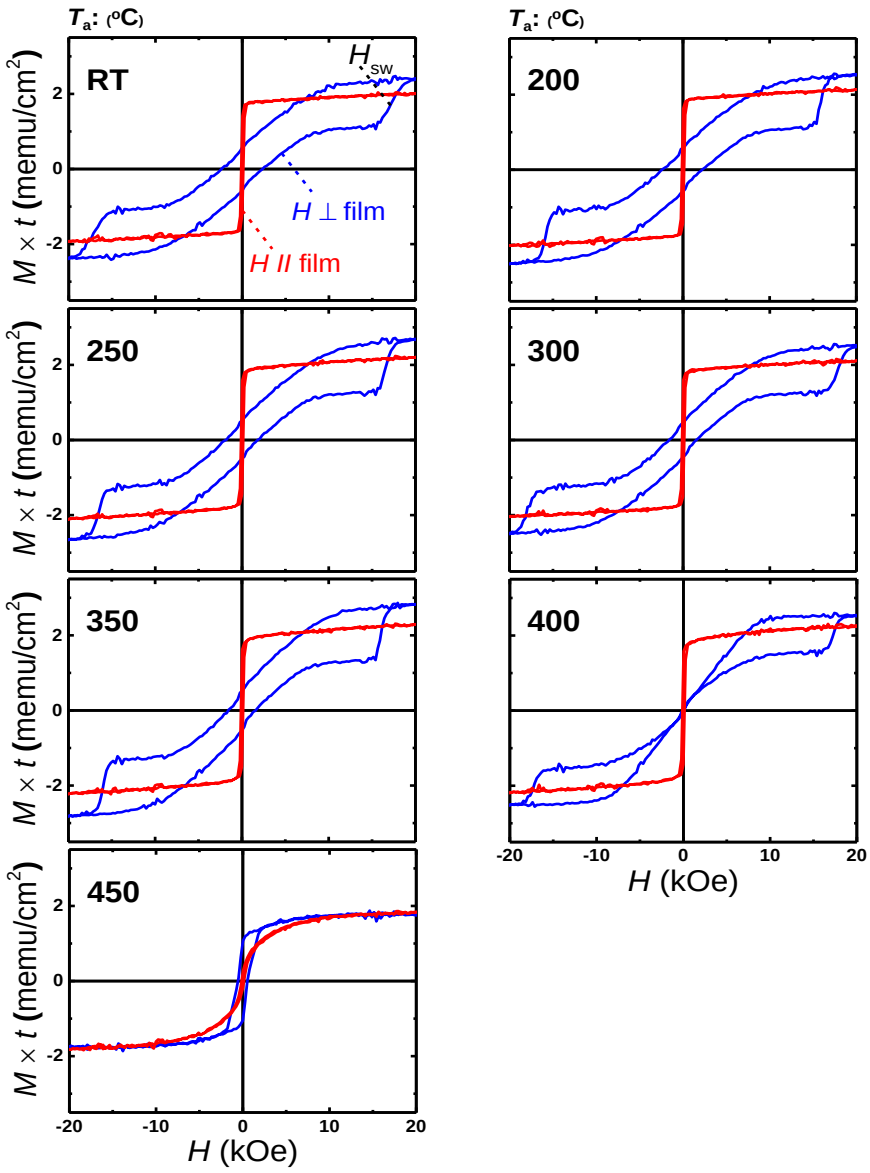

Figure 4-12 The typical out-of plane (blue colour) and in-plane (red colour) VSM *M-H* loops of CFS (20 nm)/MnGa (30 nm) bilayers for un-annealed sample and annealed samples at 200, 250, 300, 350, 400 and 450ºC.

4.3.2 Magnetic Properties

4.3.2.1 VSM

In Fig. 4-12 the typical out-of-plane and in-plane M-H loops measured by VSM system for the CFS (20 nm)/MnGa (30 nm) bilayer film for un-annealed sample and samples annealed at 200, 250, 300, 350, 400, and 450ºC are shown.

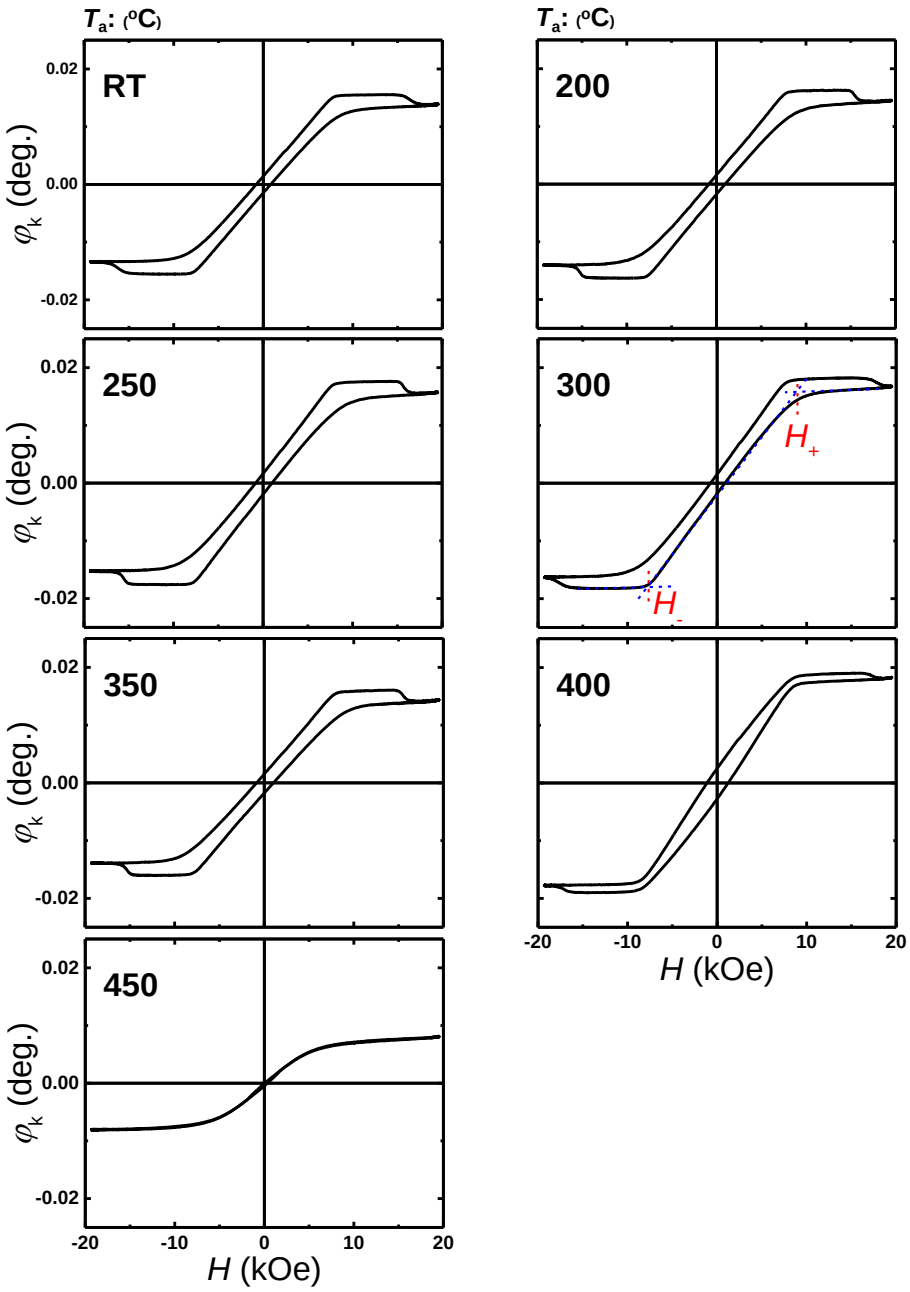

Figure 4-13 The typical polar Kerr rotation angle versus the applied field of CFS (20 nm)/MnGa (30 nm) bilayers for un-annealed sample and annealed samples at 200, 250, 300, 350, 400, and 450ºC.

The 30-nm-thick MnGa and 20-nm-thick CFS films show the hard and soft magnetic properties, respectively. *M-H* loop of un-annealed sample and samples annealed at 200, 250, 300 and 350ºC show summation of *M-H* loops for CFS and MnGa films with antiferromagnetic exchange coupling between CFS film and MnGa layer. By further annealing at 400ºC magnetic

property of CFA/MnGa bilayer completely change and finally sample annealed at 450ºC shows in plane magnetic anisotropy which is consistent with XRD result because of inter diffusion effect.

4.3.2.2 MOKE

In Fig. 4-13 the typical polar Kerr rotation angle versus the applied field of CFS (20 nm)/MnGa (30 nm) bilayers for un-annealed sample and annealed samples at 200, 250, 300, 350, 400, and 450ºC are shown. MOKE measurement is consistent with VSM result. The same switching field, H_+ and H_- were observed in this measurement. Same as CFA/MnGa bilayer different shape was observed for MOKE measurement compared to VSM measurement which originates from reflectance phase difference of the light at interface of bilayers in the MOKE measurement. Un-annealed sample and samples annealed at 200, 250, 300 and 350ºC show roughly same hysteresis loops and then magnetic properties start to change when sample annealed at 400 ºC. Finally in plane magnetic anisotropy was observed for sample annealed at 450ºC. The details of VSM and MOKE results will be discussed in the next section.

4.3.3 Discussion and Summary

Fig. 4-14 (a) show the T_a dependence of saturation magnetization which is estimated from out-of-plane M-H loop for the CFS/MnGa and CFS/Cr films. The saturation magnetization of CFS/Cr film increases monotonically with increasing T_a. On the other hand, the saturation magnetization of CFS/MnGa film increases with increasing T_a and reaches to maximum value for the sample annealed at 350ºC and then drastically decreases same as *c* lattice constant of MnGa film because of inter diffusion effect. These trends are consistent with XRD result. The value of M_s for the CFS/Cr is comparable with bulk value about 1100 emu/cm^2,[55] whereas for the CFS/MnGa is a little bit smaller. The T_a dependence of $M \times t_{(0\ kOe)}$ and H_{sw} are shown in Fig. 4-14 (b) and (c), respectively. The $M \times t_{(0\ kOe)}$ and H_{sw} of 30-nm-thick MnGa plotted with dashed line for comparison. As can be seen from Fig. 4-14(b), $M \times t_{(0\ kOe)}$ of un-annealed bilayer film is smaller than values of 30-nm-thick-MnGa film and then decreases monotonically with increasing T_a up to 350ºC. By further T_a, $M \times t_{(0\ kOe)}$ reduces too much and finally for the sample annealed at 450º large $M \times t_{(0\ kOe)}$ was observer which indicates change of PMA property to IMA. This is because of inter diffusion effect at high temperature regime. T_a dependence of H_{sw} shows the value increases with increasing of T_a up to 400ºC and then H_{sw} drastically

reduces because of IMA. The smaller and larger $M \times t_{(0\ kOe)}$ and H_{sw} compared to 30-nm-thick MnGa suggested antiferromagnetic exchange coupling between CFS film and MnGa layer.

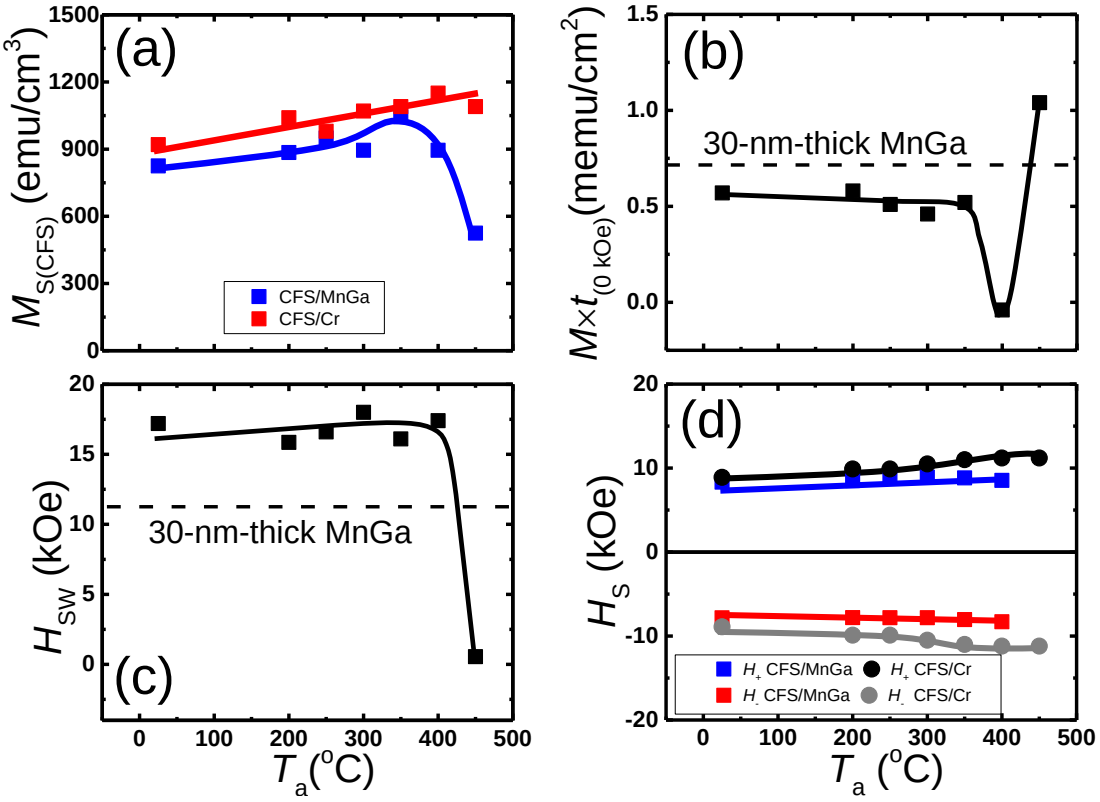

Figure 4-14 (a) The annealing temperature dependence of saturation magnetization for CFS film. (b) The annealing temperature dependence of remnant magnetization, (c) switching (d) saturation fields for CFS (20 nm)/MnGa (30 nm) bilayer film.

Fig. 4-14 (d) shows the T_a dependence of H_+ and H_- for CFS films on MnGa and Cr layers. As can be seen from this figure, H_+ and H_- for CFS films on Cr layers show a symmetry regard to x axis, as we expect for the no exchange coupling case, whereas for the CFS films on MnGa an asymmetry was observed which is due to exchange coupling between MnGa and CFS films. The difference between H_+ and absolute H_- values reaches to maximum value at 300ºC and then decreases with increasing of T_a.

Fig. 4-15 shows T_a dependence of the interfacial exchange coupling constant. The J_{ex} value was -0.4 erg/cm^2 without annealing. With increasing annealing temperature, the absolute value of J_{ex} increased up to about 1.0 erg/cm^2, and then decreases at the T_a more than 300ºC. The absolute values of negative J_{ex} is relatively smaller than those evaluated in the Co-Fe/MnGa bilayers.[37] The annealing temperature dependence of the interfacial exchange coupling in the

CFS/MnGa bilayer could be interpreted by the interface structure changes at high annealing temperature, as can be seen from XRD measurement results. At high temperature, atomic diffusion is significant at the interface between CFS film and MnGa layer, and then coupling strength is reduced. At low annealing temperature, atomic diffusion is not significant, so that the antiferromagnetic coupling in the CFS/MnGa bilayers may come from the intrinsic electronic structure at the interface, as reported in the previous studies in Co/MnAl[56] and Co/MnGa[44] bilayers. Electronic structure of B2-ordered of CFS has the Fermi level in the edge of minority conduction band which is similar to Electronic structure of Co-rich in Fe-Co alloy. Thus similar to Fe-Co/MnGa[37]bilayer antiferromagnetic exchange coupling is expected when Co composition is rich

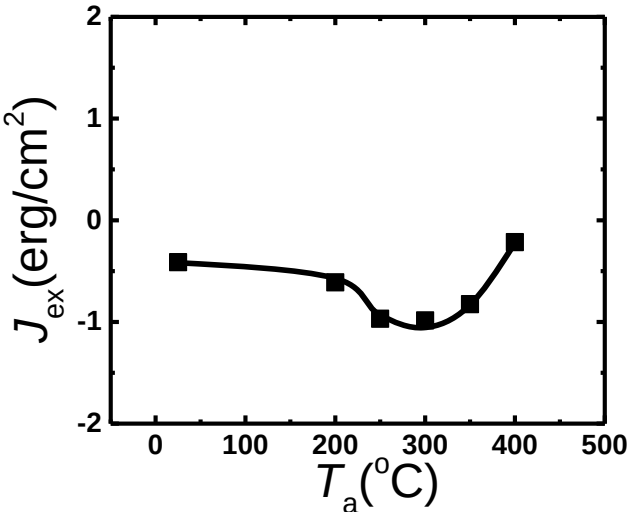

Figure 4-15 The annealing temperature dependence of interfacial exchange coupling constant CFS (20 nm)/MnGa (30 nm) bilayer film.

A short summary will be presented here. We investigated the influence of annealing temperature on the structural and magnetic properties of CFS (20 nm)/$D0_{22}$-MnGa bilayer films. The bilayer films have been successfully grown. The optimized annealing temperature was 300ºC. It seems inter diffusion effect is significant at high annealing temperature. We evaluated the interfacial exchange coupling constant for the bilayers with different annealing temperature. The antiferromagnetic interfacial exchange coupling was observed. The antiferromagnetic coupling strength (J_{ex} = -0.4 ~ -1 erg/cm^2) was larger than CoB (20

nm)/$D0_{22}$-MnGa (30 nm) bilayer film and comparable with CFA (20 nm)/$D0_{22}$-MnGa (30 nm) bilayer film.

4.4 Thickness Dependence of Co_2FeSi (t_{CFS})/$D0_{22}$-MnGa (30 nm) Bilayer

Two series samples without post annealing and with post annealing at 450ºC by RTA system with different CFS thicknesses of 1, 3, 5, 10 and 20 nm were prepared by using an ultrahigh vacuum magnetron sputtering system with a base pressure of less than 1×10^{-7} Pa. The stacking structure of each series were: the (100) single crystalline MgO substrate / Cr (10) / $D0_{22}$-MnGa (30) / CFS (t_{CFS}) / Cr (5) (thickness is in nanometers) All the layers were deposited at room temperature. The in-situ annealing was employed at 400ºC after the MnGa deposition. For characterization of structural and magnetic properties, the X-ray diffractometer (XRD) with the Cu K_α radiation, polar magneto optical Kerr effect (P-MOKE) system at laser wavelength of 400 nm, and a vibrating sample magnetometer (VSM) were used.

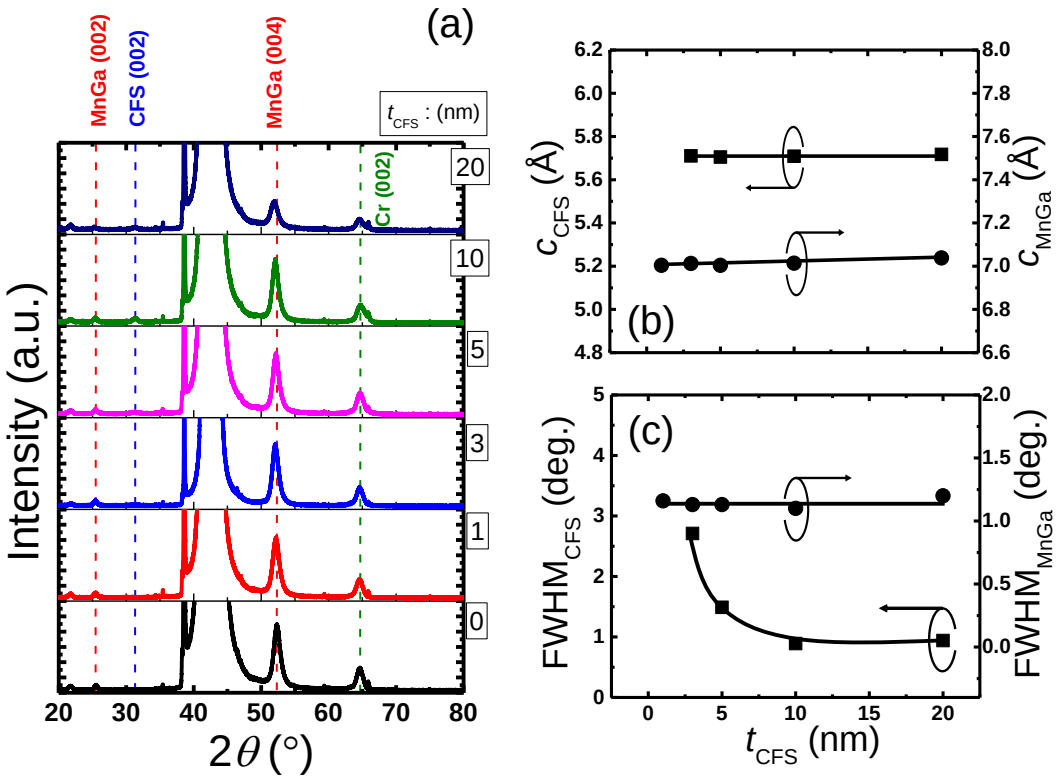

Figure 4-16 (a) The XRD pattern of CFS (0-20 nm)/MnGa (30 nm) bilayers for the un-annealed samples. (b) The CFS thickness dependence of *c* lattice constant and (c) FWHM for CFS and MnGa films.

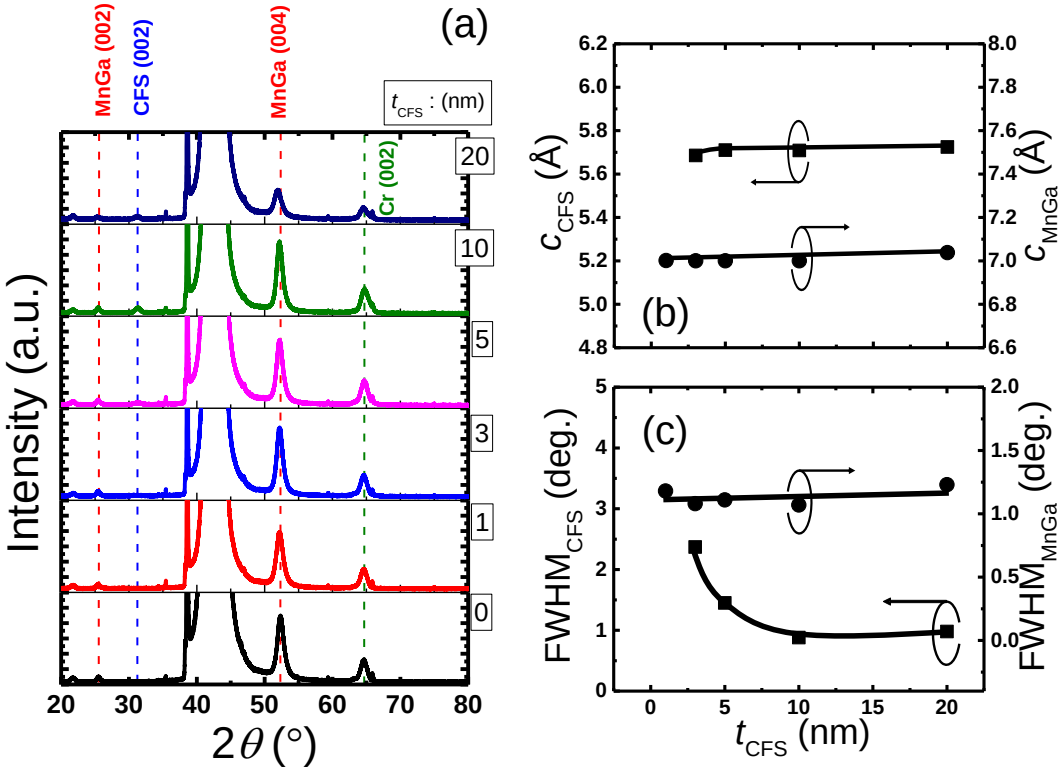

Figure 4-17 (a) The XRD pattern of CFS (t_{CFS}=0-20 nm)/MnGa (30 nm) bilayers for the samples annealed at 300ºC. (b) The CFS thickness dependence of *c* lattice constant and (c) FWHM for CFS and MnGa films.

4.4.1 Structural Properties

4.4.1.1 XRD

The XRD pattern of CFS (0-20 nm)/MnGa (30 nm) bilayers for the un-annealed samples and annealed samples at 300ºC are shown in Fig 4-16 (a) and 4-17 (a), respectively. The peaks of MnGa (002), and (004) corresponding to tetragonal structure of $D0_{22}$-MnGa are clearly observed in both series samples. The minimum thickness to see (002) peak of B2 structure of CFS film in XRD pattern is 3 nm for both series samples which is larger than CFA film. The t_{CFS} dependence of the *c* lattice constant of MnGa and CFS films without and with post annealing are shown in Fig 4-16(b) and 4-17(b), respectively. The *c* lattice constant of MnGa film is constant with increasing CFS thickness for both series samples and very close to value of the reference MnGa film (7.00 Å). The *c* lattice constant of CFS film is also constant with increasing t_{CFS} for both series samples. The t_{CFS} dependence of the FWHM (004) peak of MnGa and (002) peak of CFS films without and with post annealing are shown in Fig 4-16 (c) and 4-

17 (c). The FWHM of MnGa peak is constant for both series samples with increasing CFS thickness, whereas the FWHM of CFS peak shows a nonlinear reduction as CFS thickness increases. Finally the FWHM has saturated for thicker CFS films. This indicates quality of CFS film is improving with increasing of CFS thickness.

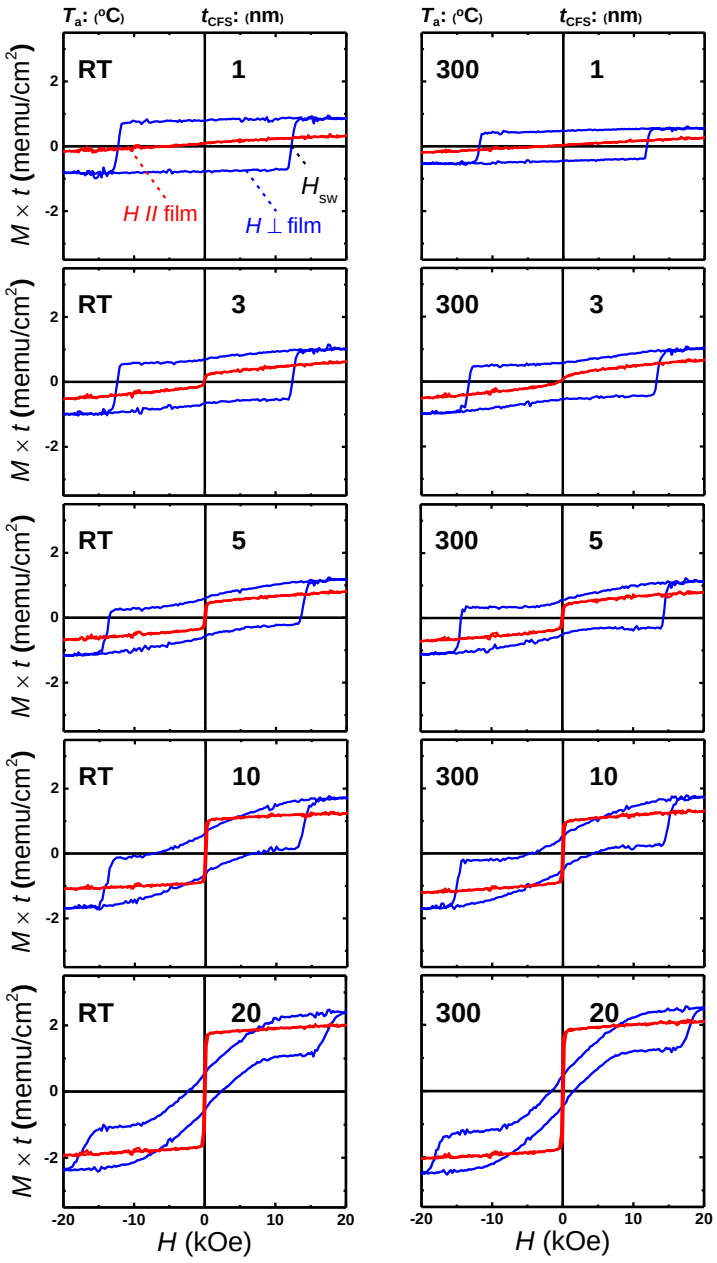

Figure 4-18 The typical out-of plane (blue colour) and in-plane (red colour) VSM *M-H* loops of CFS (1-20 nm)/MnGa (30 nm) bilayers for un-annealed samples and annealed samples at 300ºC.

4.4.2 Magnetic Properties

4.4.2.1 VSM

The typical out-of plane and in-plane VSM *M-H* loops of CFS (1-20 nm)/MnGa (30 nm) bilayers for un-annealed samples and samples annealed at 300ºC are shown in Fig. 4-18. The un-annealed sample and sample annealed at 300ºC with 1 nm CFA thickness show similar *M-H* loop shape but different values of $M \times t_{(0\ \mathrm{kOe})}$ and H_{sw} compared to with 30-nm-thick MnGa. With increasing CFS thickness, shape of *M-H* loops have changed and magnetization process step clearly appear. The in plane component of Magnetization increases as CFS thickness increase because of large in plane component of thicker CFS. It seems PMA properties improve with annealing process due to stronger antiferromagnetic exchange coupling.

4.4.2.2 MOKE

To clarify magnetization process of CFS film and MnGa layer all the sample have been measured by MOKE system. The typical polar Kerr rotation angle versus the applied magnetic field of CFS (1-20 nm)/MnGa (30 nm) bilayers for un-annealed samples and annealed samples at 300ºC are shown in Fig. 4-19. The Un-annealed bilayer film with 1 nm CFS thickness shows flat MOKE hysteresis loop with good squareness. These samples show good PMA properties which means magnetization of CFS film coupled fully perpendicular to magnetization of MnGa film. As CFS thickness increases, magnetization of CFS start to tilt from perpendicular to in-plane direction because of large in-plane component for thicker CFS film. However, the samples annealed at 300ºC with 3 nm thickness of CFS film still shows good properties. The inverted MOKE hysteresis loops were observed when thickness of CFS film is larger than 1 nm. The antiferromagnetic exchange coupling constant might be reason of the inverted MOKE hysteresis loops.

4.4.3 Discussion and Summary

Fig. 4-20 (a) shows the t_{CFS} dependence of saturation magnetization of CFS layer which is estimated from out-of-plane *M-H* loop of CFS/MnGa bilayer film. Here, we have ignored estimation value of saturation magnetization of CFS layer which are not reliable due large error especially when CFS thickness is relatively thin. The saturation magnetization value of CFS for un-annealed samples increases linearly which can interpret by using XRD result. The FWHM of (002) peak of CFS film decreases with increasing CFS film. So increasing of

magnetization value is related to better quality of film when CFS film is thick. The average of saturation magnetization of samples annealed at 300ºC is about 900 emu/cm^3 which is smaller than saturation magnetization of samples without post annealing.

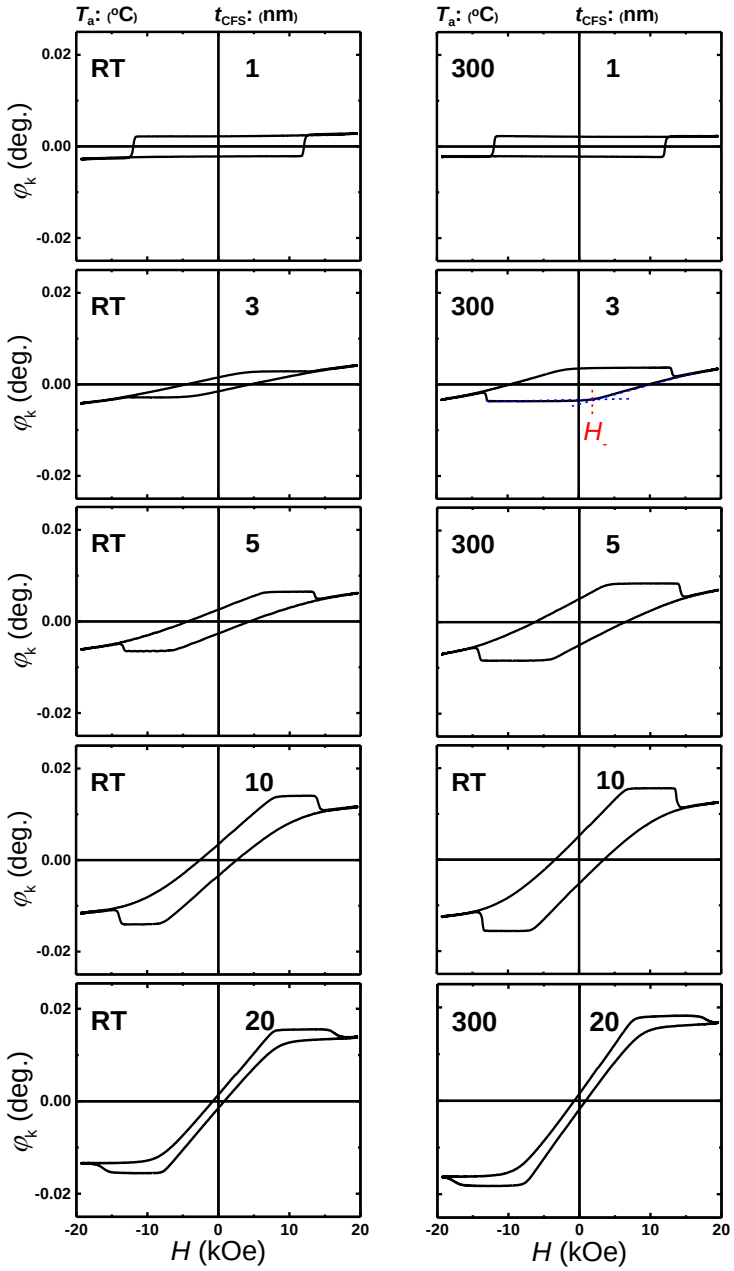

Figure 4-19 The typical polar Kerr rotation angle versus the applied field of CFS (1-20 nm)/MnGa (30 nm) bilayers for un-annealed samples and annealed samples at 300ºC.

The t_{CFS} dependence of $M \times t_{(0\ kOe)}$ and H_{sw} for un-annealed samples and samples annealed at 300ºC are shown in Fig. 4-20 (b) and (c), respectively. The $M \times t_{(0\ kOe)}$ and H_{sw} of 30-nm-thick MnGa plotted with dashed line for comparison. As can be seen from Fig. 4-20(b), $M \times t_{(0\ kOe)}$ of un-annealed bilayer film with 1 nm CFS is larger than value of 30-nm-thick MnGa film. Then $M \times t_{(0\ kOe)}$ decreases linearly as CFS thickness increase up to 5 nm. By further increasing of CFS thickness, the $M \times t_{(0\ kOe)}$ value increases and then saturated for thicker CFS film. However, both series samples show, the H_{sw} increases linearly with increasing of thickness.

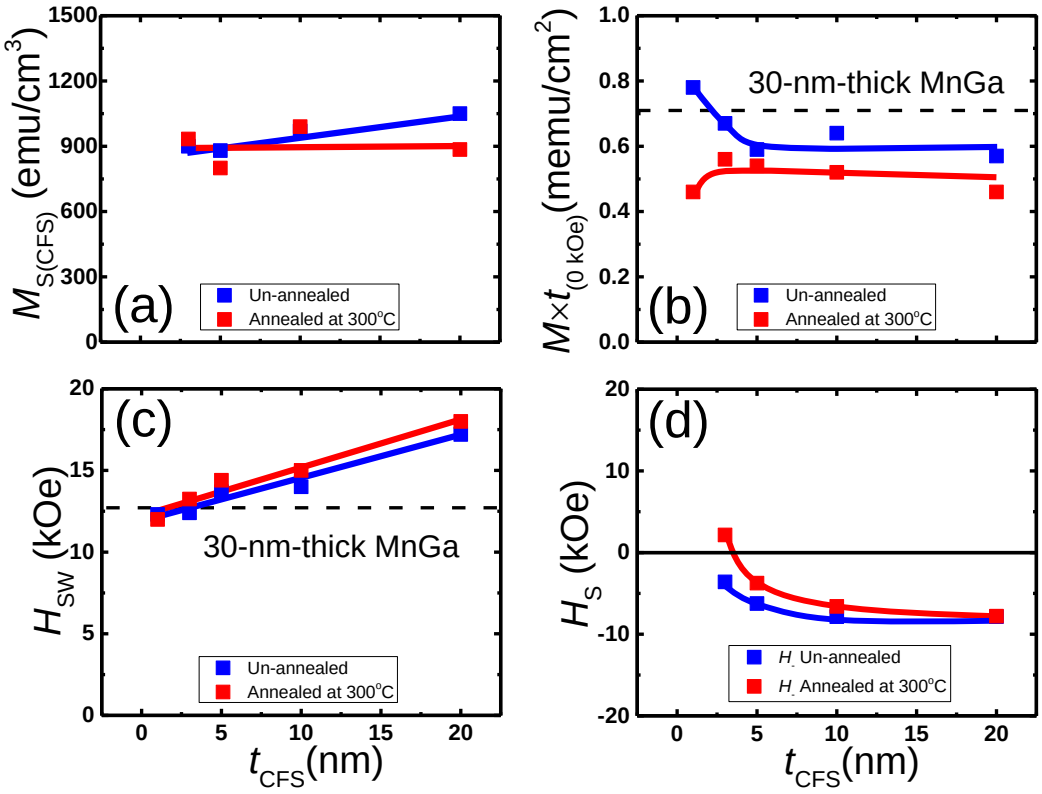

Figure 4-20 (a) The CFS thickness dependence of saturation magnetization for CFS film. (b) The CFS thickness dependence of remnant magnetization, (c) switching and (d) saturation fields for CFS (1-20 nm)/MnGa (30 nm) bilayer films.

The t_{CFS} dependence of H_+ for un-annealed samples and samples annealed at 300ºC are shown in Fig. 4-20 (d). The t_{CFS} dependence of H_+ show positive value for the annealed sample with 3 nm CFS film. As we can see from MOKE result this sample show very good PMA properties. On the other hand for the un-annealed sample PMA obtained for 1 nm thick CFS

film. The larger thickness of annealed sample for remaining PMA compared to un-annealed sample attributed to stronger antiferromagnetic exchange coupling of annealed samples.

A short summary will be presented here. We investigated the effect of CFS thickness on the structural and magnetic properties of un-annealed samples and samples annealed at 300ºC for CFS (1-20 nm)/$D0_{22}$MnGa (30 nm) bilayer films. The annealed samples and samples annealed at 300ºC show the critical thickness to remaining PMA less than 3 and 5 nm, respectively.

4.5 Annealing Temperature Dependence of Co_2MnAl (20 nm)/$D0_{22}$-MnGa (30 nm) Bilayer

The structural and magnetic properties of Co_2MnAl (CMA)/ $D0_{22}$-MnGa have been investigated in this section. To investigate post annealing influence nine samples at different post annealing temperature with the stacking structure of (100) single crystalline MgO substrate / Cr(10) / $D0_{22}$-MnGa (30) / CMA (20) / Cr(5) (thickness is in nanometers) have been fabricated. The epitaxial bilayers were fabricated using an ultrahigh vacuum magnetron sputtering system with a base pressure of less than 1×10^{-7} Pa. All the layers were deposited at room temperature. The in-situ annealing was employed at 400ºC after the MnGa deposition. Annealing temperature dependence has been investigated using post annealing by RTA system. In addition, the 30 (20)-nm-thick MnGa (CMA) films with the same stacking structure without CMA (MnGa) films were fabricated as reference films. Film compositions of Mn-Ga and CMA alloy were $Mn_{70}Ga_{30}$ and $Co_{46}Mn_{24}Al_{30}$ estimated by the inductively coupled plasma spectroscopy respectively. For characterization of structural and magnetic properties, the X-ray diffractometer (XRD) with the Cu Kα radiation, polar magneto optical Kerr effect (P-MOKE) system at laser wavelength of 400 nm, and a vibrating sample magnetometer (VSM) were used.

4.5.1 Structural Properties

4.5.1.1 XRD

The out-of-plane XRD patterns of CMA/MnGa bilayers for different annealing temperatures are shown in Fig. 4-21 (a). The peaks (002) and (004) of MnGa and CMA films

corresponding to $D0_{22}$ and B2 structures of MnGa and CMA are clearly observed even for un-annealed sample.

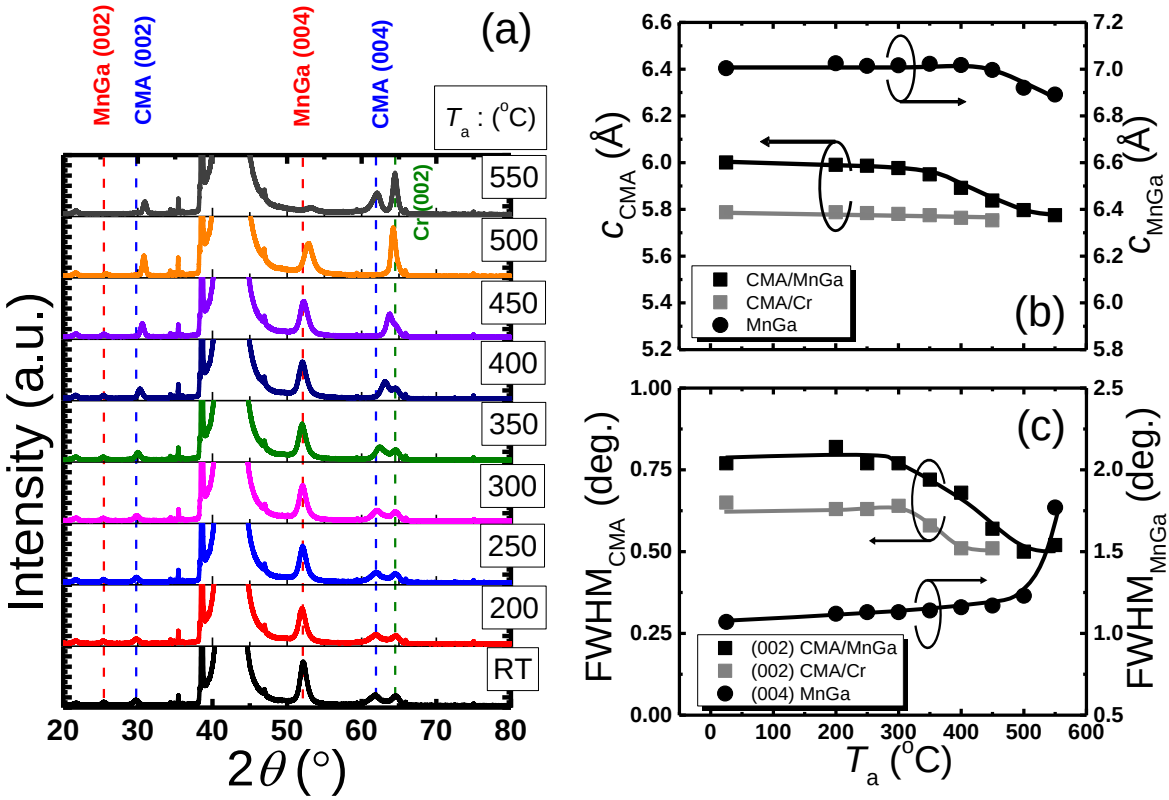

Figure 4-21 (a) The XRD pattern of CMA/MnGa bilayers for un-annealed sample and annealed samples at 200, 250, 300, 350, 400, 450, 500 and 550ºC. (b) The annealing temperature dependence of *c* lattice constant and (c) FWHM for CMA and MnGa films.

Fig. 4-21(b) show the annealing temperature dependence of the *c* lattice constant of MnGa and CMA of bilayer films (CMA/MnGa), and also CMA of reference films (CMA/Cr). The *c* lattice constant of MnGa is constant and very close to value of the reference MnGa films (7.00 Å) for the un-annealed sample and samples annealed at 200 up to 450ºC. The *c* lattice constant of MnGa reduces after annealing sample at 500 and 550ºC. This shows very good structure stability. As can be seen clearly in Fig. 4-21 (a), the CMA/MnGa bilayer film annealed at 550ºC has a broad (004) peak of MnGa and its position also changes. In addition, another peak appears close to Cr peak may come from CMA-MnGa alloy because of inter diffusion effect. The *c* lattice constant of CMA bilayer films did not change with increasing T_a up to 300ºC. Then, the

c lattice constant reduces and reaches to around bulk value (about 5.69 Å).[57] However, the *c* lattice constant of CMA on Cr is constant and close to bulk value. For the CMA/MnGa bilayer an expansion of the *c* lattice constant in the out-of-plane direction for better matching of the CMA film to the MnGa layer was observed same as CFA/MnGa and CFS/MnGa bilayer.

The annealing temperature dependence of the FWHM for the MnGa, CMA/MnGa and CMA/Cr films are shown in Fig. 4-21(c). FWHM for CMA/MnGa and CMA/Cr is constant and then decrease after annealing at 300ºC which means the quality of CMA film on MnGa and Cr are improving at high annealing temperature regime. The FWHM for the MnGa increases monotonically with increasing T_a up to 500ºC and then a drastic increasing of FWHM was observed for the sample annealed at 550ºC because of inter diffusion effect.

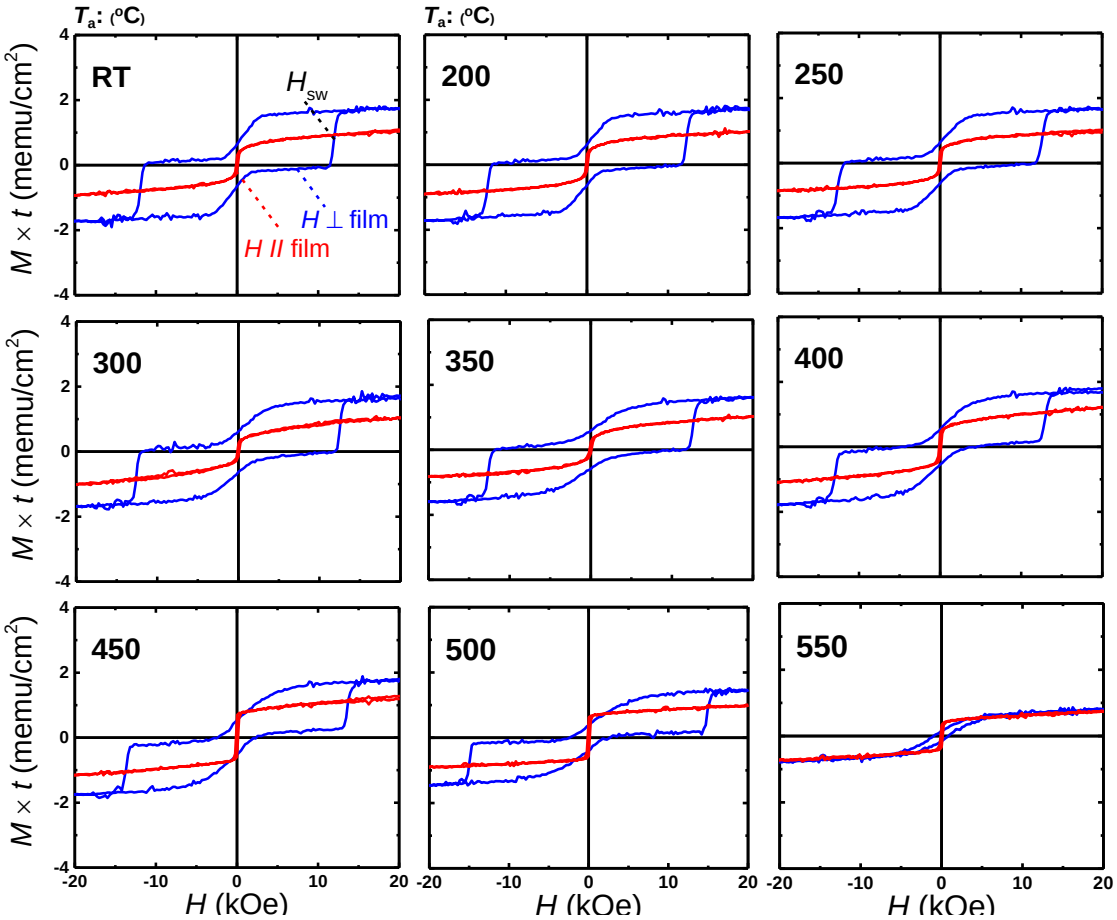

Figure 4-22 The typical out-of plane (blue colour) and in-plane (red colour) VSM *M-H* loops of CMA (20 nm)/MnGa (30 nm) bilayers for un-annealed sample and annealed samples at 200, 250, 300, 350, 400, 450, 500 and 550ºC.

4.5.2 Magnetic Properties

4.5.2.1 VSM

The typical out-of-plane and in-plane *M-H* loops measured by VSM system for the CMA (20 nm)/MnGa (30 nm) bilayer film for un-annealed sample and samples annealed at 200, 250, 300, 350, 400, 450, 500 and 550ºC are shown in Fig. 4-22. The 30-nm-thick MnGa and 20-nm-thick CMA films show the hard and soft magnetic properties, respectively. *M-H* loop of un-annealed sample and samples annealed at 200 up to 500ºC show summation of *M-H* loops of CMA and MnGa films with antiferromagnetic exchange coupling between CMA film and MnGa layer. By further annealing at 550ºC magnetic property of CMA/MnGa bilayer completely change from PMA to IMA which is consistent with XRD result because of inter diffusion effect.

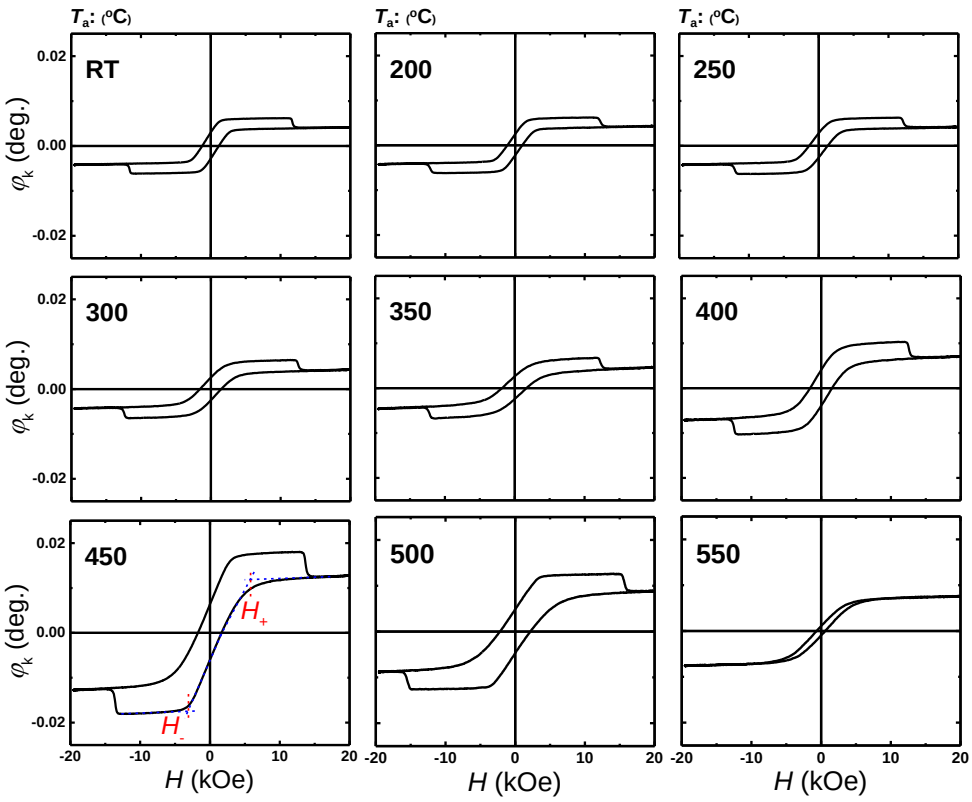

Figure 4-23 The typical polar Kerr rotation angle versus the applied field of CMA (20 nm)/MnGa (30 nm) bilayers for un-annealed sample and annealed samples at 200, 250, 300, 350, 400, 450, 500 and 550ºC.

4.5.2.2 MOKE

In Fig. 4-23 the typical polar Kerr rotation angle versus the applied field of CMA (20 nm)/MnGa (30 nm) bilayers for un-annealed sample and annealed samples at 200, 250, 300, 350, 400, 450, 500 and 550ºC are shown. MOKE measurement is consistent with VSM result. The same switching field, H_+ and H_- were observed in this measurement. Same as CMA/MnGa bilayer different shape was observed for MOKE measurement compared to VSM measurement which originates from reflectance phase difference of the light at interface of bilayers in the MOKE measurement. Un-annealed sample and samples annealed at 200 up to 500ºC show roughly same hysteresis loops but, Kerr rotation angle increases with increasing $T_{a.}$ Finally PMA property changes to IMA for the sample annealed at 550 ºC. The details of VSM and MOKE results will be discussed in the next section.

4.5.3 Discussion and Summary

Fig. 4-24 (a) shows the T_a dependence of saturation magnetization which is estimated from out-of-plane *M-H* loop for the CMA/MnGa and CMA/Cr films. The saturation magnetization of CMA/Cr film is constant with increasing T_a up to 400ºC and then small enhancement was observed for the film annealed at 400ºC. This enhancement is comes from crystallization and smaller FWHM at high temperature annealing. However, the saturation magnetization of CMA/MnGa film increases to maximum value for the sample annealed at 450ºC and then drastically reduces after annealing at 500, and 550ºC which is consistent with XRD result. As is shown in XRD pattern structure of CMA/MnGa start to change for the samples annealed at 500 and 550ºC which is attributed to inter diffusion effect. The value of saturation magnetization of CMA/MnGa bilayer is close to CMA/Cr. These values are smaller than balk value (about 700 emu/cm^3) but comparable with those films fabricated on MgO as substrate and buffer layer.[58] The T_a dependence of $M\times t_{(0\ kOe)}$ and H_{sw} are shown in Fig. 4-24 (b) and (c), respectively. The $M\times t_{(0\ kOe)}$ and H_{sw} of 30-nm-thick MnGa plotted with dashed line for comparison. As can be seen from Fig. 4-24 (b), $M\times t_{(0\ kOe)}$ of un-annealed bilayer film is smaller than values of 30-nm-thick-MnGa film and then decreases monotonically with increasing T_a up to 450ºC. By further T_a, $M\times t_{(0\ kOe)}$ drastically reduces for the sample annealed at 500 and 550ºC which is due to intermixing at the interfaces of CMA and MnGa. T_a dependence of H_{sw} shows the value increases to maximum value at 500ºC and then very small H_{sw} was observed for the sample annealed at 550ºC due to IMA property. The smaller and larger $M\times t_{(0\ kOe)}$ and

H_{sw} compared to 30-nm-thick MnGa suggested antiferromagnetic exchange coupling between CMA film and MnGa layer same as CFS/MnGa bilayer.

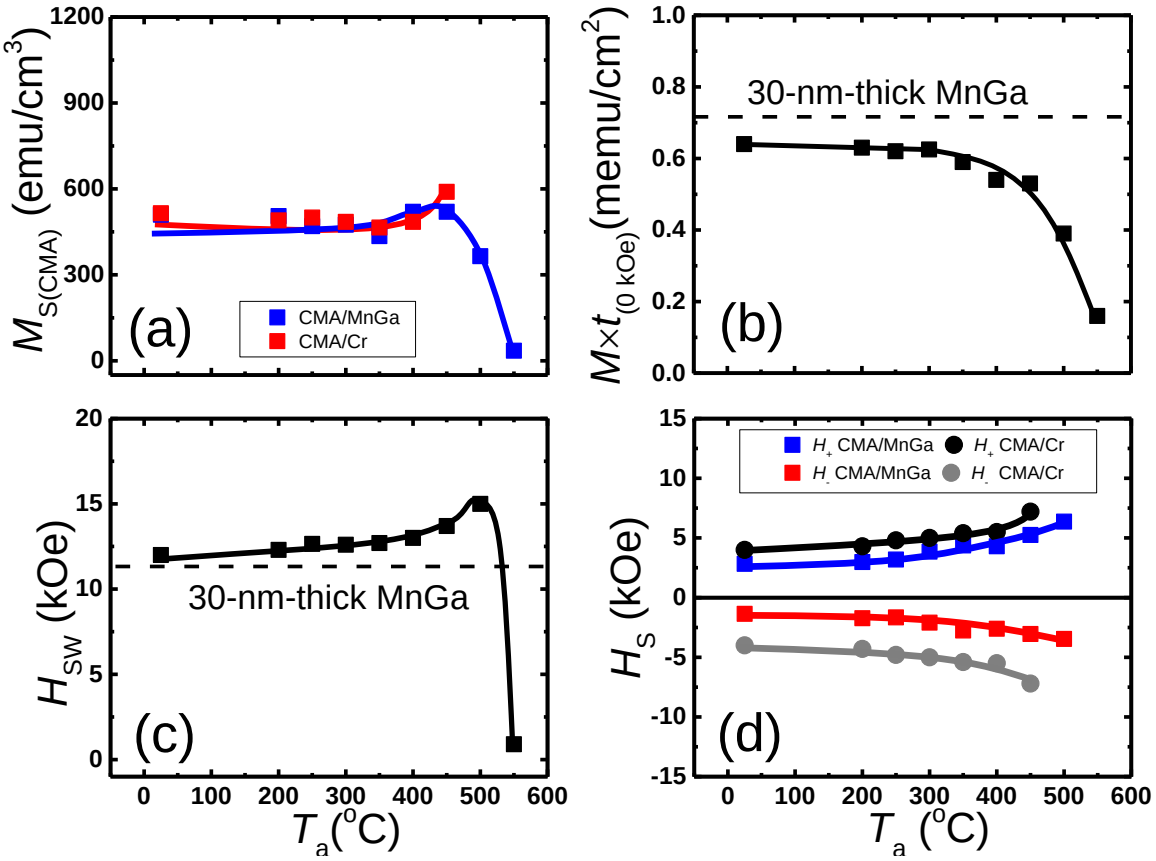

Figure 4-24 (a) The annealing temperature dependence of saturation magnetization for CMA film. (b) The annealing temperature dependence of remnant magnetization, (c) switching and (d) saturation fields for CMA (20 nm)/MnGa (30 nm) bilayer film.

Fig. 4-24 (d) shows the T_a dependence of H_+ and H_- for CMA films on MnGa and Cr layers. As can be seen from this figure, H_+ and H_- for CMA films on Cr layers show a symmetry regard to x axis, as we expect for the no exchange coupling case, whereas for the CMA films on MnGa an asymmetry clearly was observed which is due to exchange coupling between MnGa and CFS films. In addition, H_+ is larger than absolute value of H_- . Therefore exchange coupling constant should be antiferromagnetic. It seems by increasing annealing temperature difference of H_+ and absolute value of H_- is increasing which suggested stronger antiferromagnetic coupling at high temperature regime. Fig. 4-25 shows T_a dependence of the interfacial exchange coupling constant. The J_{ex} value was -0.75 erg/cm^2 without post annealing. With increasing annealing temperature, the absolute value of J_{ex} increased up to about 1.15 erg/cm^2

for sample annealed at 450ºC. The absolute values of negative J_{ex} is relatively smaller than those evaluated in the Co-Fe/Mn-Ga bilayers.[37] The annealing temperature dependence of the interfacial exchange coupling in the CMA/MnGa bilayer could be interpreted by the interface structure changes at high annealing temperature, as can be seen from XRD measurement results. Firstly, at high temperature *c* lattice constant of CMA film is close to reference film and bulk values. Secondly, Ta dependence of FWHM indicates quality of CMA film at high temperature is better. So crystallization of CMA film on MnGa is reason of stronger coupling at high temperature annealing.

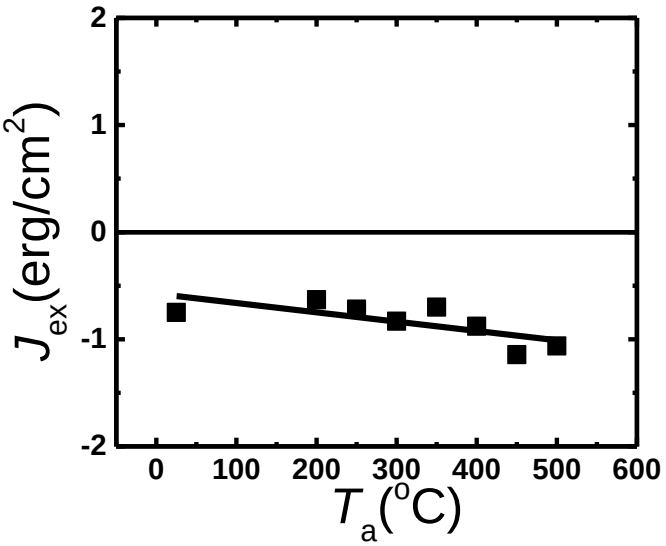

Figure 4-25 The annealing temperature dependence of interfacial exchange coupling constant CMA (20 nm)/MnGa (30 nm) bilayer film.

A short summary will be presented here. We investigated the influence of annealing temperature on the structural and magnetic properties of CMA (20 nm)/$D0_{22}$-MnGa (30 nm) bilayer films. The bilayer films have been successfully grown. The optimized annealing temperature was 450ºC. The CMA (20 nm)/$D0_{22}$-MnGa (30 nm) bilayer film show good structure stability. We evaluated the interfacial exchange coupling constant for the bilayers with different annealing temperature. The antiferromagnetic interfacial exchange coupling was observed. The antiferromagnetic coupling strength (J_{ex} = -0.75 ~ -1.15 erg/cm^2) was larger than CoB (20 nm)/$D0_{22}$-MnGa (30 nm) bilayer film and comparable with CFA (20 nm)/$D0_{22}$-MnGa CFS (20 nm)/$D0_{22}$-MnGa (30 nm) bilayer film.

4.6 Thickness Dependence of $CoMn_2Al$ (t_{CMA})/$D0_{22}$-MnGa (30 nm) Bilayer

Two series samples without post annealing and with post annealing at 450ºC by RTA system with different CMA thicknesses of 1, 3, 5, 10 and 20 nm were prepared by using an ultrahigh vacuum magnetron sputtering system with a base pressure of less than 1×10^{-7} Pa. The stacking structure of each series were: the (100) single crystalline MgO substrate / Cr (10) / $D0_{22}$-MnGa (30) / CMA (t_{CMA}) / Cr (5) (thickness is in nanometers) All the layers were deposited at room temperature. The in-situ annealing was employed at 400ºC after the MnGa deposition. For characterization of structural and magnetic properties, the X-ray diffractometer (XRD) with the Cu K_α radiation, polar magneto optical Kerr effect (P-MOKE) system at laser wavelength of 400 nm, and a vibrating sample magnetometer (VSM) were used.

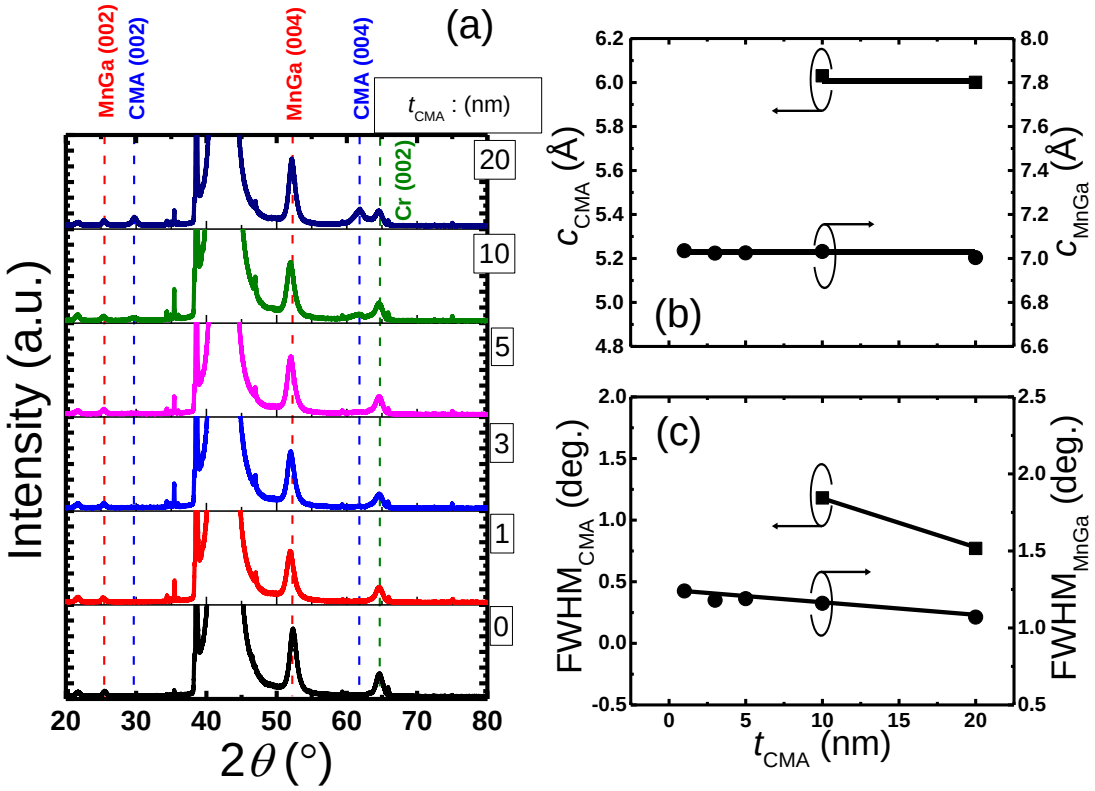

Figure 4-26 (a) The XRD pattern of CMA (0-20 nm)/MnGa (30 nm) bilayers for the un-annealed samples. (b) The CMA thickness dependence of *c* lattice constant and (c) FWHM for CMA and MnGa films.

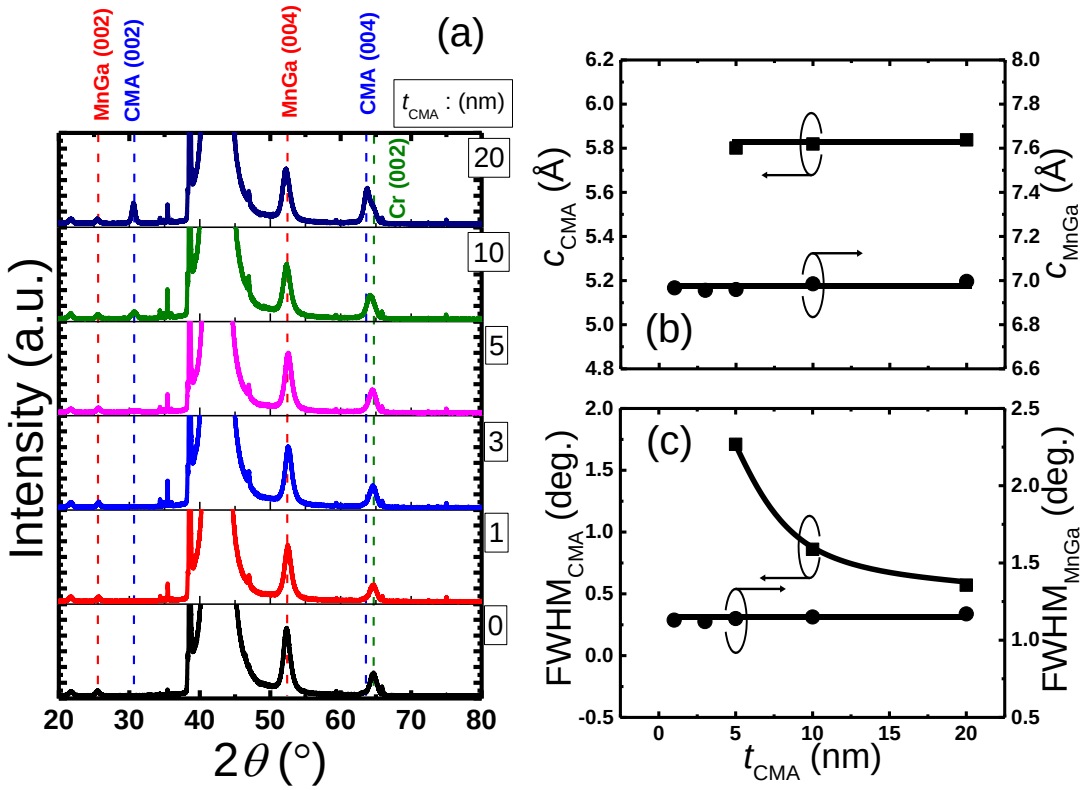

Figure 4-27 (a) The XRD pattern of CMA (0-20 nm)/MnGa (30 nm) bilayers for the samples annealed at 450ºC. (b) The CMA thickness dependence of *c* lattice constant and (c) FWHM for CMA and MnGa films.

4.6.1 Structural Properties

4.6.1.1 XRD

The XRD pattern of CMA (0-20 nm)/MnGa (30 nm) bilayers for the un-annealed samples and samples annealed at 450ºC are shown in Fig 4-26 (a) and 4-27 (a), respectively. The peaks of MnGa (002), and (004) corresponding to tetragonal structure of $D0_{22}$-MnGa are clearly observed in both series samples. The minimum thickness to see (002) peak of B2 structure of CMA film in XRD pattern is 10 and 5 nm for un-annealed samples and samples annealed at 450ºC, respectively. This indicates quality of film after annealing is improving. The t_{CMA} dependence of the *c* lattice constant of MnGa and CMA films without and with post annealing are shown in Fig 4-26 (b) and 4-27 (b), respectively. The *c* lattice constant of MnGa film is constant with increasing CMA thickness for both series samples and very close to value of the reference MnGa film (7.00 Å). The *c* lattice constant of CMA film is also constant with

increasing t_{CMA} for both series samples. However, the *c* lattice constant of CMA film for with post annealing is smaller than CMA film without post annealing.

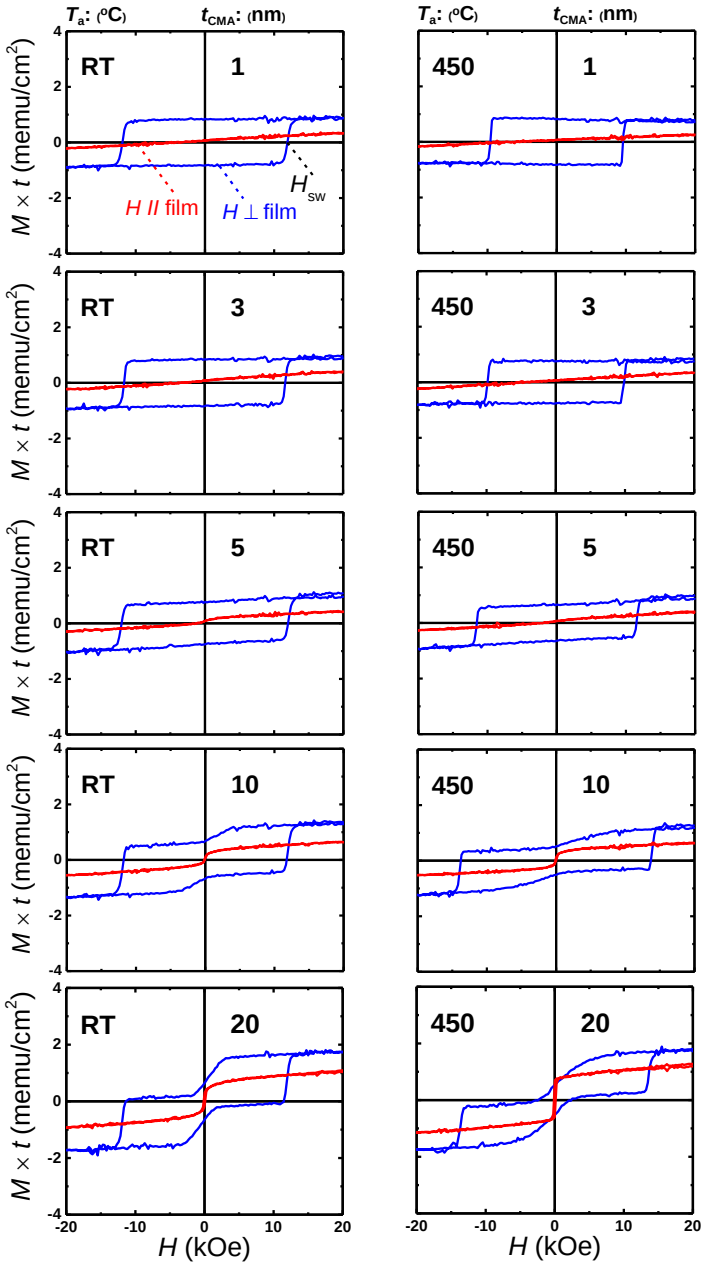

Figure 4-28 The typical out-of plane (blue colour) and in-plane (red colour) VSM *M*-*H* loops of CMA (1-20 nm)/MnGa (30 nm) bilayers for un-annealed samples and annealed samples at 450°C.

The t_{CMA} dependence of the FWHM (004) peak of MnGa and (002) peak of CMA films without and with post annealing are shown in Fig 4-26(c) and 4-27(c). The FWHM of MnGa

and CMA peaks of un-annealed samples decrease linearly with increasing thickness of CMA film which suggested better quality of CMA with thicker CMA film. On the other hand, the FWHM of MnGa peak of annealed samples is constant, whereas a nonlinear reduction was observed for FWHM of CMA peak.

4.6.2 Magnetic Properties

4.6.2.1 VSM

The typical out-of plane and in-plane VSM *M-H* loops of CMA (1-20 nm)/MnGa (30 nm) bilayers for un-annealed samples and samples annealed at 300ºC are shown in Fig. 4-28. The un-annealed sample and sample annealed at 450ºC with 1and 3 nm CMA thickness show similar *M-H* loop shape, but different values of $M \times t_{(0\ \mathrm{kOe})}$ and H_{sw} compared to with 30-nm-thick MnGa. With increasing CMA thickness up to 5 nm no in-plane component were observed for both series samples which is consistent with XRD result. The shape of *M-H* loops of 10 and 20 nm thick CMA films for both un-annealed and annealed samples have changed. The in plane component of Magnetization increases for thicker CMA film.

4.6.2.2 MOKE

To clarify magnetization process of CMA film and MnGa layer all the sample have been measured by MOKE system. The typical polar Kerr rotation angle versus the applied magnetic field of CMA (1-20 nm)/MnGa (30 nm) bilayers for un-annealed samples and annealed samples at 450ºC are shown in Fig. 4-19. The Un-annealed bilayer film with 1 and 3 nm CMA thickness show flat MOKE hysteresis loop with good squareness. These samples show good PMA properties which means magnetization of CMA film coupled fully perpendicular to magnetization of MnGa film. As CMA thickness increases, magnetization of CMA start to tilt from perpendicular to in-plane direction because of large in-plane component for thicker CMA film. The inverted MOKE hysteresis loops were observed when thickness of CFS film is larger than 3 nm. The antiferromagnetic exchange coupling constant might be reason of the inverted MOKE hysteresis loops.

4.6.3 Discussion and Summary

Fig. 4-30 (a) shows the t_{CMA} dependence of saturation magnetization of CMA layer which is estimated from out-of-plane *M-H* loop of CFS/MnGa bilayer film. The average saturation

magnetization value of CMA for un-annealed samples are about annealed samples 570 and 470 emu/cm^3 which is comparable those films fabricated on MgO as substrate and buffer layer.[58]

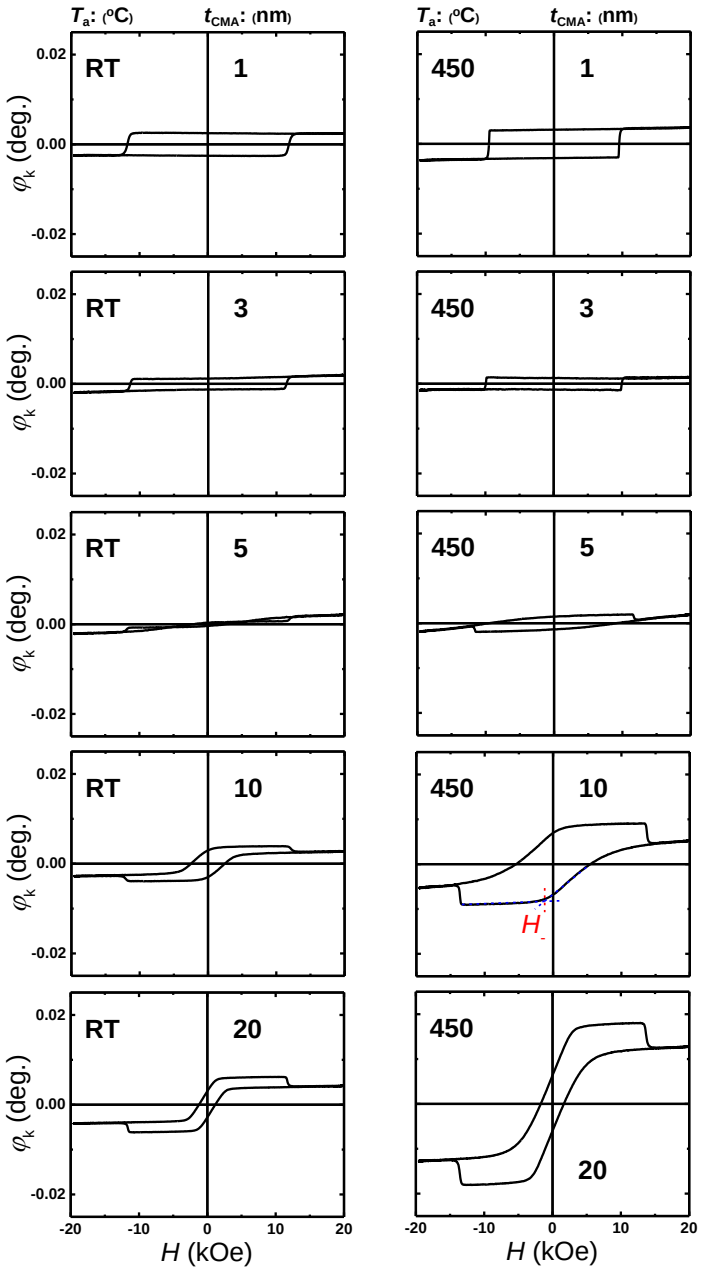

Figure 4-29 The typical polar Kerr rotation angle versus the applied field of CMA (1-20 nm)/MnGa (30 nm) bilayers for un-annealed samples and annealed samples at 450°C.

The t_{CMA} dependence of $M \times t_{(0\ kOe)}$ and H_{sw} for un-annealed samples and samples annealed at 450°C are shown in Fig. 4-30 (b) and (c), respectively. The $M \times t_{(0\ kOe)}$ and H_{sw} of 30-nm-thick MnGa plotted with dashed line for comparison. As can be seen from Fig. 4-30(b), the

t_{CMA} dependence of the $M \times t_{(0\ kOe)}$ value of un-annealed samples and samples annealed at 450ºC show similar behaviors. The $M \times t_{(0\ kOe)}$ value linearly decreases as CMA thickness increase up to 10 nm and then saturated for 10 and 20 nm thicknesses of CMA films. The reduction of the $M \times t_{(0\ kOe)}$ for annealed samples is more rapidly compared to un-annealed samples. In addition the smaller $M \times t_{(0\ kOe)}$ value was observed for samples annealed at 450ºC. The t_{CMA} dependence of H_{sw} show constant value for un-annealed samples whereas for the samples annealed at 450ºC opposite trend with the t_{CMA} dependence of $M \times t_{(0\ kOe)}$ was observed.

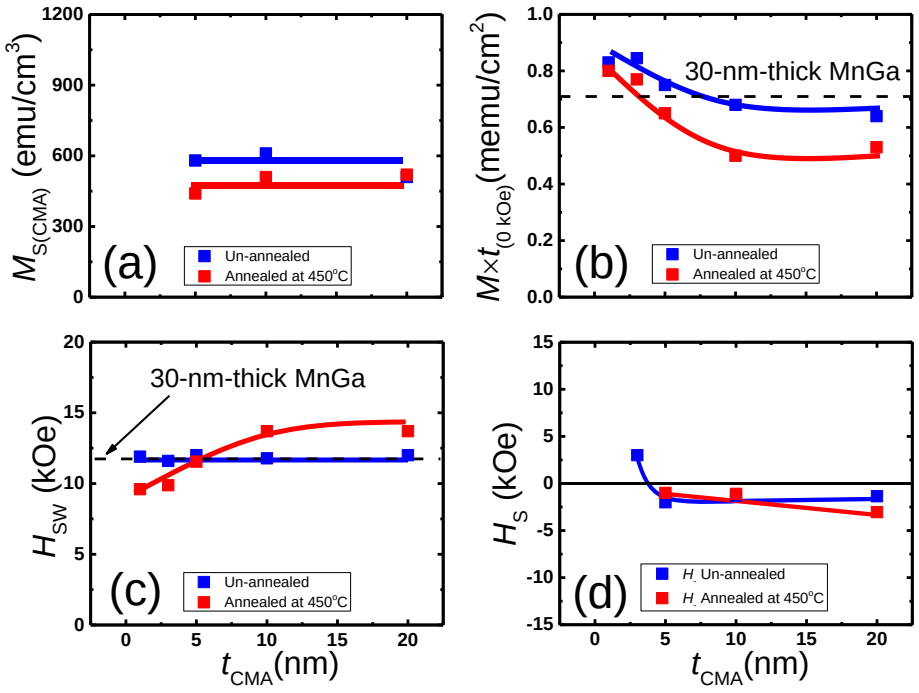

Figure 4-30 (a) The CMA thickness dependence of saturation magnetization for CMA film. (b) The CMA thickness dependence of remnant magnetization, (c) switching and (d) saturation fields for CMA (1-20 nm)/MnGa (30 nm) bilayer films.

The t_{CMA} dependence of H_+ for un-annealed samples and samples annealed at 450ºC are shown in Fig. 4-30 (d). The t_{CMA} dependence of H_+ show positive value for the un-annealed sample with 3 nm CMA film. As we can see from MOKE result this sample show good PMA property. After annealing an enhancement of PMA property was observed for 3 nm thick CMA film.

A short summary will be presented here. We investigated the effect of CMA thickness on the structural and magnetic properties of un-annealed samples and samples annealed at 300ºC for CMA (1-20 nm)/$D0_{22}$MnGa (30 nm) bilayer films. The annealed samples and samples annealed at 450ºC show the critical thickness to remaining PMA less than 5 nm.

4.7 Annealing Temperature Dependence of Co_2MnSi (20 nm)/$D0_{22}$-MnGa (30 nm) Bilayer

To investigate structural and magnetic properties of Co_2MnSi (CMS)/ $D0_{22}$-MnGa seven samples at different post annealing temperature with the stacking structure of (100) single crystalline MgO substrate / Cr(10) / $D0_{22}$-MnGa (30) / CMS (20) / Cr(5) (thickness is in nanometers) have been fabricated. The epitaxial bilayers were fabricated using an ultrahigh vacuum magnetron sputtering system with a base pressure of less than 1×10^{-7} Pa. All the layers were deposited at room temperature. The in-situ annealing was employed at 400ºC after the MnGa deposition. Annealing temperature dependence has been investigated using post annealing by RTA system. In addition, the 30 (20)-nm-thick Mn-Ga (CMS) films with the same stacking structure without CMS (MnGa) films were fabricated as reference films. Film compositions of MnGa and CMS alloy were $Mn_{70}Ga_{30}$ and $Co_{47}Mn_{25}Si_{30}$ estimated by the inductively coupled plasma spectroscopy respectively. For characterization of structural the X-ray diffractometer (XRD) with the Cu Kα radiation and high-resolution transmission electron microscope (HRTEM), and for characterization of magnetic properties, magneto optical Kerr effect (P-MOKE) system at laser wavelength of 400 nm, and a vibrating sample magnetometer (VSM) were used.

4.7.1 Structural Properties

4.7.1.1 XRD

The out-of-plane XRD patterns of CMS/MnGa bilayers for different T_a are shown in Fig. 4-31 (a). The peaks of MnGa (002), (004), and CMS (002) corresponding to $D0_{22}$ and $L2_1$ structures of MnGa and CMS are clearly observed even for un-annealed sample. This indicates the good epitaxy of CMS on MnGa film. In addition these peaks, the (004) peak of CMS film was observed which has overlap with the Cr peak. The annealing temperature dependence of

the *c* lattice constant of MnGa and CMS of bilayer films (CMS/MnGa), and also CMS of reference films (CMS/Cr) are shown in Fig. 4-31 (b). The *c* lattice constant of MnGa is constant and very close to value of the reference MnGa films (7.00 Å) for the un-annealed sample and samples annealed at 200 up to 400ºC. The *c* lattice constant of MnGa drastically reduces after annealing sample at 450ºC. For the *c* lattice constant of the CMS bilayer films the opposite behaviours were observed. These changes are attributed to inter diffusion effect at high annealing temperature regime. As can be seen clearly in Fig. 4-31 (a), the CMS/MnGa bilayer film annealed at 450ºC have broad (002) and (004) peaks of MnGa and their positions also change. By further annealing temperature we expect structure of MnGa completely change from tetragonal MnGa to cubic MnGa.

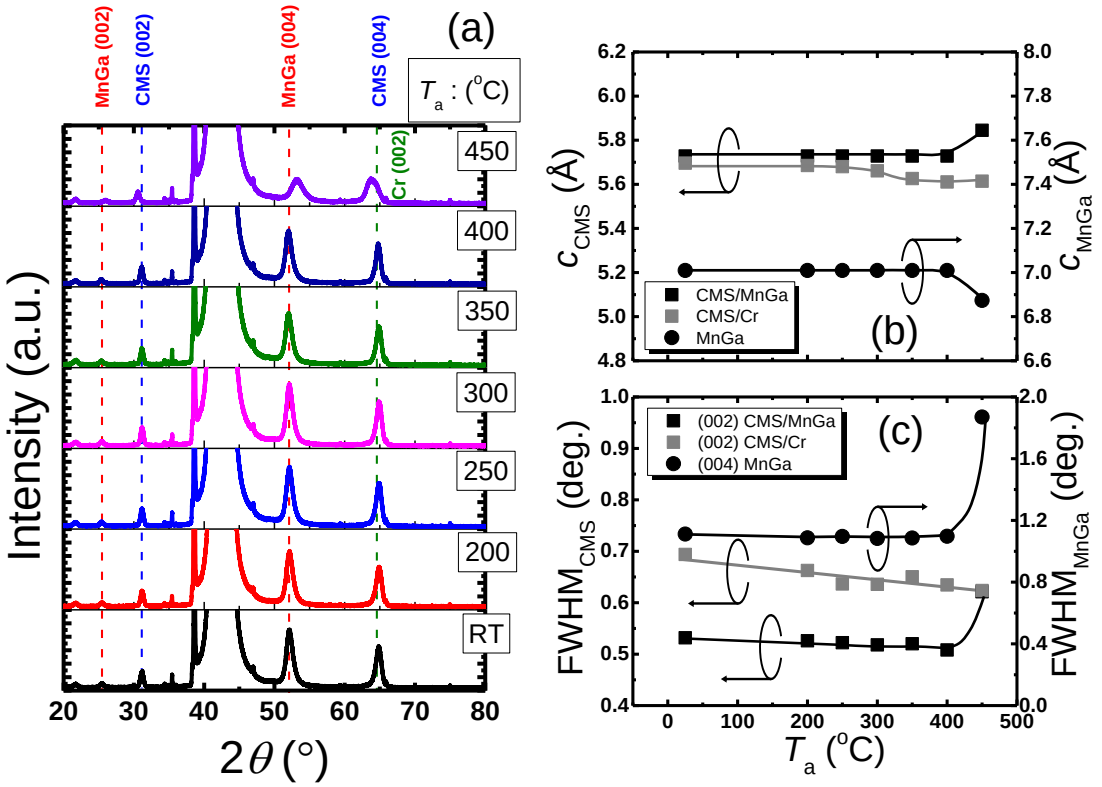

Figure 4-31 (a) The XRD pattern of CMS/MnGa bilayers for un-annealed sample and annealed samples at 200, 250, 300, 350, 400, and 450ºC. (b) The annealing temperature dependence of *c* lattice constant and (c) FWHM for CMS and MnGa films.

The *c* lattice constant of CMS reference films show a decrease after annealing at 300ºC and then it is roughly constant and very close to bulk value[59] about 5.65 Å due to crystallization of CMS on Cr at high annealing temperature. Difference between *c* lattice constant of CMS

bilayer and reference films show an expansion of the *c* lattice constant in the out-of-plane direction for better matching of the CMS layer to the MnGa layer.

The annealing temperature dependence of the FWHM for the MnGa, CMS/MnGa and CMS/Cr films are shown in Fig. 4-31(c). The FWHM for CMS/Cr decreases linearly which indicates improving of quality of film at high annealing temperature because of crystallization. The same behaviours were observed for MnGa and CMS/MnGa films, but the FWHM drastically increase after annealing temperature at 400ºC because of inter diffusion effect. The smaller FWHM for CMS/MnGa compared to CMS/Cr indicates the quality of the CMS film on MnGa layer is better than the CMS film on Cr layer.

4.7.1.2 HRTEM

A cross-sectional HRTEM image and nanobeam electron diffraction of sample annealed at 400°C are shown in Fig. 4-32 (a) and (b), respectively. This image clearly shows that all the layers of the CMS/MnGa bilayer were grown epitaxially and were single crystalline. Furthermore, nanobeam electron diffraction patterns with a beam diameter of 1 nm for CMS film showed 111 and 222 spots, indicating the $L2_1$ ordered structure.

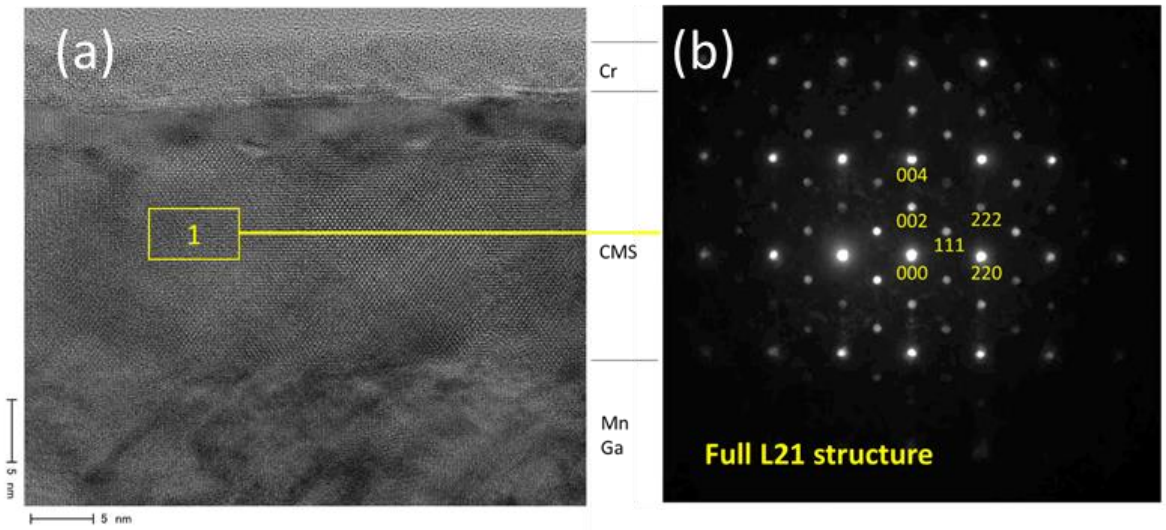

Figure 4-32 (a) A cross-sectional HRTEM image and (b) nanobeam electron diffraction (spot size 1 nm) of sample annealed at 400°C.

4.7.2 Magnetic Properties

4.7.2.1 VSM

The typical out-of-plane and in-plane *M-H* loops measured by VSM system for the CMS (20 nm)/MnGa (30 nm) bilayer film for un-annealed sample and samples annealed at 200, 250, 300, 350, 400, and 450ºC are shown in Fig. 4-33. The 30-nm-thick MnGa and 20-nm-thick CMS films show the hard and soft magnetic properties, respectively. *M-H* loop of un-annealed sample and samples annealed at 200 up to 400ºC show summation of *M-H* loops of CMS and MnGa films with antiferromagnetic exchange coupling between CMS film and MnGa layer. By further annealing at 450ºC the inverted *M-H* loop was observed. This inverted *M-H* loop is evidence of existence of antiferromagnetic exchange coupling between CMS and MnGa films. Such anomalous hysteresis has been observed for inhomogeneous films and antiferromagnetically coupled bilayer films. [60–62] However, the structure has changed due to mixing in the interfaces of CMS and MnGa as shown in XRD pattern.

4.7.2.2 MOKE

In Fig. 4-34 the typical polar Kerr rotation angle versus the applied field of CMS (20 nm)/MnGa (30 nm) bilayers for un-annealed sample and annealed samples at 200, 250, 300, 350, 400, 450, 500 and 550ºC are shown. MOKE measurement is consistent with VSM result. The same switching field, H_+ and H_- were observed in this measurement. Same as CFA, CFS and CMA studies, different shape was observed for MOKE measurement compared to VSM measurement which originates from reflectance phase difference of the light at interface of bilayers in the MOKE measurement. Un-annealed sample and samples annealed at 200 up to 400ºC show roughly same hysteresis loops, however, the Kerr rotation angle increases for the sample annealed at 400ºC. This comes from better crystallization at high temperature. Finally for the sample annealed at 450 ºC very good PMA was observed. The details of VSM and MOKE results will be discussed in the next section.

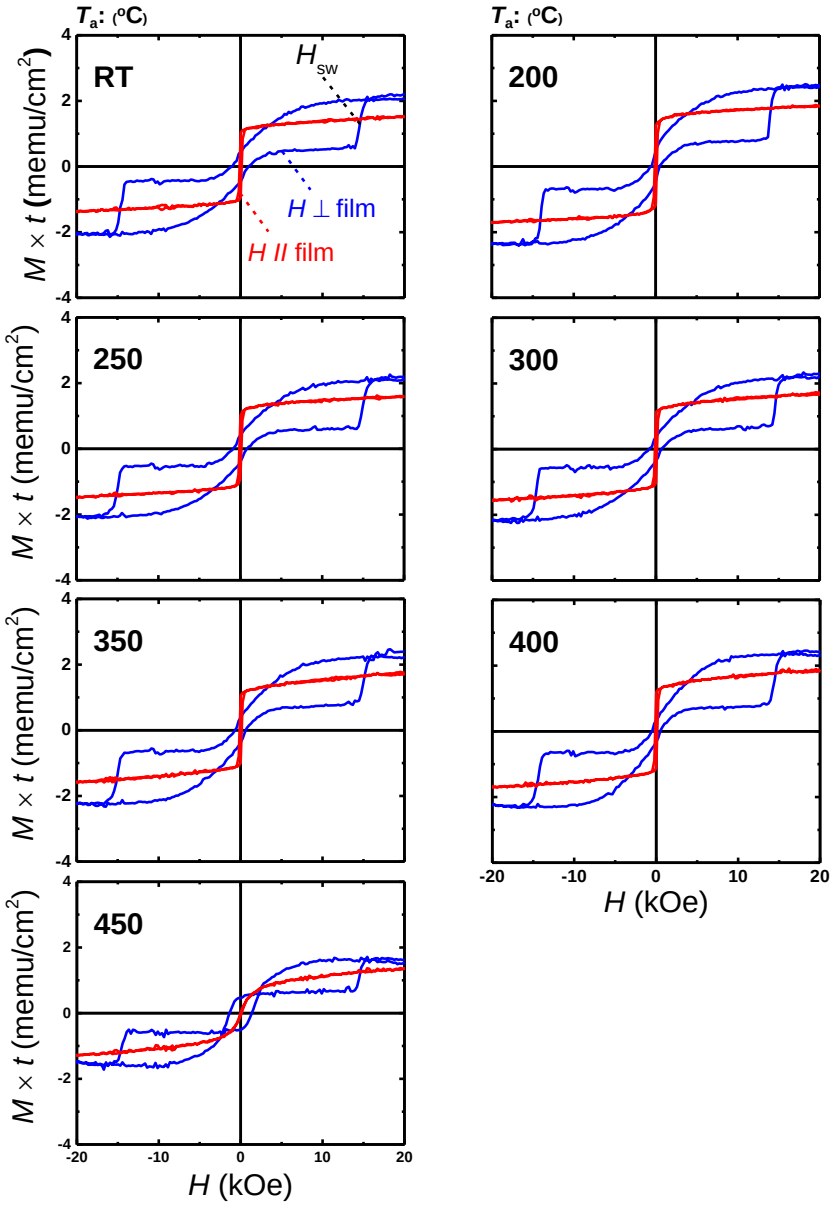

Figure 4-33 The typical out-of plane (blue colour) and in-plane (red colour) VSM *M-H* loops of CMS (20 nm)/MnGa (30 nm) bilayers for un-annealed sample and annealed samples at 200, 250, 300, 350, 400 and 450°C.

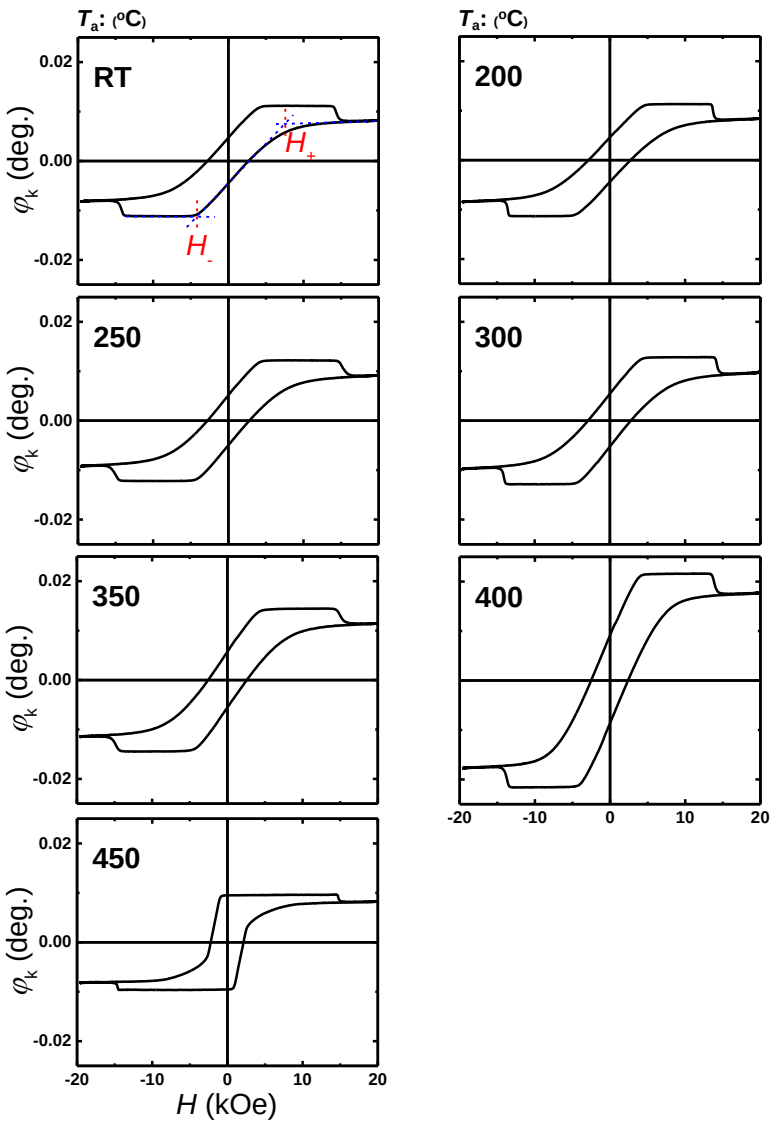

Figure 4-34 The typical polar Kerr rotation angle versus the applied field of CMS (20 nm)/MnGa (30 nm) bilayers for un-annealed sample and annealed samples at 200, 250, 300, 350, 400, and 450°C.

4.7.1 Discussion and summary

Fig. 4-35(a) show the T_a dependence of saturation magnetization which is estimated from out-of-plane *M-H* loop for the CMS/MnGa and CMS/Cr films. For the un-annealed CMS/Cr magnetization is too small. With increasing annealing temperature, magnetization of CMS increases slowly and then drastically increases after annealing temperature at 300°C. Finally the magnetization goes to maximum value for samples annealed at 400 and 450°C because of

crystallization of CMS film. The same behaviour was observed for the CMS film on MnGa layer, however, increase of magnetization is more slowly and also magnetization decreases drastically after annealing at 400ºC because of inter diffusion effect. Such a behaviours are consistent with structure changes, as can be seen from XRD result. The larger magnetization of CMS film on MnGa layer, especially for un-annealed sample, compared to the magnetization of CMS film on Cr layer suggested that better crystallization of CMS film on MnGa layer. The value of magnetization is comparable with other reports.[63,64]

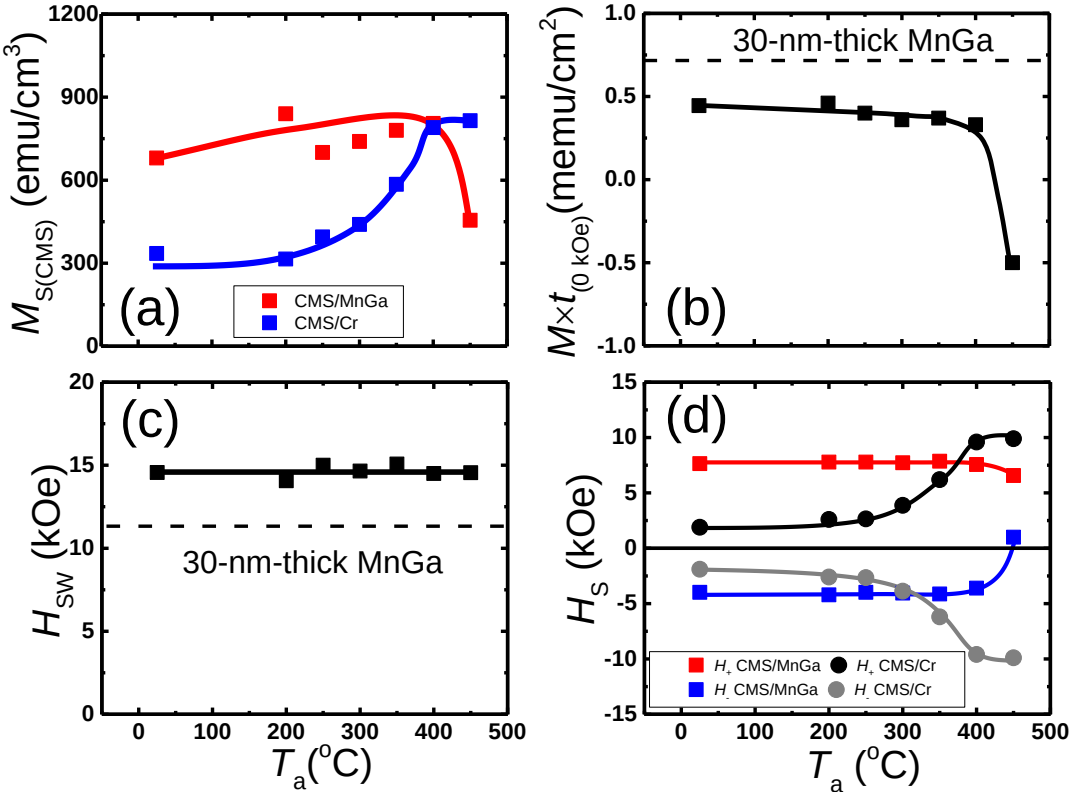

Figure 4-35 (a) The annealing temperature dependence of saturation magnetization for CMS film. (b) The annealing temperature dependence of remnant magnetization, (c) switching (d) saturation fields for CMS (20 nm)/MnGa (30 nm) bilayer film.

The T_a dependence of $M\times t_{(0\ kOe)}$ and H_{sw} are shown in Fig. 4-35 (b) and (c), respectively. The $M\times t_{(0\ kOe)}$ and H_{sw} of 30-nm-thick MnGa plotted with dashed line for comparison. When a hard magnetic film combined with the soft magnetic film in the case of no coupling H_{sw} and $M\times t_{(0\ kOe)}$ of bilayer are same as those for hard magnetic film, whereas in the case of

antiferromagnetic coupling larger H_{sw} and smaller $M \times t_{(0\ kOe)}$ are expected [3]. As can be seen from Fig. 4-35 (b), $M \times t_{(0\ kOe)}$ of CMS/MnGa bilayer films are smaller than 30-nm-thick MnGa film. The small reduction was observed for $M \times t_{(0\ kOe)}$ after annealing at 200 up to 400ºC. This indicates that magnetization of the CMS layer coupled antiferromagnetically with magnetization of MnGa. With further annealing $M \times t_{(0\ kOe)}$ decreases too much which is attributed to changes of *c* lattice constant of CMS and MnGa films because of inter diffusion effect. Fig. 4-35(c) show the H_{sw} of CMS/MnGa bilayer films are larger than value of 30-nm-thick MnGa and did not change with annealing temperature.

The T_a dependence of H_+ and H_- for CMS films on MnGa and Cr layers are shown in Fig. 4-35(d). As can be seen from this figure, H_+ and H_- for CMS films on Cr layers show a symmetry regard to H_s=0 axis as we expect for the no coupling case, whereas for the CMS films on MnGa an asymmetry was observed which is due to antiferromagnetic exchange coupling between MnGa and CMS films. For the CMS films on MnGa an asymmetry clearly was observed which is due to exchange coupling between MnGa and CMS films. In addition, H_+ is larger than absolute value of H_-. Therefore exchange coupling constant should be antiferromagnetic. It seems by increasing annealing temperature difference of H_+ and absolute value of H_- did not change too much except for the sample annealed at 450ºC.

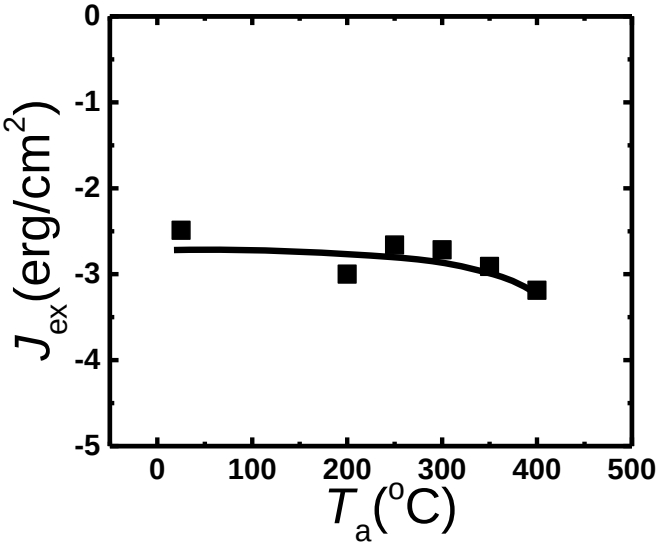

Figure 4-36 The annealing temperature dependence of interfacial exchange coupling constant CMS (20 nm)/MnGa (30 nm) bilayer film.

Figure 4-36 shows the T_a dependence of the interfacial exchange coupling constant J_{ex} for CMS/MnGa bilayer films. The sample annealed at 450ºC has been neglected for evaluation of J_{ex} because of inter diffusion effect. The J_{ex} values for the CMS/MnGa bilayer film are about -2.5 erg/cm^2 without post annealing, and reaches -3.2 erg/cm^2 with increasing the annealing temperature for sample annealed at 400ºC. These changes are attributed to different magnetization which is used for evaluation of J_{ex} at different annealing temperature. The absolute values of negative J_{ex} is comparable with those evaluated in the Co-Fe/MnGa bilayers and larger than CFA/MnGa, CFS/MnGa, and CMA/MnGa bilayer films.

A short summary will be presented here. We investigated the influence of annealing temperature on the structural and magnetic properties of CMS (20 nm)/$D0_{22}$-MnGa (30 nm)/bilayer films. The bilayer films have been successfully grown even for sample without post annealing. The optimized annealing temperature was 400ºC. We evaluated the interfacial exchange coupling constant for the bilayers with different annealing temperature. The antiferromagnetic interfacial exchange coupling was observed. The antiferromagnetic coupling strength (J_{ex} = -2.5 ~ -3.2 erg/cm^2) was relatively larger than CoB/$D0_{22}$-MnGa, CFA/$D0_{22}$-MnGa, CFS/$D0_{22}$-MnGa, and CMA/$D0_{22}$-MnGa bilayer films.

.

4.8 Thickness Dependence of Co_2MnSi (t_{CMS})/$D0_{22}$-MnGa (30 nm) Bilayer

Two series samples without post annealing and with post annealing at 400ºC by RTA system with different CMS thicknesses of 1, 3, 5, 10 and 20 nm were prepared by using an ultrahigh vacuum magnetron sputtering system with a base pressure of less than 1×10^{-7} Pa. The stacking structure of each series were: (100) single crystalline MgO substrate / Cr (10) / $D0_{22}$-MnGa (30) / CMS (t_{CMS}) / Cr (5) (thickness is in nanometers) All the layers were deposited at room temperature. The in-situ annealing was employed at 400ºC after the MnGa deposition. For characterization of structural and magnetic properties, the X-ray diffractometer (XRD) with the Cu K_α radiation, polar magneto optical Kerr effect (P-MOKE) system at laser wavelength of 400 nm, and a vibrating sample magnetometer (VSM) were used.

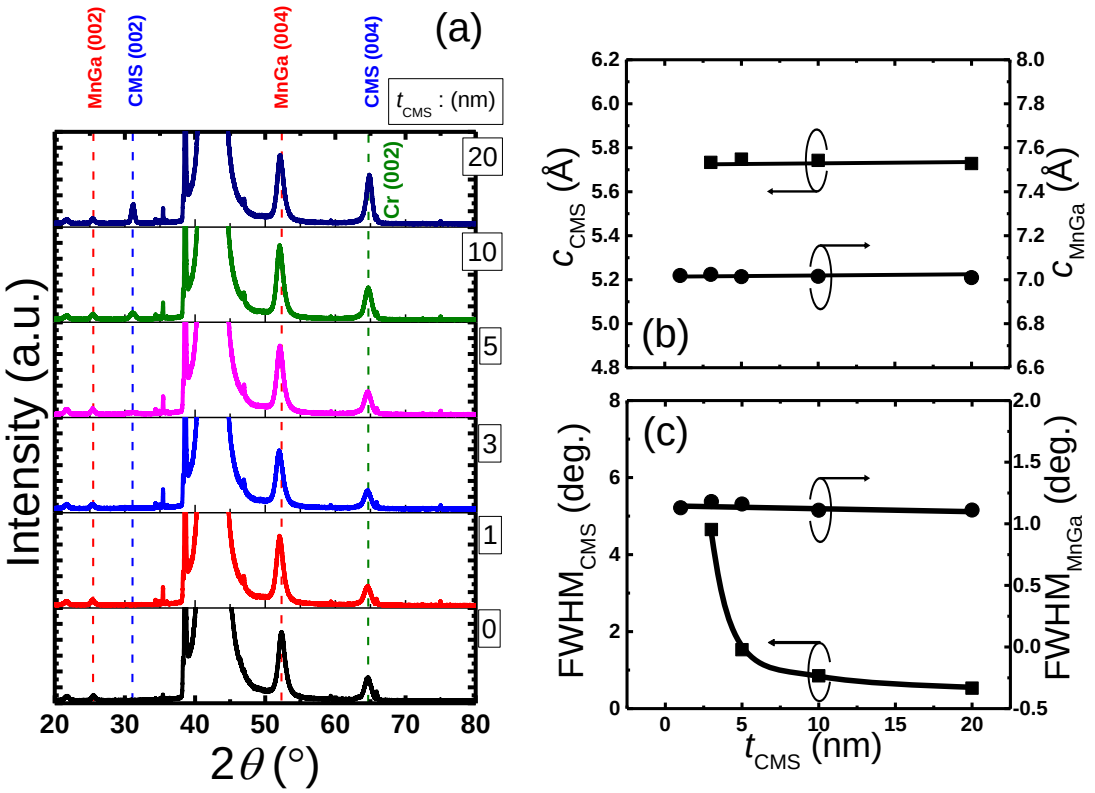

Figure 4-37 (a) The XRD pattern of CMS (0-20 nm)/MnGa (30 nm) bilayers for the un-annealed samples. (b) The CMS thickness dependence of *c* lattice constant and (c) FWHM for CMS and MnGa films.

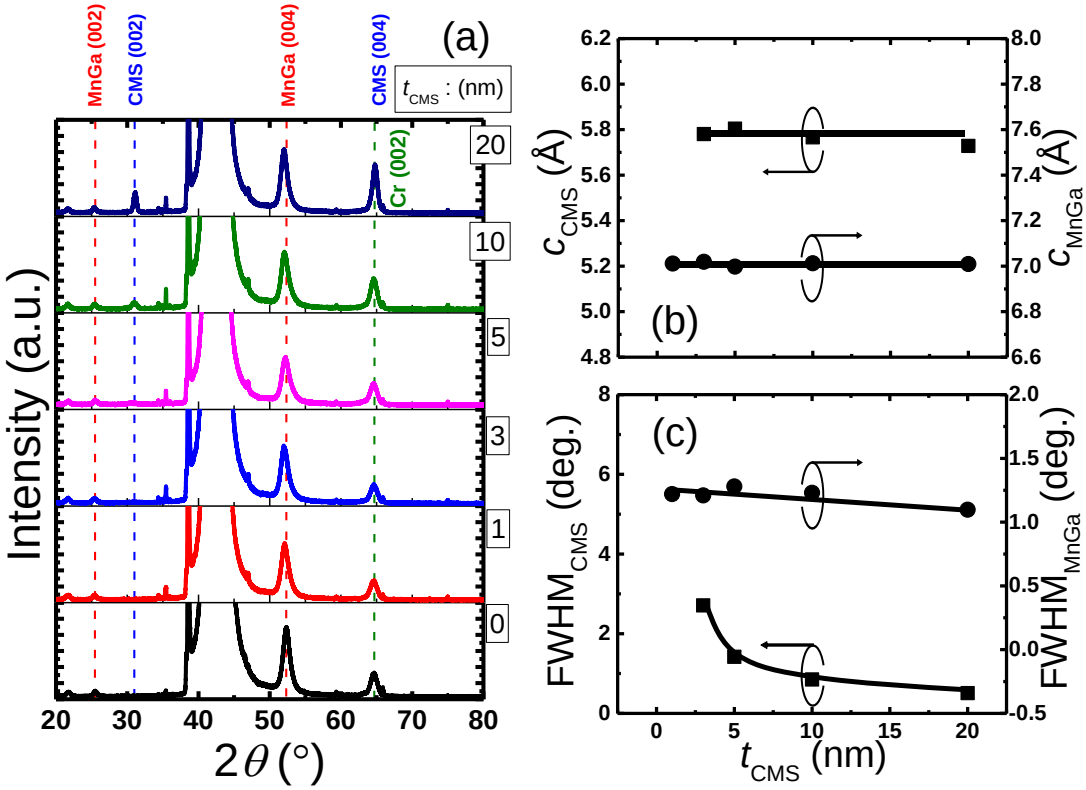

Figure 4-38 (a) The XRD pattern of CMS (0-20 nm)/MnGa (30 nm) bilayers for the samples annealed at 400ºC. (b) The CMS thickness dependence of *c* lattice constant and (c) FWHM for CMS and MnGa films

4.8.1 Structural Properties

4.8.1.1 XRD

The XRD pattern of CMS (0-20 nm)/MnGa (30 nm) bilayers for the un-annealed samples and samples annealed at 400ºC are shown in Fig 4-37 (a) and 4-38 (a), respectively. The peaks of MnGa (002), and (004) corresponding to tetragonal structure of $D0_{22}$-MnGa were clearly observed in both series samples. The minimum thickness to see (002) peak of $L2_1$ structure of CMS film (confirmed by HRTEM image in section 4.7.1.2) in XRD pattern is 3 nm for un-annealed samples and samples annealed at 400ºC, respectively. The smaller critical thickness compared to CFA, CFS, and CMA suggested better matching of CMS film to MnGa layer. The t_{CMS} dependence of the *c* lattice constant of MnGa and CMS films without and with post annealing are shown in Fig 4-37(b) and 4-38(b), respectively. The *c* lattice constant of MnGa film is constant with increasing CMS thickness for both series samples and very close to value of the reference MnGa film (7.00 Å). The *c* lattice constant of CMS film also did not change

with increasing t_{CMS} for both series samples. The t_{CMS} dependence of the FWHM (004) peak of MnGa and (002) peak of CMS films without and with post annealing are shown in Fig 4-37 (c) and 4-38 (c). For both series samples the FWHM of MnGa peak slightly decreases, whereas a nonlinear reduction was observed for the t_{CMS} dependence of FWHM for CMS peak. Such a reduction of FWHM is related to film quality.

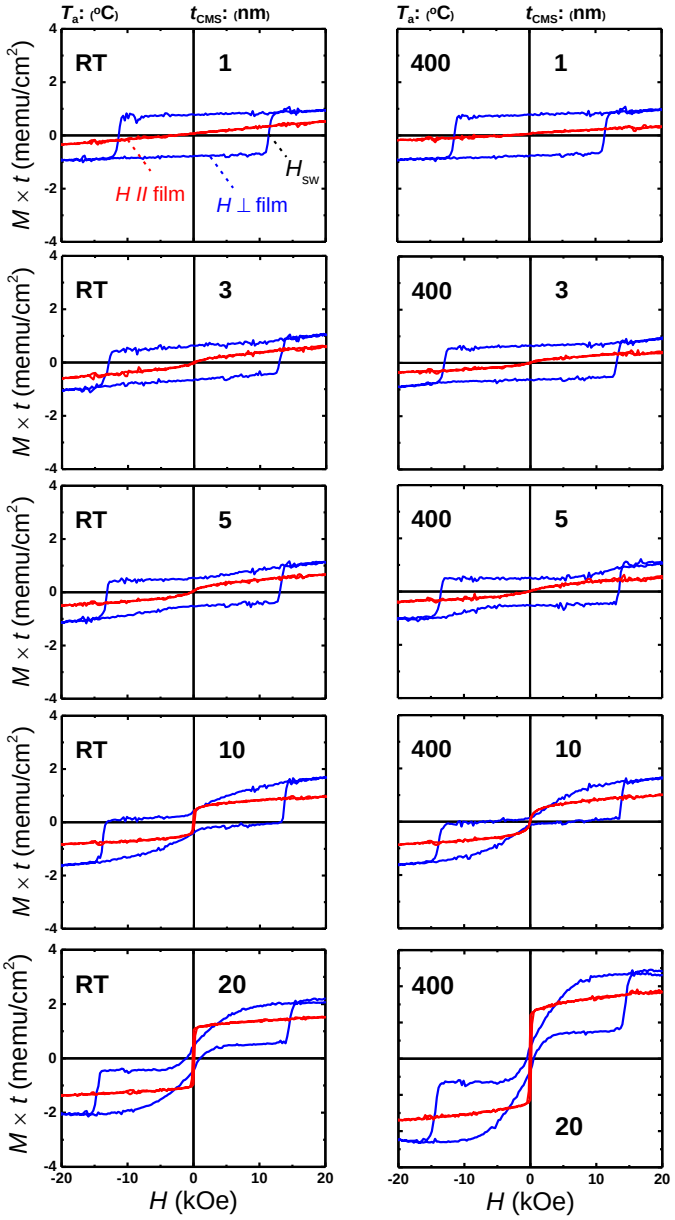

Figure 4-39 The typical out-of plane (blue colour) and in-plane (red colour) VSM *M-H* loops of CMS (1-20 nm)/MnGa (30 nm) bilayers for un-annealed samples and annealed samples at 400ºC.

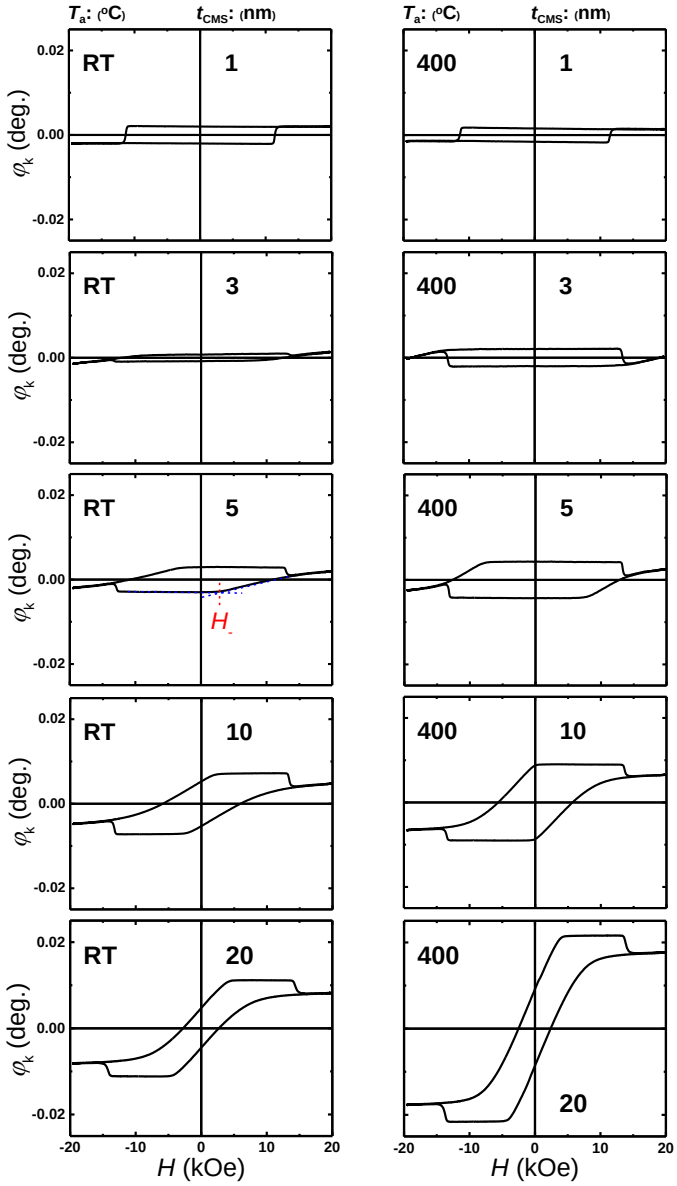

Figure 4-40 The typical polar Kerr rotation angle versus the applied field of CMS (1-20 nm)/MnGa (30 nm) bilayers for un-annealed samples and annealed samples at 4000°C.

4.8.2 Magnetic Properties

4.8.2.1 VSM

The typical out-of plane and in-plane VSM *M-H* loops of CMS (1-20 nm)/MnGa (30 nm) bilayers for un-annealed samples and samples annealed at 300°C are shown in Fig. 4-39. The

un-annealed sample and sample annealed at 400ºC with 1and 3 nm CMS thickness show similar *M-H* loop shape, but different values of $M \times t_{(0\ kOe)}$ and H_{sw} compared to with 30-nm-thick MnGa. With increasing CMS thickness up to 5 nm no in-plane component were observed for both series samples. The shape of *M-H* loops of 10 and 20 nm thick CMS films for both un-annealed and annealed samples have changed. The in plane component of Magnetization increases for thicker CMS film.

4.8.2.2 MOKE

To clarify magnetization process of CMS film and MnGa layer all the sample have been measured by MOKE system. The typical polar Kerr rotation angle versus the applied magnetic field of CMS (1-20 nm)/MnGa (30 nm) bilayers for un-annealed samples and annealed samples at 450ºC are shown in Fig. 4-40. The Un-annealed bilayer film with 1 nm CMS thickness shows flat MOKE hysteresis loop with good squareness. The inverted MOKE hysteresis loops were observed for all samples except to sample with 1 nm thick CMS film. The PMA properties were observed even for the un-annealed sample with 5 nm CMS which is due to very strong antiferromagnetic exchange coupling between CMS and MnGa films. As CMS thickness increases more, the magnetization of CMS start to tilt from perpendicular to in-plane direction because of large in-plane component for thicker CMS film.

4.8.3 Discussion and Summary

Fig. 4-41 (a) shows the t_{CMS} dependence of saturation magnetization of CMS layer which is estimated from out-of-plane *M-H* loop of CMS/MnGa bilayer film. The average saturation magnetization value of CMS for un-annealed samples are about annealed samples 800 emu/cm^3 which is comparable previous study.[63,64] The magnetization value is about 600 emu/cm^3 for the annealed sample with 5 nm thick CMS, and then increases with increasing of CMS thickness. By further increasing of CMS thickness the magnetization value saturate for samples with 10 and 20 nm thick CMS film. This trend can interpret with using FWHM data. As CMS thickness increases The FWHM decreases which means larger magnetization is due to better quality of CMS film.

The t_{CMS} dependence of $M \times t_{(0\ kOe)}$ and H_{sw} for un-annealed samples and samples annealed at 400ºC are shown in Fig. 4-41 (b) and (c), respectively. The $M \times t_{(0\ kOe)}$ and H_{sw} of 30-nm-thick MnGa plotted with dashed line for comparison. As can be seen from Fig. 4-41(b), the

t_{CMS} dependence of the $M \times t_{(0\ kOe)}$ value of un-annealed samples and samples annealed at 400ºC show similar behaviors. The $M \times t_{(0\ kOe)}$ value linearly decreases as CMS thickness increase up to 10 nm and then saturated for 10 and 20 nm thicknesses of CMS films. The reduction of the $M \times t_{(0\ kOe)}$ for annealed samples is more rapidly compared to un-annealed samples. In addition the smaller $M \times t_{(0\ kOe)}$ value was observed for samples annealed at 400ºC. The t_{CMS} dependence of H_{sw} show continues enhancement with increasing thickness of CMS film for both series samples.

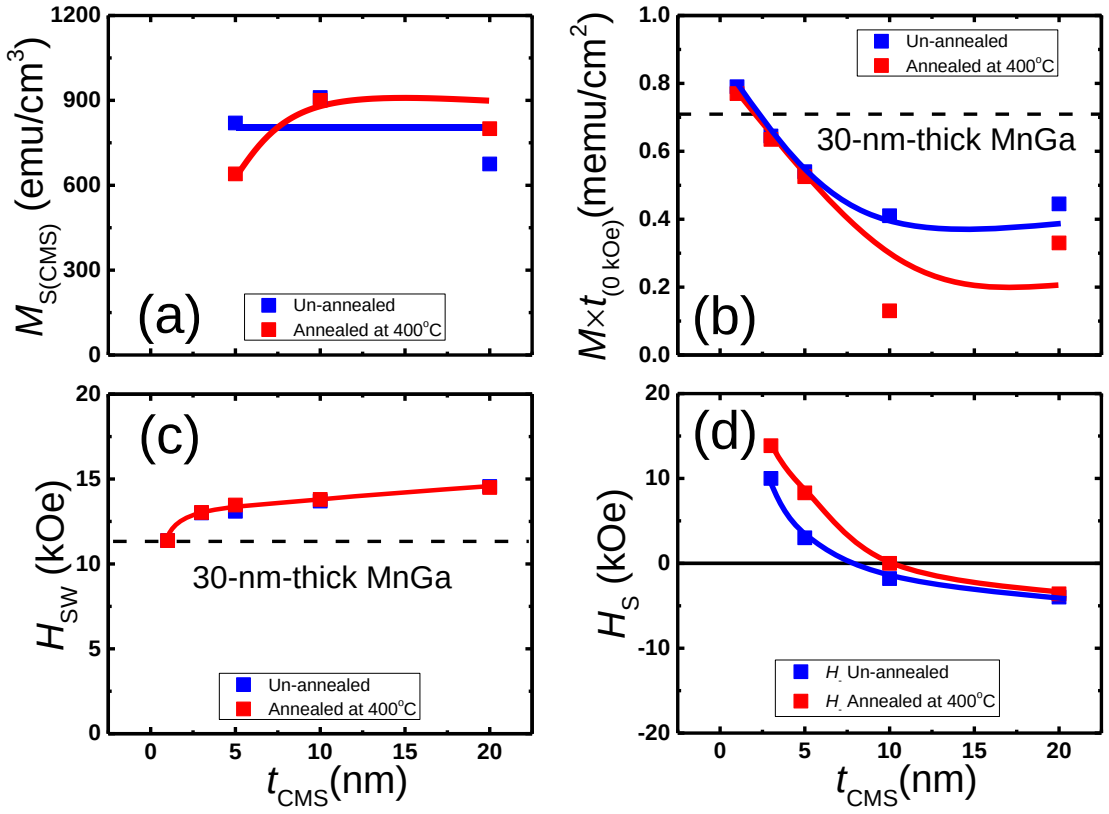

Figure 4-41 (a) The CMS thickness dependence of saturation magnetization for CMS film. (b) The CMS thickness dependence of remnant magnetization, (c) switching and (d) saturation fields for CMS (1-20 nm)/MnGa (30 nm) bilayer films.

The t_{CMS} dependence of H_+ for un-annealed samples and samples annealed at 400ºC are shown in Fig. 4-41(d). The t_{CMS} dependence of H_+ show positive value for the un-annealed and annealed samples with 5 nm CMS film. As we can see from MOKE result theses samples show very good PMA properties. This is largest critical thickness in this study. The reason is stronger

antiferromagnetic exchange coupling for CMS/MnGa bilayer compared to CFA, CFS, and CMA/MnGa bilayer films.

A short summary will be presented here. We investigated the effect of CMS thickness on the structural and magnetic properties of un-annealed samples and samples annealed at 400ºC for CMS (1-20 nm)/$D0_{22}$MnGa (30 nm) bilayer films. The annealed samples and samples annealed at 450ºC show the critical thickness to remaining PMA less than 10 nm.

Chapter 5 Reduction of the Thickness of CoMnSi (t_{CMS})/$D0_{22}$-MnGa (t_{MnGa}) Bilayer

5.1 Thickness Dependence of the $D0_{22}$-MnGa (t_{MnGa}) Films

To investigate thickness effect on structural and magnetic properties of MnGa film six film with different MnGa thicknesses of 5, 7.5, 10, 15, 20 and 30 nm were prepared by using an ultrahigh vacuum magnetron sputtering system with a base pressure of less than 1×10^{-7} Pa. The stacking structure were: the (100) single crystalline MgO substrate / Cr (10) / $D0_{22}$-MnGa (5-30) / Cr (5) (thickness is in nanometers). All the layers were deposited at room temperature. The in-situ annealing was employed at 400ºC after the MnGa deposition. For characterization of structural and magnetic properties, the X-ray diffractometer (XRD) with the Cu K_α radiation, polar magneto optical Kerr effect (P-MOKE) system at laser wavelength of 400 nm, and a vibrating sample magnetometer (VSM) were used.

5.1.1 Structural Properties

5.1.1.1 XRD

The XRD pattern of MnGa (5-30 nm) films are shown in Fig 5-1. The peaks of MnGa (002), and (004) corresponding to tetragonal structure of $D0_{22}$-MnGa clearly observed for the 30 nm thick MnGa film. As thickness of MnGa peak decreases the peak intensity and position decreases and shifted to right hand, respectively. The minimum thickness to see (002) and (004) peaks of tetragonal structure of $D0_{22}$-MnGa film in XRD pattern is 7.5. The t_{MnGa} dependence of the *c* lattice constant and FWHM of (004) peak of MnGa film are shown in Fig 51(b) and (c), respectively. The *c* lattice constant of MnGa film increases nonlinearly with increasing MnGa thickness and then reaches to maximum value for the sample with 30 nm thick MnGa film.

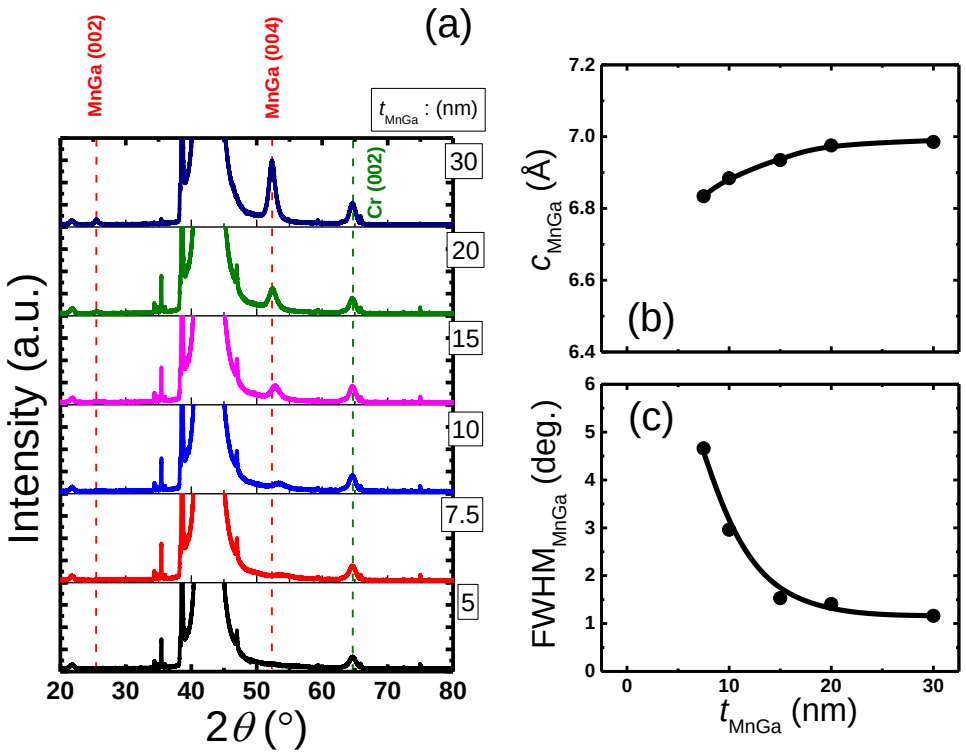

Figure 5-1 The XRD pattern for different thicknesses of MnGa (5-30 nm) film. (b) The MnGa thickness dependence of *c* lattice constant and (c) FWHM for (004) peak of MnGa film.

The t_{MnGa} dependence of the FWHM show the opposite behavior. The FWHM decrease nonlinearly to minimum value with increasing MnGa thickness. These result indicate the quality of MnGa improve with increasing thickness of MnGa film.

5.1.2 Magnetic Properties

5.1.2.1 VSM

The typical out-of plane and in-plane VSM *M-H* loops for different thicknesses of MnGa (5-30 nm) films are shown in Fig. 5-2. The *M-H* loop of 5 nm thick MnGa did not show good hysteresis curve with PMA property. With increasing thickness of MnGa film the enhancement of PMA was observed. The squareness and flatness of 7.5 nm MnGa significantly improve. As MnGa thickness increase more the hysteresis M-H loops show better PMA properties. This is consistent with XRD result which is attributed to enhancement of film quality for thicker MnGa film.

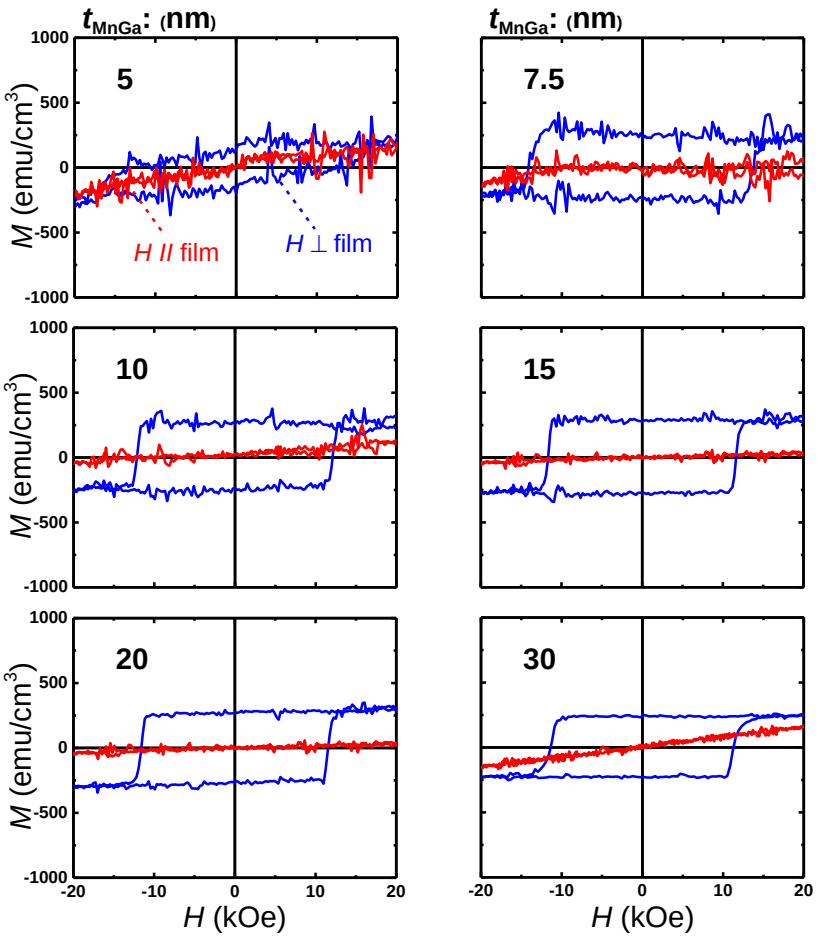

Figure 5-2 The typical out-of plane (blue colour) and in-plane (red colour) VSM *M-H* loops for different thicknesses of MnGa (5-30 nm) films.

5.1.2.2 MOKE

The typical polar Kerr rotation angle versus the applied magnetic field for different thickness of MnGa (5-30 nm) films are shown in Fig. 5-3. The MOKE measurement is consistent with VSM measurement. The minimum thickness to see hysteresis curve with good suareness and flatness is 7.5 nm which is consistent with XRD result. With increasing thickness of MnGa better hysteresis loop was obtained as well as VSM measurement. The switching filed decrease whereas Kerr rotation angle signal increases.

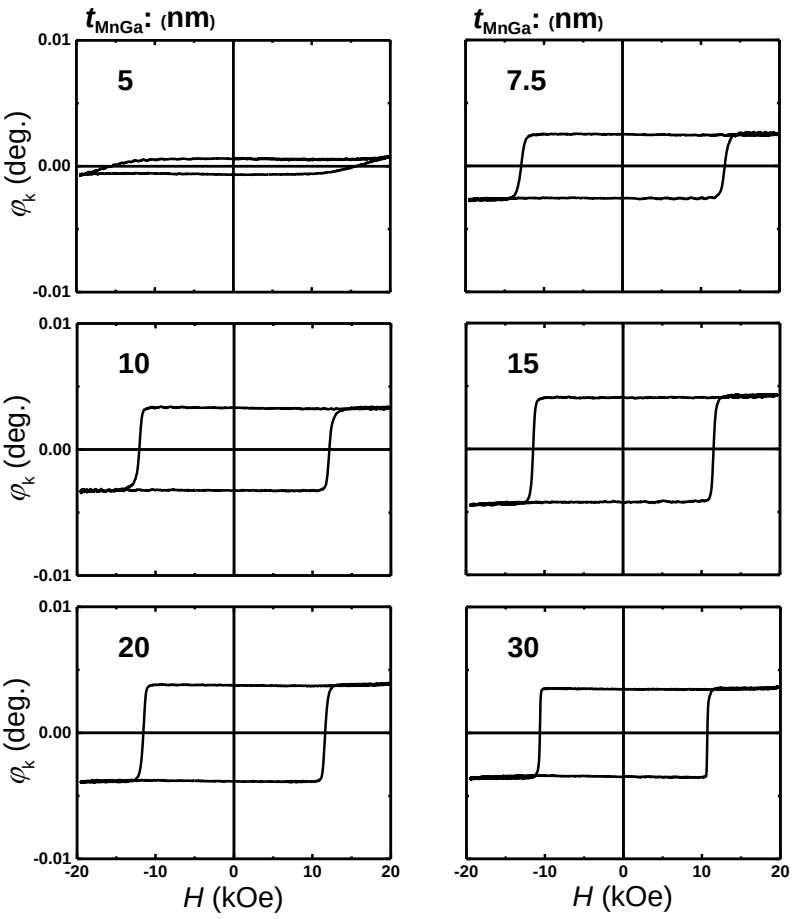

Figure 5-3 The typical polar Kerr rotation angle versus the applied field for different thicknesses of MnGa (5-30 nm) films.

5.1.3 Discussion and Summary

Fig. 5-4 (a) and (b) show the t_{MnGa} dependence of M_s and H_{sw} of MnGa film. The magnetization of MnGa value for 5 nm MnGa is about 220 emu/cm^3 and increases with increasing of MnGa thickness. For thicker MnGa film magnetization reaches to 280 emu/cm^3 which is comparable with previous report.[32]

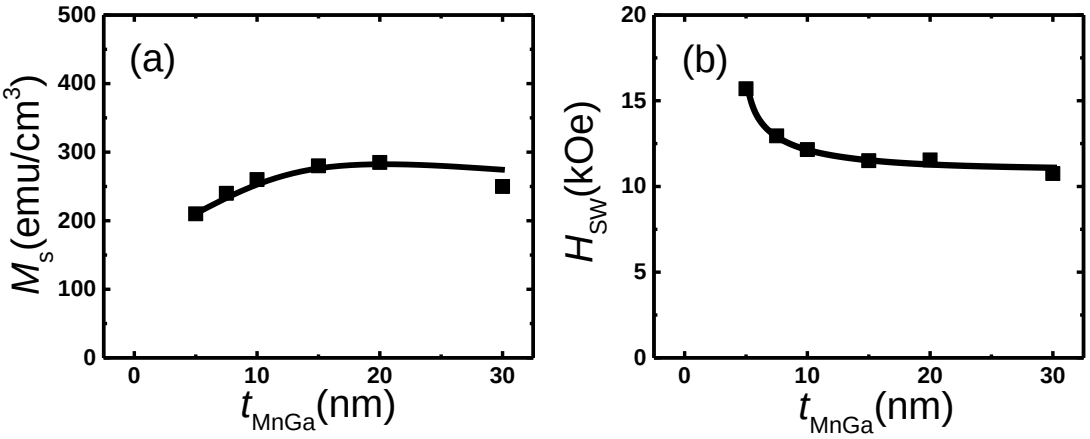

Figure 5-4 (a) The MnGa thickness dependence of saturation magnetization and (b) switching for MnGa (5-30 nm) films.

The t_{MnGa} dependence of H_{sw} shows opposite trend compared to the t_{MnGa} dependence of $M \times t_{(0\ kOe)}$. continues enhancement with increasing thickness of CMS film for both series samples. The relatively large H_{sw} about 16 kOe was observed for 5 nm thick MnGa. With increasing thickness of MnGa film H_{sw} decreases nonlinearly and the saturate for 15, 20 and 30 nm MnGa film. The trend of M_s and H_{sw} is with XRD results. The larger M_s and smaller H_{sw} are expected for MnGa film with good quality.

A short summary will be presented here. We investigated the effect of MnGa thickness on the structural and magnetic properties of $D0_{22}$MnGa (5-30 nm) films. The minimum critical thickness to see good magnetic properties with PMA was 7.5 nm.

5.2 Thickness Dependence of the Co_2MnSi (t_{CMS})/$D0_{22}$-MnGa (t_{MnGa}) Bilayer

Two series samples without post annealing and with post annealing at 400ºC by RTA system with different CMS thicknesses of 1, 3, 5, and 7 nm were prepared by using an ultrahigh vacuum magnetron sputtering system with a base pressure of less than 1×10^{-7} Pa. The stacking structure of each series were: the (100) single crystalline MgO substrate / Cr (10) / $D0_{22}$-MnGa (7.5) / CMS (t_{CMS}) / Cr (5) (thickness is in nanometers) All the layers were deposited at room temperature. The in-situ annealing was employed at 400ºC after the MnGa deposition. For characterization of structural and magnetic properties, the X-ray diffractometer (XRD) with the Cu K_α radiation, polar magneto optical Kerr effect (P-MOKE) system at laser wavelength of 400 nm, and a vibrating sample magnetometer (VSM) were used.

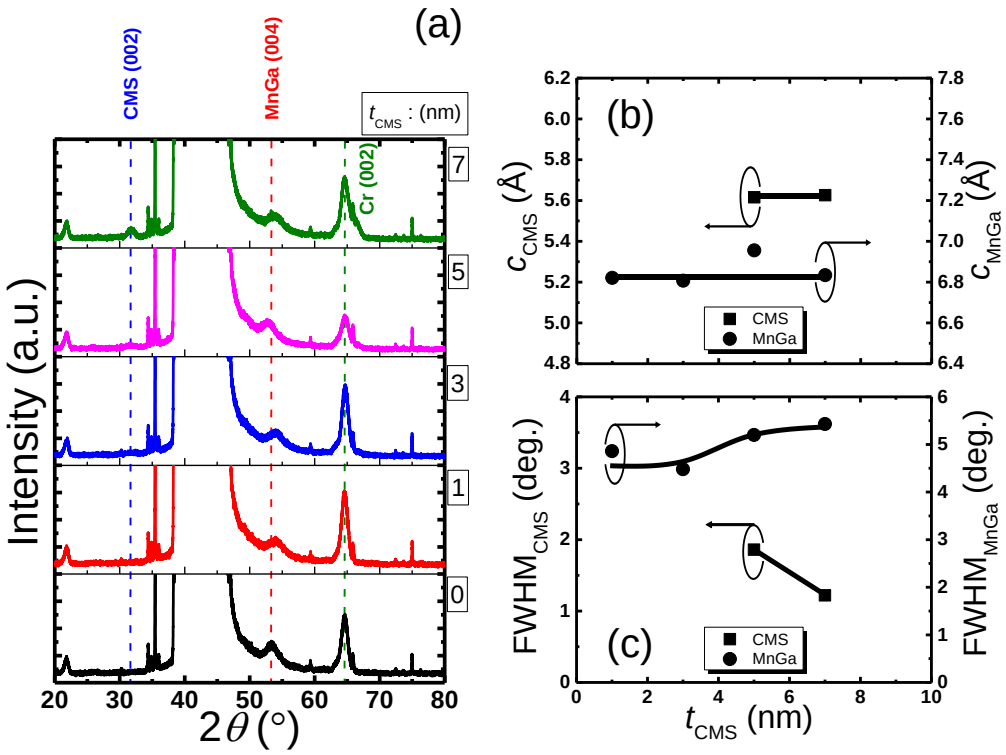

Figure 5-5 The XRD pattern of CMS (1-7 nm)/MnGa (7.5 nm) bilayers for the un-annealed samples. (b) The CMS thickness dependence of *c* lattice constant and (c) FWHM for CMS and MnGa films

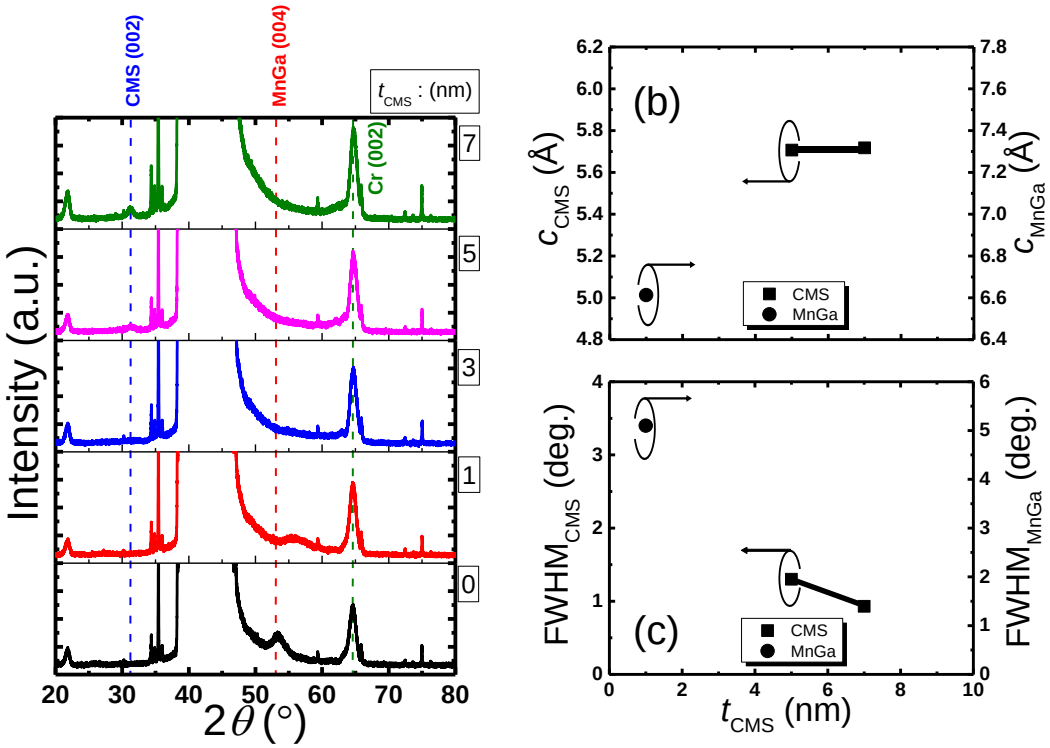

Figure 5-6 The XRD pattern of CMS (1-7 nm)/MnGa (7.5 nm) bilayers for the samples annealed at 400ºC. (b) The CMS thickness dependence of *c* lattice constant and (c) FWHM for CMS and MnGa films.

5.2.1 Structural Properties

5.2.1.1 XRD

The XRD pattern of CMS (1-7 nm)/MnGa (7.5 nm) bilayers for the un-annealed samples and samples annealed at 400ºC are shown in Fig 5-5 (a) and 5-6 (a), respectively. The (004) peak corresponding to tetragonal structure of $D0_{22}$-MnGa was clearly observed for un-annealed samples. The peak position did not change too much with increase of CMS thickness. However bilayer film with 5 nm thick CMS show a deviation from other films. This is may be due to sample fabrication or measurement problem. For the samples annealed at 400ºC, the (004) peak of MnGa was observed only for bilayer film with 1 nm thick CMS. It seems with increasing of CMS thickness inter diffusion effect is significant. So MnGa peak disappear and another peak appear which has overlap with Cr peak. This can be concluded from different intensity of Cr peak. The minimum thickness to see (002) peak of $L2_1$ structure of CMS film in XRD pattern is 5 nm for un-annealed samples and samples annealed at 400ºC. The t_{CMS} dependence of the *c*

lattice constant of MnGa and CMS films without and with post annealing are shown in Fig 5-5 (b) and 5-6 (b), respectively. The *c* lattice constant of MnGa film is constant with increasing CMS thickness for un-annealed samples and the value is smaller than the *c* lattice constant of 30 nm thick MnGa (7.00 Å). The smaller *c* lattice constant was observed for the annealed sample with 1 nm thick CMS film.

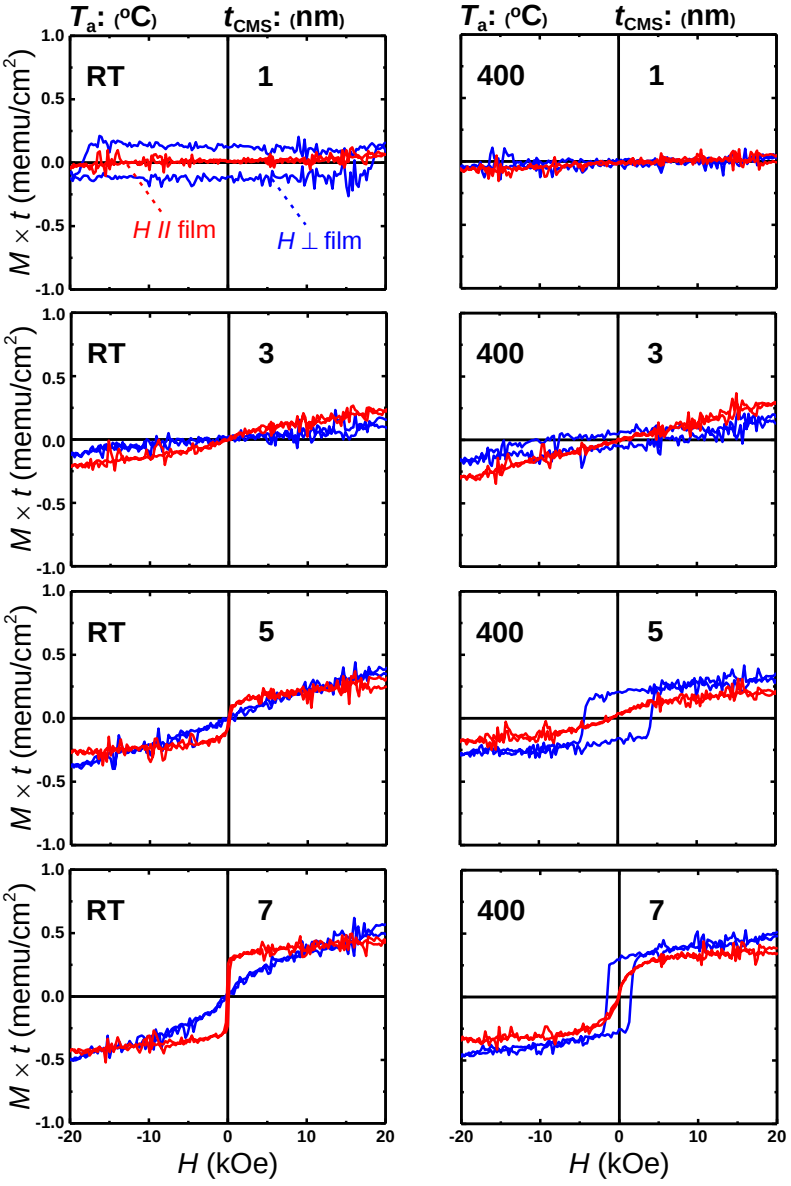

Figure 5-7 The typical out-of plane (blue colour) and in-plane (red colour) VSM *M-H* loops of CMS (1-7 nm)/MnGa (7.5 nm) bilayers for un-annealed samples and annealed samples at 400°C.

The t_{CMS} dependence of the FWHM for (004) peak of MnGa and (002) peak of CMS films without and with post annealing are shown in 5-5(c) and 5-6(c). The FWHM of MnGa peak increases with increasing of CMS film. The reason is unclear. For both series samples the smaller FWHM of CMS peak were observed for bilayer film 7 nm thick CMS compared to 5 nm thick CMS film. However, FWHM of annealed samples is smaller than un-annealed samples which suggested the quality of annealed CMS film should be better.

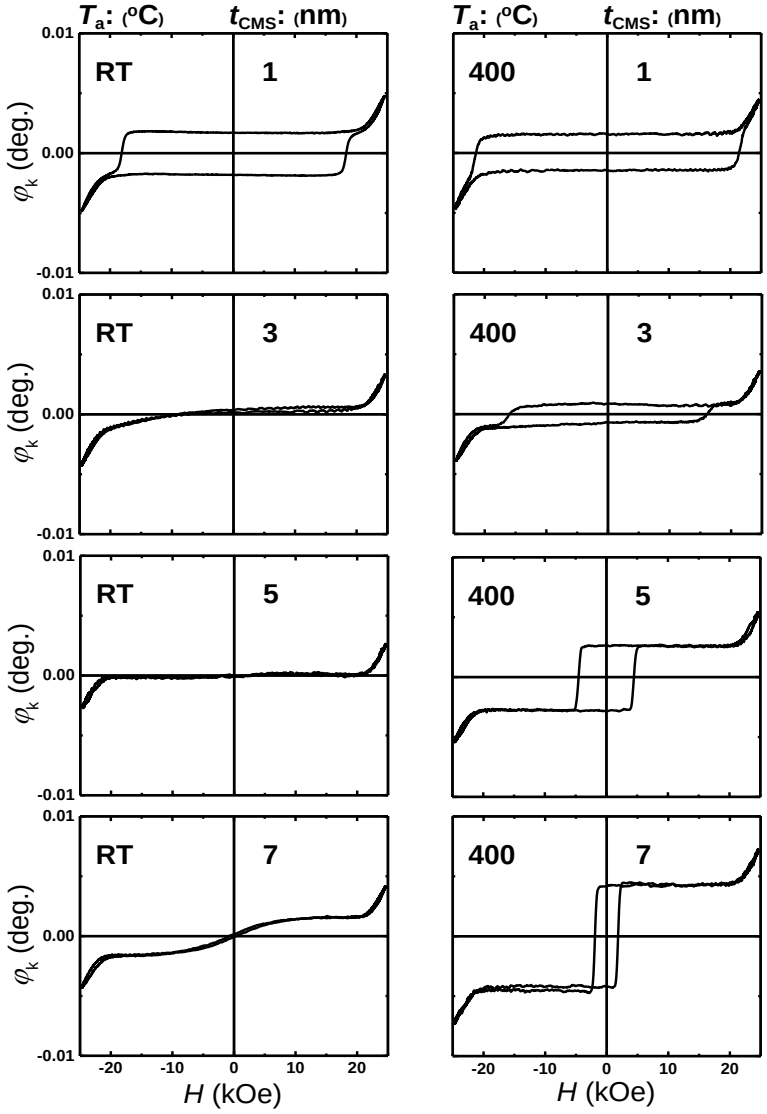

Figure 5-8 The typical polar Kerr rotation angle versus the applied field of CMS (1-7 nm)/MnGa (7.5 nm) bilayers for un-annealed samples and annealed samples at 400°C.

5.2.2 Magnetic Properties

5.2.2.1 VSM

The typical out-of plane and in-plane VSM *M-H* loops of CMS (1-7 nm)/MnGa (7.5 nm) bilayers for un-annealed samples and samples annealed at 400ºC are shown in Fig. 5-7. The un-annealed sample with 1 nm CMS thickness show PMA property. With increasing thickness of CMS film, out of plane *M-H* did not show magnetic properties, whereas in plane component of *M-H* loop increases with increasing of CMS thickness. It seems magnetic field is not enough large to detect major loop of hysteresis curves for thicker CMA film. The bilayer film with 1 nm thick CMS shows H_{sw} larger than 18 kOe. When the thickness of CMS film increases the enhancement of H_{sw} are expected as shown in Fig. 4-40 (c). Therefore large field measurement is needed to measure major *M-H* loop. The annealed sample with 1 nm thick did not show magnetic property because of same reason. However, with increasing of CMS thickness, the out of plane *M-H* loop shows hysteresis curve which originates from mixing of CMS film and MnGa as shown in XRD result.

5.2.2.2 MOKE

To clarify magnetization process of CMS film and MnGa layer all the sample have been measured by MOKE system. The typical polar Kerr rotation angle versus the applied magnetic field of CMS (1-7 nm)/MnGa (7.5 nm) bilayers for un-annealed samples and annealed samples at 400ºC are shown in Fig. 5-8. The magnetic field was set 25 kOe. The different MOKE hysteresis loop was observed for un-annealed bilayer film with 1 nm CMS thickness compared to VSM measurement due to large field measurement. So, this measurement indicates our speculation might be correct. The other MOKE measurement is consistent with VSM measurement. The slope that appears in MOKE measurement when magnetic field is larger than 20 kOe is coming from background. Both un-annealed and annealed sample with 1 nm thick CMS film show good flatness and squareness. The PMA properties clearly were observed for both sample. However, the Kerr rotation angle signal decreases due to stronger exchange coupling for the annealed sample. With increasing of CMS thickness, the annealed sample show clear hysteresis loop with relatively smal H_{sw} which originates from CMS-MnGa alloy

5.2.3 Discussion and Summary

The t_{CMS} dependence of $M \times t_{(0\ kOe)}$ and H_{sw} for un-annealed samples and samples annealed at 400ºC are shown in Fig. 5-9 (a) and (b), respectively. The $M \times t_{(0\ kOe)}$ and H_{sw} of 7.5-nm-thick MnGa plotted with dashed line for comparison. As can be seen from Fig. 5-9 (a), the t_{CMS} dependence of the $M \times t_{(0\ kOe)}$ value of un-annealed samples and samples annealed at 400ºC show different behaviors. The un-annealed sample with 1 nm thick CMS film has smaller $M \times t_{(0\ kOe)}$ and larger H_{sw} values than 7.5 nm thick MnGa film which indicates good PMA property with antiferromagnetic exchange coupling between CMS and MnGa films. With increasing CMS thickness, no $M \times t_{(0\ kOe)}$ and H_{sw} were observed. This may related to minor *M-H* loop. On the other hand, samples annealed at 400ºC show $M \times t_{(0\ kOe)}$ and H_{sw}, increases and decreases linearly with increasing of CMS thickness which originates from making CMS-MnGa alloy due to inter diffusion effect.

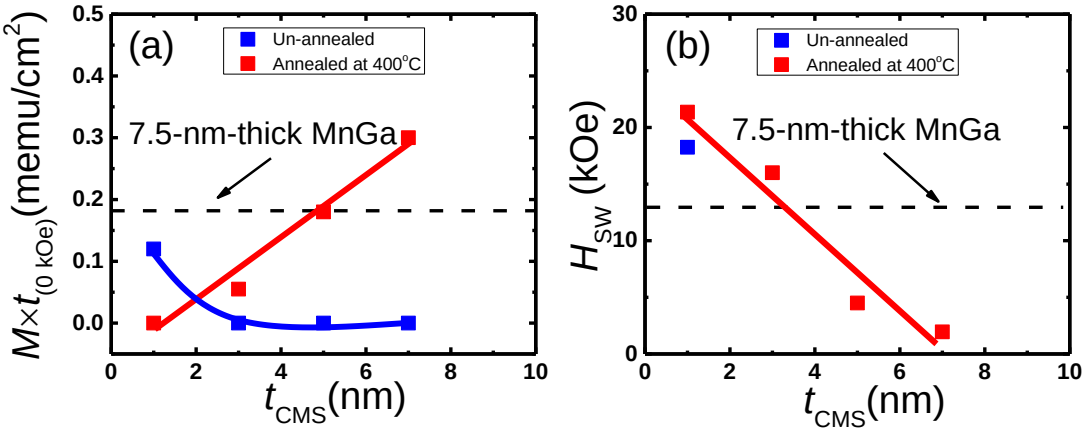

Figure 5-9 (a) The CMS thickness dependence of remnant magnetization and (b) switching for CMS (1-7 nm)/MnGa (7.5 nm) bilayer films.

A short summary will be presented here. We investigated the effect of CMS thickness on the structural and magnetic properties of un-annealed samples and samples annealed at 400ºC for CMS (1-7 nm)/$D0_{22}$MnGa (7.5 nm) bilayer films. The un-annealed sample with 1 nm thick CMS show good PMA property. It seems after annealing inter diffusion effect is significant and the CMS-MnGa alloy is formed at the interface of CMS and MnGa films.

Chapter 6 Discussion

In this chapter discussion about experimental results will be presented and then we will summarize this study. Different bilayer films were fabricated to make synthetic ferrimagnet layer with fully perpendicular magnetic anisotropy. The Co, CoB, CFA, CFS, CMA and CMS were used as IMA materials in IMA/$D0_{22}$-MnGa bilayer films. Annealing dependence has been investigated for IMA (20 nm)/$D0_{22}$-MnGa (30 nm). The interfacial exchange coupling of all bilayer film except to Co/ MnGa bilayer film were evaluated from experimental results. The annealing critical temperature which defined as maximum annealing temperature for bilayer films without significant change in structure due to inter diffusion effect will be summarized. The optimized annealing temperature were used for fabrication of IMA (1-20 nm)/$D0_{22}$-MnGa(30 nm) bilayer films to investigate thickness dependence of IMA films as well as bilayer films without post annealing. In order to which bilayer film shows good PMA properties, the critical thickness were estimated from MOKE hysteresis loop for all the IMA material in this study. To compare structural and magnetic properties, the J_{ex}, T_c, t_c, and M_s are summarized in table 6-1 for different IMA materials in this study.

Let's consider interfacial exchange coupling for different bilayer films. The CoB/MnGa bilayer film has smallest value of interfacial exchange coupling in this study. The CoB film is amorphous, whereas another material in this study have crystallized structure. This indicates ordering and arrangement of atoms at interface is very effective to get strong exchange coupling. However, Heusler alloys have crystallized structure, different kind and strength of exchange coupling were observed. The annealing temperature dependence of interfacial exchange coupling constant for different Heusler alloys is shown in Fig. 6-1. The CFA/$L1_0$-MnGa bilayer film show ferromagnetic and antiferromagnetic exchange coupling depending on annealing temperature, whereas only antiferromagnetic exchange coupling were observed for CFS/MnGa, CMA/MnGa, and CMS/MnGa bilayer films. This could be interpreted with different electronic band structure of Heusler alloys as already have been discussed in chapter 4. Here we will discussed details, more.

Table 6-1 Summary of structural and magnetic parameters for different IMA materials in this study.

IMA materials	$-J_{ex}$ (erg/cm^2)	T_c (ºC)	Un-annealed t_c (nm)	Annealed t_c (nm)	M_s (emu/cm^3)	Structure
Co	-	350	< 1	< 1	1250	crystallized
CoB	0-0.3	350	< 3	3	530	amorphous
CFA	-0.8-1.5	450	< 3	< 3	1200	crystallized
CFS	0.4-1	350	< 3	3	950	crystallized
CMA	0.75-1.15	450	< 5	< 5	500	crystallized
CMS	2.5-3.2	400	< 10	< 10	800	crystallized

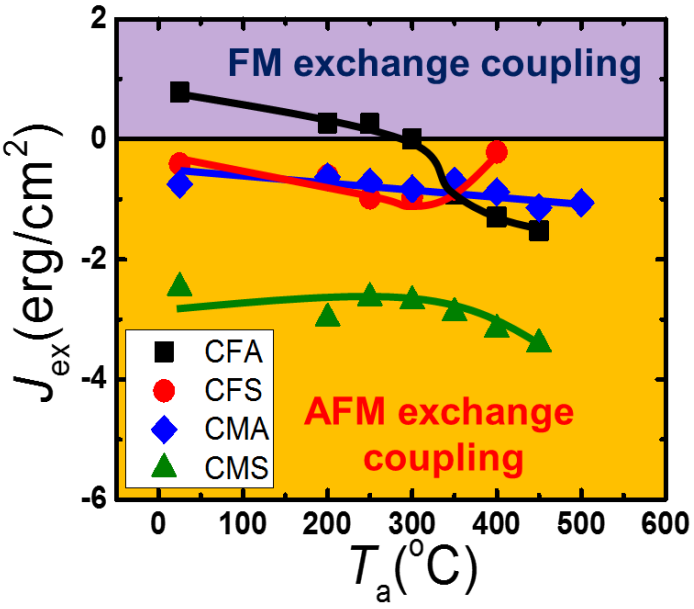

Figure 6-1 The annealing temperature dependence of interfacial exchange coupling constant for different Heusler alloys.

The composition dependence of $Fe_{1-x}Co_x$ alloy on exchange coupling for Fe-Co/MnGa bilayer film have been investigate by Ma *et al.*[37] They found an abrupt transition from ferromagnetic to antiferromagnetic exchange coupling when x is approximately 25% as shown

in Fig. 6-2 (a). They have interpreted this behavior by using electronic band structure of Fe-Co and MnGa alloys. Bcc-textured $Fe_{1-x}Co_x$ and $L1_0$-MnGa alloys are 3d transition alloys exhibiting itinerant magnetism. The coupling between 3d metals mainly depends on the Coulomb repulsion and Pauli exclusion, which are dependent on the band structure and occupancy. The density of states (DOSs) of the $Fe_{1-x}Co_x$ and MnGa alloys with bcc and $L1_0$ structures are shown in Fig. 6-2 (c). $Fe_{1-x}Co_x$ shows two major peaks in both spin-up (↑) and spin-down (↓) channels. The ↑ and ↓ bands of bcc $Fe_{1-x}Co_x$ alloys have a similar shape, with a shift in energy from exchange splitting. Because of the sharp peak in the Fermi level, the exchange coupling between these 3d alloys mainly depends on Coulomb repulsion. However, the band of $L1_0$-ordered MnGa shown in Fig. 6-2 (c) has a different structure. The ↑ spin band has a sharp peak located below the Fermi level. The ↓ band shows a broad distribution of the DOS number (N) across the Fermi level. Thus, the coupling is mainly dependent on the Pauli exclusion effect, which suggests electrons near the Fermi level with antiparallel spins coupled together. This gives a FM coupling of magnetization of MnGa and Fe layers in the MnGa/Fe interface because the Fe ↑ band is coupled with the ↓ band of MnGa alloys near the Fermi level. As the Co content increases in the $Fe_{1-x}Co_x$ alloy, the electron number increases, and the Fermi level gradually moves up, as illustrated in Fig. 6-2 (c). Therefore coupling changes from ferromagnetic to antiferromagnetic.

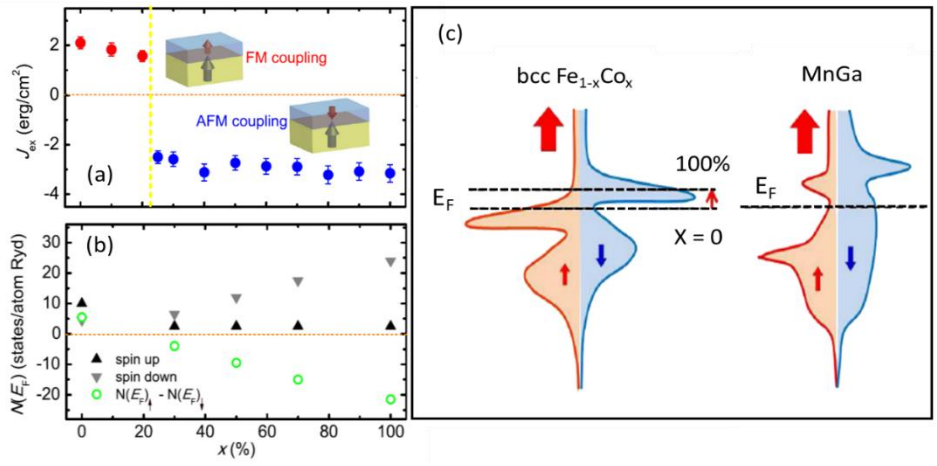

Figure 6-2 (a) J_{ex} in the $Fe_{1-x}Co_x$/MnGa interface as a function of $Fe_{1-x}Co_x$ composition. (b) Spin-up (black up triangle) and spin-down (gray down triangle) density of states at the Fermi level of $Fe_{1-x}Co_x$ alloy with bcc structure. (c) Illustration of the band structure of bcc$Fe_{1-x}Co_x$ and $L1_0$ MnGa alloys.[37]

As already shown in Fig. 1-12 in chapter 1, the electronic structure of $D0_{22}$-MnGa and $L1_0$-MnGa show roughly same trend at Fermi level. However, the $D0_{22}$-MnGa shows larger spin polarization compared with $L1_0$-MnGa. Therefore, we can use above model for interpretation of experimental results. The Electronic structure of CFA and CFS that reported by E. I. shredder[65] and also electronic structure of CMA, and CMS that reported by J. C. Tung[66] are shown in Fig. 6-3. The CFA Heusler has the Fermi level in the middle of minority spin band gap and CFS alloy has the Fermi level in the edge of minority conduction band. So, expectations for types of coupling with $D0_{22}$-MnGa alloy are ferromagnetic and antiferromagnetic coupling based on above model for CFA and CFS Heusler alloys, respectively. This is consistent with experimental results in which ferromagnetic and antiferromagnetic coupling were observed in low temperature regime for CFA and CFS Heusler alloys, respectively. The type of coupling should be ferromagnetic for CMA and CMS Heusler alloys with $D0_{22}$-MnGa alloy based on above model. However, experimental results showed only antiferromagnetic coupling exist between CMA and CMS Heusler alloys with $D0_{22}$-MnGa film.

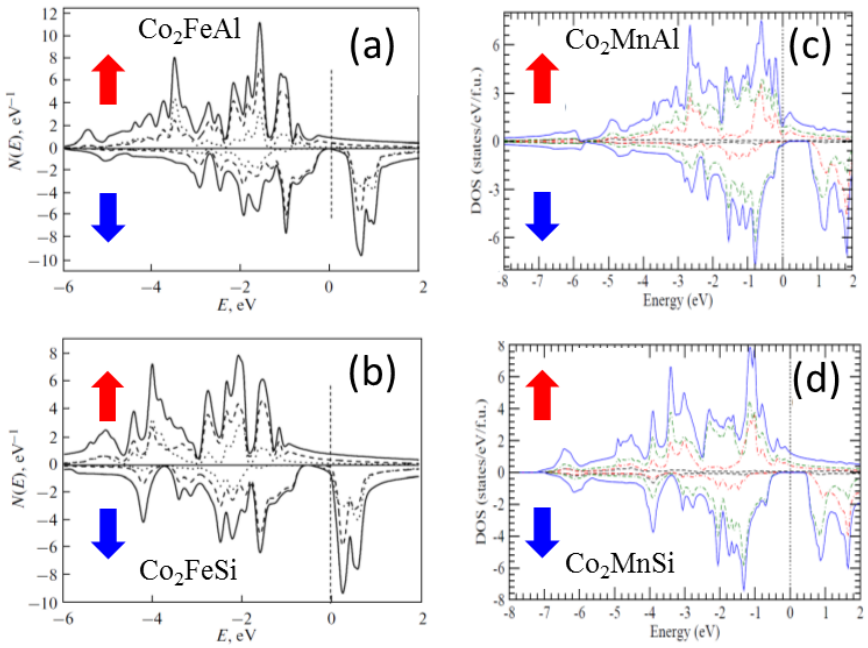

Figure 6-3 The electronic band structure of (a) Co_2FeAl, (b) Co_2FeSi, (c) Co_2MnAl, and (d) Co_2FeAl.[65,66]

The electronic structure for CMA and CMS Heusler alloys in four different structures are shown in Fig. 6-4.[67] In addition, cubic lattice structure of the Heusler compounds with four inequivalent sites and chemical elements per site for all considered structures are shown in Fig. 6-5.[67] As can be seen from Fig. 6-4 when structure changes electronic band structures show different shapes. Electronic band structures of $L2_1$A and B2-ordered for CMA and CMS Heusler alloys are similar to Fe-rich in bcc $Fe_{1-x}Co_x$ alloy. Therefore, exchange coupling type should be ferromagnetic. However, electronic band structures of $L2_1$B and XA-ordered for CMA and CMS Heusler alloys are similar to Co-rich in bcc $Fe_{1-x}Co_x$ alloy which suggest antiferromagnetic exchange coupling. The exchange coupling interaction acts at interfaces of Heusler alloys and $D0_{22}$-MnGa alloy with thickness less than 1 or 2 nm. So, determination of type of coupling is very difficult, because the coupling is very sensitive to many parameters such as lattice constant, interface structure, and inter diffusion as well as contribution of atoms at interface. As experimental results showed both types of exchange coupling for CFA Heusler alloy depending on annealing temperature. This is may be due to change of structure and lattice constant. In addition, contribution of atoms at interface can change due to annealing.

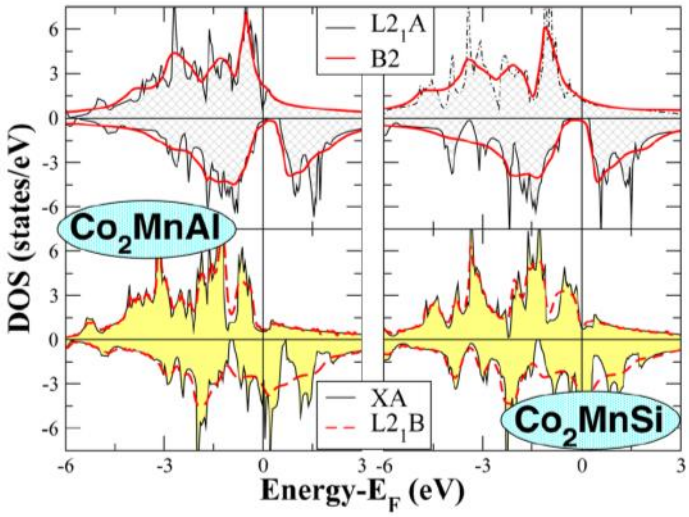

Figure 6-4 (left column) Total DOS for Co_2MnAl in four different structures; (right column) same for Co_2MnSi.[67]

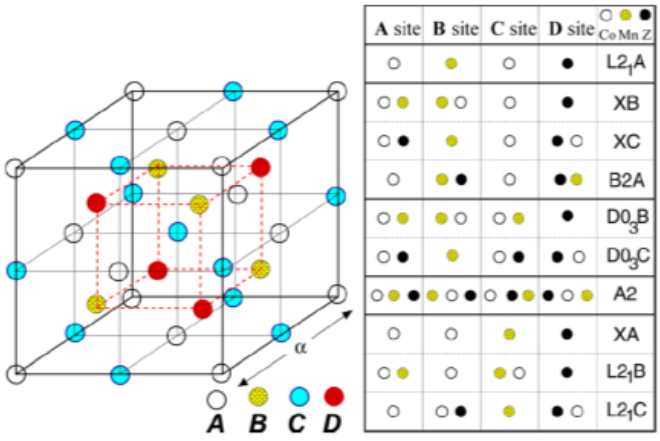

Figure 6-5 (left) Cubic lattice structure of the Heusler compounds with four inequivalent sites. (right) Chemical elements per site for all considered structures.[67]

Now, let's consider why exchange strength for different Hesuler alloys are different? To find answer for this question only un-annealed bilayer films will consider to neglect structure changes due to annealing temperature. All the Heusler alloys in this study are Co-based alloys. So Fe, Mn, Al, and Si make different properties for theses alloys. If we compare CFA with, CFS alloys and CMA with CMS alloys separately, result can help us to find roles of Heusler alloy when coupled to MnGa film. The CFS and CMS alloys show the stronger antiferromagnetic coupling compared to CFA and CMA alloys, respectively which indicates tendency of Si to make antiferromagnetic exchange coupling is larger than Al. The same comparison can be applied for CFA with CMA and CFS with CMS alloys. The CMA and CMS show the stronger antiferromagnetic coupling compared to CFA and CFS alloys, respectively which indicates tendency of Mn to make antiferromagnetic exchange coupling is larger than Fe. Further studies are needed for clarifying the origin.

The next question is: what is the reason of different annealing critical temperature observation for different Heusler alloys?

The same interpretation will be helpful to find answer of this question. The CMA and CFA show larger annealing critical temperature compared to CMS and CFS alloys, respectively which originates from different diffusivity of Al and Si.

The saturation magnetization and also the critical thickness of IMA materials to show PMA for bilayer films with and without post annealing are shown in table 6-1. The CMS show the critical thickness less than 10 nm for un-annealed and annealed samples which is largest critical thickness in this study. It seems the critical thickness depends on strength of exchange coupling constant and saturation magnetization value. The CoB and CMA alloys show roughly same saturation magnetization, but different critical thickness. The critical thickness of CMA alloy is larger than CoB alloy. As can be seen from table 6-1 CMA alloy has larger absolute value of antiferromagnetic exchange coupling than CoB alloy. So, this larger antiferromagnetic exchange coupling is the reason for larger critical thickness of CMA alloy. However, exchange coupling constant of CFS is comparable with CMA, smaller critical thickness was observed for CFS due to larger saturation magnetization of CFS alloy compared to CMA. Therefore, the relatively large critical thickness of CMS alloy originates from strong antiferromagnetic exchange coupling and moderate saturation magnetization. In addition, annealed samples show the larger critical thickness compared to un-annealed samples which suggested larger coupling strength causes to larger critical thickness to keep PMA properties.

Chapter 7: Conclusion and Future perspective

7.1 Conclusion

In this dissertation we study on the structural and magnetic properties of the bilayer consisting of in plane magnetic anisotropy materials and $D0_{22}$-MnGa film. First, Co-B binary were tested as IMA materials in this study. Then the Co-based cubic Heusler alloys including Co_2FeAl (CFA), Co_2FeSi (CFS), Co_2MnAl (CMA), and Co_2MnSi (CMS) were used as IMA materials.

The influence of annealing temperature on the structural and magnetic properties of IMA (20 nm)/$D0_{22}$-MnGa (30 nm) bilayer films were investigated. All the bilayer films have been successfully grown even for un-annealed samples. Large critical annealing temperature were observed for the CFA/MnGa (450°C) and CMA/MnGa (450°C) bilayer, which shows the good structural stability.

We evaluated the interfacial exchange coupling constant for the bilayers with different annealing temperature. The antiferromagnetic interfacial exchange coupling was observed for CoB/MnGa bilayer film. The weak coupling strength may be due to amorphous structure of CoB alloy. The antiferromagnetic interfacial exchange coupling were observed for CFS/MnGa (J_{ex} = -0.4 ~ -1 erg/cm^2), CMA/MnGa (J_{ex} = -0.75 ~ -1.15 erg/cm^2), and CMS/MnGa (J_{ex} = -2.5 ~ -3.2 erg/cm^2) bilayers, whereas both kinds of interfacial exchange couplings were observed in the CFA/MnGa (J_{ex} = 0.8 ~ -1.5 erg/cm^2) bilayer depending on annealing temperature. The ferromagnetic and antiferromagnetic interfacial exchange couplings in Co-based cubic Heusler alloys and tetragonal $D0_{22}$-MnGa film originate from their electronic band structure at Fermi level. The relative strong interfacial antiferromagnetic exchange coupling about -3.2 erg/cm^2 was observed for CMS/MnGa bilayer which is comparable with Fe-Co/MnGa work.

In order to fabricate synthetic ferrimagnet with good PMA, the thickness of Co-based cubic Heusler alloys were decreased. The critical thickness for remaining PMA properties of bilayer was estimated from magnetic properties. The largest critical thickness less than 10 nm was observed for CMS/MnGa bilayer which originates from strong antiferromagnetic coupling (J_{ex}

≈ -3.2 erg/cm^2) and moderate saturation magnetization (M_s ≈ 800 emu/cm^3) compared to another Co-based cubic Heusler alloys.

Finally the thickness of CMS cubic Heusler alloys and $D0_{22}$-MnGa film were decreased to determine minimum critical thickness for synthetic ferrimagnet with PMA. The bilayer with 1-nm-thick CMS and 7.5-nm-thick $D0_{22}$-MnGa shows good PMA.

7.2 Future perspective

These experimental results mentioned above suggest CMS/MnGa bilayer as free electrode for making p-MTJ based on MnGa alloy. The stacking structure of p-MTJ based on CMS/MnGa bilayer as free electrode is shown in Fig 7-1. To get high TMR ratio, epitaxy condition of p-MTJ such as annealing temperature should be optimized.

The window of this research still is open to decrease thickness of bilayer system more by using another deposition methods. To clarify origin of exchange coupling between MnGa and those materials used in this work, more theoretical research such as electronic band structure study is needed. In addition, to determine value of damping constant, which is important for reduction of critical current density in STT-MRAM, and make clear mechanism of spin dynamic, time resolved magneto-optical Kerr effect (TRMOKE) research will be interesting.

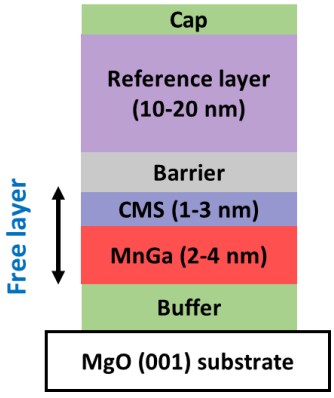

Figure 7-1 Stacking structure of p-MTJ based on CMS/MnGa bilayer as free electrode.

References

1. M. Johnson, R. H. Silsbee, "Interfacial charge-spin coupling: Injection and detection of spin magnetization in metals", *Phys. Rev. Lett.* **55**, 1790 (1985).

2. Baibich, Mario Norberto and Broto, JM and Fert, Albert and Van Dau, F Nguyen and Petroff, F and Etienne, P and Creuzet, G and Friederich, A and Chazelas, J. Giant magnetoresistance of (001) Fe/(001) Cr magnetic superlattices, *Phys. Rev. Lett.* **2472**, 1988 (61AD).

3. G. Binasch, and P. Gr"unberg, F. Saurenbach, and W. Zinn, "Enhanced magnetoresistance in layered magnetic structures with antiferromagnetic interlayer exchange", *Phys. Rev. B* **39**, 4828–4830 (1989).

4. M. Julliere, "Tunneling between ferromagnetic films". *Phys. Lett. A* **54**, 225–226 (1975).

5. S. Datta, and B. Das, "Electronic analog of the electro-optic modulator", *Appl. Phys. Lett.* **56**, 665–667 (1990).

6. T. Miyazaki, and N. Tezuka, "Giant magnetic tunneling effect in Fe/Al_2O_3/Fe junction", *J. Magn. Magn. Mater.* **139**, L231–L234 (1995).

7. T. Miyazaki, and H. Jin, "The physics of ferromagnetism", **158,** (2012).

8. R. Moodera, S. Jagadeesh, L. Kinder, R. Wong, M. Terrilyn, and R. Meservey, "Large magnetoresistance at room temperature in ferromagnetic thin film tunnel junctions", *Phys. Rev. Lett.* **74**, 3273 (1995).

9. W. H. Butler, X. G. Zhang, T. C. Schulthess, and J. Maclaren, "Spin-dependent tunneling conductance of Fe/MgO/Fe sandwiches", *Phys. Rev. B* **63**, 054416 (2001).

10. J. Mathon, and A. Umerski, "Theory of tunneling magnetoresistance of an epitaxial Fe/MgO/Fe (001) junction", *Phys. Rev. B* **63**, 220403 (2001).

11. M. Bowen, *et al*. "Large magnetoresistance in Fe/MgO/FeCo (001) epitaxial tunnel junctions on GaAs (001)", *Appl. Phys. Lett.* **79**, 1655–1657 (2001).

12. S. Yuasa, T. Nagahama, A. Fukushima, Y. Suzuki, and K. Ando, "Giant room-temperature magnetoresistance in single-crystal Fe/MgO/Fe magnetic tunnel junctions", *Nat. Mater.* **3**, 868–871 (2004).

13. S. Parkin, C. Kaiser, A. Panchula, P. Rice, B. Hughes, M. Samant, and S. H. Yang, "Giant tunnelling magnetoresistance at room temperature with MgO (100) tunnel barriers", *Nat. Mater.* **3**, 862–867 (2004).

14. S. Ikeda, J. Hayakawa, Y. Ashizawa, Y. M. Lee, K. Miura, H. Hasegawa, M. Tsunoda, F. Matsukura, and H. Ohno, "Tunnel magnetoresistance of 604% at 300 K by suppression of Ta diffusion in CoFeB/MgO/CoFeB pseudo-spin-valves annealed at high temperature", *Appl. Phys. Lett.* **93**, 082508–082508 (2008).

15. R. C. Sousa, and I. L. Prejbeanu, "Non-volatile magnetic random access memories (MRAM)", *Comptes Rendus Phys.* **6**, 1013–1021 (2005).

16. B. Dieny, *et al.* "Spin-transfer effect and its use in spintronic components", **7**, 591–614 (2010).

17. Y. Huai, F. Albert, P. Nguyen, M. Pakala, and T. Valet, "Observation of spin-transfer switching in deep submicron-sized and low-resistance magnetic tunnel junctions", *Appl. Phys. Lett.* **84**, 3118 (2004).

18. L. Berger, "Emission of spin waves by a magnetic multilayer traversed by a current", *Phys. Rev. B* **54**, 9353–9358 (1996).

19. J. A. Katine, F. J. Albert, and R. A. Buhrman, "Current-Driven Magnetization Reversal and Spin-Wave Excitations in Co-Cu-Co Pillars", *Phys. Rev. Lett.* **84**, 3149–3152 (2000).

20. D. C. Ralph, and M. D. Stiles, "Spin transfer torques", *J. Magn. Magn. Mater.* **320**, 1190–1216 (2008).

21. G. Kim, Y.Sakuraba, M. Oogane, Y. Ando, T. Miyazaki, "Tunneling magnetoresistance of magnetic tunnel junctions using perpendicular magnetization $L1_0$-CoPt electrodes", *Appl. Phys. Lett.* **92**, 172502 (2008).

22. T. Seki, S. Mitani, K. Yakushiji, and K. Takanashi, "Spin-polarized current-induced magnetization reversal in perpendicularly magnetized $L1_0$-FePt layers". *Appl. Phys. Lett.* **88**, 172504 (2006).

23. S. Ikeda, *et al.* "A perpendicular-anisotropy CoFeB-MgO magnetic tunnel junction", *Nat. Mater.* **9**, 721–4 (2010).

24. H. Meng, and J. P. Wang, "Spin transfer in nanomagnetic devices with perpendicular anisotropy", *Appl. Phys. Lett.* **88**, 172506 (2006).

25. K. Mizunuma, *et al.* "MgO barrier-perpendicular magnetic tunnel junctions with CoFe/Pd multilayers and ferromagnetic insertion layers", *Appl. Phys. Lett.* **95**, 232516 (2009).

26. S. Mangin, *et al.* "Current-induced magnetization reversal in nanopillars with perpendicular anisotropy", *Nat. Mater.* **5**, 210–215 (2006).

27. T. Hatori, H. Ohmori, M. Tada, and S. Nakagawa, "MTJ Elements With MgO Barrier Using RE-TM Amorphous Layers for Perpendicular MRAM", *IEEE Trans. Magn.* **43**, 2331–2333 (2007).

28. M. Nakayama, *et al.* "Spin transfer switching in TbCoFe/CoFeB/MgO/CoFeB/TbCoFe magnetic tunnel junctions with perpendicular magnetic anisotropy", *J. Appl. Phys.* **103**, 07A710 (2008).

29. Y. Sakuraba, *et al.* "Giant tunneling magnetoresistance in Co_2MnSi/Al–O/Co_2MnSi magnetic tunnel junctions", *Appl. Phys. Lett.* **88**, 192508 (2006).

30. X.S. Lu, J.K. Ling, M. G. Zhou, *Acta. Phys. Sin.* **29**, 469–484 (1980).

31. K. Minakuchi, , R. Y. Umetsu, K. Ishida, and R. Kainuma, "Phase equilibria in the Mn-rich portion of Mn–Ga binary system", *J. Alloys Compd.* **537**, 332–337 (2012).

32. S. Mizukami, *et al.* "Composition dependence of magnetic properties in perpendicularly magnetized epitaxial thin films of Mn-Ga alloys", *Phys. Rev. B* **85**, 014416 (2012).

33. T. A. Bither, and W. H. Cloud, "Magnetic Tetragonal δ Phase in the Mn[Single Bond]Ga Binary", *J. Appl. Phys.* **36,** 1501 (1965).

34. E. Kr′en, and G. K′ad′ar, "Neutron diffraction study of Mn_3Ga", *Solid State Commun.* **8**, 1653–1655 (1970).

35. H. Kurt, K. Rode, M. Venkatesan, P. Stamenov, and J. M. D. Coey, "High spin polarization in epitaxial films of ferrimagnetic Mn_3Ga", *Phys. Rev. B* **83**, 020405 (2011).

36. B. Balke, G. H. Fecher, J. Winterlik, and C. Felser, "Mn_3Ga, a compensated ferrimagnet with high Curie temperature and low magnetic moment for spin torque transfer applications", *Appl. Phys. Lett.* **90**, 152504 (2007).

37. Q. L. Ma, *et al.* "Abrupt Transition from Ferromagnetic to Antiferromagnetic of Interfacial Exchange in Perpendicularly Magnetized $L1_0$-MnGa/FeCo Tuned by Fermi Level Position" *Phys. Rev. Lett.* **112**, 157202 (2014).

38. Q. Ma, *et al.* "Tetragonal Heusler-Like Mn–Ga Alloys Based Perpendicular Magnetic Tunnel Junctions". *Spin.* **4**, 1440024 (2014).

39. W. Feng, D. V. Thiet, D. D. Dung, Y. Shin, and S. Cho, "Substrate-modified ferrimagnetism in MnGa films", *J. Appl. Phys.* **108**, 113903 (2010).

40. F. Wu, *et al.* "Epitaxial $Mn_{2.5}Ga$ thin films with giant perpendicular magnetic anisotropy for spintronic devices", *Appl. Phys. Lett.* **94**, 122503 (2009).

41. S. Mizukami, *et al.* "Long-Lived Ultrafast Spin Precession in Manganese Alloys Films with a Large Perpendicular Magnetic Anisotropy", *Phys. Rev. Lett.* **106**, 117201 (2011).

42. T. Kubota, *et al.* "Composition dependence of magnetoresistance effect and its annealing endurance in tunnel junctions having Mn-Ga electrode with high perpendicular magnetic anisotropy", *Appl. Phys. Lett.* **99**, 192509 (2011).

43. T. Kubota, *et al.* "Dependence of Tunnel Magnetoresistance Effect on Fe Thickness of Perpendicularly Magnetized $L1_0$-$Mn_{62}Ga_{38}$/Fe/MgO/CoFe Junctions", *Appl. Phys. Express* **5**, 043003 (2012).

44. Q. L. Ma, *et al.* "Magnetoresistance effect in $L1_0$-MnGa/MgO/CoFeB perpendicular magnetic tunnel junctions with Co interlayer", *Appl. Phys. Lett.* **101**, 032402 (2012).

45. F. Wuwei, *et al.* "Epitaxial Growth and Magnetic Properties of Mn-Ga Thin Films on GaSb(001)", *J. Korean Phys. Soc.* **56**, 1382 (2010).

46. Z. Bai, *et al.* "Magnetic and transport properties of $Mn_{3-x}Ga$/MgO/$Mn_{3-x}Ga$ magnetic tunnel junctions: A first-principles study", *Appl. Phys. Lett.* **100**, 022408 (2012).

47. K. Wang, E. Lu, J. W. Knepper, F. Yang, and A. R. Smith, "Structural controlled magnetic anisotropy in Heusler $L1_0$−MnGa epitaxial thin films", *Appl. Phys. Lett.* **98**, 162507 (2011).

48. T. Kubota, *et al.* "Magnetic tunnel junctions of perpendicularly magnetized $L1_0$ -MnGa / Fe / MgO / CoFe structures : Fe-layer-thickness dependences of magnetoresistance effect and tunnelling conductance spectra", *J. Phys. D.* **46**, 155001 (2013).

49. T. Kubota, *et al.* "Magnetoresistance Effect in Tunnel Junctions with Perpendicularly Magnetized $D0_{22}$-$Mn_{3-\delta}Ga$ Electrode and MgO Barrier", *Appl. Phys. Express* **4**, 043002 (2011).

50. J. Daillant, and A. Gibaud, "X-ray and Neutron Reflectivity", *Lect. Notes Phys.* **770**, 133–182 (2009).

51. S. Foner, "Versatile and Sensitive Vibrating-Sample Magnetometer", *Rev. Sci. Instrum.* **30**, 548 (1959).

52. G. Asti, M. Ghidini, R. Pellicelli, C. Pernechele, and M. Solzi, "Magnetic phase diagram and demagnetization processes in perpendicular exchange-spring multilayers", *Phys. Rev. B* **73**, 094406 (2006).

53. G. Ortiz, *et al.* "Static and dynamic magnetic properties of epitaxial Co2FeAl Heusler alloy thin films", *J. Appl. Phys.* **109**, 07D324 (2011).

54. P. C. Joshi, P. K. Rout, Z. Hossain, and R. C. Budhani, "Charge transport and magnetic ordering in laser ablated Co_2FeSi thin films epitaxially grown on (100) $SrTiO_3$", *J. Phys. D. Appl. Phys.* **43**, 255002 (2010).

55. M. Hashimoto, J. Herfort, , H. P. Schönherr, and K. H. Ploog, "Epitaxial Heusler alloy Co_2FeSi/GaAs (001) hybrid structures", *Appl. Phys. Lett.* **87**, 102506 (2005).

56. G. Lauhoff, *et al.* "Ferrimagnetic τ-MnAl/Co Superlattices on GaAs", *Phys. Rev. Lett.* **79**, 1–4 (1997).

57. Y. Miura, K. Abe, and M. Shirai, "Half-metallic behavior of Co_2MnSi/Co_2MnAl/MgO interface and its coherent tunneling conductance", *J. Phys. Conf. Ser.* **200**, 052016 (2010).

58. E. Ozawa, S. Tsunegi, M. Oogane, H. Naganuma, and Y. Ando, "The effect of inserting thin Co_2MnAl layer into the Co_2MnSi/MgO interface on tunnel magnetoresistance effect", *J. Phys. Conf. Ser.* **266**, 012104 (2011).

59. J. P. Wüstenberg, *et al.* "Surface spin polarization of the nonstoichiometric Heusler alloy Co_2MnSi". *Phys. Rev. B* **85**, 064407 (2012).

60. T. Kobayashi, H. Tsuji, S. Tsunashima, S. Uchiyama, "Magnetization process of exchange-coupled ferrimagnetic double-layered films", *Jpn. J. Appl. Phys.* **20**, 2089–2095 (1981)

61. A. Aharoni, "Exchange anisotropy in films, and the problem of inverted hysteresis loops", *J. Appl. Phys.* **76**, 6977 (1994).

62. J. Yang, *et al.* "Inverted hysteresis loops observed in a randomly distributed cobalt nanoparticle system". *Phys. Rev. B* **78**, 094415 (2008).

63. S. Tsunegi, Y. Sakuraba, M. Oogane, K. Takanashi, and Y. Ando, "Large tunnel magnetoresistance in magnetic tunnel junctions using a Co_2MnSi Heusler alloy electrode and a MgO barrier", *Appl. Phys. Lett.* **93**, 112506 (2008).

64. Y. Sakuraba, *et al.* "Mechanism of large magnetoresistance in Co_2MnSi/Ag/Co_2MnSi devices with current perpendicular to the plane". *Phys. Rev. B* **82**, 094444 (2010).

65. E. I. Shreder, A. D. Svyazhin, and K. A. Belozerova, "Optical properties of heusler alloys Co_2FeSi, Co_2FeAl, Co_2CrAl, and Co_2CrGa", *Phys. Met. Metallogr.* **114**, 904–909 (2013).

66. J. C. Tung, and G.Y. Guo, "High spin polarization of the anomalous Hall current in Co-based Heusler compounds", *New J. Phys.* **15**, 033014 (2013).

67. K. Özdoğan, and I. Galanakis, "Effect of order on the half-metallic gap in Heusler compounds", *J. Appl. Phys.* **110**, 076101 (2011).